University of Reading
Department of Meteorology

# Modelling the Variability of the Earth's Radiation Budget

A Thesis Submitted for the Degree of Doctor of Philosophy

Richard Philip Allan

October 1998

**Acknowledgements**

The input, encouragement and enthusiasm of my supervisors, Keith Shine and Tony Slingo are acknowledged and appreciated. Sincere thanks are also conveyed to Mark Webb and Alison Pamment. Thanks also to Keith Browning, Chris Thorncroft and David Allan for valued suggestions and comments. Typing of references from Ann Allan is also appreciated. Thanks also to R. Weller, S. Anderson, C. Long and the STAR team for help with the observational data sets at the surface. The NASA Langley Research Centre is acknowledged for the use of the ERBE data. This work is funded by a NERC studentship (GT41/95/263) under CASE award with the Meteorological Office.

*'But now they only block the sun,*
*Rain and snow on ev'ryone,*
*So many things I would have done,*
*But clouds got in my way'*[1]

[1]Both Sides Now - Joni Mitchell ©1967 Crazy Crow Music, BMI

# Contents

## *Abstract*

*The quantitative understanding of the climate system requires assessment of the variability of the Earth's radiation budget. A simulation of clear-sky longwave irradiance is employed for this purpose. The simulation uses a comprehensive re-analysis system (ERA) and samples globally. Radiometric observations at the surface and at the top of the atmosphere are also utilised.*

*Temperature variability determines the variation of clear-sky top of atmosphere outgoing longwave irradiance ($OLR_c$) for latitudes greater than 40 °. Changes in relative humidity (RH) strongly influence the $OLR_c$ variability at low latitudes. The surface clear-sky downwelling longwave irradiance ($SDL_c$) is sensitive to changes in column moisture and near-surface temperature. Evaluation of the simulated $SDL_c$ is undertaken. Simulated $SDL_c$ is generally within the observational uncertainty of 10 $Wm^{-2}$.*

*Regions exhibiting a super-greenhouse effect are characterised and explained by changes in RH associated with shifts in the large-scale circulation. The principle findings are that locally, changes in RH throughout the troposphere, but most especially in the mid-troposphere, significantly affect $OLR_c$ variability. Globally, interannual RH fluctuations do not significantly alter the nature of the water vapour feedback in ERA which is strongly positive. These conclusions depend on the realistic representation of free-tropospheric RH by ERA; validation of this quantity is required for an improved understanding of the water vapour feedback.*

*Variation in RH influences strongly the longwave and shortwave cloud radiative forcing. The net absorbed radiation variability is primarily determined by $OLR_c$ in some sub-tropical regions. Changes in RH in these dry descending regions are likely to exert a large influence on the radiation budget. The identification of interannual variability is prone to significant error due to (i) artificial drifts in ERA climate, (ii) inter-satellite calibration problems and (iii) clear-sky sampling by satellite. The present study provides a rationale for the evaluation of climate models.*

# Chapter 1

# THE EARTH'S RADIATION BUDGET AND CLIMATE

## 1.1 Introduction

The global climatic regime imposes a direct constraint on agricultural productivity and the biological carrying capacity of the Earth (e.g. Bolin *et al.* (1986)). It is therefore unsurprising that changes in climate over time-scales from years to centuries and millenia have exerted a profound impact on the social and political history of the modern world (e.g. Lamb (1982)). The distribution of climatic regimes is determined by the balance between absorbed shortwave radiation (ASR) from the sun and emitted outgoing longwave radiation to space (OLR) from the Earth's surface and atmosphere, and the subsequent re-distribution of the net energy surplus received at low latitudes to higher latitude regions which receive a net energy deficit. The dependence of this radiative balance and the large-scale redistribution of energy on atmospheric and surface properties must be extensively assessed to consolidate our understanding of the present climate and to augment our skill in the prediction of future climate change.

The influence of the atmosphere and clouds on the radiation budget may be illustrated by considering a simple energy balance model with the surface temperature ($T_s$) being determined by the equilibrium between the incoming shortwave and outgoing longwave radiation at the surface. A schematic representation of the Earth radiation budget is presented in Fig. 1.1. Firstly, consider the situation where the Earth's atmosphere and clouds were removed. Assuming the present day value of ASR, which therefore still includes the shortwave reflective component of clouds and the surface, a balance would exist at $T_s$=255 $K$ (Fig. 1.1(b)), some 33 $K$ less than the present day value (Fig. 1.1(a)). This difference in

temperature is ascribed to the greenhouse effect of the atmosphere and clouds. With neither the longwave nor the shortwave radiative effects of the atmosphere and clouds, ASR would increase from the present day value of 235 $Wm^{-2}$ to 292 $Wm^{-2}$, assuming the present surface albedo. The surface emission, $\sigma T_s^4$ ($\sigma = 5.67 \times 10^{-8}\ Wm^{-2}K^{-4}$), will therefore balance the ASR at $T_s$=268 $K$ (Fig. 1.1(c)). Thus the greenhouse effect is seen to significantly warm the Earth-atmosphere system, while the cloud radiative or albedo effect offsets this warming by approximately 40%, relative to an Earth without an atmosphere.

Arrhenius (1896) was one of the first to investigate the link between changes in carbon dioxide concentration and the global climate. Carbon dioxide is a potent absorber of longwave radiation and a so-called 'greenhouse gas'. An increase in the atmospheric concentration of greenhouse gases, due to the combustion of carbon-based fuels for example, will lead to an increased absorption of upwelling radiation. Because temperatures generally decrease with altitude in the troposphere this will effectively reduce the OLR thereby causing a net radiative heating of the Earth-atmosphere system due to the enhancement of the greenhouse effect. The recorded increases and projected future increases in the concentration of many greenhouse gases constitutes a potentially large anthropogenic warming influence on the global climate. To quantify the impact of this effect on the biosphere, a robust understanding of the physical basis of climate variability must be attained. This includes the accurate representation of feedbacks operating that may either amplify or retard the greenhouse gas forcing of climate.

The measured increases in greenhouse gas concentration and their radiative effect are well documented, as is the apparent coupling between greenhouse gas concentration and global climate in both the paleo-record and the modern instrumental record (e.g. IPCC (1990)). However, the direct linkage between greenhouse gas concentration and global warming is still a matter of intense debate. Studies described in IPCC (1996) hope to address this problem by detecting an anthropogenic component or 'finger-print' of the observed change in climate. One of the primary techniques used in the attribution of past climate change and the prediction of future climate change is the development of numerical climate models based on parameterizations that attempt to approximate the physical processes underlying the climate system. One of the primary aims of this thesis is to provide a rationale for testing climate model representations of the present climate variability. In doing so some of the radiative and dynamic processes that are important in influencing future climate change may be identified and hopefully improved.

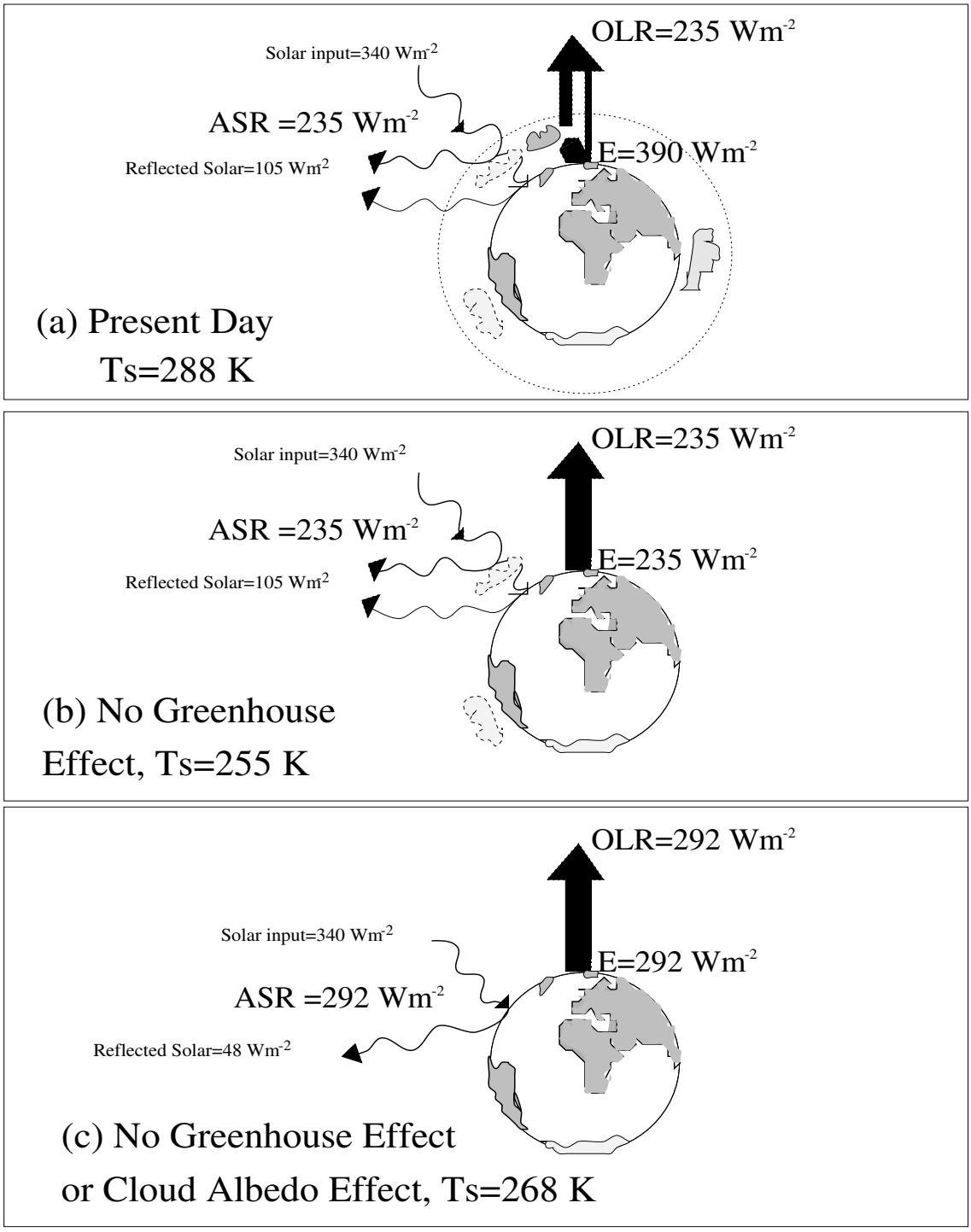


Figure 1.1: *A schematic representation of the Earth's radiation budget for (a) the present day, (b) without the longwave radiative effects of the atmosphere or clouds and (c) without the longwave or shortwave radiative effects the atmosphere and clouds. Surface temperature, $T_s$ is calculated assuming the surface emission, $\sigma T_s^4$, must balance the absorbed solar radiation (ASR) for (b) and (c).*

## 1.2 Radiative Feedbacks

The complexity of the atmospheric and oceanic circulation conspires to introduce significant feedbacks to the simple energy balance response of the climate system as depicted in Fig. 1.1. For example, reduced snow and ice cover associated with a climate warming are likely to decrease the global reflectivity (or albedo) of incoming shortwave radiation such that the enhanced greenhouse effect is compounded by an increase in ASR. Cloud amount and properties and atmospheric water vapour amount exert strong influences on both the shortwave and longwave components of the radiation budget and therefore also constitute potentially potent feedback mechanisms. The present study assesses the role of water vapour and clouds in determining the current radiation budget and its variability. In doing so the model representations of climate feedbacks involving water vapour and clouds may be evaluated.

The framework used to quantify feedbacks is described in the IPCC (1990) report. Using a simple single-level grey-body energy balance model (e.g. Webb *et al.* (1993)), the OLR may be described by,

$$OLR = (1 - \epsilon_a)\sigma T_s^4 + \epsilon_a \sigma T_a^4, \tag{1.1}$$

where $\sigma T_s^4$ approximates the black-body longwave emission, E, by the surface. A fraction of this emission, $(1 - \epsilon_a)$, is transmitted to the top of the atmosphere while the remaining fraction is absorbed by the atmosphere and emitted to space at the atmospheric temperature ($T_a$) of magnitude, $\epsilon_a \sigma T_a^4$. Assuming the atmosphere to be in radiative equilibrium with respect to longwave radiation, the absorbed radiation, $\epsilon_a \sigma T_s^4$, is balanced by emission both to the surface and out to space, $2\epsilon_a \sigma T_a^4$. Thus the effective atmospheric temperature is approximated by,

$$T_a = \frac{T_s}{2^{\frac{1}{4}}}, \tag{1.2}$$

and Eq. 1.1 thence becomes,

$$OLR = (1 - \frac{\epsilon_a}{2})\sigma T_s^4. \tag{1.3}$$

The partial derivative of Eq. 1.3 with respect to $T_s$ is,

$$\frac{\partial OLR}{\partial T_s} = 4(1 - \frac{\epsilon_a}{2})\sigma T_s^3, \tag{1.4}$$

which approximates the black-body response of the Earth's radiation budget to a change in $T_s$. Using a recent estimate of OLR and $T_s$ (Kiehl and Trenberth (1997)) the term, $(1 - \frac{\epsilon_a}{2})$, approximates to 0.60. Therefore, from Eq. 1.4, the OLR will increase with $T_s$ at the rate of 3.3 $Wm^{-2}K^{-1}$ in the absence of additional feedbacks. The overall response of the net

downward radiation at the top of the atmosphere, NET, to changes in surface temperature is given by,

$$\beta = \frac{dNET}{dT_s} = \frac{dASR}{dT_s} - \frac{dOLR}{dT_s}, \tag{1.5}$$

where $\beta$ is the feedback parameter. The feedback parameter is calculated as the sum of component feedback parameters by,

$$\beta = \beta_{BB} + \beta_{wv} + \beta_{\Gamma} + \beta_{cld} + \beta_i + ..., \tag{1.6}$$

where $\beta_{BB}$ is the black-body response, calculated as -3.3 $Wm^{-2}K^{-1}$ using Equations 1.4 and 1.5, assuming $\frac{\partial ASR}{\partial T_s} = 0$. The additional important radiative feedbacks relate to water vapour (wv), lapse rate ($\Gamma$), cloud (cld) and ice albedo (i). The climate sensitivity parameter, $\lambda$, is calculated as the reciprocal of the sum of all the feedback parameters,

$$\lambda = \frac{1}{-\beta} = \frac{1}{-(\beta_{BB} + \beta_{wv} + \beta_{\Gamma} + \beta_{cld} + \beta_i + ...)}, \tag{1.7}$$

in units of $K(Wm^{-2})^{-1}$ and essentially relates the change in surface temperature, $\Delta T_s$, to a change in net radiative input into the Earth-atmosphere system, $\Delta NET$, or radiative forcing. Climate model estimates of $\lambda$ range from between about 0.4 and 1.1 $K(Wm^{-2})^{-1}$ (IPCC (1990)) which all denote a positive feedback relative to the black-body response.

### 1.2.1 Water Vapour Feedback

One of the best understood feedbacks is that of water vapour, which is generally believed to exert a positive feedback on the climate system (e.g. Cess (1989), Rind *et al.* (1991), Shine and Sinha (1991)). Climate model studies (e.g. Cess *et al.* (1990)) suggest that the water vapour feedback amplifies the black-body climate sensitivity parameter by a factor of about 1.6 (from 0.3 to 0.48 $K(Wm^{-2})^{-1}$). The mechanism involved is physically intuitive. An increase in atmospheric water vapour amount is expected in a warmer climate since the maximum amount of water vapour for a given volume of air increases approximately exponentially with temperature as dictated by the Clausius-Clapeyron equation (e.g. Raval and Ramanathan (1989)). Thus if the fractional degree of water vapour saturation in the atmosphere, approximated by the relative humidity ($RH$), were to be fairly constant, water vapour amount will increase with temperature. Because water vapour is a powerful greenhouse gas, the increase in OLR with $T_s$ is retarded compared to the black-body response due to the effects of water vapour amount increases. This is further enhanced by the increased atmospheric absorption of shortwave radiation with increased atmospheric moisture (e.g. Cess *et al.* (1989)).

Manabe and Wetherald (1967) showed the water vapour feedback to be strongly positive using a radiative-convective single column model and prescribing fixed $RH$. The degree to which the water vapour feedback adheres to these thermodynamic constraints will influence the magnitude and possibly even the sign of the water vapour feedback. While modelling studies, such as Del Genio *et al.* (1991), show generally small changes in $RH$ with climate warming, this may be an artifact of the incomplete mechanisms involved in the parameterization of moist convection. For example, Lindzen (1990) proposed that a warmer climate may induce increasingly vigorous convection which could in turn result in the detrainment of water vapour at higher, colder altitudes. This would effectively result in less water vapour being supplied to the free troposphere, thus reducing $RH$ and offsetting the positive thermodynamic water vapour feedback. Schneider *et al.* (1997a) noted that model $RH$ in the present climate is increased by convective processes as well as the large scale mixing and vertical diffusion of water vapour, while large scale subsidence over the climatic desert regions acts to decrease relative humidity. The efficiency of precipitation is also an important agent with regard to the available atmospheric water vapour amount although its dependence on atmospheric parameters is relatively unresolved. Hence there is need for greater understanding of these atmospheric processes in climate models, such as convection and precipitation efficiency, that are crucial in determining the water vapour feedback. The effect of changes in $RH$ on the clear-sky feedbacks are discussed in Chapters 3 and 5.

### 1.2.2 Cloud Feedback and the Concept of Cloud Radiative Forcing

The effect of clouds and their interaction with climate constitutes one of the largest uncertainties involved in the prediction of future climate (e.g. IPCC (1996)). This uncertainty arises from their approximated radiative processes (e.g. Stephens (1984)), global distribution (e.g. Rossow and Schiffer (1991)), microphysical properties (e.g. Le Treut and Li (1991)) and the primitive understanding of the large-scale processes which control these parameters (e.g. J. M. Slingo (1980)). The cloud feedback, as depicted by climate models, ranges from slightly negative to strongly positive (IPCC (1990)), although again these results are uncertain given the incomplete understanding of cloud-climate interactions. Indeed, the calculated climate sensitivity is highly dependent on the cloud parameterizations used in climate models. For example, Mitchell *et al.* (1989) showed the increase of global annual-mean $T_s$ in response to the doubling of $CO_2$ to be reduced from 5.2 $K$ to 2.7 $K$ on replacing a simple cloud scheme that is dependent on $RH$ with a more sophisticated scheme that resolved the cloud water budget.

Correctly representing the cloud feedback requires the response of cloud amount and properties to changes in climate to be modelled accurately. The availability of satellite radiation budget observations that are able to identify clear-sky scenes (e.g. Barkstrom (1984)) along with satellite-derived cloud climatologies (e.g. Rossow and Schiffer (1991)) provide some information concerning the physical nature of the cloud influence on the Earth's radiation budget. For example, Tselioudis *et al.* (1992) showed cloud optical depth to decrease with increasing $T_s$ for warm continental and maritime low cloud, thus implying a positive cloud feedback to climate warming in these regions.

The framework generally used to quantify cloud radiative impacts on climate and its variability is that of cloud radiative forcing. Consider a single layer of uniform cloud that covers the fraction $A_c$ of a region. If the downward net irradiance at the top of the atmosphere for the overcast region is $F_o$ and the corresponding clear-sky irradiance is $F_c$, then the downward irradiance of the entire region ($F$) will be,

$$F = A_c F_o + (1 - A_c) F_c \tag{1.8}$$

Thus the irradiance may be expressed as a function of clear-sky irradiance and cloud amount as,

$$F = F_c + A_c(F_o - F_c). \tag{1.9}$$

The cloudy component, $A_c(F_o - F_c)$, is referred to as the cloud radiative forcing, CF, which is essentially the difference between the downward clear-sky and all-sky flux. Therefore, irradiance may be considered as a function of clear-sky and cloud forcing:

$$F = F_c + CF. \tag{1.10}$$

A strength of the cloud forcing approach is that the value of $A_c$ is not required; attempts must be made, however, at gauging the dependence of $CF$ on cloud amount separately. Using this framework, Harrison *et al.* (1990) were able to show that the presence of clouds act to increase the global-mean clear-sky atmospheric greenhouse effect by 31 $Wm^{-2}$ but to decrease ASR by 48 $Wm^{-2}$ due to increased global reflectivity of shortwave radiation. Thus clouds were shown to cool the climate relative to clear-sky conditions in a global-mean sense. However it is the *change* in cloud amount and properties, and hence the cloud radiative forcing response to climate change, that determines the nature of the cloud feedback. This is much more uncertain and the subject of continuing study (IPCC (1996)).

The calculation of cloud radiative forcing is dependent on the accurate estimates of clear-sky irradiance, of which the precise determination is non-trivial. Cess and Potter (1987) proposed two main procedures for calculating cloud radiative forcing. The purpose of these

methodologies was to minimise inconsistency with satellite measurements of clear-sky irradiance. The essence of each technique is as follows. Method I calculates a monthly mean clear-sky irradiance from the sub-set of clear-sky defined values over the monthly period. Method II calculates clear-sky irradiance as a model diagnostic for all regions (clear-sky or overcast) by setting cloud amount to zero. Atmospheric humidity is generally greater during overcast times (e.g. Udelhofen and Hartmann (1995)). This will introduce a bias between Method I and Method II. Because clear-sky OLR ($\mathrm{OLR}_c$) is reduced by increased atmospheric moisture, Method II may generate lower estimates of monthly mean $\mathrm{OLR}_c$ compared to Method I because Method II samples these moist cloudy regions whereas Method I does not. Using a climate model, Harshvardhan *et al.* (1989) showed the disparity to be as large as 5 $Wm^{-2}$ in the zonal mean. Considering Equations 1.8 to 1.10, the two methods of calculating cloud radiative forcing are described by,

$$METHOD\ I:\ CF = A_c(F_o - F_c);\quad METHOD\ II:\ CF = A_c(F_o - F_c^*), \tag{1.11}$$

where $F_c^*$ is the calculated downward clear-sky irradiance for the overcast portion of the region when the cloud amount is set to zero. The difference between Method I and II estimates of CF depend on the difference, $A_c(F_c^* - F_c)$. The disparity will therefore be largest for regions of high cloud fraction and large moisture differences between clear-sky and overcast regions. For example, assuming an $\mathrm{OLR}_c$ sensitivity to column $RH$ of about 0.5 $Wm^{-2}$ per % (e.g. Spencer and Braswell (1997); see also Chapters 3 and 5) and a $RH$ difference of about 20 % between overcast and clear-sky regions (e.g. Udelhofen and Hartmann (1995)), a disparity of $\mathrm{OLR}_c$ of 5 $Wm^{-2}$ will result between methods I and II if the region considered is half covered with cloud. The disparity will be larger when cloud is more extensive and also where the humidity difference between clear-sky and cloudy regions is greater. The question as to which methodology is the most applicable to the climate system has been the subject of much debate (e.g. Cess *et al.* (1992)). While neither method is entirely consistent with the Earth Radiation Budget Experiment (ERBE) processing of clear-sky irradiance (Brooks *et al.* (1986)), Method II is of greater versatility with regard to climate model inter-comparisons. A hybrid technique, combining methods I and II (Method III), was proposed by Cess *et al.* (1992) to mimic ERBE diurnal modelling used to derive clear-sky irradiance. $\mathrm{OLR}_c$ calculated using this method was found by Cess *at al.* to be of order 5 $Wm^{-2}$ greater than Method II calculations in the zonal mean. The inconsistency between all methodologies must be considered when comparing ERBE and climate model estimates of cloud radiative forcing and is the subject of further debate in Chapter 6.

A further potential mis-interpretation arises in the calculation of the clear-sky and cloud feedbacks. The calculation of the black-body feedback parameter, $\beta_{BB}$, was calculated previously for all-sky conditions. However, the water vapour feedback is often inferred using the dependence of clear-sky OLR on $T_s$ (e.g. Raval and Ramanathan (1989)). This is significant because the OLR and $\mathrm{OLR}_c$ dependence on $T_s$ differs. For example, using Equations 1.1 to 1.5 but employing estimates of global mean $\mathrm{OLR}_c$ from Kiehl and Trenberth (1997) of 265 $Wm^{-2}$, results in a clear-sky $\beta_{BB}$ of 3.7 $Wm^{-2}K^{-1}$. Thus the presence of clouds acts to amplify the clear-sky sensitivity from 0.27 to 0.3 $K(Wm^{-2})$, an increase of about 10%. This is because the presence of cloud causes more of the increased emission, due to $T_s$ increases, to be absorbed compared to the same profile with no cloud present. Thus, when the water vapour feedback is interpreted for clear-sky conditions, the difference in the black-body feedback parameter between clear-sky and all-sky conditions must be considered. This effect may be included as part of the cloud radiative forcing component as will be discussed in Chapter 3.

## 1.3 Definitions

In the remainder of this thesis the following definitions of all-sky and clear-sky irradiance apply. The net downwelling radiation at the top of the atmosphere is given by,

$$NET = ASR - OLR, \tag{1.12}$$

where ASR is the absorbed solar radiation at the top of the atmosphere and OLR is the outgoing longwave radiation. At the surface the net irradiance is given by,

$$NET_s = ASR_s + F_{net}, \tag{1.13}$$

where $\mathrm{ASR}_s$ is the surface absorbed shortwave irradiance and $F_{net}$ is the net longwave irradiance at the surface,

$$F_{net} = SDL - E, \tag{1.14}$$

where E is the surface longwave emission and SDL is the surface downwelling longwave emission from the atmosphere to the surface. E may be approximated by the black-body emission, $\sigma T_s^4$.

The clear-sky longwave component of the radiation budget is determined primarily by surface and atmospheric temperature profiles and atmospheric humidity, as well as by the concentration of 'greenhouse-gases' such as carbon dioxide ($CO_2$), ozone ($O_3$), methane ($CH_4$), nitrous oxide ($N_2O$) and chlorofluorocarbons (CFCs). Shortwave radiation is absorbed by atmospheric constituents such as ozone, water vapour and aerosol and scattered

by nitrogen and oxygen and aerosols in clear-sky conditions. Clear-sky irradiance is denoted by a subscript, $c$.

The presence and distribution of clouds affects the Earth's radiation budget significantly, although they have counteracting effects on the shortwave and longwave components; as shown by Harrison *et al.* (1990), an increase in cloud amount generally decreases OLR (increasing NET) but increases shortwave radiation reflected to space, thus decreasing ASR (decrease in NET). In the context of cloud radiative forcing, as discussed in Sec. 1.2.2, the longwave cloud radiative forcing (LWCF) is defined at the top of the atmosphere as,

$$LWCF = OLR_c - OLR, \tag{1.15}$$

and at the surface as,

$$LWCF_s = SDL - SDL_c. \tag{1.16}$$

Similarly, the definition of shortwave cloud radiative forcing at the top of the atmosphere is expressed as,

$$SWCF = ASR - ASR_c, \tag{1.17}$$

and at the surface as,

$$SWCF_s = ASR_s - ASR_{c\ s}, \tag{1.18}$$

where $\mathrm{ASR}_{c\ s}$ denotes the absorbed solar radiation at the surface for clear-sky conditions. The overall net effect of clouds on the radiation budget may be quantified by the net cloud radiative forcing (NCF),

$$NCF = LWCF + SWCF. \tag{1.19}$$

Therefore, changes in the Earth's radiation budget may be ascribed to changes in the clear-sky component due to variations in atmospheric and surface properties, and also to changes in cloud amount and properties. In this framework, the clear-sky water vapour and temperature lapse rate feedback as well as the cloud feedback may be evaluated. The effects of atmospheric constituents and clouds on the Earth's radiation budget and its variability are discussed in Chapters 2 and 3.

## 1.4 Key Questions and Aims

The motivation for the present work is the need to test climate models and improve their ability to predict future climate. This demands a thorough understanding of the radiative and dynamic processes that determine climate variability. Climate models are constructed using the physical conservation laws which govern the redistribution of momentum, heat and water vapour by atmospheric motions. Given the importance of the Earth's radiation

budget in driving future climate change, it is paramount that the parameterizations of radiation and the dynamic processes which affect the radiative heating and cooling of the atmosphere and the surface are represented accurately.

A key area of interest concerns the fluctuations of the clear-sky greenhouse effect and its dependence on atmospheric moisture. While early attempts at assessing the water vapour feedback were mainly model based (e.g. Manabe and Wetherald (1967), Ramanathan (1981)), many recent advances have benefited from the observational determination of the atmospheric greenhouse effect by satellite (e.g. Harries (1996)). For example, Raval and Ramanathan (1989) highlighted the strong dependence of the clear-sky atmospheric greenhouse effect on column moisture which in turn was deduced to be thermodynamically linked to $T_s$. The consolidation between observations and model representations of the greenhouse effect have increased confidence in the proficiency of climate models in accounting for the water vapour and cloud feedbacks (e.g. Cess *et al.* (1989), Cess *et al.* (1990), Cess *et al.* (1997)). The dependence of the greenhouse effect and its variability on atmospheric temperature and moisture have been thoroughly explored using radiative calculations in conjunction with satellite observations (e.g. Webb *et al.* (1993), Bony *et al.* (1995), Soden and Fu (1995), Sinha and Harries (1997)). The dependence of atmospheric moisture on $T_s$ is a key component of this research and has provoked discussion concerning the paucity of upper tropospheric water vapour observations (e.g. Lal and Ramanathan (1984), Spencer and Braswell (1997)) and the potential impact of this uncertainty on the water vapour feedback (e.g. Lindzen (1990)). Although the entire troposphere has been shown to influence the water vapour feedback (e.g. Shine and Sinha (1991)), reducing the deficiency of information concerning the upper tropospheric humidity and its variability remains an important area of continuing study (e.g. Jackson *et al.* (1998), Chaboureau *et al.* (1998)). The effect of $RH$ variability and its influence on the positive thermodynamic water vapour feedback is considered in Chapter 5.

Recent attention has focused on the feedbacks operating in tropical regions. The influence of tropical surface temperature and convective processes on the global circulation has been shown to be considerable (e.g. Schneider *et al.* (1997a)). Large perturbations to the atmospheric circulation associated with the El Niño Southern Oscillation (ENSO) exert significant impacts on the Earth's climate (e.g. Philander (1990)). An enhanced greenhouse effect over warm, tropical ocean regions was first noted at the surface by Vonder Haar (1986) and subsequently, using satellite data, at the top of the atmosphere (e.g. Raval and Ramanathan (1989)). An unstable longwave radiative feedback was found to exist whereby increases in $T_s$ were accompanied by a decrease in longwave cooling. Ramanathan and

Collins (1991) termed this the super-greenhouse effect (SGE) and explained it by considering the increases in temperature lapse rate, increased absorption due to the continuum of water vapour and increases in $RH$ with increases in $T_s$ (see also Hallberg and Inamdar (1993), Inamdar and Ramanathan (1994), Weaver *et al.* (1994)). In situ observations by Valero *et al.* (1997) have shown a strong SGE of greater magnitude than satellite observations. Lubin (1994) argued that the unstable feedback operates at the surface due to large increases in the $\mathrm{SDL}_c$ with increased $T_s$.

The spatial distribution of the SGE was shown to be linked with shifts in the large scale circulation (e.g. Bony *et al.* (1997b), Sinha and Harries (1997), Gershunov *et al.* (1998)), a consequence of the associated changes in $RH$ required to decouple $\mathrm{OLR}_c$ from the surface emission. The relatively equable temperatures of the tropical oceans necessitate the existence of a stabilising feedback. Proposed mechanisms have included evaporation (e.g. Hartmann and Michelsen (1993)), shortwave cloud radiative forcing (e.g. Ramanathan and Collins (1991)) and heat export to the extra tropics (e.g. Pierrehumbert (1995)). However, using an atmospheric model forced with sea surface temperature anomalies related to ENSO variability, Lau *et al.* (1996) argued that the radiative feedback remained secondary to the dynamical response to the sea surface temperature perturbation. More recently, Sun and Trenberth (1998) asserted that the stabilisation of tropical sea surface temperatures over the ENSO cycle arises from the combined effect of shortwave cloud radiative forcing, atmospheric heat export and, most especially, oceanic heat export to the extra tropics. They further postulated that ENSO is fundamentally linked to the need for the equatorial Pacific oceans to lose heat. The spatial distribution and temporal scales on which these feedbacks hold is required for further understanding of the tropical radiative-dynamical interactions and is the subject of further debate in Chapters 5 and 6.

The surface response to greenhouse gas increases was shown by Ramanathan (1981) to operate directly and indirectly via surface fluxes, especially the surface longwave irradiance. Indeed, increases in $\mathrm{SDL}_c$ appear to explain much of the warming in climate model experiments on doubling the atmospheric concentration of $CO_2$ (e.g. Watterson and Dix (1986), Schneider *et al.* (1997b), Wild *et al.* (1997)). Also, the surface SGE is generally assumed to supply a significant positive feedback to the ocean surface temperature (e.g. Seager *et al.* (1995)). Therefore the accurate representation of this flux is required in climate models. The poor spatial coverage of surface radiation budget observations, compared to recent satellite coverage at the top of the atmosphere, demand the derivation of the surface fluxes using alternative methods. Many attempts have been made at reducing the $\mathrm{SDL}_c$ to an empirical formula based either on radiometric observations (e.g. Prata (1996)) or on radi-

ative transfer calculations (e.g. Dilley and O'Brien (1998)). Satellite data have also been used extensively to either parameterize the surface fluxes (e.g. Gupta (1989)) or to derive a surface flux climatology (e.g. Rossow and Zhang (1995)).

Meteorological and radiometric observations are limited by measurement uncertainties and also by their incomplete spatial and temporal coverage. While climate models offer good global coverage, imperfect understanding of the physical processes limit model-based estimates of climate variability. A recent comprehensive and consistent atmospheric re-analysis undertaken by the European Centre for Medium Range Weather Forecasts (ERA; Gibson *et al.* (1997)) offers a hybrid between the two extremes. Essentially a forecast model was integrated from 1979 to 1993, being continually constrained by available conventional and satellite-based observations. Slingo *et al.* (1998) used this analysis in conjunction with a radiation scheme (Edwards and Slingo (1996)) to construct a simulation of the clear-sky radiation budget. The simulation provides estimates of clear-sky longwave irradiance not only at the top of the atmosphere but also at the surface as well as heating rates throughout the atmosphere which cannot be practicably measured in situ. The simulation output of clear-sky irradiance pertain to Method II as described previously: skies are assumed clear globally throughout the period. This must be considered when comparing with satellite and ground-based observations. A distinct advantage of the simulation, over observations, is that components of the radiation budget variability may be directly attributed to atmospheric and surface parameters. A key question is, can this observationally constrained model reproduce the observed variability of the clear-sky greenhouse effect? A primary aim of the present work is to extend the investigation of Slingo *et al.* (1998) into the major sources of simulation error by evaluating the simulated irradiance at the surface using the limited radiometric observations and empirical estimates (Chapter 4). If the re-analysis cannot adequately represent the clear-sky longwave radiation budget, the use of free-running climate models in the prediction of climate must be seriously questioned. However, assuming a reasonable performance of the simulation, compared to observations, such a system constitutes a powerful tool in the evaluation of climate models (Slingo (1997)).

The remainder of this thesis is arranged as follows. The radiative transfer models used to simulate the Earth's radiation budget are presented in Chapter 2 along with discussion of uncertainties. A framework for interpreting the irradiance variability of later chapters is presented in Chapter 3 along with further analysis of potential errors involved. Chapter 4 uses surface radiometric observations both to evaluate simulated surface clear-sky irradiance and to assess the variability of surface fluxes on short time-scales. Chapter 5 investigates the dependence of $\mathrm{OLR}_c$ on temperature and humidity and gauges the effect that changes

in $RH$ have on the water vapour feedback. The clear-sky simulation is used in conjunction with satellite radiometric observations in Chapter 6 thus extending the work of Chapter 5 to include the effects of clouds and shortwave radiation. Key questions to be addressed are:

1) What parameters are important in determining the clear-sky longwave irradiance and its variability at the top of the atmosphere and at the surface?

2) To what extent can a simulation of clear-sky longwave radiation using re-analysed fields represent the irradiance and its variability at the top of the atmosphere and at the surface?

3) Which regions of the globe exhibit a super-greenhouse effect over the seasonal and interannual time-scale and what determines this distribution?

4) How do changes in $RH$ and the presence and variability of cloud influence the super-greenhouse effect and the water vapour feedback?

5) Which parameters need to be more accurately prescribed to improve the representation and understanding of the Earth's radiation budget?

These points will be revisited in the concluding Chapter.

Finally, a key philosophical point should be noted. It concerns the thermodynamic and dynamic determination of feedbacks and their effect on the global mean climate. The thermodynamic (constant $RH$) water vapour feedback is likely to operate globally, thus strongly influencing the global mean climate. However, changes in relative humidity and cloud amount are primarily determined by the large-scale circulation. Therefore it is important to separate the local radiative perturbations that are dependent on subtle shifts in the large-scale circulation from the feedbacks operating at a global scale. Thus feedbacks implied locally over shorter time-scales than that of climate change are likely to overestimate the effects of changes in cloud amount and relative humidity compared to the global feedback to uniform surface warming (e.g. Lau *et al.* (1996)). Entire circulation systems must therefore be considered in attempting to provide information with regard to the effect of changes in relative humidity and cloud amount on the Earth's radiation budget and hence the climate feedbacks operating.

# Chapter 2

# DESCRIPTION OF MODELS AND DATA

## 2.1 Introduction

The realistic representation of radiative processes by climate models determines their ability to simulate well the direct radiative forcing of climate and also the indirect influence of feedback processes on this forcing. Therefore attempts must be made to ensure the accuracy of both the radiative transfer models employed and the simulated variability of radiatively important input parameters to the radiation schemes before the prediction of future climate change can be presented with confidence. Thus it is important to apportion errors to the radiation schemes or the input data in evaluating the performance of climate models. This chapter describes the radiation schemes and input data used extensively in this thesis and the associated uncertainty in radiative transfer calculations are discussed. The following section outlines a narrow-band radiative transfer scheme that is used to perform idealised calculations that illustrate the parameters important in determining the variability and uncertainty of simulated irradiance. The primary tool utilised in this thesis is a simulation of the Earth's clear-sky radiation budget which is described in detail in Sec. 2.3. Potential limitations are also discussed. The simulation is evaluated using radiometric and meteorological observations at the surface in Chapter 4 and used in conjunction with satellite radiation budget data in Chapter 6; the additional observational data is described in these chapters.

## 2.2 The Narrow-Band Model

The narrow-band longwave and shortwave radiative transfer schemes used in this thesis are those employed by Forster and Shine (1997). The longwave scheme is a Malkmus narrow-band model of resolution 10 $cm^{-1}$. Spectral line data was provided by the HITRAN data base (Rothman *et al.* (1992)) and water vapour lines were prescribed using the Clough *et al.* (1989) specification. Both the self and foreign components of the water vapour continuum were accounted for; the recently updated CKD_2.2 version was incorporated. Temperature profiles between levels were calculated using cubic spline interpolation and absorber amount was assumed to vary linearly with the natural logarithm of pressure. This allowed both the simple incorporation of the Curtis-Godson approximation and the temperature dependent line parameters (Rodgers and Walshaw (1966)). Transmittance, $Tr$, was calculated as, $Tr = exp(-W/\Delta v)$, where $W$ is the equivalent line width and $\Delta v$ is the spectral interval (both in $cm^{-1}$). While the present study concentrates primarily on the clear-sky longwave component of the radiation budget, the shortwave irradiance and the radiative effects of cloud are also considered for completeness. A four-stream discrete-ordinate model of resolution 5 $nm$ in the ultra violet regions, 10 $nm$ resolution in the visible regions of the spectrum and about 18 bands in the near infra-red was used to calculate the shortwave irradiance. Cloud was assumed to occupy an homogeneous layer of given horizontal fraction. Cloud emittance and albedo were calculated from cloud liquid water path.

### 2.2.1 Radiative Transfer Equations

Longwave irradiance was calculated by a numerical adaptive integration of the radiative transfer equations at each spectral interval for the upwelling component,

$$F_u(z) = [F_u(0) - \pi B(0)]Tr(0,z) + \pi B(z) - \int_0^z \left[\pi Tr(z^{'},z)\left(\frac{dB(z^{'})}{dz^{'}}\right)\right] dz^{'}, \qquad (2.1)$$

and the downwelling component,

$$F_d(z) = \pi B(z) + \int_0^\infty \left[\pi Tr(z^{'},z)\left(\frac{dB(z^{'})}{dz^{'}}\right)\right] dz^{'} + [\pi B(\infty)Tr(z,\infty)], \qquad (2.2)$$

where z is a log-pressure coordinate. $B$ is the Planck function of spectral irradiance and $Tr(z,z^{'})$ is the mean transmittance explicitly integrated over the zenith and azimuth angle between the flux calculation level, $z$, and the integrating level, $z^{'}$. The integrating level varies between the surface, $z$=0, and the top of the atmosphere, $z = \infty$. The net irradiance is then calculated as, $F_n(z) = F_u(z) - F_d(z)$, in which the the term, $\pi B(z)$, is removed. Calculating $dB/dz = (dB/dT)(dT/dz)$ is a simpler method than to compute the vertical gradient, $dTr/dz$, required using other forms of the radiative transfer equation.

Using the equivalent form of the radiative transfer equations is more illustrative of the dependence of irradiance on the temperature and absorber amount profiles. Thus, outgoing longwave radiation to space for clear-sky conditions ($OLR_c$) may be expressed as:

$$OLR_c = \int_{v=0}^{v=\infty} \left[ (E_v Tr_v(p_s, 0)) + \int_{p_s}^{0} B_v(p) \frac{dTr_v(p, 0)}{dp} dp \right] dv, \tag{2.3}$$

where $B_v(p)$ denotes the black body emission at pressure, $p$, and $Tr_v(p_s, 0)$ denotes the transmittance between the surface pressure, $p_s$, and the top of the atmosphere. E is the surface emission. The subscript $v$ denotes wavenumber and both $B$ and $Tr$ include implicit integration over the zenith angle to convert radiance to irradiance. Thus OLR is seen to be determined by a surface component (first right term) and an atmospheric component (second right term). Both terms depend on emission and therefore temperature at a given pressure level, and the fraction of that emission which is transmitted through an atmospheric path, which is determined by absorber amounts. The equivalent surface downward longwave irradiance for clear-sky conditions ($SDL_c$) is represented by,

$$SDL_c = \int_{v=0}^{v=\infty} \int_{0}^{p_s} B_v(p) \frac{dTr_v(p, p_s)}{dp} dp dv. \tag{2.4}$$

The $SDL_c$ is dependent on the emission and therefore the temperature of each pressure level, weighted by the fraction of that emission which may be transmitted through the atmospheric path to the surface depending on the absorber amounts.

### 2.2.2 Irradiance Uncertainty Within Narrow-Band Scheme

#### (a) Spectroscopic Uncertainties

Pinnock and Shine (1998) examined the effect of spectroscopic uncertainties on the clear-sky longwave irradiance calculations. The changes in the HITRAN spectral data-base were estimated to incur a 0.5% uncertainty in wavenumber-integrated irradiance and a 5% uncertainty in radiative forcing calculations. Using standard atmospheric profiles the irradiance calculated by the narrow band model fell within about 2% of the more detailed line-by-line models. Validation of irradiance calculated by the narrow-band model against spectrally resolved radiometric observations showed the model to agree to within, at worst, 5% of the observations (Pinnock pers. comm. (1996)). About one fifth of this uncertainty is attributable to the errors in the atmospheric profile retrieved by radiosonde ascents. Approximately one third of the remaining error is likely to be due to the error inherent in the radiometric observations. Therefore the instantaneous calculated irradiance is likely to be accurate to within 3% (or about 10 $Wm^{-2}$) with a lower value for more spatially and temporally averaged profiles. Sinha and Shine (1995) estimated the narrow-band model calculations of $OLR_c$ to be accurate to within about $\pm 5$ $Wm^{-2}$ in comparisons with monthly-mean satellite data.

### (b) Water Vapour Continuum Parameterization

The parameterization of water vapour continuum absorption has led to increased accuracy of modelled clear-sky irradiance compared to satellite observations (e.g. Stephens *et al.* (1981)). However, the physical basis for continuum absorption is still in question and therefore poses an uncertainty in radiative transfer modelling. In the light of new irradiance observations in the tropics (Kilsby *et al.* (1992)) and in mid-latitudes (Rudman *et al.* (1994)) an increase in the self broadening coefficient, $C_{self}$, of 30% or an increase in the temperature coefficient of the continuum parameterization was proposed. Work by Han *et al.* (1997) has also led to refinement of the Clough *et al.* (1989) continuum which the narrow-band scheme employs in this thesis.

Using the Clough *et al.* (1989) formalism for the water vapour continuum, increases in $C_{self}$ result in $SDL_c$ of up to 0.3 ($Wm^{-2}$ per 10 $cm^{-1}$) larger but with decreases as great as -0.05 ($Wm^{-2}$ per 10 $cm^{-1}$) at about 850 $cm^{-1}$. Overall, a 30% increase in $C_{self}$ results in increases in $SDL_c$ of 8 $Wm^{-2}$ for the tropical profile and changes of less than 1 $Wm^{-2}$ for the sub-arctic winter profile. $OLR_c$ is decreased by almost 2 $Wm^{-2}$ for the tropical profile and remains unchanged for the sub-arctic profile. Because observations were confined to 11 and 12 $\mu m$ spectral bands, increasing $C_{self}$ across the spectrum as proposed by Kilsby *et al.* (1992) is likely to overestimate the change in broadband irradiance. More detailed measurements by Han *et al.* (1997) resulting in the CKD_2.2 parameterization yielded smaller changes in irradiance from the Clough *et al.* (1989) method. For the tropical profile, changes in irradiance at about 900 $cm^{-1}$ are offset by changes at about 1200 $cm^{-2}$. Overall the Clough-continuum parameterization update yields changes in irradiance less than about 1% for the standard atmospheric profiles. The effect of the update is to decrease the magnitude of $OLR_c$ sensitivity to relative changes in column water vapour by approximately 10% and acts to increase $SDL_c$ sensitivity to profile relative changes in water vapour amount by about 1% for the two most moist profiles, while decreasing the sensitivity by about 10% for the two driest profiles. Thus an uncertainty in calculated irradiance sensitivity to water vapour amount changes of order 10% should be considered inherent in the narrow band code; errors in water vapour variability are likely to increase this uncertainty further.

### (c) Surface Emissivity and Irradiance Error

For calculations performed in the present study, the surface is assumed to emit as a black-body, that is with a surface emissivity, $\epsilon_s$, set to unity. In reality, the upwelling irradiance at the surface is modified with the surface emitting a fraction, $\epsilon_s$, of the black body emission and reflecting back the fraction, $(1 - \epsilon_s)$, of the SDL. Therefore OLR is reduced by an

amount ($\delta$OLR) depending on the divergence of $\epsilon_s$ from unity:

$$\delta OLR = [\sigma T_s^4 - SDL](1 - \epsilon_s)Tr(p_s, 0), \tag{2.5}$$

where $\sigma T_s^4$ is the black-body wavenumber integrated surface emission. The effect on OLR will therefore be largest for regions where $\epsilon_s$ is significantly less than 1.0, atmospheric transmission to space ($Tr(p_s, 0)$) is high and the the difference, $\sigma T_s^4$-SDL$_c$, is large. Dry, clear, warm desert regions adhere to all these criteria and so the emissivity error in these regions may be large. For $\sigma T_s^4$-SDL=150 $Wm^{-2}$, $\epsilon_s$=0.9 (e.g. Sutherland (1986)) and $Tr(p_s, 0)$=0.3, which are values typical of desert regions, the error, $\delta$OLR, is of order 9 $Wm^{-2}$ or about 3% of OLR. This is comparable with the overall irradiance uncertainty, as discussed previously, and so should be considered when comparing model-calculated OLR$_c$ with observed values. The surface net longwave irradiance, $F_{net}$, is even more sensitive to surface emissivity errors than OLR$_c$. The error involved ($\delta F_{net}$) is given by,

$$\delta F_{net} = (1 - \epsilon_s)[\sigma T_s^4 - SDL], \tag{2.6}$$

which would lead to errors of order 15 $Wm^{-2}$ for the desert conditions described previously. Over the oceans, where $\epsilon_s$ is close to 1.0, the error will be small (less than about 3 $Wm^{-2}$).

### 2.2.3 Input Data

To compute the irradiance using Eq. 2.1 and 2.2, vertical profiles of pressure, temperature, water vapour mass mixing ratio and ozone are required. In this thesis, profiles are provided by standard atmospheres from McClatchey *et al.* (1972) and climatological profiles described in Freckleton *et al.* (1998). The climatological profiles are generated using satellite, aircraft and ground-based observations. Global mean cloud amounts and liquid water path from this profile are displayed in Table 2.1 and are derived from the International Satellite Cloud Climatology Project (ISCCP) (Rossow and Schiffer (1991)) with one important modification: the high level cloud optical depth was increased to reduce OLR to the values measured by satellite, as given for example by Harrison *et al.* (1990). In the present study, clouds were assumed to comprise entirely of water droplets of mean effective

Table 2.1: *Cloud amount, $A_c$ (%), and liquid water path, LWP ($kgm^{-2}$), for the global mean profile.*

| TYPE | PRESSURE LEVEL ($hPa$) | $A_c$ (%) | LWP ($kgm^{-2}$) |
|---|---|---|---|
| HIGH | 150 | 13.8 | 0.028 |
| MEDIUM | 500 | 19.0 | 0.054 |
| LOW | 850 | 25.7 | 0.038 |

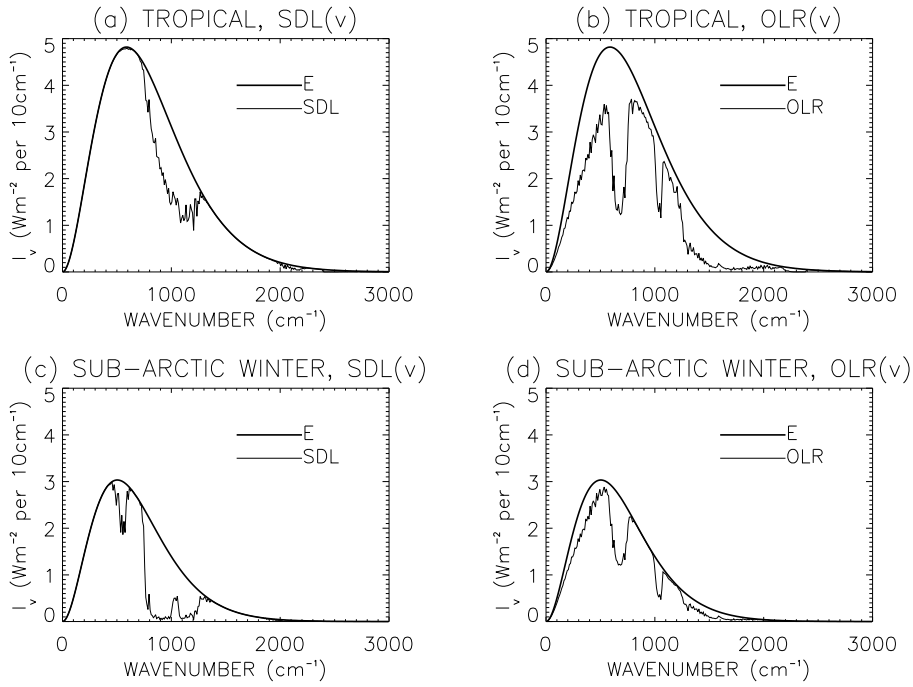


Figure 2.1: *Surface longwave emission, E, surface downwelling longwave irradiance, SDL, and outgoing longwave irradiance, OLR, as a function of wavenumber (all in $Wm^{-2}$ per $10cm^{-1}$) for clear-sky conditions. E and SDL are shown for (a) tropical and (b) sub arctic profiles, while E and OLR for the tropical profile are shown in (c) and for the sub arctic winter profile in (d).*

radius, 10 $\mu m$. Therefore calculations of cloud radiative forcing are made for illustrative purposes only and are likely to incur a large uncertainty relative to the clear-sky longwave calculations. Additional re-analysed profiles from Gibson *et al.* (1997) described in Sec. 2.3 and a range of radiosonde profiles described in Chapter 4 were also used in conjunction with the narrow-band scheme. Unless stated, calculations include the effect of trace gases $CO_2$ (360 ppmv), $N_2O$ (0.31 ppmv) and $CH_4$ (1.72 ppmv) where ppmv is the absorber concentration in parts per million by volume throughout the atmosphere.

### 2.2.4 Calculated Spectral Irradiances

Using the narrow-band model, the $SDL_c$ and $OLR_c$ were calculated for the tropical and sub-arctic winter McClatchey *et al.* profiles. The purpose of this exercise was to illustrate the basic features of the radiation field and its spectral dependence. $SDL_c$ and $OLR_c$ are plotted with wavenumber for both profiles in Fig 2.1 with the surface black-body emission, E, also plotted for comparison. Much of the spectrum behaves like a black-body in the tropical near-surface layers. The window region of the spectrum, between about 800 and 1200 $cm^{-1}$, is relatively more transparent with $SDL_c$ being considerably less than E, thus allowing longwave radiative cooling of the surface. For the sub-arctic profile (Fig. 2.1(c))

there is only a small emission from the atmosphere to the surface in the window region. Much of this emission is from a peak at about 1050 $cm^{-1}$ due to ozone. A separate window region is also visible at about 500 $cm^{-1}$ which is not significant for the tropical profile. This is referred to as the 'dirty' window (Pinto *et al.* (1997)) and arises because absorption by the wings of the water vapour pure-rotation lines is small at low water vapour concentration in the sub-arctic troposphere.

The window regions of the spectrum allow a significant fraction of the surface emission to reach the top of the atmosphere as OLR. This is particularly so in the main window region either side of the 1050 $cm^{-1}$ ozone band for the sub-arctic winter profile (Fig. 2.1(d)). In other spectral regions of the tropical profile, absorption of upwelling radiation and re-emission at temperatures generally colder than the surface result in $\mathrm{OLR}_c$ being markedly less than surface emission. This occurs primarily in the 15 $\mu m$ $CO_2$ band between about 600 and 750 $cm^{-1}$ and also the water vapour pure rotation band at wavenumbers less than about 500 $cm^{-1}$ and the water vapour rotation-vibration bands between about 1200 and 2000 $cm^{-1}$. The difference between the E and OLR curves in Fig. 2.1(b) and (d) represents the spectral greenhouse parameter, $G_\nu$, which has been proposed by Frey *et al.* (1996) as a useful diagnostic variable in the measurement of the greenhouse effect. Integrating $G_\nu$ over the longwave spectrum results in the calculation of the greenhouse parameter, $G$ (e.g. Raval and Ramanathan (1989)).

The product of emission from each layer and the change in transmittance across the layer ($B_\nu(p)\Delta Tr_\nu(\Delta p)$) was computed for the tropical profile to ascertain the contribution of each atmospheric layer to $\mathrm{OLR}_c$ and $\mathrm{SDL}_c$. Unsurprisingly, considering Fig. 2.1(a), much of the $\mathrm{SDL}_c$ in the non-window regions originates from a thin layer near to the surface (not shown). The $\mathrm{SDL}_c$ contribution from the window region originates from higher altitudes of colder temperature. The direct contribution of the surface emission to $\mathrm{OLR}_c$ is high in the window regions of the spectrum (not shown) although contribution from the lower troposphere due to continuum absorption and emission is also important for the tropical profile. In the non-window regions, most of the surface emitted radiation is absorbed by the atmosphere. While atmospheric emission tends to decline with increasing altitude due to the decreasing temperature, the transmission from the emission level to the top of the atmosphere increases. The result is that atmospheric contribution to $\mathrm{OLR}_c$ in the non-window regions of the spectrum is concentrated on a relatively thin vertical slab of the atmosphere of which altitude is dependent on the mean line strength of each band of the spectrum (e.g. Harries (1997)). This is highlighted by plotting the fraction of the atmospheric contribution to $\mathrm{OLR}_c$ with wavenumber for the tropical profile (Fig. 2.2(a)).

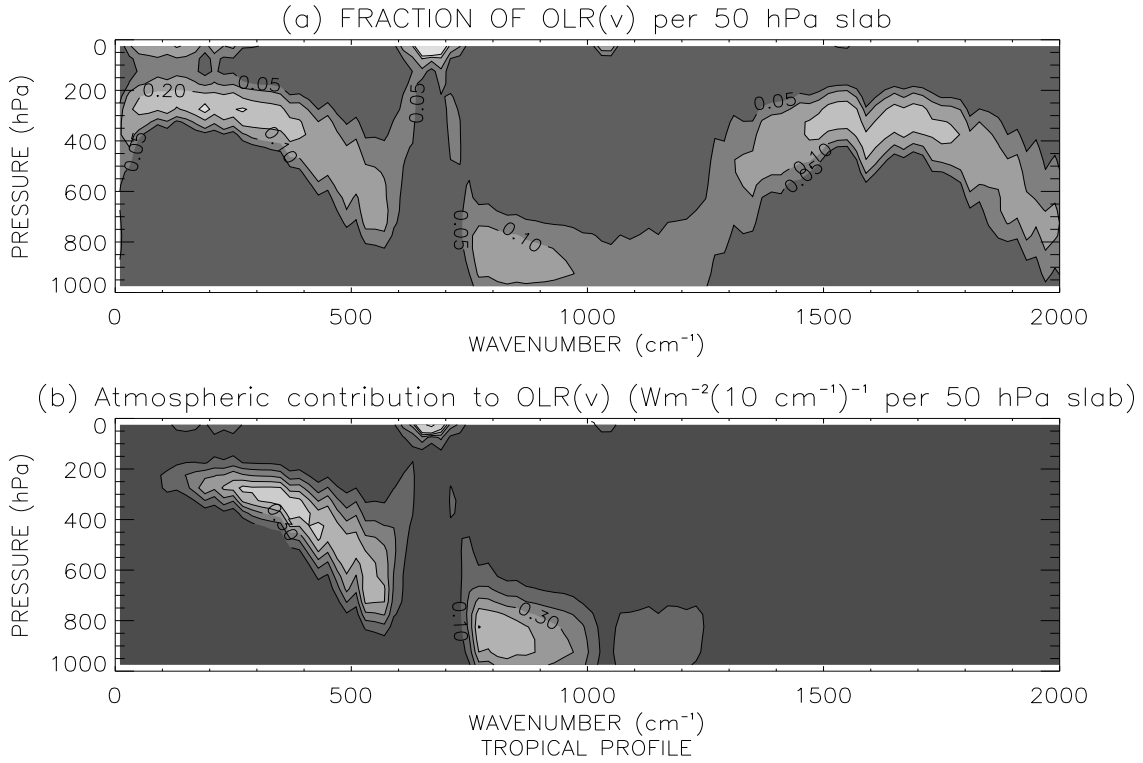


Figure 2.2: *Fraction contribution to the $OLR_c$ for each 10 $cm^{-1}$ spectral band (a) and the absolute contribution to $OLR_c$ (contours at 0.1 $Wm^{-2}$ per 10 $cm^{-1}$ intervals) (b) of each 50 hPa vertical slab of the tropical profile.*

The contribution of each 50 $hPa$ vertical slab to the $\mathrm{OLR}_c$ ($Wm^{-2}$ per 10 $cm^{-1}$) is displayed in (Fig. 2.2(b)). In the strongly absorbing water vapour bands (e.g. 200 $cm^{-1}$ or 1500 $cm^{-1}$) much of the $\mathrm{OLR}_c$ originates from the upper troposphere between about 200 and 300 $hPa$ for the tropical profile. Where water vapour absorption is less strong, for example at 500 $cm^{-1}$, emission to space mainly emerges from the 400 to 600 $hPa$ layer. The intense $CO_2$ absorption at about 700 $cm^{-1}$ results in emission in this band from levels above the troposphere. The absorption and re-emission by the water vapour continuum is potent only in the warm, moist lower troposphere. Thus in the the window region emission is mainly determined by the surface and by the lower troposphere for pressures greater than about 700 $hPa$.

The result of variations of line strength and black body emission with wavenumber is for $\mathrm{OLR}_c$ to originate from both the surface and throughout the troposphere with an additional small contribution from the stratosphere (e.g. Clough *et al.* (1992)). This is a salient point and one which has been discussed by Harries (1997): longwave radiation emitted to space is determined by the entire surface-atmosphere system rather than a single level.

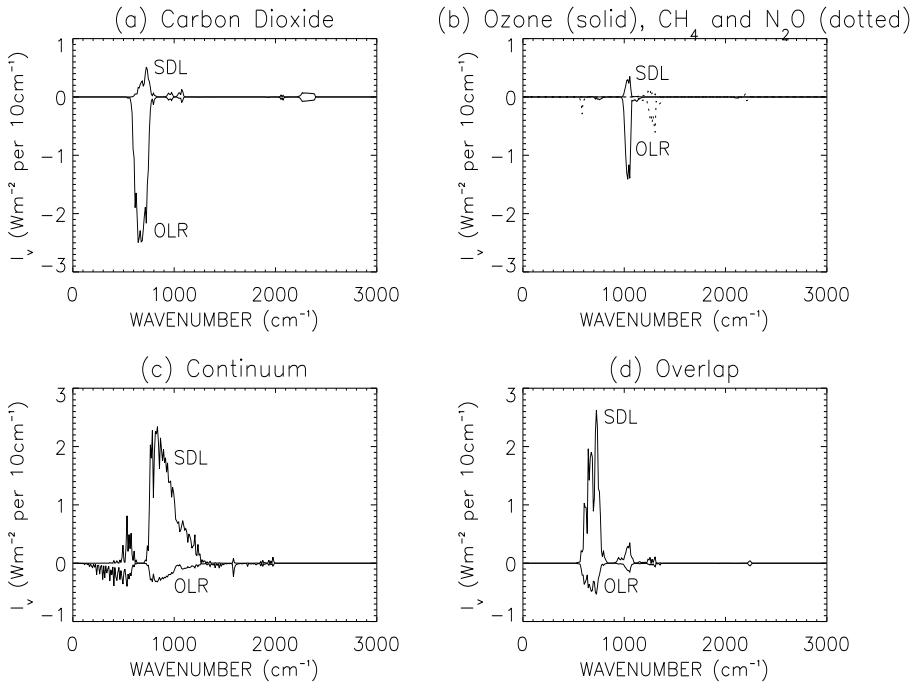


Figure 2.3: *Contribution to clear-sky surface downwelling longwave irradiance, SDL, and clear-sky outgoing longwave irradiance, OLR, with wavenumber (both in $Wm^{-2}$ per 10 $cm^{-1}$) for (a) Carbon Dioxide, (b) Ozone (solid), Methane and Nitrous Oxide (dotted), (c) the water vapour continuum and (d) the overlap contribution between the aforementioned trace gases for the tropical profile.*

### 2.2.5 Dependence of Calculated Irradiance on Absorbing Gases

Using the narrow-band scheme, the contribution of $CO_2$, $O_3$, the water vapour continuum and the trace gases, $CH_4$ and $N_2O$, to the tropical profile $SDL_c$ and $OLR_c$ were computed. Figure 2.3 shows the contribution to clear-sky irradiance plotted with wavenumber. The contribution of each gas was calculated by differencing the irradiance without the radiative properties of the gas included from the irradiance calculated with the radiative properties included. By summing the individual contribution to the clear-sky irradiance from $CO_2$, $O_3$, $CH_4$, $N_2O$ and the water vapour continuum and subtracting this from the change in the clear-sky irradiance when all these gases are removed at once, a 'hidden' contribution to the irradiance is highlighted. This is due to spectral overlap between the radiative properties of each gas which cannot be attributed unambiguously to an individual gas. The gases considered contribute positively to $SDL_c$ and negatively to $OLR_c$. Table 2.2 shows the absolute and percentage contribution to $SDL_c$ and to the clear-sky greenhouse effect $G_c$=E-$OLR_c$. When all gases are considered, the surface emission of 459 $Wm^{-2}$ is reduced due to absorption and re-emission of the upwelling irradiance through the atmospheric profile by about 178 $Wm^{-2}$ at the top of the atmosphere. This is the magnitude of the greenhouse

Table 2.2: *Gaseous contribution to $SDL_c$ and $G_c$(=E-$OLR_c$) for the tropical McClatchey profile ($Wm^{-2}$). The contribution of water vapour lines to $OLR_c$ is calculated as $OLR_c$ for water vapour lines minus the surface black-body emission of 459 $Wm^{-2}$ and the percentage contribution of each gas is relative to the total clear-sky greenhouse effect, $G = E - OLR_c$, when all gases are included.*

| Gas | Contribution to $SDL_c$ ($Wm^{-2}$) | Contribution to $G_c$ ($Wm^{-2}$) |
|---|---|---|
| $H_2O$ lines | 297 (75 %) | 106 (60 %) |
| $CO_2$ | 6 (2 %) | 34 (19 %) |
| $O_3$ | 2 (<1 %) | 9 (5 %) |
| $CH_4$, $N_2O$ | 1 (<1 %) | 5 (3 %) |
| $H_2O$ continuum | 61 (15 %) | 16 (9 %) |
| Overlap | 29 (7 %) | 8 (4 %) |
| All | 396 (100 %) | 178 (100 %) |

parameter, $G_c$, for the tropical profile. Both $SDL_c$ and $G_c$ are dominated by the water vapour lines for the tropical profile, although continuum emission in the window region is also important (Fig. 2.3(c)). Absorption by $CO_2$ between 600 and 750 $cm^{-1}$ contributes significantly (19 %) to the clear-sky greenhouse effect (Fig. 2.3(a)). Overlap between the radiative effects of $CO_2$ and the continuum is also important in considering the contribution of these gases to both $SDL_c$ and $G_c$ (Fig. 2.3(d)).

### 2.2.6 Dependence of Calculated Irradiance on Clouds

The effect of clouds on the calculated clear-sky irradiance of the previous sub-section is now examined briefly. Using the global atmospheric mean profile, the narrow-band code was used to calculate the instantaneous cloud radiative forcing due to the prescribed global mean cloud amount and properties. Again, it must be noted that the assumptions regarding the properties of clouds are highly simplified compared to the real world. Significant uncertainty is attached to these calculations which serve merely as an illustration of the radiative effects of clouds that are useful in the references to cloud effects in later chapters. The calculations were completed for all cloud layers and for each cloud layer separately. The wavenumber integrated longwave, shortwave and net cloud radiative forcing for each cloud layer and all cloud layers combined is presented in Table 2.3. Global mean insolation and albedo were prescribed for the shortwave calculations. Much of the longwave cloud radiative forcing, LWCF, operates in the window regions of the spectrum (not shown). This

Table 2.3: *Longwave, shortwave and net cloud radiative forcing at the surface and at the top of the atmosphere, defined in Sec. 1.3, for the global atmospheric profile and cloud amount and properties, with global mean insolation and surface albedo.*

| Profile | $SWCF_s$ $(Wm^{-2})$ | $LWCF_s$ $(Wm^{-2})$ | $NCF_s$ $(Wm^{-2})$ | SWCF $(Wm^{-2})$ | LWCF $(Wm^{-2})$ | NCF $(Wm^{-2})$ |
|---|---|---|---|---|---|---|
| High | -13 | 1 | -12 | -14 | 17 | + 2 |
| Medium | -24 | 8 | -16 | -24 | 9 | -15 |
| Low | -28 | 17 | -11 | -25 | 2 | -23 |
| All | -65 | 26 | -39 | -63 | 28 | -35 |

is because gaseous absorption here is weak. Thus the relatively large upwelling longwave irradiance in the window is absorbed and re-emitted both back to the surface and up to the top of the atmosphere. Downward emission from clouds is strongest when cloud emitting temperature is high. Therefore the surface longwave cloud radiative forcing, $LWCF_s$, is most effective for warm, low-level clouds. As is well known, the greenhouse effect of clouds is strongest for clouds of high altitude because longwave emission from the cloud top is small due to low temperatures. Because cloud-top emission is low, the greenhouse effect of high cloud is comparable with the albedo effect (e.g. Stephens and Webster (1981)) with LWCF dominating over the shortwave cloud radiative forcing, SWCF. Kiehl (1994) showed, using the ERBE data, that high clouds produce a cancelling effect with regard to the shortwave and longwave radiation budget at the top of the atmosphere in the tropics. For the simple model and global mean properties employed in the present study, it is illustrated that high-level clouds have the potential to heat the Earth-atmosphere system radiatively. For lower level clouds, this is not the case; the net effect of clouds is to cool the Earth-atmosphere system. The LWCF is similar to the globally averaged value calculated by the Earth Radiation Budget Experiment (ERBE) satellite observations of 31 $Wm^{-2}$ (Harrison *et al.* (1990)). However, the SWCF is significantly more negative (by about 15 $Wm^{-2}$) than ERBE. This is likely to be a result of the simplifications involved in the shortwave calculations such as using global mean insolation, assuming water clouds and not including the effects of aerosols.

Using the illustrative estimates of surface cloud radiative forcing in Table 2.3, it is shown that clouds at all levels act to cool the surface due to the dominance of the 'shading' effect of clouds over their greenhouse effect. This is a well known result, although the global surface cloud radiative forcing has not previously been well represented. The lack of a

coherent surface radiometric and cloud observing system has required surface cloud forcing to be derived by satellite (e.g. Rossow and Zhang (1995)) or to be estimated using a simple column model (e.g. Kiehl and Trenberth (1997)). The global mean $\mathrm{LWCF}_s$ estimated by Kiehl and Trenberth (1997) of 44 $Wm^{-2}$ is significantly larger than the illustrative calculations and is due to the spatial coverage of low cloud amount being almost double that used in the present study. The satellite derived $\mathrm{LWCF}_s$ of 25 $Wm^{-2}$ by Rossow and Zhang (1995) is in good agreement with Table 2.3 although the $\mathrm{SWCF}_s$ is about 13 $Wm^{-2}$ more negative in the present study. The lack of surface radiometric and cloud observations require further studies to ensure that the surface component of the cloud radiative forcing is of an accuracy comparable to the top of the atmosphere satellite observations.

## 2.3 Clear-sky Simulation

A comprehensive re-analysis of atmospheric variables for a 15-year period was performed by the European Centre for Medium-Range Weather Forecasts Re-Analysis project (ERA) (Gibson *et al.* (1997)). Rather than being a perfect analysis of the atmosphere, ERA represents a model simulation that is continually forced by a varying spatial and temporal array of observations. Therefore inadequacies in the model and also the observation systems represent sources of error and uncertainty in the re-analysis. In regions of minimal observational input, the atmospheric moisture distribution will be highly dependent on the convection scheme used (Tiedtke (1989)). A distinct advantage, over other sets of analyses, is the use of a consistent assimilation model throughout the ERA period, January 1979 to December 1993. The use of satellite radiance data to infer atmospheric parameters allows better global coverage than is attainable using conventional observations. Aspects of the ERA climate are presented by Kallberg (1997), while an evaluation of ERA is provided by comparison with the satellite and radiosonde observing systems (Uppala (1997)).

Slingo *et al.* (1998) used the ERA analyses to perform simulations of clear-sky longwave fluxes and heating rates, with the acronym CLERA (Clear-sky Longwave from ERA). Radiative calculations were performed with the 9 spectral-band version of the Edwards and Slingo (1996) radiation code for every 6 hours over the entire ERA period. The radiation scheme used a separate, detailed line-by-line radiation scheme to calculate high spectral resolution (1 $cm^{-1}$ in the longwave) transmittances. The line-by-line code utilised the HITRAN spectral lines and the Clough *et al.* (1989) prescription of water vapour lines and continuum. Doppler broadening was also accounted for. The transmittances were calculated for each gas as a function of absorber amount, wavenumber, pressure and temperature. They were subsequently weighted with the black-body emission, for the given temperature,

and summed across each broad band to compute the band-averaged transmittances. An exponential sum fitting technique was employed to fit the transmissions for the reference curve while the remaining curves, dependent on temperature and pressure, were used to optimally derive scaling coefficients.

Edwards and Slingo (1996) showed calculated $OLR_c$ to agree to within about 2 $Wm^{-2}$ and $SDL_c$ to within about 4 $Wm^{-2}$ of line-by-line models using standard atmospheres utilised by the Intercomparison of Radiation Codes used in Climate Models (ICRCCM) project (Ellingson *et al.* (1991)). The ERA data was used on a 2.5° by 2.5° horizontal grid, with 31 sigma levels in the vertical for the atmosphere and also the surface temperature. The vertical resolution was estimated by Slingo *et al.* (1998) to cause an underestimation of $OLR_c$ of up to 2-3 $Wm^{-2}$ in the tropics. The well-mixed greenhouse gas concentrations ($CO_2$, $CH_4$, $N_2O$, CFC11, CFC12) were updated annually in accordance with IPCC (1995). Ozone was derived from a monthly mean climatology used in the Met. Office Unified Model (Cullen (1993)) and was assumed to be fixed throughout the analysis period. Interannual variability in ozone profiles is unlikely to be important with regard to the longwave radiation budget variability. Clear-sky profiles were assumed throughout, even in cloudy regions, thus ensuring that information on clear-sky irradiance was sampled globally. The definition of clear-sky irradiance therefore differs from that used by satellite studies such as the Earth Radiation Budget Experiment (e.g. Barkstrom (1984)), which sampled clear-sky radiance from cloudless regions only. As discussed in Chapter 1, the CLERA simulation provides clear-sky irradiance that is consistent with the method utilised with climate models (i.e. Method II; Cess and Potter (1987)). Therefore, the simulation constitutes a powerful tool in the validating and improving of climate models; initial results were presented by Slingo (1997).

Errors inherent in ERA are also likely to affect CLERA. Kallberg (1997) highlighted the main problems encountered in the assimilation process. The potential effect of these errors on the CLERA simulation are as follows:

1) The latent heat of freezing was incorrectly specified leading to a cooler tropical mid-troposphere and an over-active Inter Tropical Convergence Zone (ITCZ) with an over-estimation of total column moisture. This may cause overestimates in the $SDL_c$ and underestimates of the $OLR_c$ in tropical regions.

2) A cold bias in the surface temperature of high latitude land regions is likely to have caused an underestimate in E, $SDL_c$ and $OLR_c$ simulated by CLERA in these regions (e.g. Slingo *et al.* (1998)).

3) The unrealistic desert conditions produced over the western Amazon regions res-

ulted in a suppression of convection and cloudiness in this region. A change in the assimilation of surface pressure beginning January 1987 of the ERA period was installed to fix this problem. The effect on the global climate is uncertain although potentially significant. The change in local climate coincided with a global increase in total column moisture and also with a southward shift in the African ITCZ (Kallberg (1997)). The local effect of the change in Amazonian climate at this time is likely to have caused an erroneous increase in $SDL_c$ and decrease in $OLR_c$ simulated by CLERA. However, the global impact of both the Amazonian and African ITCZ changes on the CLERA simulation are uncertain.

A further error was caused by the top-level ERA soil temperature being used in the CLERA simulation over land regions rather than the surface skin temperature. This is likely to cause an underestimate in the surface emission during the day-time. However, ERA surface skin temperatures are also thought to be in error at local noon (Saunders pers. comm. (1998)) so would not have increased the simulation accuracy markedly in this respect. In view of all these considerations, the irradiance accuracy may be estimated to be within about $\pm 5\ Wm^{-2}$ for most regions of the globe when considering monthly mean irradiance. This may be larger locally and for 6-hourly irradiance is likely to be within about $\pm 10\ Wm^{-2}$ which is comparable with instantaneous surface irradiance observations (e.g. Weller and Anderson (1996)).

Slingo *et al.* (1998) attempted to highlight the major sources of error in CLERA $OLR_c$. The present study extends this analysis by comparing the simulated irradiance at the surface with ground-based observations. Errors in ERA total column moisture and near surface temperatures are likely to constitute the largest uncertainties with regard to the simulated $SDL_c$. Further errors to surface irradiance, and to a lesser extent $OLR_c$, are likely to be caused by the black-body surface emission assumption as discussed in Sec. 2.2 (CLERA sets surface longwave emissivity to unity for consistency with ERA). However, by considering the $SDL_c$, which is dependent only on atmospheric parameters, potential irradiance errors due to incorrect specification of surface emissivity are avoided in Chapter 4. The $OLR_c$ error will depend on errors in surface and atmospheric temperature and atmospheric moisture error as discussed in Chapters 3 and 5. Regions of sparse observational data such as the Indian Ocean and the southern Hemisphere oceans and also at higher altitudes (e.g. Uppala (1997), Spencer and Braswell (1997)) introduce an uncertainty into ERA and hence the CLERA simulation. The quantification of uncertainty of the ERA climate *variability* between months and years is a further difficulty.

# Chapter 3

# SENSITIVITY STUDIES

## 3.1 Introduction

Satellite observations of the Earth's radiation budget and cloud distributions provide valuable information regarding the nature of the water vapour and cloud feedbacks when considered in conjunction with analyses of the surface and the atmosphere (e.g. IPCC (1996)). However, attributing the radiative perturbations to specific fluctuations in atmospheric parameters is non-trivial. This is a consequence of the multiple dependence of irradiance variability on an array of atmospheric and surface parameters, all of which are fluctuating over contrasting spatial and temporal scales. Therefore to understand the dependence of the Earth's radiation budget variability on atmospheric and surface variables, it is necessary to assess the irradiance changes in conjunction with idealised calculations of the radiation budget sensitivity to relevant parameters. These idealised calculations serve as a reference point from which irradiance variations may be interpreted and attributed. Thus the primary aim of this chapter is to provide such idealised sensitivity calculations that may be used, in subsequent chapters, as a framework for interpreting the irradiance variability observed or simulated at the surface and at the top of the atmosphere.

The primary focus of this Chapter is to quantify the clear-sky longwave irradiance sensitivity to changes in water vapour amount and temperature changes. These parameters are important in assessing the clear-sky feedbacks involving water vapour and the temperature lapse rate. The strong thermodynamic coupling between water vapour and temperature has long been noted. Increasing the temperature of air results in an increase in the maximum potential amount of non-condensed water. This is explained by the thermodynamically derived Clausius-Clapeyron equation (e.g. Hess (1959)) which predicts that the water vapour partial pressure increases exponentially with (-1/$T$) where $T$ is the temperature in Kelvin. Theory dictates that atmospheric water vapour amount will therefore increase

quasi-exponentially with temperature if relative humidity, $RH$, remains constant. Indeed observations have shown that the spatial variation of total column moisture is consistent with this premise (e.g. Raval and Ramanathan (1989)). Temporal increases in $T_s$ have also been observed to accompany increases in total column moisture (e.g. Bony *et al.* (1995)) due to relatively small changes in lapse rates and humidity profiles, thus highlighting the thermodynamic coupling.

Vertical diffusion and convection as well as the horizontal mixing of air masses of different temperature act to increase the relative humidity, while large scale subsidence combined with the efficiency of precipitation act to decrease $RH$ (e.g. Schneider *et al.* (1997a)). These compensating effects therefore imply that only small changes in relative humidity are likely when entire circulation systems are considered. Manabe and Wetherald (1967) showed, using a single column model, that when temperatures are increased in response to greenhouse gas forcing, a strongly positive water vapour feedback to the warming results when $RH$ is fixed. However, it has been proposed, for example by Lindzen (1990), that departures from this constant $RH$ criteria could significantly influence and potentially counteract this positive water vapour feedback. Modelling studies such as Del Genio *et al.* (1991) have shown only small changes in $RH$ with time, although these studies are limited by the inadequate knowledge of the physical processes involved in the atmospheric water budget. Thus a further design of this Chapter is to provide information regarding the sensitivity of the radiation budget to changes in water vapour amount that either varies with temperature by assuming constant $RH$ or varies independent of temperature (i.e. changing $RH$).

A secondary motivation for this chapter is to assess the effect of cloud on the clear-sky computation of irradiance sensitivity. The calculations are presented mainly for illustrative purposes and are therefore not as detailed as the clear-sky longwave computations. However, the illustrative calculations serve to highlight the relative importance of clouds in both influencing the clear-sky feedbacks and also in producing cloud radiative feedbacks to surface temperature changes. The results of these studies, used in conjunction with the clear-sky calculations, provide useful information with regard to irradiance observations at the surface in Chapter 4 and at the top of the atmosphere by satellite as in Chapter 6.

While the present study cannot quantify the radiative feedbacks operating in the climate system, a first estimate of the relative importance of the individual changes in atmospheric structure/properties may be assessed. Also, as stated previously, the results of this analysis may be used as a framework for the primary investigations of this thesis. The remainder of this chapter is organised as follows. The next section presents a framework in which

the sensitivity of the Earth's radiation budget to temperature, humidity and cloud amount and properties can be interpreted. Section 3.3 will assess the height dependence of surface and top of atmosphere irradiance to changes in atmospheric properties. Attempt is made in Sec. 3.4 to partition the water vapour feedback into a constant $RH$ component and also a component involving changes in relative humidity. The shortwave radiative effects and cloud radiative effects on these calculations are also discussed using illustrative calculations and simple assumptions regarding the shortwave and cloud radiative specifications. Potential errors to the clear-sky radiative calculations introduced by uncertainty in the input parameters to the radiation scheme are examined in Sec 3.5. Conclusions are presented in the final section.

## 3.2 Framework

Changes in temperature and humidity affect directly the longwave and shortwave components of the radiation budget by altering the absorption and emission properties of the atmosphere. Indirect effects due to, for example, an increase in cloud amount in response to an increase in atmospheric humidity, further modify the radiation budget. The purpose of this section is to provide a framework for interpreting the changes in the radiation budget components due to direct and indirect dependence on changes in temperature and humidity fields. As discussed in Chapter 1, the net radiation may be expressed as a function of clear-sky and cloud radiative forcing components at the top of the atmosphere:

$$NET = ASR - OLR = ASR_c + SWCF - OLR_c + LWCF, \tag{3.1}$$

and at the surface:

$$NET_s = ASR_s - E + SDL = ASR_{s\ c} + SWCF_s - E + SDL_c + LWCF_s, \tag{3.2}$$

where NET is the net downwelling irradiance, ASR is the absorbed shortwave irradiance, OLR is the outgoing longwave radiation at the top of the atmosphere, E is the surface emission, SDL is the surface downwelling longwave irradiance and LWCF and SWCF are the longwave and shortwave cloud radiative forcing components. The subscripts, $c$ and $s$ denote clear-sky and surface irradiance quantities respectively.

### 3.2.1 Clear-sky Sensitivity

The SDL, may be considered a function of surface and atmospheric temperature and atmospheric clear-sky emissivity, $\epsilon_a$. Because SDL is highly sensitive to the temperature near to the surface (e.g. Zhao *et al.* (1994)), and the near-surface temperature is strongly

coupled to the surface temperature, $T_s$ is used in place of the near-surface atmospheric temperature in the following expression:

$$SDL_c = \epsilon_a \sigma T_s^4 \tag{3.3}$$

A change in $\mathrm{SDL}_c$ may therefore be expressed as a function of a change in $T_s$ with constant $RH$ (denoted by $\overline{RH}$), and a change in $RH$:

$$\Delta SDL_c = \left[\left(4\sigma T_s^3 \overline{\epsilon_a} + \sigma T_s^4 \frac{\partial \epsilon_a}{\partial T_a}\frac{dT_a}{dT_s}\right) + \sigma T_s^4 \frac{\partial \epsilon_a}{\partial u}\frac{du}{dT_s}\right]_{\overline{RH}} \Delta T_s + \sigma T_s^4 \frac{\partial \epsilon_a}{\partial RH}\Delta RH, \tag{3.4}$$

where $u$ is the total column moisture and $\overline{\epsilon_a}$ denotes the mean value of $\epsilon_a$ for the given change in atmospheric parameters. The term, $4\sigma T_s^3 \overline{\epsilon_a}$ relates to the direct changes in $\mathrm{SDL}_c$ due to temperature changes. To complete the calculation of $\partial SDL_c/\partial T_s$ the additional term, $\sigma T_s^4 \frac{\partial \epsilon_a}{\partial T_a}\frac{dT_a}{dT_s}$, which is of order 0 to -1 $Wm^{-2}K^{-1}$, is required. This is because the continuum emission decreases with increasing temperature (e.g. Clough *et al.* (1992)). Also, the departure of wavelength dependent $\mathrm{SDL}_c$ from broad band theory and the consequent dependence of SDL on colder temperatures away from the surface layer cause the effective broad band atmospheric emissivity to vary with temperature. The remaining two terms relate to the changes in $\mathrm{SDL}_c$ due to changes in water vapour amount associated with changes in temperature if $RH$ were to remain constant and due to changes in $RH$. From Eq. 3.4 it follows,

$$\Delta SDL_c = \left[\frac{\partial SDL_c}{\partial T_s} + \frac{\partial SDL_c}{\partial u}\frac{du}{dT_s}\right]_{\overline{RH}} \Delta T_s + \frac{\partial SDL_c}{\partial RH}\Delta RH. \tag{3.5}$$

Considering Eq. 2.3 in Chapter 2, $\mathrm{OLR}_c$ may be expressed as:

$$OLR_c = \sigma {T_s}^4 Tr + OLR_a(T(p), q(p)), \tag{3.6}$$

where $\sigma {T_s}^4$ is the wavelength integrated (black-body) surface emission and $Tr$ is the *effective* atmospheric transmittance. It is an effective transmittance because the transmission varies with wavelength and therefore the Planck function becomes more important in the relatively transparent window regions of the spectrum. The second right hand term represents the atmospheric emission to space ($\mathrm{OLR}_a$) which is dependent primarily on temperature, $T$, and specific humidity, $q$, throughout the profiles as well as the concentration of $CO_2$ and other greenhouse gases.

Increasing $T(p)$ in Eq. 3.6 acts to enhance the longwave emission to space from the atmosphere, while increases in $q$ act to decrease the surface component of the OLR and also reduce $\mathrm{OLR}_a$ by shifting emission to a higher, generally colder layer. Thus it is useful to explain the $\mathrm{OLR}_c$ in terms of surface and atmospheric temperature and water vapour

amounts. Shine and Sinha (1991) showed that $\mathrm{OLR}_c$ is sensitive to relative changes in $q$ throughout the atmosphere but that $\mathrm{OLR}_c$ is far more sensitive to absolute changes in $q$ in the upper troposphere than at other levels. Therefore, in developing an atmospheric humidity parameter that describes adequately the $\mathrm{OLR}_c$ variability, it is more useful to consider the $RH$ rather than the total column moisture. A further reason for using $RH$ is that $T$ and $q$ have opposing effects on the $\mathrm{OLR}_c$, which almost cancel in the water vapour bands if relative humidity is held constant (Slingo and Webb (1997), Harries (1997)). However, the cancellation is not complete because water vapour does not absorb strongly over the entire spectrum. Because atmospheric temperature, $T_a$, is coupled to a certain degree with $T_s$, a change in $\mathrm{OLR}_c$ may be expressed as a function of a change in $T_s$ and a change in atmospheric relative humidity, $RH$:

$$\Delta OLR_c = \left[4\sigma T_s^3 \overline{Tr} + \left(\sigma T_s^4 \frac{\partial Tr}{\partial T_a} + \frac{\partial OLR_a}{\partial T_a}\right)_{(\overline{RH})} \frac{dT_a}{dT_s}\right] \Delta T_s$$

$$+ \left(\sigma T_s^4 \frac{\partial Tr}{\partial RH} + \frac{\partial OLR_a}{\partial RH}\right) \Delta RH, \tag{3.7}$$

from which it follows that,

$$\Delta OLR_c = (4\sigma {T_s}^3 \overline{Tr} + \alpha)\Delta T_s + \frac{\partial OLR_c}{\partial RH}\Delta RH. \tag{3.8}$$

Equation 3.8 shows that there is dependence of OLR variability on $T_s$ and $RH$ and is a similar model to that developed by Thompson and Warren (1982). The parameter, $\alpha$ $(Wm^{-2}K^{-1})$, denotes an amplification of $\mathrm{OLR}_c$ response to $\Delta T_s$ by changes in atmospheric temperature with constant $RH$. Relative humidity is calculated with respect to water at temperatures greater than 270 $K$ and with respect to ice at temperatures less than 250 $K$ (e.g. Liou (1980)). Between 270 and 250 $K$, a linear interpolation between the calculation over water and ice was assumed. The sensitivity of $\mathrm{OLR}_c$ to changes in temperature, with constant $RH$, are within about 5% of the value calculated for $RH$ over water only. For a given *specific* humidity profile, a change in $RH$ calculated with respect to water and ice gives rise to a sensitivity of between 10 and 35% less than when $RH$ is calculated with respect to water only. However, the profile $RH$ calculated for each method is different. For the given column mean $RH$ calculated by each method, the sensitivity of $\mathrm{OLR}_c$ to changes in $RH$ calculated over water is within 5% of the corresponding value for $RH$ calculated over water and ice.

### 3.2.2 Cloud radiative forcing sensitivity

The concept of cloud radiative forcing was presented in Chapter 1. Using this methodology, the radiation budget may be separated into clear-sky and cloud components utilising

the clear-sky framework described previously. Cloud radiative forcing will be affected by changes in cloud amount or properties associated with the change in temperature or humidity. Cloud radiative forcing is also dependent directly on changes in temperature and humidity (e.g. Weare (1995)). For a fixed cloud distribution, an increase in $T_s$ will result in an increased LWCF at the top of the atmosphere because most of the increased emission to space for clear-sky conditions ($4\sigma T_s^3 \overline{Tr}$ term in Eq. 3.8) will be absorbed by the cloud, thus increasing $OLR_c - OLR$. An increase in cloud optical depth due, for example, to increases in $T_s$ (e.g. Tselioudis *et al.* (1992)), will also affect cloud radiative forcing. Therefore the change in cloud radiative forcing may be approximated by:

$$\Delta CF = \left( \frac{\partial CF}{\partial T_s(\overline{RH})} \Delta T_s + \frac{\partial CF}{\partial RH} \Delta RH \right) + \left( \frac{\partial CF}{\partial A_c} \frac{dA_c}{dx} + \sum_{i=1,n}^{n} \frac{\partial CF}{\partial c_i} \frac{dc_i}{dx} \right) \Delta x, \qquad (3.9)$$

where the term CF may be replaced by $LWCF$, $SWCF$ or $NCF$ at the surface or at the top of the atmosphere. $A_c$ denotes fractional cloud amount, $x$ denotes a change in atmospheric properties and $c_i$ denotes a change in cloud property, $i$. The calculations involving shortwave and cloud radiative effects are presented mainly for illustrative purposes and to aid the analyses of later chapters. The effect of changes in aerosol and ozone concentrations on the radiation budget components are not considered in the present study.

## 3.3 Height Dependent Irradiance Sensitivity

The narrow band radiative transfer scheme and McClatchey *et al.* (1972) standard atmospheres described in Chapter 2 were used initially to assess the sensitivity of the Earth's clear-sky longwave radiation budget to height dependent changes in water vapour mass mixing ratio and temperature.

### 3.3.1 Absolute and Relative Increases in Water Vapour Amount

Figure 3.1 shows the effect of absolute (1 $g/kg$) and relative (10%) increases in water vapour mass mixing ratio in 50 $hPa$ vertical slabs, on the $\mathrm{OLR}_c$ and $\mathrm{SDL}_c$ for a range of standard atmospheres. $\mathrm{OLR}_c$ is most sensitive to absolute increases in water vapour amount at 125 $hPa$ for the tropical profile and at 325 $hPa$ for the sub-arctic winter profile (Fig. 3.1(a)). The strong peak in sensitivity results from the balance between decreasing temperature and decreasing water vapour path to space with increasing altitude (e.g. Harries (1997)). When relative increases in water vapour amount are considered (Fig. 3.1(b)), $\mathrm{OLR}_c$ is sensitive to perturbations throughout much of the troposphere. The response is similar to the net longwave irradiance at the tropopause as shown in Fig. 3 of Shine and Sinha (1991). A peak in $\mathrm{OLR}_c$ sensitivity in the upper troposphere is evident for all four

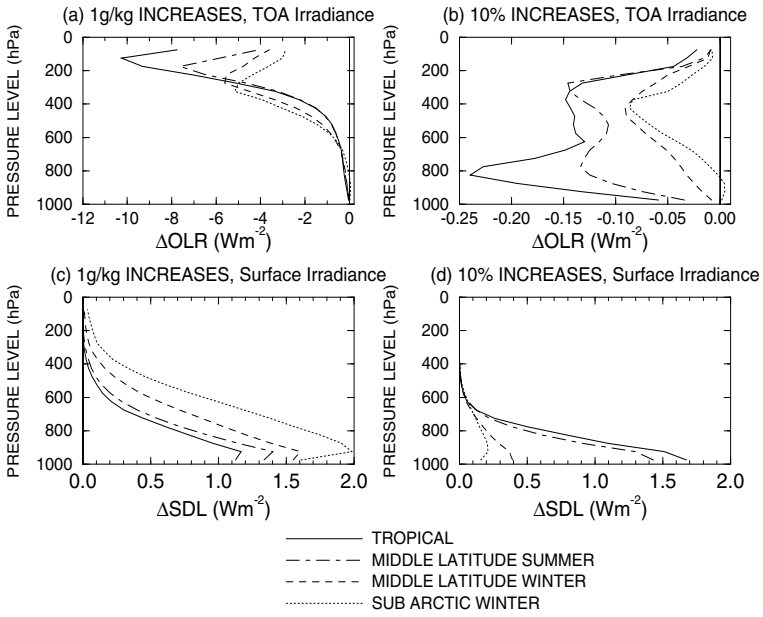


Figure 3.1: *Irradiance sensitivity at the top of the atmosphere (a and b) and at the surface (c and d) to 50 hPa vertical slab height dependent increases in water vapour mass mixing ratio using four standard atmospheric profiles and assuming clear-skies. The change in irradiance is shown for absolute increases of 1 g/kg (a and c) or relative increases of 10% (b and d) in water vapour mass mixing ratio.*

profiles. This is a consequence of water vapour rotational effects (e.g. Sinha and Harries (1995)). Again, the altitude of this peak is dependent on atmospheric temperature and water vapour vertical structure. For the tropical profile, a second peak at about $800hPa$ is highly important. This peak is ascribed to the self-broadening component of the water vapour continuum absorption; without the continuum parameterization, the $\mathrm{OLR}_c$ sensitivity is reduced by a factor of 4 at 800 $hPa$ (not shown). This second peak is not discernible for the cold, dry, mid-latitude and sub-arctic winter profiles because the water vapour continuum absorption is weak.

A 1 $g/kg$ increase in water vapour amount results in increases in $\mathrm{SDL}_c$ for perturbations throughout much of the troposphere. The maximum response is at about 925 $hPa$ of over 1 $Wm^{-2}$ for all atmospheres considered (Fig. 3.1(c)). The profiles with lower moisture amounts yield the largest response at the surface for two reasons. Firstly, the dry profiles contain a smaller water vapour path between the perturbation level and the surface and consequently transmission is high. The second reason is that for a given change in absorber amount, a greater change in emittance will result when starting from a lower amount of the absorber. Relative increases in water vapour amount at pressures less than about 400 $hPa$ give a negligible surface response (Fig. 3.1(d)). Perturbations to lower layers give

progressively larger increases in $SDL_c$. For the tropical case, an increase in $SDL_c$ larger than 1.5 $Wm^{-2}$ results from water vapour amount increases at pressures greater than 950 $hPa$. This sensitivity is reduced to below 0.5 $Wm^{-2}$ without the water vapour continuum effects (not shown). The sub-arctic winter atmosphere response is maximum for the 900 to 950 $hPa$ layer with $SDL_c$ increasing by 0.25 $Wm^{-2}$; the layer immediately below this is colder and drier which causes a smaller rise in $SDL_c$.

Water vapour variability also affects the shortwave components of the surface and top of atmosphere radiation budget. To illustrate this effect, the tropical profile was prescribed January mean tropical insolation and an oceanic albedo of 0.07. For the 10% increases in water vapour amount, the $ASR_s$ decreases while the ASR increases. The sensitivity was greatest for perturbations in the lowest 50 $hPa$ slab, with the shortwave effect offsetting the longwave surface downward irradiance increases by 16%. The increased net downwelling irradiance at the top of the atmosphere, due to the $OLR_c$ decrease in response to the 950 to 1000 $hPa$ slab water vapour amount increase, was amplified by 36% because of an increase in ASR.

### 3.3.2 Water Vapour Amount and Temperature Changes Assuming Constant Relative Humidity

As stated previously, $RH$ is observed to vary only slightly when considering entire circulation systems. Thus it is useful to consider the radiative effects of increases in water vapour amount with temperature assuming constant $RH$. The sensitivity of the $OLR_c$ and $SDL_c$ to temperature increases and water vapour mass mixing ratio increases for constant $RH$ are now considered for the tropical and sub-arctic winter profile (Fig. 3.2). Water vapour amount was varied in response to a 1 $K$ increase in temperature at each 50 $hPa$ layer by holding constant the $RH$. The combined and relative effects of temperature and water vapour were determined.

The irradiance response to the changes in water vapour amount assuming constant $RH$ resembles the response to 10% increases in water vapour amount rather than the absolute changes shown in Fig. 3.1. The water vapour amount changes are smaller than the 10% increases in the tropical profile lower troposphere. This results in a smaller $OLR_c$ and $SDL_c$ response (about 40% lower at 800 $hPa$). The changes in $OLR_c$ and $SDL_c$ due to a 10% height dependent increase in water vapour amount in Fig. 3.1 is found to correspond with $RH$ increases of approximately 4% at about 800 $hPa$ and 2% for the upper troposphere (about 300 $hPa$). Increases in temperature overwhelm the $OLR_c$ response to increases in water vapour amount for all but the 150 to 200 $hPa$ layer in the tropical profile. This is

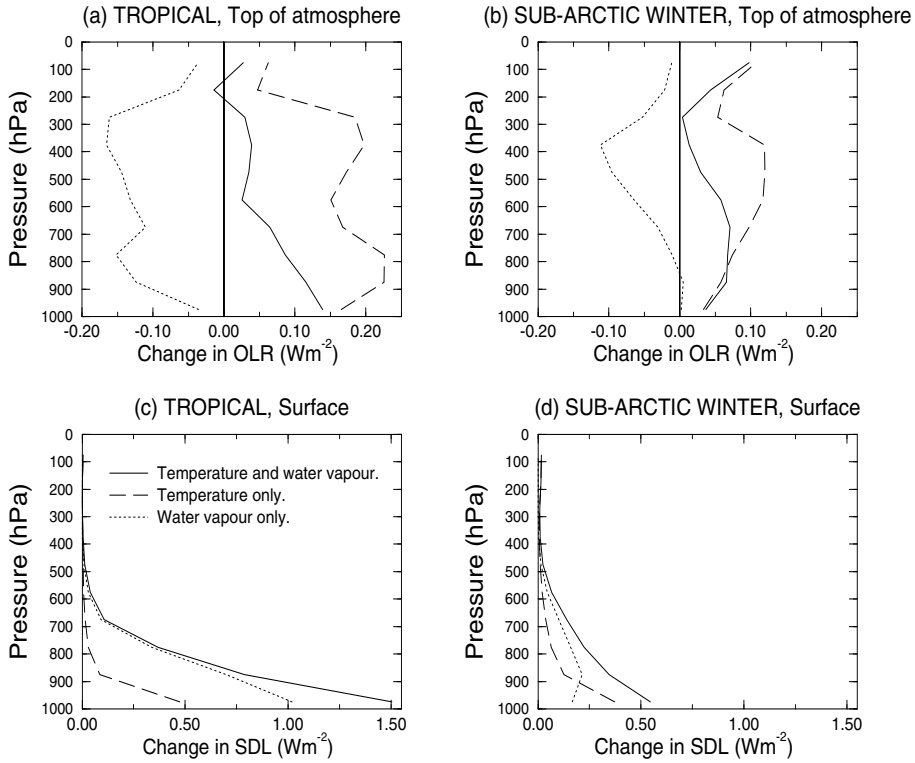


Figure 3.2: *Changes in clear-sky irradiance ($Wm^{-2}$) at the top of the atmosphere (a and b) and at the surface (c and d) for height dependent increases in temperature and water vapour mass mixing ratio in 50 hPa vertical slabs of the tropical profile (a and c) and the sub-arctic winter profile (b and d). Temperature increases are 1 K and water vapour increases correspond to the change that would occur for a 1 K increase in temperature if relative humidity were to remain constant.*

a salient feature; increases in temperature and water vapour amount with constant $RH$ can generate *decreases* in $\mathrm{OLR}_c$, albeit for a small region of the tropical upper troposphere. Generally, temperature changes dominate over the water vapour mass mixing ratio change, causing an increase in the $\mathrm{OLR}_c$, especially near to the surface in the tropical profile.

Clear-sky SDL is most sensitive to changes in temperature and water vapour amount in the 50 $hPa$ layer nearest to the surface. This is because much of the downward emission of longwave radiation from higher altitudes is absorbed by lower altitude layers. The sensitivity to changes in temperature is important for a much smaller vertical layer near to the surface compared to the $\mathrm{SDL}_c$ sensitivity to water vapour amount. Considering a 36 $m$ thick layer directly above the surface, 1 $K$ increases in temperature were found to increase the $\mathrm{SDL}_c$ significantly (by 1 $Wm^{-2}$) for the tropical profile. This is explained by considering that the atmosphere approximates to a black body emitter over much of the longwave spectrum near to the surface most especially for the moist tropical profile (i.e. see Fig. 2.1). Therefore for these regions of the spectrum, $\mathrm{SDL}_c$ is determined primarily by the near-

surface temperature. In the window regions of the spectrum, $\epsilon_a$ is small and fluctuations in temperature affect $SDL_c$ only slightly. However, the quadratic dependence of the water vapour continuum emission on water vapour amount (e.g. Clough *et al.* (1989)) result in a large sensitivity of $SDL_c$ to the column moisture, which mainly resides in the lower troposphere. The spectral radiative effects of changes in temperature and water vapour amount are discussed further in Sec. 3.4.

## 3.4 Changes in Temperature and Water Vapour Profiles assuming constant and varying Relative Humidity

This section provides information concerning the water vapour feedback by allowing the entire water vapour profile to vary either in accordance with the constant $RH$ criteria (e.g. Manabe and Wetherald (1967)) or for changes in column $RH$. Further experiments were carried out in which cloud amount and properties were specified and perturbed. A key question to be addressed is, what changes in relative humidity or cloud amount/properties would be required to counteract the constant $RH$ water vapour feedback?

### 3.4.1 Experimental Design

Three sensitivity studies were performed using the standard atmospheres as follows:

1) THERM - Surface and atmospheric temperatures at pressures greater than 100 $hPa$ were increased by 1 $K$. Water vapour amount was increased to conserve the $RH$ of the initial profile.

2) LAPSE - As experiment THERM, but the temperature lapse rate was increased. Atmospheric temperature at pressure, $p$, was varied throughout the atmosphere with $T_s$ by,

$$\Delta T(p) = \frac{\Delta T_s(p - 200)}{(p_s - 200)}, \tag{3.10}$$

where $\Delta T_s$ was 1 $K$. This experiment was carried out to be more consistent with the observed temperature increases in the troposphere and stratospheric cooling (e.g. Angell (1988)). Again, the $RH$ was fixed at the initial profile.

3) RHI - Relative humidity was increased by 1% for pressures greater than 100 $hPa$ with no change in temperature.

A further experiment was performed in which temperature was increased by 1 $K$ and $RH$ was increased by 1 % for pressure levels greater than 100 $hPa$. The resulting irradiance changes were within 4 % of the sum of changes for experiments THERM and RHI, thus validating the use of Eq. 3.5 and 3.8.

The effect of global mean cloud amount and properties on the clear-sky sensitivities for each experiment were also calculated for the global mean profile with cloud parameters prescribed in Table 2.1, Chapter 2. Finally the sensitivity of the Earth's radiation budget to a 10% increase in cloud amount and an increase in liquid water path (LWP) of 0.1 was computed. The clear-sky shortwave and the longwave and shortwave cloud radiative forcing calculations are presented merely as an illustration and to place the calculated clear-sky sensitivities in context. They also aid the interpretation of Chapter 4 and Chapter 6, both of which consider the effects of cloud and its variability on the longwave and shortwave irradiance.

### 3.4.2 Results

The changes in longwave radiation budget components are shown in Table 3.1 with the changes in total column moisture, $u$, and the mean atmospheric effective transmissivity ($\overline{Tr} = \partial OLR_c/\partial E$) and atmospheric emissivity at the surface ($\overline{\epsilon_a} = \partial SDL_c/\partial E$). The over-bar represents an average of the parameter calculated from the initial profile and the perturbed profile. It is noted that, to first order approximation, $\overline{Tr} = 1 - \overline{\epsilon_a}$, which validates

Table 3.1: *Changes in total column moisture, u ($kgm^{-2}$), surface longwave emission, E ($Wm^{-2}$), clear-sky surface downward longwave emission, $SDL_c$ ($Wm^{-2}$), and clear-sky outgoing longwave radiation, $OLR_c$ ($Wm^{-2}$), for experiment THERM. The mean atmospheric effective transmissivity, $\overline{Tr}$ and the effective atmospheric emissivity at the surface, $\overline{\epsilon_a}$, are also shown for five standard atmospheres.*

| Profile | $\Delta u$ ($kgm^{-2}$) | $\Delta E$ ($Wm^{-2}$) | $\Delta SDL_c$ ($Wm^{-2}$) | $\Delta OLR_c$ ($Wm^{-2}$) | $\overline{\epsilon_a}$ | $\overline{Tr}$ |
|---|---|---|---|---|---|---|
| TRP | 2.7 | 6.1 | 9.1 | 1.8 | 0.87 | 0.13 |
| MLS | 2.0 | 5.8 | 8.1 | 2.0 | 0.83 | 0.18 |
| SAS | 1.6 | 5.4 | 6.9 | 2.0 | 0.78 | 0.23 |
| MLW | 0.7 | 4.6 | 4.8 | 2.2 | 0.72 | 0.31 |
| SAW | 0.4 | 3.9 | 3.9 | 2.1 | 0.71 | 0.34 |
| GAM | 1.6 | 5.4 | 7.4 | 2.0 | 0.81 | 0.21 |

the use of broadband emissivity models as a useful diagnostic tool in climate studies. The increase in $u$, for the prescribed uniform increase in temperature, rises dramatically from the cold sub arctic winter profile to the warm, moist tropical profile. This is explained by the quasi-exponential dependence of saturated water vapour partial pressure on temperature (e.g. Raval and Ramanathan (1989)). $SDL_c$ increases at approximately the same rate as

surface emission for the sub-arctic winter profile. However, the much larger changes in $u$ for the warmer profiles causes $\mathrm{SDL}_c$ to increase at a greater rate than surface emission; this constitutes a surface super-greenhouse effect (SGE; e.g. Vonder Haar (1986)) where the surface longwave cooling diminishes with increased temperature.

Clear-sky OLR increases are similar for all profiles considered. The modest increases in $\mathrm{OLR}_c$, relative to the increase in surface emission, were first considered in detail by Simpson (1927). In the strong water vapour absorption bands, emission to space of a given wavelength is centred on a relatively thin vertical layer of the atmosphere. Below this level, radiation of this wavelength is increasingly absorbed by the higher water vapour path aloft as altitude decreases. At higher altitudes than the important emitting layer direct emission to space also decreases rapidly due to decreasing water vapour amount and low temperatures. Therefore the relative importance of each layer in determining $\mathrm{OLR}_c$ of the given wavelength is maximum at a given pressure level depending on the profiles of temperature and moisture (e.g. Harries (1997)). This is clearly seen in Fig. 2.2 in Chapter 2. Because the majority of the emission is determined by a relatively thin vertical atmospheric slab of given water vapour path to space, increases in temperature assuming constant $RH$ merely cause the altitude of this layer to increase to a level of the initial water vapour path to space. This therefore also corresponds with the initial temperature of the important emitting layer. Therefore $\mathrm{OLR}_c$ cannot increase as both temperature and water vapour path to space of the important emitting layer remain constant (Slingo and Webb (1997)). This effect applies only to the strong water vapour bands, so an increase in $\mathrm{OLR}_c$ is observed in the window region (Simpson (1928)).

The changes in $E$, $\mathrm{SDL}_c$ and $\mathrm{OLR}_c$ for experiment THERM are plotted with wavenumber in Fig. 3.3 for the tropical profile (a) and the sub arctic winter profile (b). The corresponding change in irradiance with wavenumber is shown for tropical minus sub-arctic winter profiles in 3.3(c) by way of a comparison. The Simpson-effect is clearly visible away from the window region for the tropical case with only small increases in $\mathrm{OLR}_c$. This effect is not so marked in the sub-arctic winter case because the strong water vapour absorption is confined to fewer regions of the spectrum than for the tropical case. $\mathrm{OLR}_c$ increases at the same rate as surface emission in the window region for the sub-arctic profile because continuum absorption is weak. Significant increases in $\mathrm{OLR}_c$ at about 500 to 600 $cm^{-1}$ show a secondary window, or 'dirty' window (Pinto *et al.* (1997)), which is important for the sub-arctic profile.

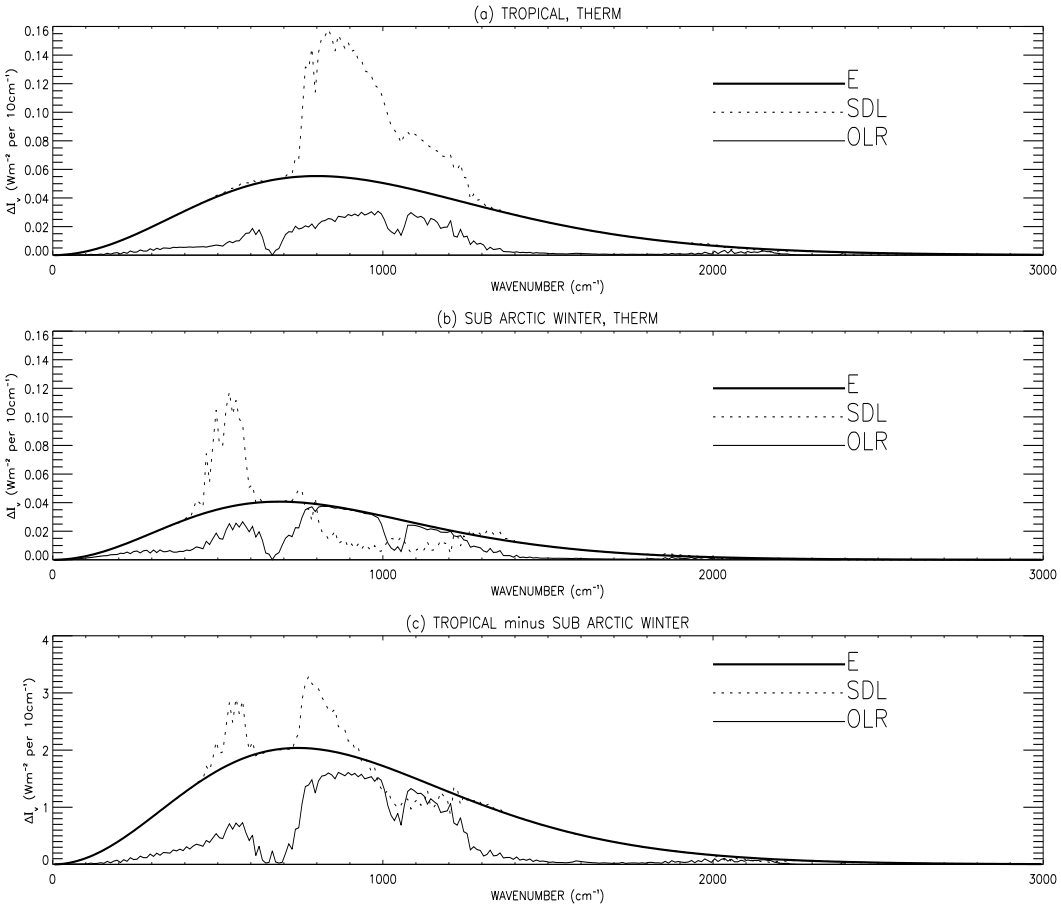


Figure 3.3: *Changes in surface longwave emission, E, clear-sky surface downwelling longwave irradiance, SDL and clear-sky outgoing longwave irradiance, OLR, (all* $Wm^{-2}$ *per* $10cm^{-1}$*), as a function of wavenumber for the experiment THERM for (a) tropical and (b) sub arctic winter profiles, and (c) for tropical minus sub arctic winter profile irradiance.*

Increases in $\mathrm{SDL}_c$ for the tropical profile are approximately equal to the increases in $E$ in all but the window region where $\mathrm{SDL}_c$ increases at a greater rate than the surface emission. Therefore the surface SGE is explained by the strong increase in emission from the window region of the spectrum. As stated previously, this stems from the quadratic dependence of water vapour continuum emission on the partial pressure of water vapour. When experiment THERM is run without the water vapour continuum parameterization, no surface SGE results (i.e. $\mathrm{SDL}_c$ increases are less than surface emission increases). A surface SGE is not seen for the main window region for the sub-arctic profile, with only small increases in $\mathrm{SDL}_c$. However, a surface SGE operates in the dirty-window region as denoted by $\mathrm{SDL}_c$ increases greater than $E$ (Fig. 3.3(b)). In the tropical profile this secondary window is effectively filled by absorption due to the wings of the pure rotation lines (e.g. Clough *et al.* (1992)). The tropical minus sub-arctic winter plot (Fig. 3.3(c)) shows much

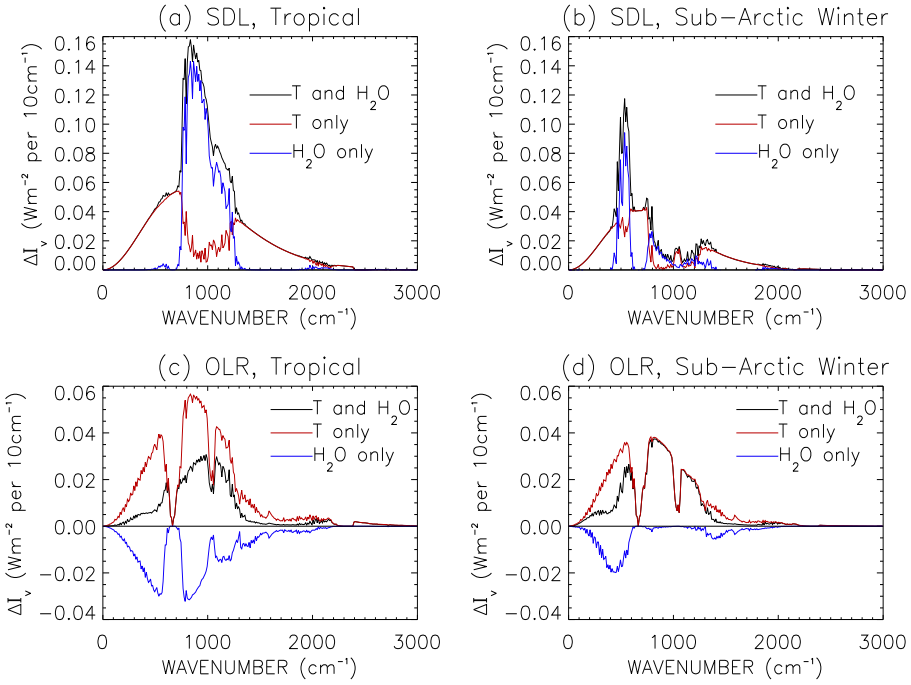


Figure 3.4: *Changes in clear-sky surface downwelling longwave irradiance, SDL, and clear-sky outgoing longwave irradiance, OLR, as a function of wavenumber ($Wm^{-2}$ per $10cm^{-1}$) for experiment THERM. Changes in SDL are shown for (a) tropical and (b) sub arctic profiles, while changes in OLR for the tropical profile are shown in (c) and for the sub arctic winter profile in (d). The irradiance change due to changes in temperature (red lines), water vapour (blue lines) and the combined temperature and water vapour contribution (black lines) are displayed.*

of the $OLR_c$ increase to be due to increases in emission from the window regions and to a lesser extent the dirty window. $OLR_c$ increases in the main water vapour bands and main carbon dioxide band are minimal. A surface SGE operates either side of the 15 $\mu m$ carbon dioxide band, although $SDL_c$ increases between about 1000 to 1200 $cm^{-1}$ are less than surface emission increases.

Figure 3.4 shows the relative contribution of temperature and water vapour amount changes to the changes in $OLR_c$ and $SDL_c$ for experiment THERM using the tropical and sub-arctic winter profiles. As stated in Sec. 3.3, the changes in $SDL_c$ are determined by temperature changes near to the surface in the non-window regions while it is primarily variations in column moisture that determine the $SDL_c$ response in the window regions of the spectrum. Increases in $OLR_c$ due to temperature increases in the tropical profile are shown to be offset significantly by the decrease in $OLR_c$ due to increases in water vapour amount. For the sub-arctic profile, increases in $OLR_c$ are exclusively due to temperature increases in the window region of the spectrum, while increases in $OLR_c$ at wavenumbers

less than about 600 $cm^{-1}$, due to temperature increases, are offset significantly by decreases in $OLR_c$ caused by increased absorption of upwelling irradiance in the water vapour pure rotation bands.

Increasing atmospheric temperatures by a progressively lower rate with altitude, compared to the change in $T_s$, (experiment LAPSE) causes $SDL_c$ increases 10 to 15% lower and $OLR_c$ increases 20% lower than for experiment THERM where temperature increases are uniform. The LAPSE column moisture increases are about 25% lower than for THERM which accounts for much of the difference in $SDL_c$ changes between experiments. The smaller $OLR_c$ sensitivity to changes in $T_s$ in experiment LAPSE arise because the atmospheric contribution to $OLR_c$ increases are smaller. This is because the temperature increases are largest in the lower troposphere; $OLR_c$ is more sensitive to increases in temperature and water vapour amount assuming constant $RH$ here than in the upper troposphere (Fig. 3.2). Thus increasing the temperature lapse rate and holding constant the $RH$ effectively increases the water vapour feedback of the Earth-atmosphere system but diminishes the direct water vapour feedback at the surface.

The contribution towards changes in $SDL_c$ and $OLR_c$ from the constant $RH$ and changing $RH$ components are finally discussed with reference to the framework described in Sec. 3.2. Table 3.2 shows the components of $SDL_c$ changes as described by Eq. 3.5. The sensitivity

Table 3.2: *Contribution to the change in clear-sky SDL from changes in temperature, changes in water vapour for constant RH and changes in relative humidity using experiments THERM, LAPSE (values shown in parenthesis) and RHI for the five standard atmospheres.*

| Profile | $\frac{\partial SDL}{\partial T_s}$ $(Wm^{-2}K^{-1})$ | $\frac{\partial SDL}{\partial u}\frac{du}{dT_s}$ $(Wm^{-2}K^{-1})$ | $\frac{\partial SDL}{\partial RH}$ $(Wm^{-2}$ per %) |
|---|---|---|---|
| TRP | 4.5 (4.4) | 4.6 (3.9) | 1.1 |
| MLS | 4.1 (3.9) | 4.0 (3.4) | 1.0 |
| SAS | 3.7 (3.5) | 3.2 (2.7) | 0.6 |
| MLW | 3.0 (2.8) | 1.7 (1.4) | 0.3 |
| SAW | 2.5 (2.3) | 1.3 (1.0) | 0.2 |

of $SDL_c$ to temperature and column moisture becomes greater from the cold, dry sub-arctic winter profile to the warm, moist tropical profile. This is due to the large increase in the $4\sigma T_s^3\overline{\epsilon_a}$ term in Eq. 3.5 with temperature. Also, the increase in $u$ with atmospheric temperature is larger for warmer profiles, thus causing $\frac{\partial SDL}{\partial u}\frac{du}{dT_s}$ to increase with surface

temperature. Because $du/dT_s$ in experiment LAPSE is smaller than experiment THERM, the water vapour contribution to changes in $SDL_c$ are less in experiment LAPSE (values shown in parentheses). Changes in $RH$ result in larger increases in total column moisture and hence larger increases in $SDL_c$ for the warmer profiles. A reduction in $RH$ of about 8% is required to counteract the increase in $SDL_c$ due to the temperature and moisture increases prescribed in experiment THERM. This rises to about 19% for the sub arctic winter case.

Table 3.3 shows the direct contribution of the surface emission to the change in $OLR_c$ to be comparable with the atmospheric contribution, as denoted by $\alpha$ in Eq. 3.8, for THERM. For LAPSE, $\alpha$ is smaller than the surface contribution because changes in atmospheric temperature are less than changes in $T_s$. The surface emission contribution to $OLR_c$ increases are lowest for the tropical profile, despite the largest increases in surface emission. This is due to the small transmission through the atmosphere ($\overline{Tr}$; see Table 3.1). $OLR_c$ is most

Table 3.3: *Contribution to the change in $OLR_c$ from changes in surface temperature ($4\sigma T_s^3\overline{Tr}$) and the amplification of this term by increases in atmospheric upwelling emission due to increases in temperature for constant relative humidity ($\alpha$) and for changes in relative humidity ($\frac{\partial OLR}{\partial RH}$) using experiments THERM, LAPSE (values shown in parenthesis) and RHI for the five standard atmospheres.*

| Profile | $4\sigma T_s^3\overline{Tr}$ ($Wm^{-2}K^{-1}$) | $\alpha$ ($Wm^{-2}K^{-1}$) | $\frac{\partial OLR}{\partial RH}$ ($Wm^{-2}$ per %) |
|---|---|---|---|
| TRP | 0.8 | 1.0 (0.6) | -0.6 |
| MLS | 1.0 | 1.0 (0.5) | -0.5 |
| SAS | 1.2 | 0.8 (0.4) | -0.3 |
| MLW | 1.4 | 0.8 (0.3) | -0.2 |
| SAW | 1.3 | 0.7 (0.3) | -0.1 |

sensitive to changes in $RH$ for the warmer profiles. This is because changes in water vapour amount are largest for a given change in $RH$ at higher temperature. Also, the upwelling clear-sky longwave irradiance throughout the atmosphere tends to be largest for the warmer profiles. However, for a given temperature profile, $OLR_c$ is most sensitive to changes in $RH$ when the relative humidity is low (e.g. Spencer and Braswell (1997)). This will be discussed further in Chapter 5.

### 3.4.3 Effect of Clouds on Clear-sky Irradiance Sensitivity

The computations thus far apply to clear-sky profiles and for longwave radiation only. In reality, the presence of cloud and the effect of shortwave radiation act to modify these clear-sky sensitivities even without changes in cloud amount or properties (e.g. Weare (1995)). Further calculations were performed to illustrate the height dependent nature of the cloud radiative effect and subsequently to assess the effect of cloud and the variability of cloud amount and properties on the idealised clear-sky computations described previously. These illustrative calculations are presented primarily to aid the interpretation of cloud radiative effects as discussed in later Chapters. They therefore do not constitute a thorough investigation; such studies are presented elsewhere (e.g. Stephens and Webster (1981), Slingo (1990) and Sinha and Shine (1995)).

#### (a) Height Dependent Effect of Cloud

It is well known that clouds near to the surface exert only a small effect on the OLR (e.g. Stephens and Webster (1981)). This is because low-level clouds emit longwave radiation at similar temperatures to the surface. Because clouds near to the surface effectively increase the albedo of the Earth-atmosphere system they exert a strong cooling effect. Slingo (1990) showed that changes in low-level cloud properties and spatial extent have the potential to significantly modify greenhouse gas induced warming. Clouds at high altitudes are known to exert a strong greenhouse effect because emission to space from the cold cloud top is small, compared to the surface emission. The effect of cloud altitude and liquid water path on the longwave and net cloud radiative forcing are considered briefly to illustrate some of the main points regarding the effect of clouds on surface and top of atmosphere irradiance.

The surface and top of atmosphere LWCF and NCF were calculated for height dependent introduction of a 50 $hPa$ cloud of liquid water paths of 0.057 $kgm^{-2}$, 0.025 $kgm^{-2}$ and 0.012 $kgm^{-2}$ (Fig. 3.5). A tropical profile was used with spatial cloud coverage of 20%. There are several assumptions made that over-simplify the problem. Firstly, clouds are specified to contain water only. Secondly a fixed 'effective' cloud-drop radius is assumed. In calculating the NCF, tropical insolation for January was prescribed. With regard to the radiation budget at the surface (Fig. 3.5(a)), clouds at lower altitudes and of larger liquid water path are more effective at increasing the $LWCF_s$. However, the dominance of the cloud 'shading' effect on the surface over the longwave heating is apparent, with a negative NCF calculated, most especially for high level cloud where the LWCF$s$ is small. Also, increases in liquid water path alter the $SWCF_s$ more than $LWCF_s$, resulting in a net cooling of the

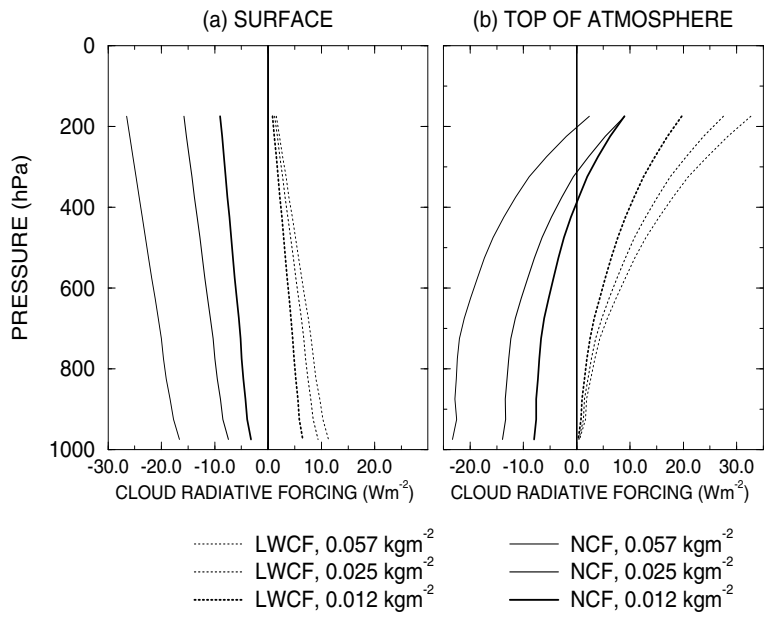


Figure 3.5: *Height dependence of longwave cloud radiative forcing, LWCF, and net cloud radiative forcing, NCF, on introducing 20% spatial coverage of a 50 hPa thick cloud of liquid water content 0.057, 0.025 or 0.012 $kgm^{-2}$ at (a) the surface and (b) the top of the atmosphere. A tropical profile with tropical January mean insolation and a surface albedo of 0.14 were prescribed.*

surface. This is well known and is explained by considering the relationship between cloud albedo and cloud emissivity with liquid water path (e.g. Stephens and Webster (1981)). Thus, to reiterate, clouds generally act to cool the surface, more especially clouds of high liquid water path and of high altitude.

As stated previously, the top of atmosphere LWCF is strongest for clouds of high altitude. This is apparent for the illustrative calculations presented in Fig. 3.5(b). At low levels, the cloud albedo effect strongly dominates over the small longwave cloud greenhouse effect, causing a cooling of the Earth-atmosphere system. At about 200 $hPa$, the cloud greenhouse effect is shown to dominate over the cloud albedo effect for the simple assumptions employed. This is especially true for the lowest value of liquid water path considered of 0.012 $kgm^{-2}$. The degree to which the shortwave and longwave radiative effects of high-level cloud compensate depend on the micro-physical composition of these clouds which, in reality, are composed of ice crystals (e.g. Sinha and Shine (1995)). However, these simple calculations highlight the strong compensation between SWCF and LWCF for high level clouds. The strong gradient of NCF with pressure in Fig. 3.5(b) for high level clouds highlights another well known property of high clouds: changes in their altitude constitutes a potentially significant feedback mechanism in the climate system. The dominance of negative SWCF over positive LWCF for low-level clouds illustrates the important cooling effect

Table 3.4: *Changes in net irradiance at the surface, $NET_s$ ($Wm^{-2}$), and at the top of the atmosphere, NET ($Wm^{-2}$), for experiments THERM, LAPSE and RHI applied to the global mean profile. Calculations are performed for clear-sky longwave only ($LW_c$), clear-sky longwave and shortwave ($LW_c$+$SW_c$) and with global mean cloud amount and properties for longwave and shortwave irradiance (ALL).*

| STUDY | $\Delta NET_s$ ($Wm^{-2}$) | | | $\Delta NET$ ($Wm^{-2}$) | | |
|---|---|---|---|---|---|---|
| | $LW_c$ | $LW_c$+$SW_c$ | ALL | $LW_c$ | $LW_c$+$SW_c$ | ALL |
| THERM | 2.0 | 1.2 | 0.8 | -2.0 | -1.8 | -1.8 |
| LAPSE | 1.3 | 0.7 | 0.2 | -1.6 | -1.5 | -1.0 |
| RHI | 0.65 | 0.49 | 0.30 | 0.32 | 0.29 | 0.22 |

of low clouds on the the top of atmosphere radiation budget. Thus changes in low-level cloud amount and properties may also exert sizeable feedbacks on the climate system.

### (b) The Effect of Cloud on Clear-sky Sensitivities

The effect of clouds on the calculated sensitivities in Sec. 3.4.2 are now considered. Illustrative calculations were performed to estimate the effect of shortwave irradiance (using global mean insolation and surface albedo) and of global mean cloud amount and properties (prescribed by Table 2.1) on the clear-sky net downward irradiance at the surface ($NET_s$) and at the top of the atmosphere (NET). Calculations were performed considering only the clear-sky longwave component ($LW_c$), the clear-sky longwave and shortwave components ($LW_c$+$SW_c$) and considering the all-sky longwave and shortwave components (ALL) for the 3 experiments, THERM, LAPSE and RHI (Table 3.4). For the global mean profile and insolation, the clear-sky shortwave radiative response to the column moisture increases results in the increase in clear-sky longwave heating of the surface being offset by between 30 and 50% for all experiments. The presence of cloud reduces the $NET_s$ increases further, most especially for experiment LAPSE. Including the shortwave and cloud radiative effects the sensitivity of $NET_s$ to the 1 $K$ increase in $T_s$ in THERM results in an increase of 0.8 $Wm^{-2}$. This still constitutes a surface SGE. At the top of the atmosphere the inclusion of shortwave radiative effects acts to decrease the clear-sky longwave NET sensitivity magnitude to the change in $T_s$ for THERM from -2.0 to -1.8 $Wm^{-2}$. The presence of cloud does not alter this sensitivity significantly. The presence of cloud, considering experiment LAPSE, conspires to reduce the clear-sky NET sensitivity magnitude from -1.5 to -1.0 $Wm^{-2}$. This is because the increased emission from the surface and lower troposphere is mostly absorbed by cloud decks, while the prescribed increases in temperature at the cloud tops is small in experiment LAPSE, resulting in only small increases in OLR. The

presence of cloud reduces the change in NET for experiment RHI by about 15%.

In conclusion, the surface net clear-sky longwave irradiance sensitivity to the idealised changes in temperature and water vapour amount is reduced when including both the shortwave and the cloud radiative effects. At the top of the atmosphere, the clear-sky net longwave irradiance sensitivity to changes in $RH$ are reduced when including the shortwave and cloud radiative effects. For uniform warming and water vapour amount increases for constant $RH$, the clear-sky longwave irradiance sensitivity is not altered significantly by the shortwave and cloud radiative effects. However, when the lapse rate is also increased, the presence of clouds act to significantly decrease the clear-sky longwave irradiance sensitivity because changes in cloud top temperature, and therefore emission, are small compared to the changes in surface emission.

**(c) Changes in Cloud Amount and Properties**

Further changes in cloud radiative forcing result from changes in cloud amount and properties. Comprehensive sensitivity experiments have been performed previously, for example by Sinha and Shine (1995). Simple calculations are now presented that serve to illustrate the effects of changes in cloud amount and liquid water path on the Earth's radiation budget. Changes in irradiance were calculated for (a) a 0.1 increase in cloud fraction and (b) a 10% increase in cloud liquid water path for high, medium and low-level clouds for the global mean profile and cloud amount (Table 3.5) and assuming global mean insolation and surface albedo. Increases in cloud amount and liquid water path cause a decrease in ASR and the longwave net upwelling irradiance at the surface and at the top of the atmosphere. As is well known, the shortwave effects of clouds tend to dominate over the longwave effects when cloud amount and LWP are increased. Thus a decrease in net absorbed irradiance at the surface or at the top of the atmosphere results, inferring that clouds generally act to cool the Earth-atmosphere system. This is consistent with satellite observations of the Earth's radiation budget (e.g. Harrison *et al.* (1990)). However, the longwave cloud-emissivity effect of high cloud dominates over the cloud-albedo effect implying that spatial increases in high cloud amount causes a heating of the Earth-atmosphere system. The uncertainty in cirrus cloud properties and the simple parameterization used in the narrow-band model and the simple assumptions used render this argument over-simplistic (e.g. Sinha and Shine (1995)). Absorbed shortwave irradiance is sensitive to changes in cloud amount and properties throughout the atmosphere. However, as stated previously, LWCF at the top of the atmosphere is relatively insensitive to changes in low cloud amount and properties due to the cloud top temperatures being similar to surface temperatures. Therefore the *net* radiation of the earth-atmosphere system is most sensitive to changes in cloud amount

Table 3.5: *Changes in cloud radiative forcing components at the surface and top of the atmosphere for increases in cloud fraction ($A_c$) by 0.1 and for 10% increases in liquid water path (LWP) for the global mean profile.*

| Cloud Level | $\Delta LWCF_s$ ($Wm^{-2}$) | $\Delta SWCF_s$ ($Wm^{-2}$) | $\Delta NCF_s$ ($Wm^{-2}$) | $\Delta LWCF$ ($Wm^{-2}$) | $\Delta SWCF$ ($Wm^{-2}$) | $\Delta NCF$ ($Wm^{-2}$) |
|---|---|---|---|---|---|---|
| $A_c$+0.1 | | | | | | |
| High | 0.10 | -0.94 | -0.84 | 1.19 | -1.03 | 0.16 |
| Medium | 0.12 | -1.25 | -1.13 | 0.50 | -1.27 | -0.77 |
| Low | 0.64 | -1.09 | -0.45 | 0.07 | -0.97 | -0.90 |
| $1.1 \times LWP$ | | | | | | |
| High | 0.04 | -0.60 | -0.56 | 0.43 | -0.65 | -0.22 |
| Medium | 0.01 | -0.91 | -0.90 | 0.15 | -0.90 | -0.75 |
| Low | 0.34 | -1.20 | -0.86 | 0.08 | -1.07 | -0.99 |

and properties if the cloud-altitude is low. Many previous studies, such as Slingo (1990) and Sinha and Shine (1995), have concluded that modest changes in low-cloud amount and properties may influence climate feedbacks significantly.

### 3.4.4 Summary

Considering Table 3.4 and 3.5 and the framework in section Sec. 3.2, a change in all-sky surface net irradiance may be described for the global mean profile with specified cloud amount and liquid water path:

$$\Delta NET_s = 0.8\Delta T_s(\overline{RH}) + 0.30\Delta RH - 25\Delta A_c - 0.23\Delta LWP. \tag{3.11}$$

The first right hand term denotes the sensitivity of $\mathrm{NET}_s$ to changes in temperature and water vapour amount prescribed by experiment THERM, while the second right term uses results from RHI. The third right term is calculated as the sum of changes in $\mathrm{NET}_s$ in Table 3.5 for fractional changes in cloud amount at each cloud level $((0.84 + 1.13 + 0.45)\Delta A_c/0.1)$ while $((0.56 + 0.90 + 0.86)\Delta LWP/10)$, the last term, is the sum of changes in $\mathrm{NET}_s$ for changes in cloud liquid water path at each cloud level from Table 3.5. $\Delta RH$ is the change in relative humidity (%), $\Delta A_c$ is the change in cloud fraction and $\Delta LWP$ is the percentage change in liquid water path. Therefore, to counteract the increase in $\mathrm{NET}_s$ due to a 1 $K$ increase in $T_s$ for experiment THERM ($\Delta NET_s = 0.8\ Wm^{-2}$), a 3% decrease in $RH$ or a 0.04 increase in cloud fraction for all cloud levels or a 4 % increase in cloud liquid water path for all cloud layers is required.

The change in net downwelling irradiance at the top of the atmosphere may be calculated as a function of changes in $T_s$, for the thermodynamic atmospheric water vapour and temperature increases in THERM, and for changes in $RH$ prescribed by RHI using Table 3.4. The irradiance response to changes in cloud fraction and percentage changes in $LWP$ using Table 3.5 completes Eq. 3.12 which is relevant for the global mean profile and cloud amount:

$$\Delta NET = -1.8\Delta T_s(\overline{RH}) + 0.25\Delta RH - 15\Delta A_c - 0.20\Delta LWP. \quad (3.12)$$

Thus an increase in $RH$ of 8% is required to produce a SGE (defined here as positive $dNET/dT_s$) for the changes in temperature and water vapour amount prescribed by experiment THERM and using the global mean profile and prescribed cloud amount and liquid water path. Decreases of 0.12 in cloud fraction at all cloud levels or a 9% reduction in $LWP$ at all cloud levels is required to offset the decreases in all-sky NET produced by experiment THERM.

To quantify more fully the water vapour feedback, the OLR changes for experiment THERM using global mean cloud amount and properties are calculated when specific humidity is held constant. The resulting value of $dNET/dT_s$ of -3.2 $Wm^{-2}K^{-1}$ is similar to the black body response of -3.3 $Wm^{-2}K^{-1}$ for the global mean surface temperature as described in Chapter 1 and about 1.4 $Wm^{-2}K^{-1}$ less than when water vapour amounts are increased with temperature to hold $RH$ constant. This corresponds to an amplification of the feedback parameter, $\lambda$, of about 1.7. To offset this positive thermodynamic water vapour feedback, a decrease in $RH$ of 6% per $K$ or an increase in cloud fraction at all cloud levels of 0.1 or an increase in $LWP$ at all cloud levels of 7% is required. For experiment LAPSE, the water vapour feedback is weaker, amplifying the black body feedback by only 1.3. However, there is a strong lapse rate feedback and the presence of global mean cloud amount also acts to increase the clear-sky black-body feedback, with the resulting amplification being a factor of about 3.

## 3.5 Potential Sources of Error

Uncertainties related to spectroscopy, the black-body surface emission assumption and the parameterization of water vapour continuum are inherent in the narrow-band model. These were discussed in Chapter 1. Further sources of error are now discussed which relate to the input profiles used by the radiation schemes such as the calculation of water vapour mass mixing ratio from $RH$, the vertical resolution employed, the inclusion of minor trace gases and errors in temperature and moisture profiles.

### 3.5.1 Calculation of Relative Humidity

The measurement of atmospheric humidity constitutes a potential error in the calculation of irradiance and atmospheric cooling rates (e.g. Spencer and Braswell (1997)). To estimate the magnitude of this error on the clear-sky irradiance a radiosonde profile from Barrow, Alaska (30 June 1992, 00z; see Fig. 4.15 and 4.16 (d) in Chapter 4) was used to construct a model atmosphere containing temperature and water vapour mass mixing ratio. The profile was chosen for its high vertical resolution and because it contains temperatures above and below the freezing point of water. The radiosonde retrieval provided 47 levels between the surface and 311 $hPa$. A sub-arctic standard atmosphere was used to provide temperature and water vapour mass mixing ratio for 6 levels above the top radiosonde level and ozone profiles were interpolated from the standard atmosphere onto the radiosonde vertical grid. Observations of temperature and dew point depression temperature, $T_d$, were provided by the radiosonde retrieval from which vapour pressure, $e$, was calculated as $e = e_s(T_d)$. The saturated vapour pressure ($e_s$) was calculated using Liou (1980). To assess the potential error associated with the computation of specific humidity using these empirical fits, the following calculations were performed:

W: $e_s$ was calculated with respect to water only,

WI: $e_s$ was calculated with respect to water at temperatures greater or equal to 273 $K$ and with respect to ice at temperatures less than 273 $K$,

WIT: $e_s$ was calculated with respect to water at temperatures greater or equal to 270 $K$ and with respect to ice at temperatures less than 250 $K$. Between 250 and 270 $K$ a linear interpolation between the $e_s$ calculation for water and for ice was assumed.

WIT was performed to be more consistent with observations of the water/ice transition at temperatures much less than 273 $K$ (e.g. Heymsfield and Miloshevich (1995)). Using the narrow band scheme, the column moisture, $RH$ (calculated using the WIT method), $\mathrm{SDL}_c$ and $\mathrm{OLR}_c$ were calculated (see Table 3.6). Using the 3 methods of calculating $e_s$

Table 3.6: *Calculated total column moisture, u ($kgm^{-2}$), relative humidity, RH (%), clear-sky SDL ($Wm^{-2}$) and clear-sky OLR ($Wm^{-2}$) for a sub-arctic radiosonde profile using 3 methods of calculating specific humidity.*

| Experiment | $u$ ($kgm^{-2}$) | $RH_{WIT}$ (%) | SDL ($Wm^{-2}$) | OLR ($Wm^{-2}$) |
|---|---|---|---|---|
| W | 19.0 | 68.9 | 277.1 | 249.5 |
| WI | 18.2 | 62.8 | 276.6 | 251.9 |
| WIT | 18.4 | 63.4 | 276.8 | 251.6 |

results in differences in $u$ of less than 5%. Column mean $RH$, using the WIT method to calculate $RH$ from specific humidity, is about 9% lower when calculating $e_s$ with respect to water and ice (WI) compared to calculating over water only (W). $SDL_c$ is relatively insensitive to the calculation of $e_s$, because the near-surface layers important in determining the surface irradiance tend to have temperatures greater than the freezing point of water. Thus all three methods of calculating $e_s$ are identical at these levels. However, significant errors may arise for mid-latitude/arctic winter profiles where surface temperature is close to the transition temperature. The range of $OLR_c$ using the three methods is of order 2.5 $Wm^{-2}$ (or 1%). Using a water-ice transition as in WIT gives rise to similar results to a specific transition temperature (WI) in the calculation of $e_s$ over water or ice.

### 3.5.2 Vertical Resolution

Using the 30 June sub-arctic profile, calculations were performed to assess the effect of vertical model resolution on calculated irradiance. A sub-arctic profile was used because temperature and moisture inversions near to the surface constitute a good test for model vertical resolution. Radiosonde observations of temperature and water vapour mass mixing ratio were interpolated onto grids of varying resolution. This was computed using two methods. Firstly equally spaced pressure levels were used. The second method assumed a logarithmic dependence of pressure level with pressure, with a greater number of levels near to the surface than method 1. The pressure level, $p$ was calculated as,

$$p = p_s - \frac{1 - (ln(N - n + 1))}{ln(N)} \Delta p, \tag{3.13}$$

where $p_s$ is the surface pressure, N is the number of levels between the top and bottom radiosonde pressure level, n is the model level number (with 1 being the surface) and $\Delta p$ is the pressure difference between the top and bottom radiosonde pressure levels. Above the highest altitude radiosonde level, the sub-arctic summer atmospheric profile was used (6 additional levels). Ozone and greenhouse gas concentrations were prescribed as in Sec. 3.5.1 and Chapter 2. Method WIT was used to calculate water vapour amount from dew point depression temperature. The calculated total column moisture, $SDL_c$ and $OLR_c$ are plotted with number of levels (including the sub-arctic summer profile levels) in Fig. 3.6.

For greater than 30 levels, using evenly spaced pressure slabs results in $OLR_c$ to within 0.5 $Wm^{-2}$ of the radiosonde calculation. However, $SDL_c$ is overestimated by up to 3 $Wm^{-2}$ compared to the radiosonde profile. This is because there are a greater number of levels in the radiosonde profile for a given pressure interval near to the surface than at higher altitudes. Therefore, using evenly spaced pressure levels essentially decreases the model resolution near to the surface. The $SDL_c$ overestimate is due to a thin, cold 20 $hPa$ layer

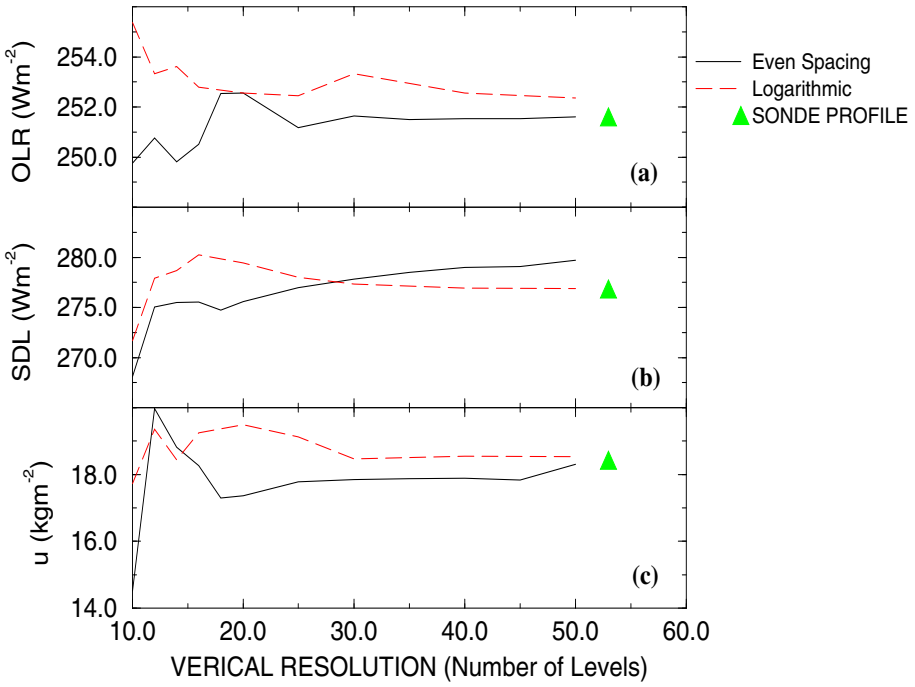


Figure 3.6: *(a) Clear-sky OLR ($Wm^{-2}$), (b) clear-sky SDL ($Wm^{-2}$) and (c) total column moisture, $u$ ($kgm^{-2}$) with vertical resolution (including 6 levels supplied by a sub-arctic standard atmosphere), using evenly spaced or logarithmically spaced pressure levels interpolated from the sub-arctic 30 June radiosonde profile pressure levels. Triangles show values calculated using the 47-level radiosonde profile above which 6 additional levels are provided by the sub-arctic standard atmosphere.*

near to the surface. This is not resolved using the coarser grid. Applying the logarithmic spacing, this near-surface layer is well represented with calculated $\mathrm{SDL}_c$ being within about 1 $Wm^{-2}$ of the radiosonde profile for 30 or more model levels. This $\mathrm{SDL}_c$ overestimate due to the inadequate representation of the lowest 20 $hPa$ layer is encountered for the logarithmic pressure level spacing when the number of model levels drops to about 20.

Using 10 model levels, both methods result in underestimates of $\mathrm{SDL}_c$ and $u$ because the high temperature and moisture above the surface layer inversion are essentially lost in this coarse resolution. This effect was also noted by Räisänen (1996). $\mathrm{OLR}_c$ is overestimated for 10 model levels and logarithmic spacing because the region of high specific humidity at about 800 $hPa$ (see Fig. 4.16(d)) is underestimated using this grid. Using an evenly spaced grid, $\mathrm{OLR}_c$ is underestimated for 10 levels because the warm layer above the cold surface layer is not well represented. A similar conclusion is drawn using alternative sub-arctic and tropical radiosonde profiles (not shown); the present example was chosen as an extreme case with generally the largest irradiance error of all the profiles considered. In summary, using 30 or more model levels results in reasonable irradiance and column moisture estimates

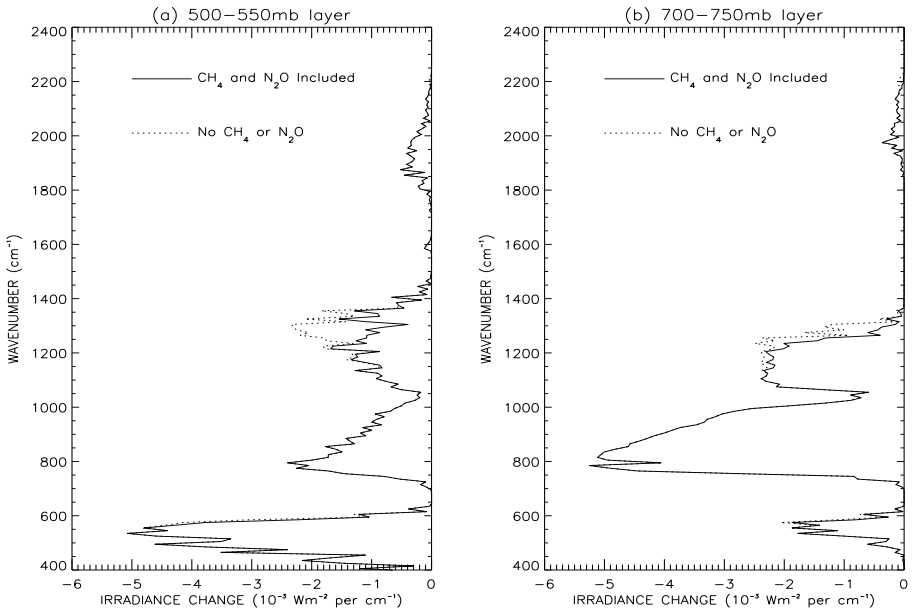


Figure 3.7: *Changes in $OLR_c$ as a function of wavenumber for 10% increases in (a) 500 to 550 hPa and (b) 700 to 750 hPa layer water vapour mass mixing ratio when $CH_4$ and $N_2O$ are included (solid line) and not included (dotted line) in the calculations.*

compared to the high resolution instantaneous radiosonde profile (within 3%). However, while the $SDL_c$ depends on the resolution near to the surface, the $OLR_c$ is more accurately estimated for even spacing of pressure levels throughout the atmosphere.

### 3.5.3 The Effect of Trace Gases on Irradiance Variability

An uncertainty in calculating irradiance variability arises if radiatively important minor trace gases are not accounted for in the radiative computations. When $CH_4$ and $N_2O$ concentrations were set to zero, the $OLR_c$ response to 10% profile increases in water vapour mass mixing ratio was increased by about 5% for the tropical and mid-latitude summer profiles compared to when present day concentrations of $CH_4$ and $N_2O$ are prescribed. The effect is most prominent in the mid-troposphere at about 500 $hPa$. The effects were less discernible for the sub-arctic winter case. Thus the inclusion of these trace gases acts to significantly diminish the radiative effect of water vapour variability.

The changes in $OLR_c$ in response to 10% increases in water vapour mass mixing ratio in the 500 to 550 $hPa$ and the 700 to 750 $hPa$ slabs are plotted as a function of wavenumber in Fig. 3.7 with and without the radiative effects of $CH_4$ and $N_2O$. The main spectral region of interaction between water vapour and the two trace gases is between 1200 and 1300 $cm^{-1}$ which is on the edge of the vibration-rotation water vapour bands and the

window region of the spectrum. The degree to which $CH_4$ and $N_2O$ alters the radiative effects of water vapour, and therefore influences the water vapour feedback, depends mainly on how important water vapour perturbations are in determining the $OLR_c$ primarily over the 1200 to 1300 $cm^{-1}$ spectral region. This region is relatively unimportant for the sub-arctic winter profile. Thus the effect of $CH_4$ and $N_2O$ on the radiative effects of water vapour is negligible for the sub-arctic case. The influence of these two trace gases on the surface irradiance is small because much of the $SDL_c$ is determined by a thin layer near to the surface. Therefore just a small fraction of the total column of $CH_4$ and $N_2O$ will affect the radiative impact of water vapour changes to the surface irradiance. The effect of including present day concentrations of chlorofluorocarbons CFC-11 and CFC-12 on the sensitivity of the clear-sky radiation budget to changes in water vapour amount is negligible. Changes in $OLR_c$ due to profile 10% increases in water vapour mass mixing ratio, when the CFCs are included, are within 0.1% of the corresponding value when they are not included.

### 3.5.4 Atmospheric Profiles and Surface Properties

Considering the results of Sections 3.3 and 3.4, it is apparent that errors in atmospheric profiles of temperature and water vapour and surface temperature are likely to incur significant errors in the calculated irradiance and its variability. To assess the relative importance of profile errors in determining the accuracy of clear-sky irradiance, the change in a parameter required to produce a 3 $Wm^{-2}$ change in irradiance (equivalent to a 0.5 to 1.5% change in $E$ for the standard atmospheres considered) was computed. Table 3.7 shows the error in surface emissivity ($\delta\epsilon_s$) surface temperature ($\delta T_s$) atmospheric temperature between the surface and 100 $hPa$ ($\delta T_a$) and the column $RH$ between the surface and 100 $hPa$ ($\delta RH$) required to produce an error in $OLR_c$ or clear-sky $F_{net}$ (=$SDL_c$-E) of 3 $Wm^{-2}$. The surface emissivity error is calculated using Eq. 2.5 and 2.6 in Chapter 2 and allows for the reflected component of SDL. To incur $OLR_c$ errors of 3 $Wm^{-2}$, relatively large errors in $T_s$ but more modest errors for profile temperature, $RH$ and $u$ errors are required for the tropical profile. The sub-arctic profile surface and profile temperature error is of similar magnitude because of the lower absorption of upwelling longwave radiation by the atmosphere. However, it must be noted that errors in surface temperature can be large, especially over land regions (e.g. Slingo *et al.* (1998)). Changes in $RH$ and $u$ for the sub-arctic winter profile much larger than observed variability are required to produce a 3 $Wm^{-2}$ $OLR_c$ response. Relatively large changes in $\epsilon_s$, compared to observed fluctuations (e.g. Sutherland (1986)) are required to produce a change in $OLR_c$ of 3 $Wm^{-2}$ for the two profiles. However, as noted in Chapter 2, this is not the case for some desert regions. Using Eq. 2.5 in Chapter 2 along with estimates of surface longwave cooling and atmospheric transmission typical of desert

Table 3.7: *Errors in surface emissivity, $\delta\epsilon_s$, surface temperature, $\delta T_s$ (K), atmospheric temperature between the surface and 100 hPa, $\delta T_a$ (K) and column mean RH between the surface and 100 hPa (%) required to produce an $OLR_c$ or $F_{net}$ error of 3 $Wm^{-2}$.*

| Profile: | Tropical | | Sub arctic winter | |
|---|---|---|---|---|
| Parameter | $OLR_c$ | $F_{net}$ | $OLR_c$ | $F_{net}$ |
| $\delta\epsilon_s$ | 0.4 | 0.05 | 0.2 | 0.04 |
| $\delta T_s$ $(K)$ | 3.8 | 0.5 | 2.4 | 0.8 |
| $\delta T_a$ $(K)$ | 1.0 | 0.7 | 2.0 | 1.2 |
| $\delta RH$ (%) | 5.0 | 2.8 | 27.0 | 17.8 |
| $\delta u$ $(kgm^{-2})$ | 4.0 | 1.8 | 1.9 | 1.0 |

regions used in Sec. 2.2.2(c), only a small error in $\epsilon_s$ of less than 0.1 is required to produce a change in $OLR_c$ of 3 $Wm^{-2}$. This error is less than the observed divergence of $\epsilon_s$ from unity over desert regions (Sutherland (1986)). The surface emissivity is found to be important in determining $F_{net}$ as is surface and near-surface temperature. Small relative changes in tropical $RH$ and $u$ are required to induce a 3 $Wm^{-2}$ change in $F_{net}$; this is again not the case for the sub-arctic winter profile. In conclusion, accurate calculation of surface clear-sky irradiance requires good representation of surface and near-surface temperature and surface emissivity with column moisture also becoming important for warmer moister profiles. With regard to $OLR_c$, atmospheric temperature and moisture is of greater importance than surface parameters for the moist profiles, while surface and atmospheric temperature are most important for the drier profiles.

## 3.6 Summary and Discussion

The sensitivity of the Earth's radiation budget to changes in water vapour mass mixing ratio and temperature was assessed using a narrow-band radiative transfer scheme and a variety of atmospheric profiles. The purpose of the investigation was to provide a framework from which the remainder of this thesis may be interpreted. $OLR_c$ is found to be highly sensitive to absolute changes in water vapour mass mixing ratio in the upper troposphere. However, relative changes in water vapour mass mixing ratio throughout the troposphere are important with regard to $OLR_c$ variability. Increases in column $RH$ and increases in water vapour amount with temperature for constant $RH$ also give rise to this result. Shine and Sinha (1991) argued that percentage changes in water vapour amount are physically meaningful because satellite and radiosonde observed variations over the seasonal cycle and

climate models forced by increases in carbon dioxide show water vapour changes which are closer to a relative rather than an absolute variation. However, Spencer and Braswell (1997) state that in dry descending regions of the Hadley circulation, where $RH$ is very low, relative changes in water vapour amount will also be very small. They further argue that the results of Shine and Sinha may therefore be misleading, albeit only for the driest regions. This argument can be answered simply by realising that absolute *decreases* in relative humidity in very dry regions must be necessarily small or a negative water vapour amount will be calculated, which is physically meaningless. Nevertheless, humidity variation in these dry descending regions remain an important potential perturbation to the Earth's radiation budget.

The $\mathrm{SDL}_c$ is sensitive to changes in column moisture, mainly due to the continuum emission in the window region of the spectrum, and to changes in near-surface temperature for the strongly absorbing regions of the spectrum. The strong dependence of clear-sky and all-sky SDL on near-surface temperature requires a realistic representation of temperature between the lowest model level and the surface for an accurate estimate of the irradiance. This is an important consideration when comparing model calculated SDL with radiometric observations. Column moisture is also an important parameter in determining the $\mathrm{SDL}_c$ for the warmer, moister profiles. The $\mathrm{SDL}_c$ is an important component of the water vapour feedback known to operate in the climate system (e.g. Ramanathan (1981)) and therefore further studies are required to assess the performance of climate models in simulating this flux; this subject will be dealt with in Chapter 4.

By performing idealised experiments in which water vapour was increased with increasing temperature to conserve the initial profile of $RH$, a super-greenhouse effect (SGE) was found to operate at the surface but not at the top of the atmosphere. This is in agreement with Inamdar and Ramanathan (1994). The large increases in continuum emission in the window regions causes $\mathrm{SDL}_c$ to increase at a greater rate than surface emission for all but the sub-arctic profile, thus constituting an unstable feedback to the surface warming. Considering a global mean profile, the presence of cloud and the shortwave radiative response to the warming scenario act to offset this clear-sky SGE, but do not remove the unstable radiative heating of the surface with increasing temperature of 0.8 $Wm^{-2}K^{-1}$. A decrease in $RH$ of 3% or an increase in cloud amount at all levels of 0.04 or an increase in cloud liquid water path of 4% at all levels is required to offset the unstable radiative heating of the surface for each $K$ of surface warming assuming constant $RH$. Warming with constant $RH$ is unable to produce a super-greenhouse effect at the top of the atmosphere, in agreement with Hallberg and Inamdar (1993). However, small regions of the tropical upper-troposphere may behave

contrary to this result with a SGE arising for the tropical profile at about 175 $hPa$ (Fig. 3.2) when temperatures increase with constant $RH$. For the tropical clear-sky profile, increases in column mean $RH$ of 3% are required to produce a SGE for a uniform atmospheric temperature increase of 1 $K$. When the temperature lapse rate is increased, a smaller $RH$ increase is required. To counteract the idealised constant $RH$ water vapour feedback for the global mean profile and cloud parameters, a decrease in $RH$ of 6%, or an increase in cloud fraction of 0.1 at all levels or an increase in cloud liquid water of 7% at all levels is required per $K$ surface and atmospheric temperature increase for the constant $RH$ criteria.

The sensitivity studies performed indicate the initial response of the radiation budget to a change in surface or atmospheric parameters. Therefore the effect on the climate system cannot be realistically appraised. Climate model experiments are required for this purpose. The present study gives an idea of the relative importance of surface and atmospheric parameters required to accurately simulate the Earth's climate. Significant uncertainty is associated with the calculation of irradiance and its variability. This stems from the uncertainty in the radiation parameterizations (e.g. Stephens (1984)), the spectroscopic input data (e.g. Pinnock and Shine (1998)), the resolution and vertical interpolation methods (e.g. Räisänen (1996)) and also a significant uncertainty attached to the atmospheric profiles used.

The present study has shown that errors in near-surface temperature and column moisture are significant in determining $\mathrm{SDL}_c$ uncertainty, especially for warm, moist profiles. The degree to which the surface deviates from a black-body emitter ($\epsilon_s$ less than 1) is significant for the surface net longwave irradiance over land. It is only likely to be significant with regard to $\mathrm{OLR}_c$ over some desert regions. Surface and atmospheric temperature are important in determining $\mathrm{OLR}_c$ for cold, dry profiles. The surface temperature error is less important for warm, moist profiles with column moisture and $RH$ becoming increasingly important in determining the irradiance error at the surface and at the top of the atmosphere in tropical regions. A clear-sky irradiance uncertainty of order $\pm 5\ Wm^{-2}$ is estimated for monthly mean, climatological mean profiles. In considering instantaneous profiles taken locally, the uncertainty is likely to be approximately $\pm 10\ Wm^{-2}$ which is similar to that obtainable by surface observations (e.g. Weller and Anderson (1996)). With regard to irradiance variability, an uncertainty of order 10% is estimated for the standard profiles. The uncertainty is gauged by considering the effect of trace gases and the effect of recent changes in the water vapour continuum parameterization (see Chapter 2) on the irradiance sensitivity to changes in water vapour amount. This compares with Pinnock and Shine (1998) who estimated a 5% uncertainty in radiative forcing calculations based on the

recent updates in spectroscopic line parameters. Where a paucity of observations exist, for example in the upper troposphere over dry, subsiding, oceanic regions, the calculated irradiance variability is anticipated to cause an uncertainty greater than $\pm 10\%$. This will be discussed further in Chapter 5. The results of this Chapter will be used as a reference point for the remainder of this thesis.

# Chapter 4

# EVALUATION OF SIMULATED IRRADIANCE AT THE SURFACE

## 4.1 Introduction

The atmospheric emission of longwave radiation to the surface constitutes a significant component of the surface energy balance. It is also an important parameter with regard to the water vapour feedback to changing surface temperature: increases in water vapour amount in the lower troposphere, a likely consequence of increased evaporation in response to surface warming (IPCC (1996)), will lead to increased back emission of longwave irradiance from the atmosphere to the surface. Modelling studies indeed show the clear-sky surface downwelling longwave irradiance ($SDL_c$) to be an important amplifier of greenhouse gas forced surface warming by way of a strong water vapour feedback (e.g. Ramanathan (1981)). Climate model predictions of future climate change may only carry weight if the feedbacks operating are simulated correctly. It is therefore important that climate models correctly simulate the $SDL_c$ and consequently the water vapour feedback. This is particularly relevant when considering the more physically based climate models which include surface irradiance as part of a flux into fully dynamic oceans (e.g. Johns *et al.* (1997)).

In validating simulated surface irradiance, it is first necessary to highlight uncertainties within the radiation scheme used in the model, the input data to the radiation scheme and the observations with which model comparison may be undertaken. In this vein, Dutton (1993) compared observed SDL, which were filtered to remove cloudy observations, to values calculated by applying a radiative transfer scheme to radiosonde profiles. The

model-observation difference was found to fall within experimental error. This uncertainty was large ($\pm$ 10 $Wm^{-2}$), thus precluding the validation of either model or observed irradiance. Wild *et al.* (1995) compared surface irradiance simulated by a climate model with both surface observations and also radiative transfer calculations using radiosonde profiles as input data. For clear-sky conditions the model SDL tended to be underestimated compared to radiative transfer scheme calculations. The model underestimate, when compared to surface irradiance observations, was even larger. A similar result was found by Garratt and Prata (1996), who compared SDL simulated by four climate models with observations over continental surfaces. They argued that the model underestimate in SDL was caused by underestimates in near surface temperature.

Validation of model simulated surface irradiance is limited by the observational network. Firstly, the accuracy of ground-based radiometers are poor ($\pm$ 10 $Wm^{-2}$) (e.g. Dutton (1993), Weller and Anderson (1996), Grant and Hignett (1998)). Also, the surface network of radiometers is spatially limited and confined almost exclusively to land-based regions (e.g. Garratt and Prata (1996)). The derivation of clear-sky observations, in order to compare with model clear-sky irradiance, reduces the spatial and temporal coverage still further. One possible solution to this problem is to infer radiative fluxes at the surface by using satellite radiances at the top of the atmosphere (e.g. Gupta (1989) ). Using this method, Rossow and Zhang (1995) found model-observation all-sky SDL differences to be large; this is unsurprising as SDL is dependent mainly on near-surface conditions, which are the most difficult variables to derive remotely from satellite. Indeed, temperature and humidity fields near to the surface are highly important in determining clear-sky SDL (e.g. Gupta (1989), Zhao *et al.* (1994)); differences in these fields from five separate assimilation agencies were found by Wu and Chang (1991) to cause disparities in $SDL_c$ much larger than 10 $Wm^{-2}$.

An alternative method of estimating the $SDL_c$ is presented in this study. A simulation of the Earth's clear-sky longwave radiation budget is employed. The simulation (described in Chapter 2) exploits a comprehensive analysis of atmospheric parameters in conjunction with a flexible new radiation scheme. Advantages of the simulation include the high spatial and temporal resolution and coverage. Also, observed atmospheric parameters are utilised in deriving atmospheric profiles using a consistent assimilation system. The simulation provides a new method of assessing the ability of climate models to represent the clear-sky longwave radiation budget (Slingo (1997)). However, limitations inherent in the simulation itself necessitate the validation of its irradiance products before employing it for this purpose. Slingo *et al.* (1998) evaluated the simulated clear-sky outgoing longwave radiation at the top of atmosphere by comparing with Earth Radiation Budget Experiment (ERBE)

satellite data. The purpose of this study is to evaluate the simulated $SDL_c$ by comparing with observations.

Initially, $SDL_c$ was compared globally with values calculated using a simple formula developed by Prata (1996) (Sec. 4.3). While semi-empirical climatologies of surface fluxes have significant uncertainties (e.g. Budyko (1974)), the use of the Prata formula provides a good test for the simulation because its form is derived from radiative transfer theory and uses observations to empirically determine the internal parameters. Comparisons with simulated irradiance were undertaken globally which is not possible with the limited surface-based observational network. However, observed surface irradiance provides the most rigorous test for the simulation of longwave irradiance at the surface. Therefore a comprehensive comparison of simulated clear-sky longwave irradiance at the surface with observations in the tropical central Pacific (Sec. 4.4) and also from a land based sub-arctic site in Alaska (Sec. 4.5) were undertaken. These sites were chosen for their high temporal resolution and good quality radiation datasets which are complemented by an abundance of meteorological observations. The surface radiation budget in the tropics is thought to be important in determining the character of the global circulation (e.g. Schneider *et al.* (1997a)). Therefore observations from the tropical warm pool are particularly important in this respect. The sub-arctic site provides an entire annual cycle and is a good further test for the simulation of $SDL_c$ due to its vastly different climatic regime compared to the tropical warm pool. The disparity between observed and simulated clear-sky irradiance is assessed, and the effects of clouds on the surface radiation budget are discussed.

## 4.2 Models and Observations

### 4.2.1 CLERA simulation

The simulation of the Earth's clear-sky longwave radiation budget is described in Chapter 2 and by Slingo *et al.* (1998). The present study uses both monthly mean and 6-hourly simulated $SDL_c$ together with the ERA data. As stated in Chapter 2, errors in ERA column moisture and near surface temperatures are likely to incur the largest errors in the $SDL_c$ calculated by CLERA. Further errors due to incorrect specification of surface emissivity in CLERA are avoided by considering the SDL which depends upon atmospheric parameters only.

### 4.2.2 Semi Empirical Formula

There have been many past attempts at representing the surface irradiance by means of simple empirical formulae. A recent attempt, by Prata (1996), assumes $SDL_c$ to be a function of screen-level temperature, $T_0$, and total column moisture, $u$,

$$SDL_{prata} = \sigma T_0^4[1 - \delta\epsilon - (1 + 0.1u)exp\{-(a + bu)^{\frac{1}{2}}\}], \tag{4.1}$$

where $\sigma$ is the Stefan-Boltzmann constant and $u$ is estimated by

$$u = C\frac{e_0}{T_0}, \tag{4.2}$$

where $e_0$ is the screen-level water vapour pressure. The formula thus represents a simple method for calculating $SDL_c$ from conventional measurements. Eq. 4.1 is based on radiative transfer theory and implicitly accounts for greenhouse gas and water vapour continuum emission. The term, $\delta\epsilon$, corrects for high altitude regions and is described by,

$$\delta\epsilon = 0.05\frac{p_0 - p_s}{p_0 - 710}, \tag{4.3}$$

where $p_0$ is 1013.25 $hPa$ and $p_s$ is the observed surface pressure in $hPa$. The correction is required because the Prata model is empirically derived from low-altitude observations, above which there is a greater depth of atmosphere compared to high-altitude regions. The internal constants, $a$=1.2 and $b$=0.3, were set by correlating with observations of surface clear-sky irradiance and column water vapour amount; the column water vapour is approximated by Eq. 4.2 in which $C$ was determined, by considering climatological water vapour and temperature scale heights, to be 4.65 $K(ms^{-2})^{-1}$. As such, the formula constitutes a quasi-observational measure of $SDL_c$ due to its physical basis in radiative transfer theory, and the use of irradiance observations to empirically set the model constants.

The use of observed surface irradiance to tune the Prata formula, while being an advantage over purely model based climatologies (e.g. Dilley and O'Brien (1998)), is limited by the uncertainties inherent in the observations, which measure at best to within about 10 $Wm^{-2}$. Also the contamination of clear-sky observations with cloud and the variable aerosol optical depth are likely to introduce further uncertainties.

### 4.2.3 Observations in the Tropical West Pacific

Irradiance and meteorological measurements from the Woods Hole Oceanographic Institute (WHOI) floating buoy were presented by Weller and Anderson (1996) and form part of the Tropical Ocean/Global Atmosphere Coupled Ocean Atmosphere Response Experiment (TOGA COARE) (Webster and Lukas (1992)). The mooring was positioned at

1.75° S, 156° E, situated in the tropical warm pool region. The SDL is influenced by the warm, moist atmospheric profiles as well as the effects of cumulus clouds which are frequently present. There exists no discernible seasonal cycle, although periods of active and suppressed convective phases of the Intra Seasonal Oscillation (ISO) (e.g. Gutzler *et al.* (1994)) and the occurrence of Westerly Wind Bursts (WWBs) (e.g. Meyers *et al.* (1986)) act to introduce irradiance variability on various time scales.

All-sky longwave irradiance was measured using a Precision Infrared Radiometer (PIR) which is sensitive to radiation mainly between 4 and 50 $\mu m$ (about 200 to 2500 $cm^{-1}$). The PIR was calibrated in a black body cavity [Anderson pers. comm. (1997)] which will ensure irradiance measurements are accurate providing the atmosphere remains close to a black-body emitter. Although the clear-sky tropical atmosphere is optically thick, the deviation from a black body emitter, especially in the window region (800 to 1200 $cm^{-1}$), will cause a slight underestimate in observed SDL. Performing calculations using the narrow-band radiation scheme applied to the tropical standard atmosphere the underestimate is found to be less than 1 $Wm^{-2}$. This is small compared to the overall instrumental error of about 10 $Wm^{-2}$ (Weller and Anderson (1996)). Solar heating errors, which can cause underestimates in SDL of order 40 $Wm^{-2}$ at local noon (e.g. Wild *et al.* (1995)) were removed by Weller and Anderson using the Alados-Arboledas *et al.* (1988) technique.

Hourly irradiance observations were utilised from 21 October 1992 to 4 March 1993. Comparison with 6-hourly $\mathrm{SDL}_{clera}$ from the nearest grid point (2.5° S, 155° E) is undertaken in Sec. 4.4. Radiosonde measurements of atmospheric temperature and moisture from the near by site of Kavieng (2.6° S, 150.8° E) were used in conjunction with ERA profiles for the nearest grid point (2.5° S, 150° E) to help evaluate simulation-observation disparity. The radiosonde profiles and additional radiative measurements were conducted as part of the Atmospheric Radiation Measurement (ARM) Pilot Radiation Observation Experiment (PROBE) and were described in detail by Long (1996). All radiation, meteorological and radiosonde data were acquired from the TOGA COARE data information system[1].

### 4.2.4 Sub Arctic Observations

Measurements of all-sky surface irradiance at Barrow, Alaska (71.3° N, 156.6° W) as part of the Solar and Thermal Atmospheric Radiation (STAR) project[2] were used to evaluate simulated $\mathrm{SDL}_c$. Radiosonde profiles from the Barrow site[3] were used in conjunction

[1]WWW address(1998): http://wwwarc.essc.psu.edu/data/togacoare/TOGACOAREdataindex.html
[2]WWW address(1998): http://www.cmdl.noaa.gov/star/
[3]FTP address(1998): ftp://ftp.cmdl.noaa.gov/met/raobs/brw/

with ERA atmospheric profiles to aid the evaluation. The sub-arctic site contrasts greatly with the warm, moist tropical warm pool, with cold, mainly overcast conditions prevailing (e.g. Stone (1997)). The presence of strong temperature and moisture inversions present a challenge to the modelling of surface irradiance (Räisänen (1996)). Unlike the tropical warm pool, there exists a strong seasonal cycle due to the large variability in incident solar radiation; continuous darkness is encountered for 2 months in the winter while continuous daylight occurs during the summer. An advantage over the tropical data is that an entire seasonal cycle is available.

Hourly observations from 3 January to 28 December 1992 were compared with the average of the 6 hourly $\mathrm{SDL}_{clera}$ from the four surrounding grid points bounded by 70 to 72.5° N and 155 to 157.5° W. The Eppley PIRs used measure radiation between about 3.5 and 50 $\mu m$ (about 200 to 2800 $cm^{-1}$). The black-body calibration observational error was found to be of order 1 $Wm^{-2}$ using the narrow band scheme with the sub-arctic summer and winter profiles, and so is not likely to hinder the comparison. Again solar heating errors had been removed from the data set.

## 4.3 Comparison of Surface Irradiance with a Simple Formula

### 4.3.1 Global Comparison

Using the lowest atmospheric model level in ERA to prescribe $T_0$ and $e_0$ in Equations 4.1 to 4.3, and setting $C$ to 4.65 $Km^{-1}s^2$, $\mathrm{SDL}_{prata}$ was calculated at the surface for each point on the ERA grid. Comparison was undertaken for January and July monthly means for 1985 but the results are applicable to the other years in the ERA period. The comparison with CLERA $\mathrm{SDL}_c$ ($\mathrm{SDL}_{clera}$) is presented in Table 4.1. $\mathrm{SDL}_{prata}$ is generally larger in the

Table 4.1: *Mean SDL calculated by CLERA and the Prata formula for July and January, 1985, for land only, ocean only and all grid points.*

| Month | CLERA | $\mathrm{SDL}_c$ | ($Wm^{-2}$) | PRATA | $\mathrm{SDL}_c$ | ($Wm^{-2}$) |
|---|---|---|---|---|---|---|
| (1985) | Global | Ocean | Land | Global | Ocean | Land |
| JAN | 301.6 | 330.1 | 248.0 | 306.5 | 337.7 | 247.1 |
| JUL | 318.4 | 330.8 | 303.1 | 324.4 | 338.0 | 306.1 |

mean compared with CLERA values for ocean points in July and January. The general pattern of $\mathrm{SDL}_{clera}$ is well represented, although there are notable differences. These are highlighted in Fig. 4.1. The general positive bias over ocean regions is apparent for both January and July, especially over the dry descending sub-tropical ocean regions. This bias

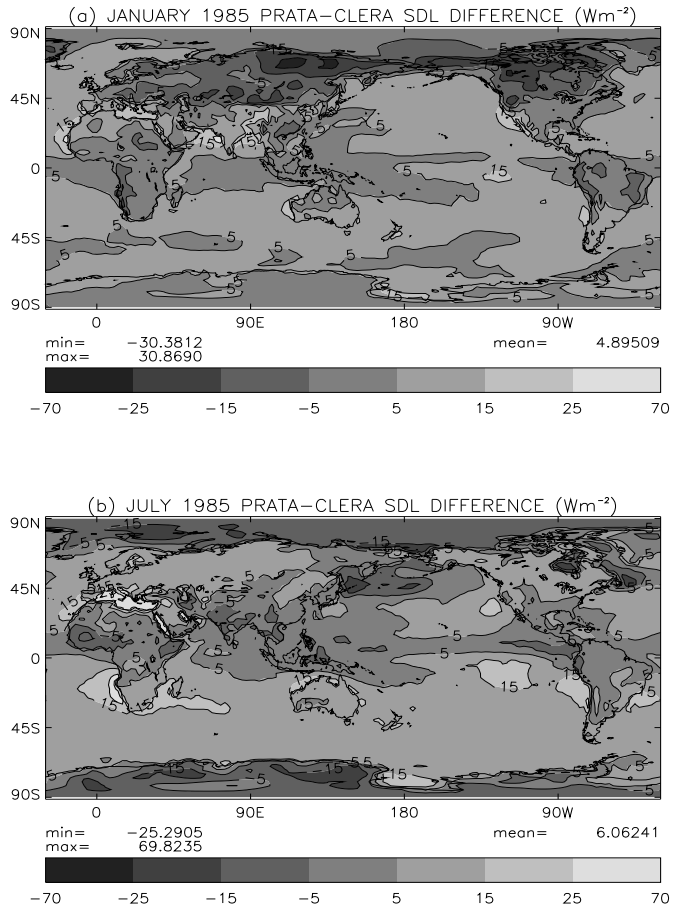


Figure 4.1: *Prata minus CLERA SDL$_c$ differences for (a) January and (b) July 1985.*

is substantial over the Mediterranean and the Gulf during July with SDL$_{prata}$ being over 40 $Wm^{-2}$ greater than CLERA values. This positive bias is explained by the high moisture lapse rates that dominate these regions near to the surface: a moist surface layer disguises a predominantly dry profile, thereby $u$ and consequently SDL$_{prata}$ will be overestimated.

SDL$_{prata}$ is significantly less than CLERA values (negative bias) over polar regions and the northern Pacific in July and over Siberia and Canada in January. This stems from the inability of the formula to take into account the temperature and moisture inversions present over these regions. A tendency for SDL$_{prata}$ to be less than SDL$_{clera}$ is also apparent over tropical regions. This trend can be explained by the tendency for deep convective regions to sustain smaller moisture lapse rates compared to non-convective regions. Another explanation for this trend is the increasing opacity of moister tropical profiles causing downwelling emission to originate from lower, warmer altitudes, thus causing emission to

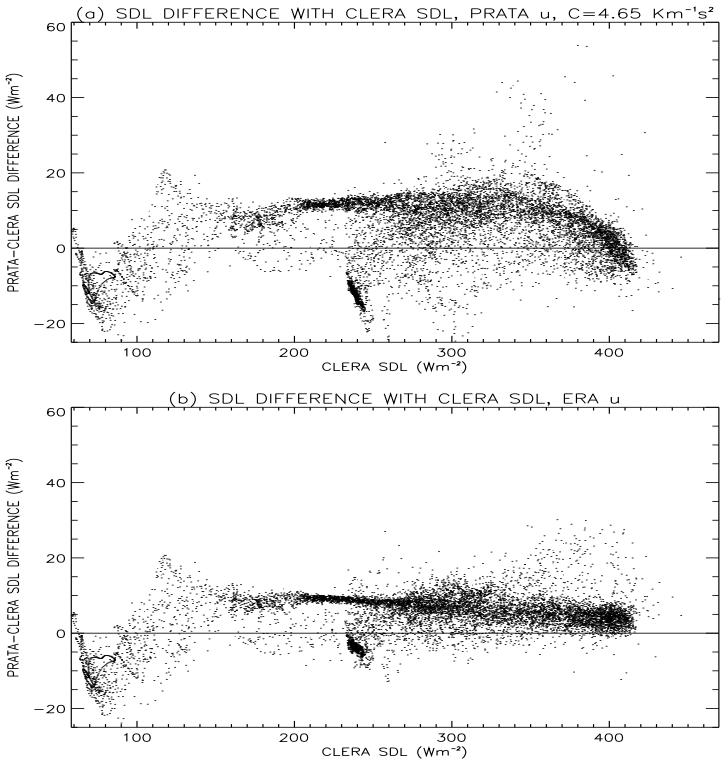


Figure 4.2: *Prata minus CLERA clear-sky SDL differences as a function of CLERA SDL for (a) Prata estimated u and (b) ERA prescribed u for July 1985.*

be greater than that estimated by the formula.

### 4.3.2 Irradiance Sensitivity to Prata Parameters

The effect of altering the internal parameters in the Prata model on the $\mathrm{SDL}_c$ bias with respect to CLERA is now examined. Table 4.2 summarises the global mean $\mathrm{SDL}_c$ differences for land only, ocean only and all grid points for a variety of parameter specifications. The control comparison refers to the specifications described in Sec. 4.3.1. For all comparisons much of the positive bias globally of $\mathrm{SDL}_{prata}$ is due to the positive bias over ocean regions. Using the surface level rather than the lowest model level of ERA to prescribe $T_0$ results in an increase in root mean squared (RMS) difference from about 8 $Wm^{-2}$ for the control comparison to about 12 $Wm^{-2}$ for both January and July.

Varying the parameter $C$ acts to alter significantly the estimated column moisture in the Prata formula and consequently also the estimated $\mathrm{SDL}_c$. Regions where temperature and moisture lapse rates are greater than those implicitly assumed by setting $C$ to 4.65 $Km^{-1}s^2$ incur smaller differences in $\mathrm{SDL}_c$ when $C$ is decreased. The reverse is true for regions of small or negative moisture and temperature lapse rates such as the Antarctic. Reducing $C$

Table 4.2: *Prata minus CLERA SDL difference for July and January, 1985, for the spatial mean of land only, ocean only and all grid points. Parameters are as defined in Eq. 4.1 to 4.3 unless stated. RMS denotes the root mean squared of Prata minus CLERA SDL difference. Units of C are* $Km^{-1}s^2$.

| Month: | JAN | | | | JUL | | | |
|---|---|---|---|---|---|---|---|---|
| | PRATA SDL Global | minus Diff Ocean | CLERA ($Wm^{-2}$) Land | RMS ($Wm^{-2}$) Global | PRATA SDL Global | minus Diff Ocean | CLERA ($Wm^{-2}$) Land | RMS ($Wm^{-2}$) Global |
| Control | 4.9 | 7.7 | -1.0 | 7.5 | 6.1 | 7.2 | 3.0 | 8.4 |
| $T_0$=$T_s$ | 8.3 | 13.2 | -2.4 | 11.8 | 9.4 | 12.4 | 2.3 | 12.0 |
| $C$=4.5 | 3.8 | 6.4 | -1.7 | 6.7 | 4.8 | 5.9 | 1.9 | 7.8 |
| $C$=4.8 | 6.0 | 9.0 | -0.3 | 8.4 | 7.3 | 8.5 | 4.1 | 9.2 |
| ERA $u$ | 4.2 | 5.3 | 2.1 | 5.9 | 5.5 | 5.1 | 6.0 | 6.2 |

to 4.5 $Km^{-1}s^2$ results in a decreased global mean $SDL_c$ difference compared to the control comparison with positive biases over ocean regions decreasing. However, the negative bias over high latitude land regions in January tend to increase. Increasing $C$ to 4.8 $Km^{-1}s^2$ acts to increase RMS differences compared to the control comparison with high latitude and some tropical regions showing a reduction in mean $SDL_c$ difference, but at the expense of many ocean regions in which the positive bias tends to increase.

One important source of error in the Prata model stems from the estimation of $u$ from screen level conditions. To assess the importance of this uncertainty, $SDL_{prata}$ is calculated using ERA total column moisture to prescribe $u$ in Eq. 4.2. This produces the lowest RMS difference of all comparisons in Table 4.2. Mean $SDL_{prata}$ minus $SDL_{clera}$ differences over land grid points become more positive. Biases in regions where $u$ calculated by Eq. 4.2 is significantly different to ERA total column moisture are diminished somewhat when ERA $u$ is prescribed. Figure 4.2 shows the July 1985 Prata minus CLERA $SDL_c$ difference at each grid point as a function of $SDL_{clera}$ for (a) the control comparison, and (b) where $u$ is prescribed by ERA. In tropical convective regions, where $SDL_{clera}$ is above 400 $Wm^{-2}$, Eq. 4.2 tends to underestimate $u$ compared to ERA. This explains the tendency for Prata $SDL_c$ to become less than $SDL_{clera}$ with increasing $u$ in the control comparison. This tendency is diminished when ERA $u$ is prescribed, although there still remains a systematic trend for decreasing Prata minus CLERA $SDL_c$ differences with increasing $SDL_{clera}$.

The cluster of values of negative difference at $SDL_{clera}$ of about 240 $Wm^{-2}$ in Fig. 4.2(a) corresponds to Arctic grid points. The disparity is much reduced when ERA is used to prescribe $u$ (Fig. 4.2(b)). However differences over the Antarctic region (i.e. $SDL_{clera} <$ 100 $Wm^{-2}$) are not decreased when $u$ is prescribed by ERA. A systematic positive difference

(i.e. $SDL_{prata} > SDL_{clera}$) of 5.5 $Wm^{-2}$ is still evident when $u$ is prescribed by ERA. This suggests a disparity between the Prata model and the Edwards-Slingo code. The fact that the Prata model internal constants $a$ and $b$ were tuned to land based observations may explain the positive $SDL_c$ bias over ocean regions. An adjustment may be required because of inadequacies in the observational data used by Prata to derive the empirical constants. For example cloud contamination of observed irradiance and inaccuracy in observed irradiance and total column moisture may introduce an error that varies systematically with changing $SDL_c$. Alternatively the CLERA simulation may be in error due to a lack of account for the longwave emission from aerosol or the incorrect parameterization of the water vapour continuum emission. Using a least squares fit regression the values of constants $a$ and $b$ in Eq. 4.1 are set, using ERA $u$ and $T_0$ in conjunction with $SDL_{clera}$ for July 1985. The best fit occurs when $a$ is reduced to 0.985 and $b$ is reduced to 0.289. Using these values and ERA $u$, Prata minus CLERA differences are less than 5 $Wm^{-2}$ over most of the globe. The disparity over polar regions, however, remains. This is likely to be a failure of the simple emissivity model used by Prata. At low water vapour path, the longwave spectrum becomes progressively more transparent. Therefore the height dependent changes in water vapour amount and temperature become increasingly more important with regard to the calculation of $SDL_c$.

## 4.4 Comparison with Observations in the Tropical Warm Pool

### 4.4.1 Direct Comparison

Observations of surface longwave irradiance in the tropical Western Pacific were compared with the corresponding CLERA simulated values. The hourly observations are averaged to match the 6-hourly simulated values in Fig. 4.3. Mean $SDL_{clera}$ over the observational period is 411 $Wm^{-2}$ while the corresponding WHOI value is 414 $Wm^{-2}$. Because the observations are taken for all-sky conditions, it is expected that WHOI values should be greater than $SDL_{clera}$ because of the additional downward longwave emission by clouds. If both datasets were entirely accurate, the CLERA-WHOI $SDL_c$ difference of about 3 $Wm^{-2}$ would constitute the mean surface longwave cloud radiative forcing, $LWCF$. However, the estimated $LWCF$ is rather low compared with values obtained by Collins *et al.* (1996) of between about 5 and 15 $Wm^{-2}$ for the central and eastern equatorial Pacific, and less than the 20 $Wm^{-2}$ calculated by Long (1996) for the ARM PROBE experiment. The ARM PROBE mean surface downwelling long-wave irradiance over the TOGA COARE period is 417 $Wm^{-2}$ and the calculated clear-sky value is 397 $Wm^{-2}$.

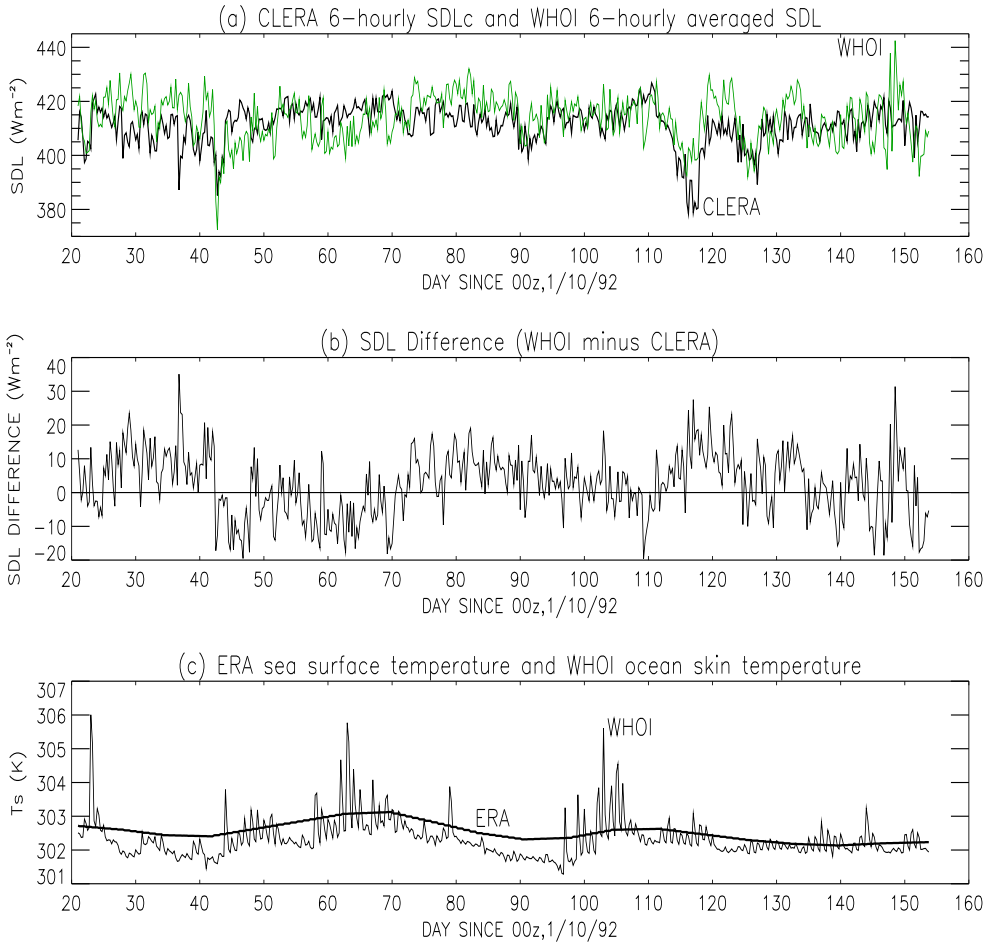


Figure 4.3: *Time-series of WHOI 6-hourly averaged and CLERA 6-hourly surface downwelling longwave irradiance, SDL ($Wm^{-2}$), and surface temperature, $T_s$ (K), for the period 20 October 1992 to 4 March 1993: (a) all-sky $SDL_{whoi}$ (green) and clear-sky $SDL_{clera}$, (b) $SDL_{whoi}$ minus $SDL_{clera}$ and (c) WHOI and ERA surface temperature.*

There are periods when observed $SDL$ is significantly less than $SDL_{clera}$ (negative SDL difference in Fig. 4.3(b)). This is unlikely given the generally decreasing temperatures with altitude in the tropical troposphere and the importance of near-surface layers in determining surface long-wave irradiance (Zhao *et al.* (1994)). This suggests errors are present in the simulation and/or the observations. A potentially significant source of error are the ERA atmospheric profiles. Errors of order 10 $Wm^{-2}$ in TOGA COARE observations (Weller and Anderson (1996)) are inherent, implying that cloud forcing estimates should be interpreted with extreme caution. However, if a fairly constant bias is present in observations and calculations, changes in cloudiness may be inferred from changes in calculated cloud forcing over longer periods of time (i.e. days to weeks). Periods of high irradiance variability over about 5 to 10 days are present in both the observations and the calculations (Fig. 4.3(a)). Most

of the variability in the net long-wave irradiance is due to fluctuations in the downwelling irradiance. Therefore SDL variability will be considered in detail. Of particular interest are the periods centred on day numbers 43, 90 and 117.

Fig. 4.3(c) shows the WHOI $T_s$, which was modelled from 0.45 $m$ ocean temperatures by Weller and Anderson (1996), to vary more markedly than the simulated $T_s$. ERA sea surface temperature is essentially fixed over the period of a day. Thus the large diurnal signal apparent in the observations (amplitudes up to 5 $K$) are not reproduced. This causes surface emission (E) to fluctuate more than CLERA values (not shown).

### (a) Comparisons over five time periods

The period 21 October 1992 to 4 March 1993 is split into five time periods corresponding to differing meteorological regimes, summarised in table 4.3. The periods correspond

Table 4.3: *Dates and meteorological regimes of five time periods during the TOGA COARE measurements. ISO is the intraseasonal oscillation.*

| Period | Dates | Meteorological regime |
|---|---|---|
| 1 | 21 OCT - 12 NOV 92 | Active ISO phase; 3-7 day SW'ly wind events |
| 2 | 12 NOV - 14 DEC 92 | Convection suppressed ISO phase; low wind speed |
| 3 | 14 DEC - 2 JAN 93 | Active ISO phase; WWBs |
| 4 | 2 JAN - 23 JAN 93 | Convection suppressed ISO phase; low wind speed |
| 5 | 23 JAN - 4 MAR 93 | Active ISO phase; Squalls, then moderate NW winds |

loosely to active and convection-suppressed phases of the Intra-seasonal Oscillation (ISO) highlighted by Gutzler *et al.* (1994). Table 4.4 sets out the means of observed meteorological variables, and includes the WHOI observed and CLERA calculated SDL, and their mean difference, $\mathrm{SDL}_{diff}$, over the five periods. Also shown is the observed skin temperature, $T_{skin}$, 2.3 $m$ air temperature, $T_{air}$, and the surface incoming shortwave irradiance, $SW_{sfc}$.

The meteorological conditions and flux variability were described in detail by Weller and Anderson (1996). By considering Tables 4.3 and 4.4 it is apparent that high values of $SW_{sfc}$ correspond with suppressed phases of the ISO and also with lower values of $SDL_{diff}$. This may be explained by considering that during convection suppressed regimes, the presence of cloud is less frequent, thus allowing greater transmittance of shortwave irradiance to the surface. A greater proportion of clear-skies also results in lower longwave emission by clouds to the surface and consequently low $SDL_{whoi}$. Because $SDL_{clera}$ is not affected by the presence of cloud, $SDL_{diff}$ will also be low. This is particularly the case for period 2 in which $SW_{sfc}$ is high (238 $Wm^{-2}$) and $SDL_{diff}$ is low (-4.4 $Wm^{-2}$).

Table 4.4: *Meteorological and irradiance measurements and calculations during the five periods.* $T_{skin}$ *is the sea surface skin temperature,* $T_{air}$ *is the 2.3m surface air temperature,* $q$ *is the surface atmospheric specific humidity,* $RH$ *is the surface atmospheric relative humidity and* $SW_{sfc}$ *is the surface incoming solar irradiance.* $SDL_{whoi}$ *is the WHOI surface downwelling long-wave irradiance,* $SDL_{clera}$ *is the CLERA calculated surface downwelling long-wave irradiance and* $SDL_{diff} = SDL_{whoi} - SDL_{clera}$.

| Period | $T_{skin}$ $(K)$ | $T_{air}$ $(K)$ | $SW_{sfc}$ $(Wm^{-2})$ | $SDL_{whoi}$ $(Wm^{-2})$ | $SDL_{clera}$ $(Wm^{-2})$ | $SDL_{diff}$ $(Wm^{-2})$ |
|---|---|---|---|---|---|---|
| 1 | 302.2 | 300.8 | 186.5 | 416.4 | 408.6 | +7.6 |
| 2 | 302.7 | 301.2 | 237.8 | 409.7 | 414.1 | -4.4 |
| 3 | 302.2 | 300.8 | 170.1 | 419.6 | 412.4 | +7.2 |
| 4 | 302.4 | 301.2 | 212.9 | 415.8 | 414.7 | +1.1 |
| 5 | 302.2 | 301.2 | 200.3 | 411.6 | 408.0 | +3.6 |

Table 4.4 also shows that for all periods considered, the mean 2.3 $m$ air temperature is more than 1 $K$ below that of the mean surface skin temperature. The strong sensitivity of $SDL$ to the near surface temperature (Chapter 3) make this disparity all the more important. The reasons for the high variability in observations and calculations over the 5 day events are discussed further in Sec. 4.4.3.

**(b) Longwave and Shortwave Irradiance Relationship over Daily Time-scales**

To explore the relationship between the effects of cloudiness on the surface longwave and shortwave irradiance further, the dependence of observed all-sky SDL and all-sky $SW_{sfc}$ over daily time-scales are considered. Figure 4.4(a) and (c) shows WHOI and ARM daily averaged SDL to be negatively correlated with corresponding $SW_{sfc}$. Correlation between $SDL_{clera}$ and $SW_{sfc}$ is not significant (Fig. 4.4(b)), implying that the all-sky relationship is due to the effect of clouds. Complementary results are described by Grant and Hignett (1998) who used aircraft irradiance observations in conjunction with clear-sky irradiance calculated by the Edwards-Slingo radiation code.

The large scatter of $SDL_{diff}$ with $SW_{sfc}$ in Fig. 4.4(d)) is explained thus: surface shortwave cloud radiative forcing is sensitive to clouds throughout the atmospheric path while surface longwave cloud forcing is significant only for clouds relatively near to the surface due to higher cloud base temperature and lower water vapour path below the cloud than for clouds at greater altitude. The minimum $SDL_{diff}$ corresponds with the maximum $SW_{sfc}$

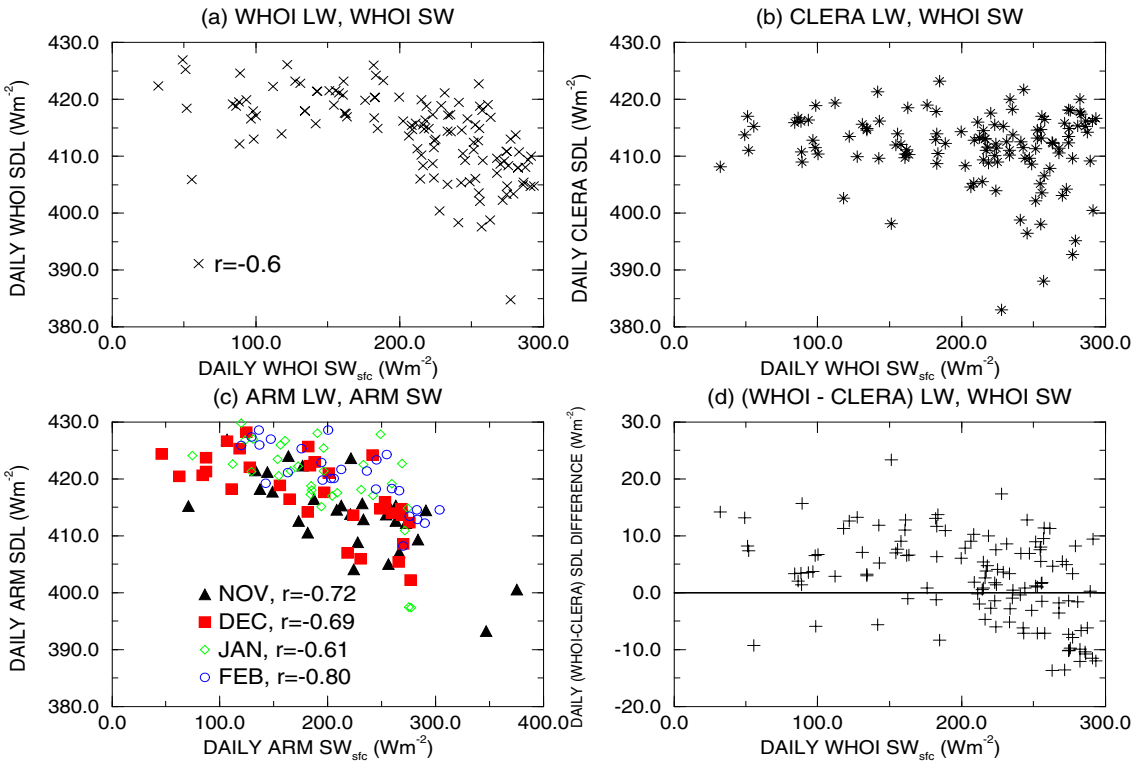


Figure 4.4: *Daily average surface downwelling shortwave and longwave irradiance relationships for: (a) WHOI, (b) WHOI and CLERA, (c) ARM and (d) WHOI-CLERA and WHOI.*

because periods of reduced cloud amount allow strong transmission of shortwave radiation while there is only a small contribution to the observed SDL from longwave cloud emission. Errors in both datasets also introduce greater scatter in the relationship between $SDL_{diff}$ and $SW_{sfc}$. Negative $\mathrm{SDL}_{diff}$ show errors in observational/calculated long-wave irradiances rather than implying negative surface long-wave cloud forcing.

As is well known, shortwave cloud forcing dominates over longwave cloud forcing at the surface in the tropics (e.g. Grant and Hignett (1998)). For a given change in $SW_{sfc}$, the change in all-sky SDL is generally much smaller (Fig 4.4). However, the existence of a relationship between longwave and shortwave cloud radiative forcing suggests that shortwave irradiance may be used in the determination of clear-sky observations. Therefore a more realistic comparison of observed and calculated surface long-wave irradiance may be undertaken.

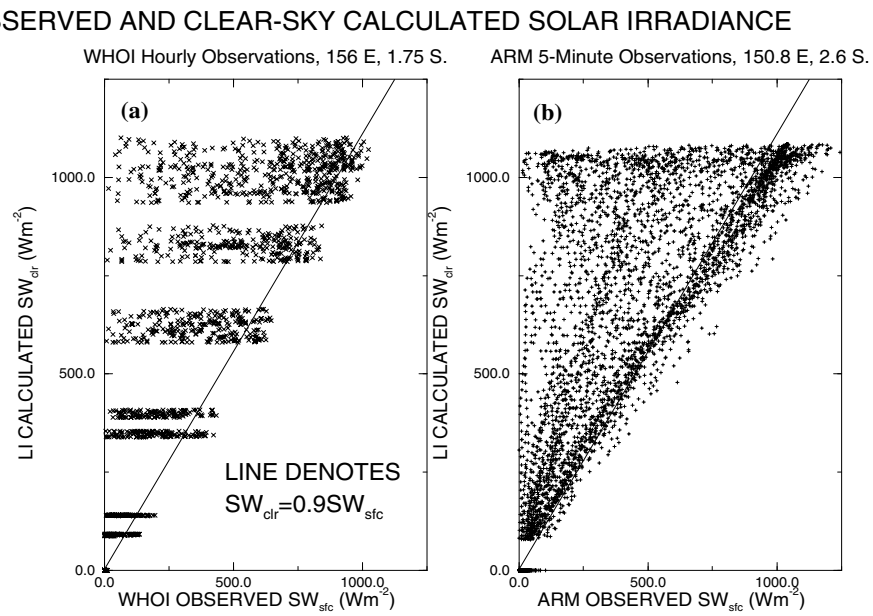


Figure 4.5: *Calculated clear-sky surface downwelling shortwave irradiance, $SW_{clr}$ ($Wm^{-2}$), using the Li* et al. *(1993) method, plotted with observed surface downwelling shortwave irradiance, $SW_{sfc}$ ($Wm^{-2}$), for (a) WHOI hourly observations from October 1992 to March 1993 and (b) ARM 5-minute average observations for November 1992 in the tropical Pacific. The solid line denotes $SW_{sfc} = k_{sw} SW_{clr}$, where $k_{sw} = 0.9$.*

### 4.4.2 Estimating Clear-sky Observations

#### (a) Method

For a realistic comparison of observed and calculated irradiance it is necessary to extract clear-sky observed values. Because observations were collected automatically by the WHOI buoy, no parallel record of cloud amount was available to directly obtain clear-sky irradiance values. Therefore the following approach was undertaken to estimate clear times: 1) time intervals where rainfall is observed are assumed overcast and 2) day-time observations are assumed cloudy if the measured $SW_{sfc}$ is less than a specified fraction ($k_{sw}$) of modelled clear-sky values of $SW_{sfc}$. Method 2 is problematic as only day-time values can be exploited. Also cloud information may only be inferred from the region of the sky occupied by the sun. Dutton (1993) argues that this method is unsatisfactory for these reasons and prefers a method using the net surface longwave irradiance as will be discussed in Sec. 4.5. However, he notes that the longwave method is not suitable for tropical environments due to low level moisture obscuring the cloud signal in the net long-wave irradiance. Also the net long-wave irradiance method is likely to introduce a systematic oversampling of dry profiles. These reasons and the lack of direct cloud observations necessitate the use of a solar method combined with rainfall observations to infer clear skies in this comparison.

To calculate the clear-sky incoming solar irradiance, a parameterization by Li *et al.* (1993) was employed. Downwelling short-wave irradiance at the ocean surface ($SW_{clr}$) is given by,

$$SW_{clr} = S\mu \left[1 - \left(\frac{0.1487}{\sqrt{\mu}} - \frac{0.01124}{\mu}\right) + \frac{1 - exp(-\mu)}{\mu}(0.0699 - 0.0216u^{\frac{1}{2}})\right], \quad (4.4)$$

where $\mu$ is the cosine of the solar zenith angle. The incident solar flux at the top of the atmosphere ($S$) varies with Earth-sun distance and was approximated by,

$$S = 1368 + 45cos\left(\frac{2\pi t}{365}\right), \quad (4.5)$$

where $t$ is the time in days from perihelion on 3 January (Liou (1980)). The total column water vapour ($u$) was taken from ERA 6-hourly values. The observation was deemed clear when $SW_{sfc} > k_{sw}SW_{clr}$. $k_{sw}$ is not known precisely and therefore was estimated. Values were only considered where $\mu$ was greater than 0.1. No explicit method of accounting for the effect of aerosols was included.

Figure 4.5 shows $SW_{clr}$ plotted against $SW_{sfc}$ for ARM and WHOI observations; the values to the right of the solid line ($SW_{sfc} = k_{sw}SW_{clr}$) are retained as clear if $k_{sw} = 0.9$. The banded structure present in Fig. 4.5(a) is explained by the hourly nature of calculated irradiance. Throughout the months considered, the daily cycle of $\mu$ alters with the declination of the sun, thus causing a range of $SW_{clr}$ values for each hour of the day considered. ARM $SW_{sfc}$ values are occasionally greater than the calculated values; this is likely to be caused by reflection off clouds that are not affecting the direct incident solar irradiance locally.

**(b) Clear-sky SDL sensitivity to filtering parameter**

Increasing the parameter, $k_{sw}$, results in a decreasing quantity of observations that are deemed to be made under clear-sky conditions. Because of errors inherent in both the shortwave and longwave observations and calculations it was necessary to determine the most reasonable value of $k_{sw}$ such that cloud contamination of clear-sky filtered observations was minimised, while the number of clear-sky observations were maximised. Also, because $SW_{clr}$ is not adjusted to account for the effects of aerosols, the optimum value of $k_{sw}$ could not be derived theoretically. Therefore comparison was undertaken for a range of $k_{sw}$.

Figure 4.6 shows the change in mean $SDL_{diff}$ (a) and the mean $SDL_{clera}$ and $SDL_{whoi}$ (b) on varying the clear-sky filtering parameter, $k_{sw}$. Only observations where no rainfall was recorded and where $\mu > 0.1$ were considered. The WHOI and CLERA means for all values are shown (filled symbols) by way of a comparison. The removal of values for times when rainfall is observed accounts for much of the difference between WHOI SDL

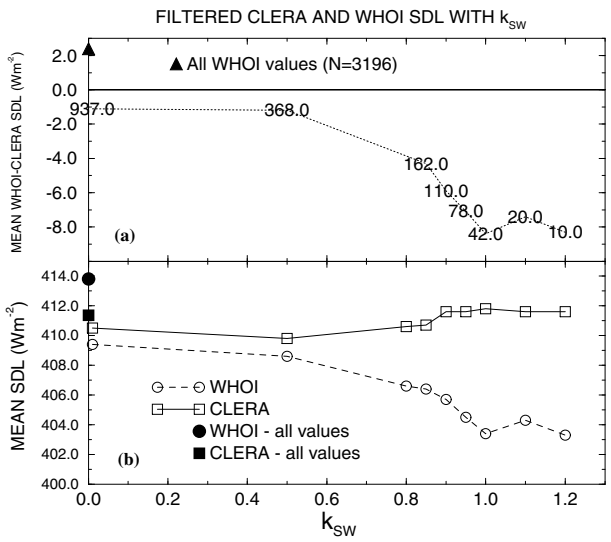


Figure 4.6: *Effect of varying $k_{sw}$ on (a) $SDL_{diff}$ and (b) $SDL_{whoi}$ and interpolated $SDL_{clera}$ for times where no rainfall is recorded and $\mu > 0.1$. Means of all values are also shown as a comparison. Numbers in frame of (a) refer to the sample size of clear-sky observations.*

at $k_{sw}$=0.0 and the mean of all WHOI values (filled circle) in Fig. 4.6(b). This is because observations taken during rainfall will preferentially sample humid, overcast times of high longwave cloud emission compared to other times. $\mathrm{SDL}_{clera}$ is also slightly higher when not filtered for rainfall; this is a likely occurrence of the higher column moisture at times when rainfall is observed.

The mean clear-sky $SDL_{whoi}$ generally decreases with increasing $k_{sw}$, while mean interpolated $SDL_{clera}$ remains fairly constant (Fig. 4.6(b)). This implies that, as expected, increasing $k_{sw}$ acts to increase the proportion of cloud-free observations which, for a given clear-sky profile, will yield lower SDL. For $k_{sw} > 1.0$, further increases in $k_{sw}$ yield marginally smaller decreases in mean clear-sky $SDL_{whoi}$. Mean $\mathrm{SDL}_{whoi}$ of 414 $Wm^{-2}$ compares to the mean clear-sky $\mathrm{SDL}_{whoi}$ of 404 $Wm^{-2}$ when $k_{sw}$ is set to 1.0. Therefore the surface longwave cloud radiative forcing is about 10 $Wm^{-2}$; this is consistent with the method used by Harrison *et al.* (1990) to calculate cloud radiative forcing at the top of the atmosphere from the ERBE satellite data.

### (c) Clear Sky Irradiance Comparison

Setting $k_{sw}$ to 0.9 leaves 110 WHOI observations that are deemed cloud free while 42 observations remain at $k_{sw} = 1.0$. A large number of these observations are during late November and early December (period 2 in Table 4.3) adding to the evidence of Sec. 4.4.1 that this convectively suppressed ISO phase contains relatively more clear-sky periods than

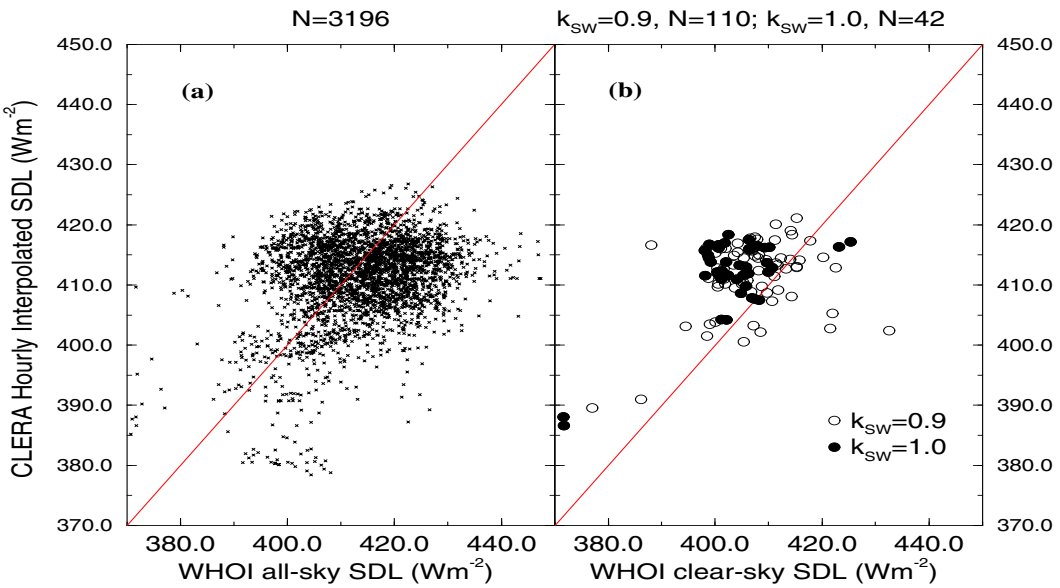


Figure 4.7: *(a) All-sky $SDL_{whoi}$ with $SDL_{clera}$ and (b) clear-sky $SDL_{whoi}$ plotted against $SDL_{clera}$ for $k_{sw}$ = 0.9 (all circles) and $k_{sw}$ = 1.0 (filled circles) over the TOGA COARE period. Solid lines represent $SDL_{whoi}$ = $SDL_{clera}$ irradiances.*

over the remaining TOGA COARE observation period.

Figure 4.7(a) shows all-sky $SDL_{whoi}$ plotted against $SDL_{clera}$ for the entire TOGA COARE period while clear-sky filtered $SDL_{whoi}$ is plotted against $SDL_{clera}$ for $k_{sw} = 0.9$ (all circles) and $k_{sw} = 1.0$ (filled circles) in Fig. 4.7(b). Discarding observations deemed to be made under cloudy conditions causes the removal of most points to the right of the 1:1 line in Fig 4.7(a). The remaining values in Fig 4.7(b) tend to be to the left of the 1:1 line, showing $\mathrm{SDL}_{whoi}$ to be less than $\mathrm{SDL}_{clera}$. The tendency for $\mathrm{SDL}_{clera}$ to be greater than clear-sky filtered $\mathrm{SDL}_{whoi}$ is consistent with results from Dutton (1993) who found observed $\mathrm{SDL}_c$ to be less than model calculated values in the tropics. The mean $\mathrm{SDL}_c$ difference for $k_{sw}$=1.0 is 10 $Wm^{-2}$ and may be explained either by a systematic error in the observations or by errors in the CLERA simulation. The latter explanation is examined in the following section by assessing the potential error in simulated $\mathrm{SDL}_c$ due to ERA atmospheric profiles used. The root mean squared difference between observed and simulated $\mathrm{SDL}_c$ for $k_{sw}$=1.0 is 9.2 $Wm^{-2}$, although when the systematic bias is removed this falls to 5.1 $Wm^{-2}$. Both values are within observational uncertainty.

### (d) ERA-radiosonde profile comparison

To assess potential simulation errors due to ERA profile disparities, the ARM radiosonde ascents were utilised in conjunction with corresponding ERA profiles at the nearest grid

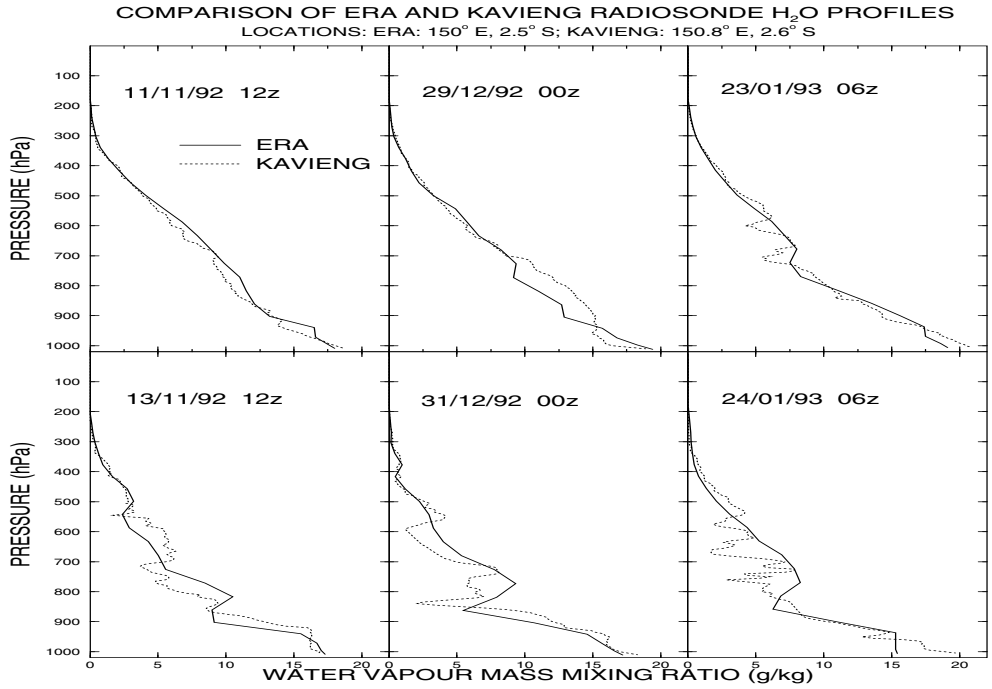


Figure 4.8: *ECMWF Re-analysis and Kavieng radiosonde profiles of water vapour mass mixing ratio. Location: 150.8 °E, 2.6 °S.*

point. The profiles considered are chosen to sample relatively dry ($u < 50\ kgm^{-2}$) and relatively moist ($u > 50\ kgm^{-2}$) conditions for a range of times. Figure 4.8 shows ERA and radiosonde water vapour mass mixing ratio profiles. The differences between observed and simulated profiles are generally quite small. The mean ERA profile $u$ is 3.9% greater than for the radiosonde profiles. Near-surface temperature for ERA profiles and ARM radiosonde profiles are shown in Fig. 4.9. Differences between surface temperatures by as much as 3 $K$ are noted. Also, ERA fails to capture the temperature inversion at about 850 $mb$ present in the observations on 31 December.

The radiative effects of profile differences are now examined, using the narrow-band radiation model. For this purpose, profiles are interpolated onto a 183 point vertical grid containing surface values and values every 5 $hPa$ from 1000 $hPa$ to 105 $hPa$, above which there are two levels (at 75 $hPa$ and 25 $hPa$) which are prescribed by the tropical standard atmosphere. Ozone is interpolated from the standard profile. Nitrous oxide and methane concentrations are assumed constant through the profile at 310 and 1720 ppbv respectively and carbon dioxide concentration is set at 360 ppmv (IPCC (1996)). The effects of aerosols are not accounted for. Mean calculated $\mathrm{SDL}_c$ for the ERA profiles is 4.6 $Wm^{-2}$ greater than mean calculated irradiance for the radiosonde profiles (Table 4.5). It is shown that by replacing radiosonde surface temperatures with ERA values, and consequently altering the

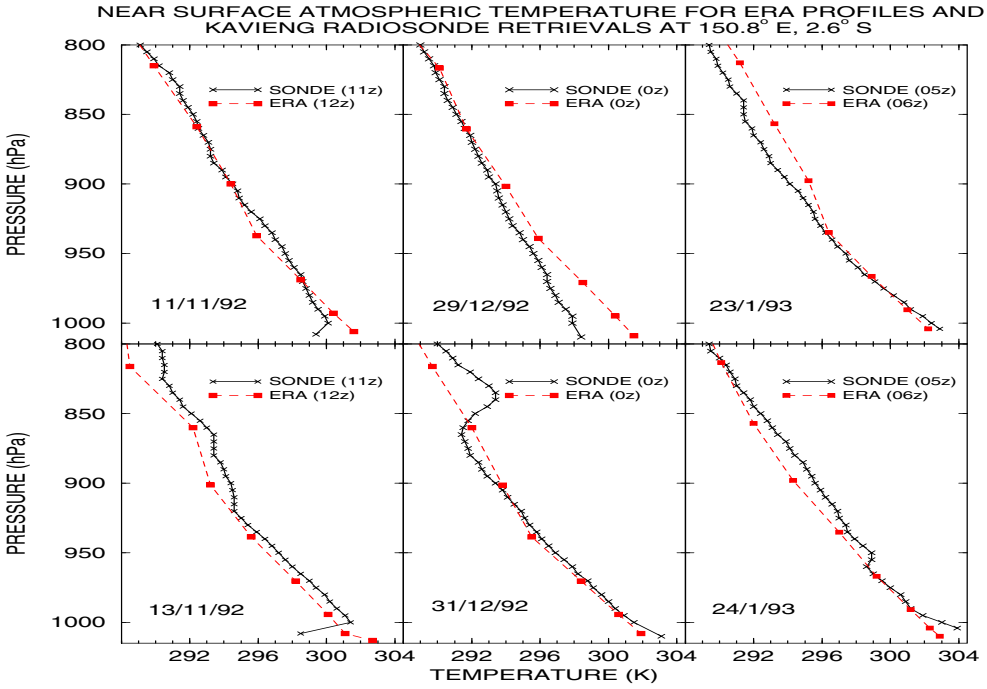


Figure 4.9: *ERA and Kavieng radiosonde profiles of temperature between 800 hPa and the surface. Location: 150.8 °E, 2.6 °S.*

interpolated near-surface temperature, (radiosonde′ in Table 4.5) that much of the disparity in calculated irradiance is attributable to near-surface temperature differences rather than profile temperature and moisture differences. Root mean squared ERA minus radiosonde irradiance differences of 8.2 $Wm^{-2}$ decrease to 1.8 $Wm^{-2}$ for ERA minus radiosonde′ values. This again highlights the importance of near-surface layer temperature in determining SDL. Therefore specification of surface temperature and interpolation of near-surface temperature is likely to significantly influence the accuracy of simulated $SDL_c$. The interpolation of temperature between the lowest ERA model level and the surface assumed in the Edwards-Slingo radiation code is in contradiction with observations (Weller and Anderson (1996)), thus potentially introducing a bias of order 5 to 10 $Wm^{-2}$ into the simulated $SDL_c$.

### 4.4.3 Episodes of High Irradiance Variability

The radiosonde profiles from the ARM site and ERA profiles from the corresponding grid point are now used to assess the relative importance of atmospheric profiles of temperature and water vapour in driving the significant longwave irradiance variability observed and calculated over the 5-day events.

Table 4.5: *Narrow band model calculated surface downwelling longwave irradiance for ERA profiles, and radiosonde profiles, and radiosonde profiles with ERA surface temperature (radiosonde′) at 150.8 °E, 2.6 °S.*

| Date, Time (GMT) | ERA ($Wm^{-2}$) | Radiosonde ($Wm^{-2}$) | Radiosonde′ ($Wm^{-2}$) |
|---|---|---|---|
| 11/11/92, 12z | 418.9 | 406.5 | 415.2 |
| 13/11/92, 12z | 407.5 | 397.6 | 408.6 |
| 29/12/92, 00z | 415.9 | 404.8 | 415.3 |
| 31/12/92, 00z | 403.2 | 406.0 | 403.5 |
| 23/1/93, 06z | 419.9 | 421.9 | 421.6 |
| 24/1/93, 06z | 405.5 | 406.2 | 404.1 |
| Mean: | 411.8 | 407.2 | 411.4 |

Table 4.6: *Change in calculated clear-sky SDL due to to changes in radiosonde profile, $\Delta SDL$ ($Wm^{-2}$), and for changes due to profile temperature changes ($\Delta SDL_{\Delta T(z)}$) and water vapour amount changes only ($\Delta SDL_{\Delta w(z)}$) for 13-11 November and 30-28 December 1992 and 24-23 January 1993.*

| Date | $\Delta$SDL ($Wm^{-2}$) | $\Delta SDL_{\Delta T(z)}$ ($Wm^{-2}$) | $\Delta SDL_{\Delta w(z)}$ ($Wm^{-2}$) |
|---|---|---|---|
| 13-11 NOV | -8.9 | -0.4 | -8.4 |
| 30-28 DEC | +1.2 | +17.6 | -16.5 |
| 24-23 JAN | -15.7 | +3.9 | -19.6 |

### (a) November Event

Between 11 and 13 November, temperature increased in the mid-troposphere while the total column moisture drops significantly with all but a layer between about 900 and 950 $hPa$ experiencing a fall in water vapour mass mixing ratio. The decrease in calculated $SDL_c$ of 9.1 $Wm^{-2}$ is revealed, using the narrow band scheme, to be caused primarily by the changes in water vapour concentration between profiles (Table 4.6). Changes in water vapour amount in the 700 $hPa$ to the surface layer cause 77% of the change in $SDL_c$ due to profile water vapour variations.

To ascertain whether the November event constitutes a large-scale feature, the CLERA 6-hourly simulated $SDL_c$ for the large-scale region bounded by 150 to 160° E and within 20°

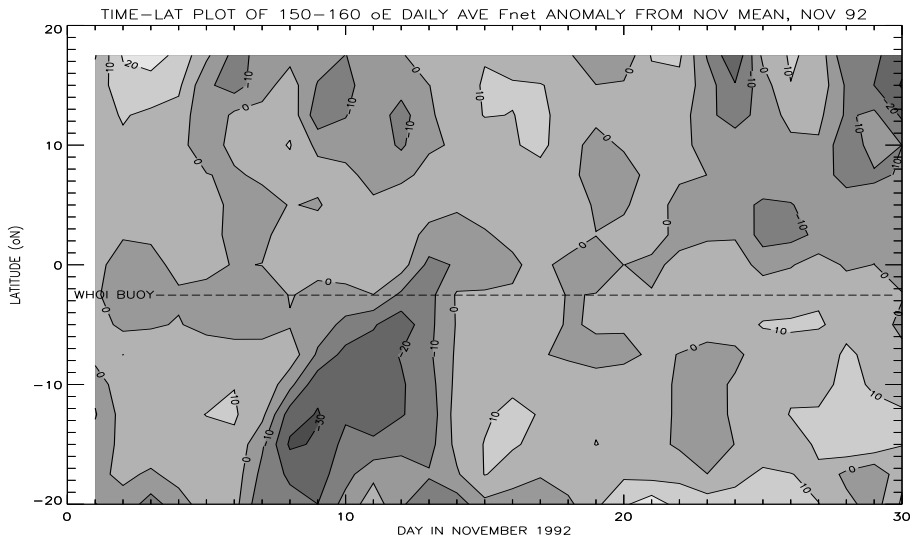


Figure 4.10: *Time-latitude plot of 6-hourly 150 to 160 ° E mean $SDL_{clera}$ anomalies from the November monthly mean values, plotted between 17.5 and -20 ° N.*

of the equator was examined. Over the tropical western Pacific, $SDL_{clera}$ is highest over the warm, moist equatorial ocean regions and lower over the drier land regions. Plotting irradiance as a function of latitude and time shows a tongue of low irradiance to propagate from the south during the November event (Fig. 4.10). This resulted from a latitudinally propagating large-scale flow of relatively dry air from Australia. This large-scale event may mark the transition between phases of the ISO as discussed by Weller and Anderson (1996).

### (b) December Event

Between 28-30 December a moist profile was replaced by a dry profile above a temperature inversion at about 830 $hPa$, below which the near-surface layer is both warm and moist (see Figures 4.9 and 4.8). However, calculated $SDL_c$ is similar for both profiles. This is because decreased atmospheric emission due to less water vapour is offset by the high temperatures of the the profile on 30 December between about 700 $hPa$ and the surface. The total change in calculated $SDL_c$ of 1.2 $Wm^{-2}$ represents the residual between the 16.5 $Wm^{-2}$ decrease due to profile water vapour changes and a 17.6 $Wm^{-2}$ increase due to profile temperature changes (Table 4.5). The changes in near-surface temperature are particularly important in this respect. The increases in surface temperature between 28-30 December causes the net surface longwave cooling to increase by 27.5 $Wm^{-2}$.

**(c) January Event**

ARM radiosonde ascents show temperature and water vapour profiles to vary significantly between 23-28 January. A moist profile on the 23rd was replaced by a very dry profile on the 24th with total column moisture dropping from 55.8 $kgm^{-2}$ to just 38.7 $kgm^{-2}$. The $SDL_c$ falls from 421.9 to 406.2 $Wm^{-2}$ and are primarily (about 80%) due to water vapour changes in the lowest 300 $hPa$ slab, despite a similar magnitude of increase in water vapour amount in the 300 $hPa$ thick slab immediately above. Examining the large scale changes in simulated irradiance over January shows no noticeable latitudinally propagating $SDL_c$ anomaly as was encountered during November. The decrease in $SDL_c$ appears to propagate from the west and is associated with a convectively active regime, although with a cooler, drier near surface layer (not shown)

## 4.5 Comparison with Observations in Alaska

### 4.5.1 Direct Comparison

Observations of SDL and $T_s$ from Alaska were compared with interpolated hourly values simulated by CLERA over the entire annual cycle of 1992 (Fig. 4.11). Also shown is the ERA column water vapour and the observed SDL minus simulated $SDL_c$ which may be interpreted as the surface longwave cloud radiative forcing ($LWCF$). Times of missing data are not considered in the comparison. Observed $T_s$ ranges from less than 240 $K$ during the winter to above 280 $K$ during the summer (Fig. 4.11(a)). The seasonal cycle is well depicted by ERA. However, diurnal fluctuations are less well represented, due in part to the poorer temporal resolution of the ERA products. Notably, a 10 $K$ overestimation of $T_s$ by ERA is present at the end of April. ERA $u$ also shows a strong seasonal cycle, ranging from about 2 $kgm^{-2}$ in February up to nearly 30 $kgm^{-2}$ at the end of June. However, the daily fluctuations of $u$ are also very strong, especially in summer months, varying by as much as 20 $kgm^{-2}$ over the first few days of July. Both the seasonal and daily fluctuations of $u$ are correlated strongly with $SDL_{clera}$ highlighting the strong dependence of $SDL_c$ on total column moisture. The observed all-sky SDL is less well correlated with ERA column moisture because clouds act to both dampen the $u$-related signal as well as introduce their own mode of SDL variability. CLERA and STAR SDL both show a strong seasonal cycle. This illustrates that the clear-sky component of SDL is the dominating cause of SDL variability over a year. All-sky $SDL_{star}$ tends to be significantly greater than CLERA values. This is to be expected due to the increased downward longwave emission caused by the presence of clouds.

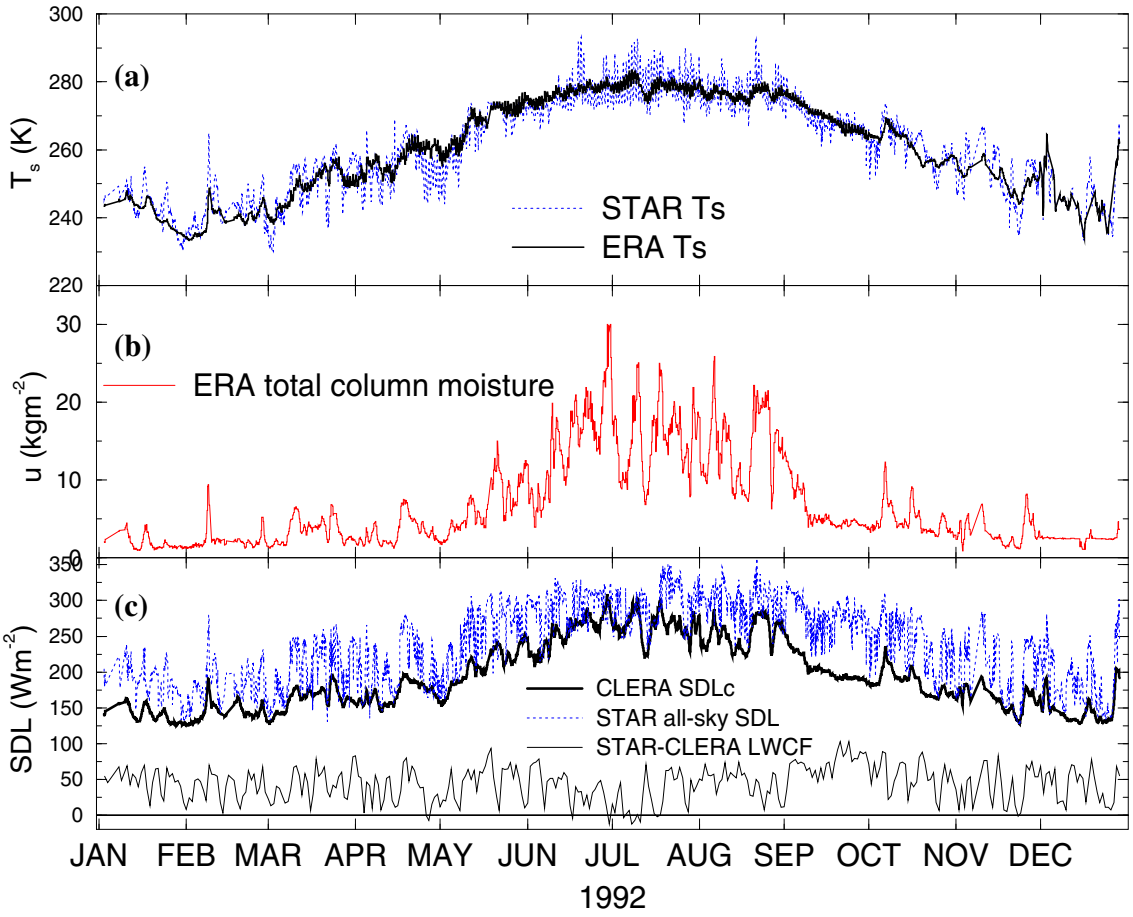


Figure 4.11: *STAR hourly and ERA interpolated hourly $T_s$ (a), ERA hourly u (b) and STAR hourly SDL, CLERA interpolated hourly $SDL_c$ and the STAR minus CLERA LWCF (c) for Barrow (72.3 ° N, 156.6 ° W), 1992.*

Mean observed all-sky SDL is 238 $Wm^{-2}$ which is significantly greater than the mean $SDL_{clera}$ of 194 $Wm^{-2}$. It is encouraging to note that the minimum $SDL_{star}$ values tend to coincide approximately with CLERA $SDL_c$ (Fig. 4.11(c)), thus indicating that clear-sky periods in the observational data produce similar SDL to simulated clear-sky values. This inference is discussed further in Sec. 4.5.2. The difference between all-sky observed SDL and clear-sky simulated SDL can be as much as 100 $Wm^{-2}$ (Fig. 4.11(c)). If both observed and simulated irradiance are accurate, this indicates that instantaneous surface $LWCF$ can be as large as 100 $Wm^{-2}$.

### 4.5.2 Clear-sky Comparison

#### (a) Method

Comparing SDL measured when skies are free of cloud with simulated $SDL_c$ is of greater value in identifying the causes of observation-model biases that the direct comparison in the previous section. However, removing measurements from the time-series that are deemed to be taken during cloudy conditions is problematic due to the lack of *in situ* observations of cloud amount at the STAR site. Two alternative methods were used to identify clear-sky periods:

1) Clear-sky conditions were assumed when observed surface downwelling shortwave irradiance was above a prescribed fraction, $k_{sw}$, of calculated clear-sky surface downwelling shortwave irradiance. This was the method implemented in Sec. 4.4

2) The sky was assumed clear when SDL was below a specified fraction, $k_{lw}$, of the surface emitted irradiance, E.

Method 2 is illustrated in Fig. 4.12 which shows the observed surface emitted longwave irradiance plotted against observed SDL. The lines correspond to $E = k_{lw}SDL$ for two different values of $k_{lw}$; points above each line are defined as clear-sky measurements for the given value of $k_{lw}$. Thus by decreasing the value of $k_{lw}$, the number of measurements deemed to be made under clear-sky conditions is reduced. This method of clear-sky sampling differs slightly to the technique used by Dutton (1993) who defined clear-sky measurements when the observed surface net longwave cooling was greater than a pre-determined fraction of the surface emission.

Using the SDL to infer clear-sky conditions is undesirable because it is also the parameter from which model-observation comparison is undertaken. The strong dependence of SDL on parameters other than cloud amount will potentially introduce systematic biases into the clear-sky filtered data. For example the strong apparent positive dependence of $SDL_c$ on temperature and column water vapour highlighted in Fig. 4.11 is likely to result in an oversampling of cold, dry profiles using method 2. The longwave method is utilised because of the shortcomings of the solar method (Dutton(1993)) and the strong influence of clouds on the surface net longwave irradiance for the relatively dry sub-arctic profiles. Clear-sky sampling was performed using method 1 only, method 2 only and both methods in unison for a range of $k_{sw}$ and $k_{lw}$. Comparisons were subsequently undertaken between observed and simulated $SDL_c$ considering only the portions of the time-series deemed to be free of cloud-cover.

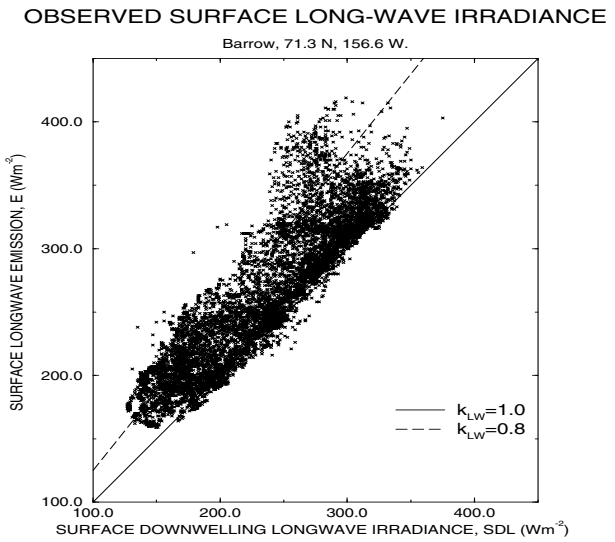


Figure 4.12: *STAR hourly surface upwelling longwave irradiance plotted against STAR SDL for 1992. Solid and dashed lines denote* $E = k_{lw}SDL$.

### (b) Irradiance sensitivity to filtering specifications

It is desirable to minimise cloud contamination in the clear-sky radiometric data while maximising the number of suitable $\mathrm{SDL}_c$ measurements. Decreasing $k_{lw}$ and increasing $k_{sw}$ is likely to reduce cloud contamination of the clear-sky measurements but also reduces the amount of clear-sky data. The optimum values of $k_{lw}$ and $k_{sw}$ may only be obtained by experiment.

Figure 4.13 shows the mean STAR minus CLERA $\mathrm{SDL}_c$ difference for various values of $k_{sw}$ and $k_{lw}$. Numerals in the frame correspond to the number of inferred clear-sky observations (N). Increasing $k_{sw}$ and decreasing $k_{lw}$ act to decrease N and also to decrease the mean STAR minus CLERA SDL difference. This is consistent with the increasingly rigorous filtering of clear-sky values with increasing $k_{sw}$ and decreasing $k_{lw}$. However, increasing $k_{sw}$ above 0.85 fails to decrease the STAR minus CLERA $\mathrm{SDL}_c$ difference further. This is likely to be due to minimal cloud contamination of observed $\mathrm{SDL}_c$ for $k_{sw}$ greater than 0.85. Therefore there is no benefit of using higher values of $k_{sw}$ because this will reduce the amount of available clear-sky data while not significantly increasing the quality of the clear-sky sampling.

For $k_{lw} = 0.65$, there remain only 21 observations and the mean STAR $\mathrm{SDL}_c$ is 5.5 $Wm^{-2}$ less than $\mathrm{SDL}_{clera}$. It is unclear whether this represents the sampling of predominantly dry profiles, or merely an error in the STAR observed or CLERA simulated $\mathrm{SDL}_c$; if erroneously low SDL is measured, these values are more likely to be deemed clear-sky by the longwave filtering technique because the fraction $SDL/E$ will be small. Using $k_{lw}$=0.75 produces

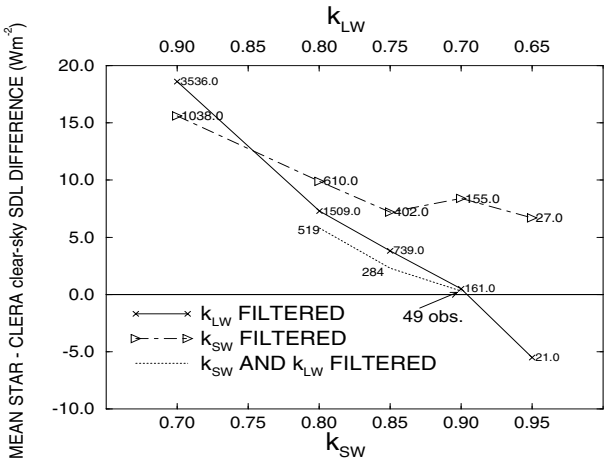


Figure 4.13: *Mean STAR minus CLERA clear-sky SDL difference with $k_{sw}$ and $k_{lw}$. Numbers within the frame denote N (the number of clear-sky observations).*

the lowest root mean squared $SDL_c$ difference of 8.4 $Wm^{-2}$ and the strongest correlation between observed and simulated $SDL_c$. Therefore this is estimated to be the optimal value to use in the clear-sky comparisons. Using only values which are deemed clear-sky using both the shortwave and longwave filtering produces smaller still mean STAR minus CLERA SDL differences for the given $k$ values. However the lowest root mean squared SDL differences are computed using the longwave filtering technique only.

### (c) Comparison

A detailed comparison between CLERA interpolated hourly $SDL_c$ and STAR hourly filtered $SDL_c$ is considered using both the longwave and shortwave filtering techniques for $k_{sw}$=0.85 and $k_{lw}$=0.75. Figure 4.14 shows the correlation between CLERA SDL and STAR all-sky and clear-sky inferred SDL. Diagonal lines denote a 1:1 relationship, while red lines denote the least squares linear regression fit. Table 4.7 summarises yearly mean values for the specified values of $k_{lw}$ and $k_{sw}$.

A strong positive correlation is apparent between $SDL_{star}$ and $SDL_{clera}$ (Fig. 4.14(a)). Most STAR values are much greater than CLERA SDL due to the extra emission of longwave radiation by clouds. Annual mean STAR all-sky (non filtered) SDL is 44.1 $Wm^{-2}$ greater than the CLERA value which may be interpreted as the annual mean surface longwave cloud radiative forcing. This irradiance difference is drastically reduced when STAR data was filtered for clear-skies. This is because cloudy times, when the difference between all-sky STAR data and clear-sky CLERA values is large, are filtered out. The remaining difference may be interpreted as the residual error in clear-sky irradiance computation, and may be

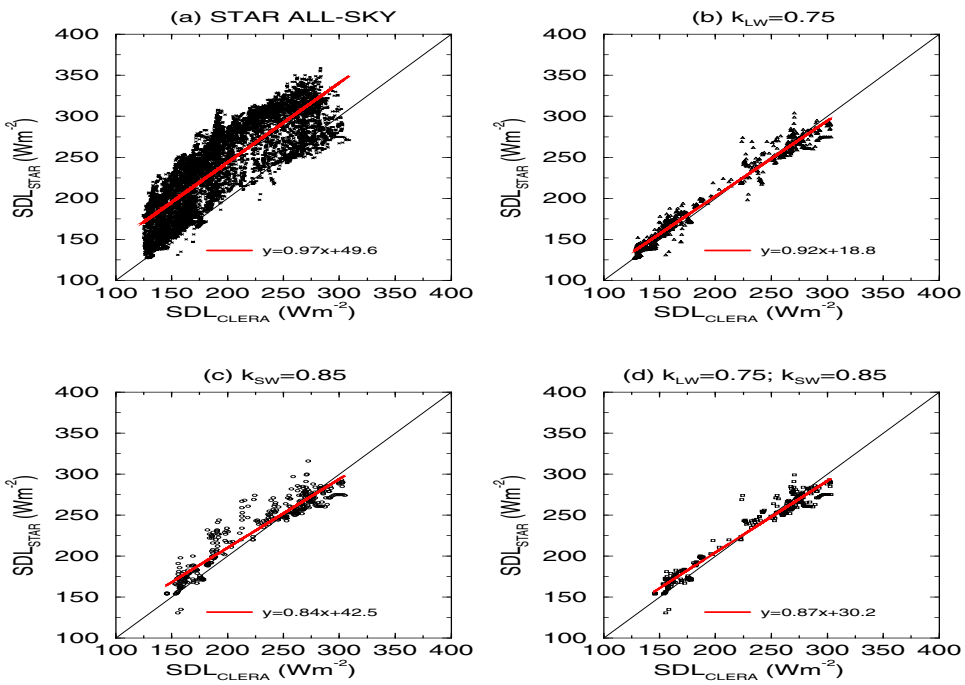


Figure 4.14: *Hourly STAR SDL with CLERA SDL for (a) All-sky STAR SDL, (b) shortwave filtered STAR clear-sky SDL, (c) longwave filtered STAR clear-sky SDL and (d) shortwave and longwave filtered STAR clear-sky SDL. Diagonal lines represent STAR SDL = CLERA SDL, while thick red lines represent the line of best fit to the data points.*

ascribed to observational and simulation errors, as well as cloud contamination errors in the clear-sky filtering.

In considering the residual clear-sky irradiance error, it is informative to calculate the root mean squared deviation of STAR minus CLERA $SDL_c$. The lowest RMS deviation for the values of $k$ considered in Table 4.7 is for the longwave filtering technique (8.4 $Wm^{-2}$). A strong correlation of $r$=0.99 is calculated, although there is a tendency for the regression slope to be less than the 1:1 relationship (Fig. 4.14(b)). This tendency is stronger still when clear-skies are filtered using the shortwave technique (Fig. 4.14(c)). The tendency for STAR $SDL_c$ to be greater than that of CLERA for low SDL is most prominent for the shortwave filtering case, most especially for $SDL_{clera}$ of about 200 $Wm^{-2}$. This may be explained by cloud contamination in the clear-sky observations. Because the bias is most discernible for the shortwave filtering case, it is likely that broken cumulus cloud is the cause. While well broken cloud allows long periods of strong solar irradiance to reach the surface, and therefore will be considered as 'clear-sky' using the shortwave filtering technique, there is still a significant longwave radiation emission to the surface due to these clouds. Further possible reasons for the bias include aerosols, or 'Arctic Haze' (e.g. Shaw *et al.* (1993)),

Table 4.7: *CLERA and STAR all-sky and clear-sky filtered annual mean SDL (surface downwelling longwave irradiance) and their correlation. $SDL_{diff}$ denotes the mean STAR minus mean CLERA SDL difference, while the RMS denotes the root mean squared difference between STAR and CLERA SDL. N is the number of values and r is the least squares fit correlation coefficient between STAR and CLERA SDL.*

| Filtering | STAR $SDL_c$ $(Wm^{-2})$ | CLERA $SDL_c$ $(Wm^{-2})$ | $SDL_{diff}$ Diff $(Wm^{-2})$ | RMS $SDL_{diff}$ $(Wm^{-2})$ | N | r |
|---|---|---|---|---|---|---|
| None | 238.3 | 194.4 | 44.1 | 44.9 | 7995 | 0.84 |
| $k_{lw}$=0.75 | 194.8 | 191.0 | 3.8 | 8.4 | 739 | 0.99 |
| $k_{sw}$=0.85 | 232.4 | 225.2 | 7.2 | 12.6 | 402 | 0.95 |
| $k_{lw}$=0.75 $k_{sw}$=0.85 | 230.4 | 228.1 | 2.3 | 9.4 | 284 | 0.98 |

which the CLERA simulation does not account for, or errors in the profiles of temperature and moisture given by ERA.

There is a tendency for STAR $SDL_c$ to be less than CLERA values during the summer. The overall tendency for observed $SDL_c$ to be greater in the winter and lower in the summer than simulated values is consistent with the finding of Dutton(1993). Dutton explained these findings in terms of water vapour measurement problems in cooler and drier conditions and aerosol uncertainties in the tropics. Again errors in CLERA could provide an explanation for this disparity.

Filtering for clear-skies using both shortwave and longwave techniques improves slightly the correlation between STAR and CLERA $SDL_c$ compared to the shortwave method only, with a root mean square difference of $9.4\,Wm^{-2}$. There is still a tendency for observed $SDL_c$ to be greater than simulated $SDL_c$ for colder, drier times and the opposite to be true for warmer, moister times. Also, the loss of all points for $\mu < 0.1$ remains a disadvantage. Using the longwave technique for $\mu < 0.1$ and either the shortwave method only or both filtering techniques at other times fails to decrease the residual clear-sky error. Observational errors due to the heating of the dome by shortwave irradiance (e.g. Alados-Arboledas *et al.* (1988)) are also investigated by using the longwave technique at night only and during daylight times only (not shown). However, the Barrow data already account for this possible error, and there appears no significant difference between the residual error for the day and night-time

values.

### 4.5.3 Comparison of Vertical Profiles

In order to understand the reasons for the discrepancy between observed and simulated $SDL_c$ at Barrow, eight radiosonde profiles of temperature and water vapour mass mixing ratio were considered in detail. The profiles were selected for times deemed to be clear-sky by the analysis of Sec. 4.5.2 and were compared to corresponding ERA profiles averaged over the same grid points as the CLERA $SDL_c$. All radiosonde profiles were launched at 23z and sample at intervals of between 2 and 50 $hPa$ up to about 400 $hPa$, above which sub-arctic standard atmospheric water vapour and temperature profiles were assumed. Temperature from ERA profiles at 00z are compared with radiosonde ascents in Fig. 4.15. All dates correspond to the ERA profiles for GMT.

The observed temperature profiles are generally well represented by ERA. Errors in radiative calculations due to the inadequate representation of temperature inversions (e.g. Räisänen (1996)) are unlikely, therefore, to be the cause of disparities between simulated and observed irradiance. The large overestimate in surface temperatures by ERA during late April, as noted in Sec. 4.5.1, is highlighted in Fig. 4.15(c) for the 28 April comparison. Surface temperatures are also generally overestimated by ERA during summer months (d to g). Profiles of water vapour mass mixing ratio for ERA and the eight radiosonde ascents are presented in Fig. 4.16. It is apparent that ERA profiles are too moist during the summer months (i.e. Fig. 4.16(c) to (g)) while for the remaining dates vertical profiles of moisture are in reasonable agreement. The apparent overestimate of column moisture by ERA, however, may be a consequence of the temporal sampling. Observed profiles have been chosen to represent clear-sky times and therefore the water vapour content of the profiles is likely to be low compared to overcast times. Because ERA profiles represent all-sky conditions, the 6-hourly averaged profiles are likely to contain more water vapour amount than the radiosonde profiles that sample for instantaneous clear, dry conditions. It is not obvious why this explanation should apply preferentially to summer months.

To quantify more fully the role of surface temperature and column moisture differences in determining irradiance disparities, radiative calculations using the narrow-band scheme were performed on the ERA and radiosonde profiles. Sub-arctic ozone amounts are interpolated from the standard atmosphere and all trace gases are set as in Sec. 4.4.2(d). Temperature and column moisture differences for each profile are presented in Table 4.8 along with calculated $SDL_c$. STAR observations of SDL for the corresponding times are also shown.

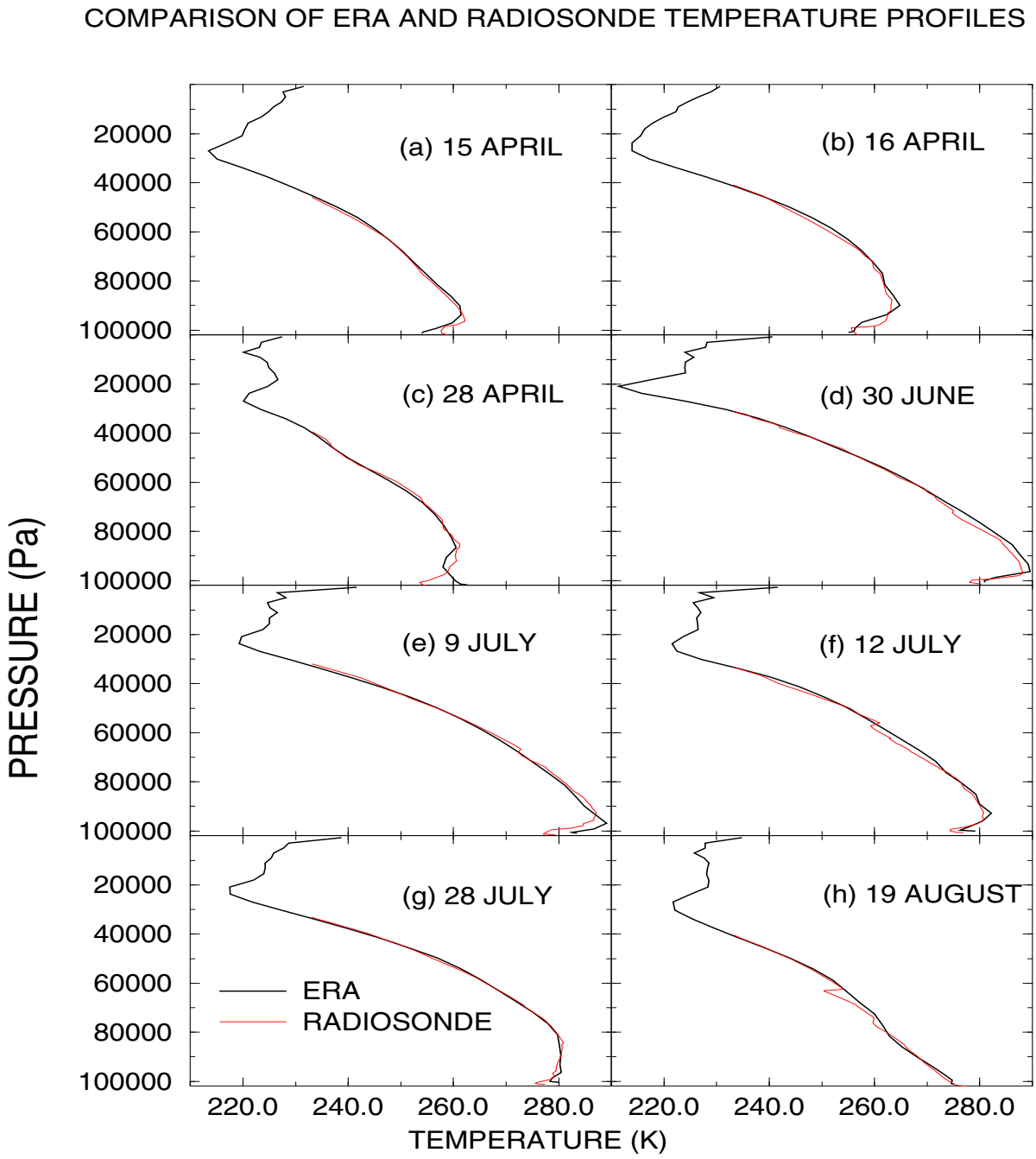


Figure 4.15: *Temperature profiles from radiosonde ascents over Barrow, Alaska (71.3 ° N, 156.6 ° W) and from ERA (70 to 72.5 ° N, 155 to 157.5 ° W). Profiles are for 00z GMT for which the dates correspond.*

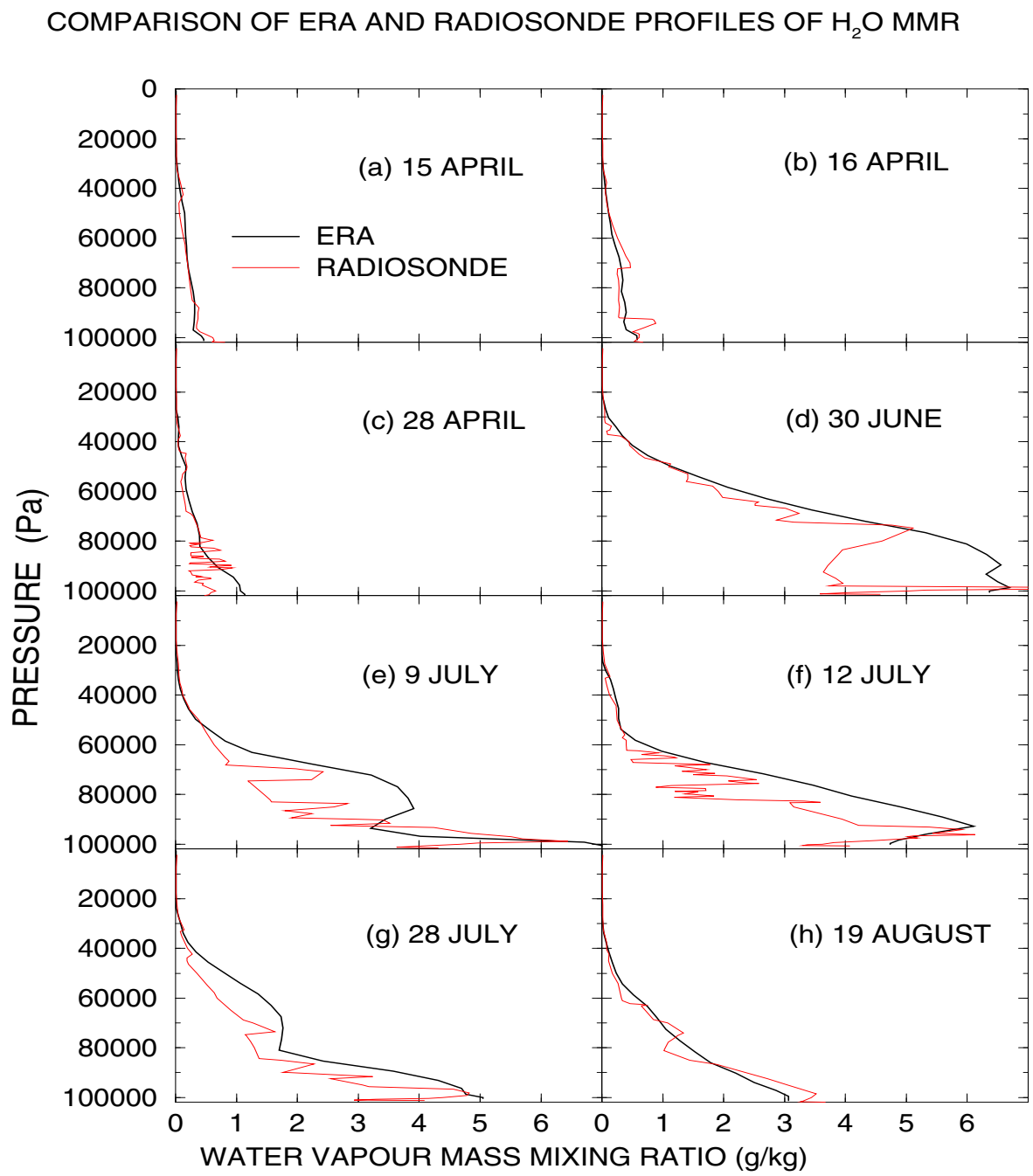


Figure 4.16: *Profiles of water vapour mass mixing ratio from radiosonde ascents over Barrow, Alaska (71.3 °N, 156.6 °W) and from ERA (70 to 72.5 °N, 155 to 157.5 °W). Profiles are for 00z GMT for which the dates correspond.*

Table 4.8: *Surface temperature differences ($\delta T_s$) total column moisture differences ($\delta u$) and clear-sky calculated SDL for eight profiles for ERA and radiosonde ascents at 71.3 °N, 156.6 °W. Differences are for ERA minus radiosonde values. The STAR observed SDL is also shown for the corresponding times and the percentage ERA-radiosonde $SDL_c$ difference that is due to profile column moisture differences is given by $\delta SDL_{\delta u}$.*

| Date (1992) (00z GMT) | $\delta T_s$ $(K)$ | $\delta u$ $(kgm^{-2})$ | ERA SDL $(Wm^{-2})$ | Sonde SDL $(Wm^{-2})$ | STAR SDL $(Wm^{-2})$ | $\delta SDL_{\delta u}$ (%) |
|---|---|---|---|---|---|---|
| 15 April | -4.9 | -0.1 | 158.4 | 163.9 | 170 | 10 |
| 16 April | -1.8 | -0.3 | 165.2 | 168.0 | 170 | 57 |
| 28 April | +6.0 | +0.6 | 178.3 | 163.7 | 171 | 37 |
| 30 June | +0.7 | +5.8 | 294.6 | 276.8 | 271 | 77 |
| 9 July | +4.1 | +4.0 | 282.4 | 261.9 | 260 | 36 |
| 12 July | +2.2 | +4.5 | 268.1 | 253.7 | 252 | 70 |
| 28 July | +2.5 | +3.6 | 260.8 | 248.2 | 252 | 62 |
| 19 August | -2.8 | -0.3 | 230.1 | 235.1 | 243 | 38 |

Firstly it must be noted that differences between radiosonde calculations of $SDL_c$ fall within the observational uncertainty of about 10 $Wm^{-2}$ when compared to STAR observations. However, differences in ERA and radiosonde calculated $SDL_c$ are large in some cases with the $SDL_c$ values calculated from the ERA profiles between 28 April and 28 July showing a positive bias of greater than 10 $Wm^{-2}$ with respect to the radiosonde calculated $SDL_c$. This may be explained by considering that surface temperature and column moisture are greater for the ERA profiles compared to the radiosonde profiles. For the remaining profiles (15 and 16 April and 19 August) ERA $T_s$ and $u$ are less than radiosonde values and consequently ERA calculated $SDL_c$ is less than for the radiosonde profiles. By replacing ERA temperature or moisture profiles with those of the radiosonde observations and on performing further radiative calculations it is found that differences in column moisture amounts explain over two thirds of the calculated $SDL_c$ difference for the 30 June and 12 July profiles. Profile temperature differences explain more than two thirds of the differences for the 15 April profile, while for the remaining profiles, both temperature and column moisture differences contribute significantly to the $SDL_c$ discrepancy. Thus in conclusion, it appears that the ERA positive $SDL_c$ bias in summer months compared to observations may be due to greater total column moisture amounts and surface temperature compared to the observed profiles at times of clear-skies, while a negative bias in winter is explained more by the underestimation of surface temperature and column moisture by ERA. The un-

derestimation of $T_s$ in winter is consistent with the ERA land surface model error discussed by Slingo *et al.* (1998).

## 4.6 Discussion and Conclusions

A simulation of the Earth's clear-sky radiation budget that uses the ECMWF Re-Analysis (ERA) has been developed by Slingo *et al.* (1998) as a tool for understanding the dependence of the clear-sky greenhouse effect on physical variables. It also provides a test for the ability of climate models to correctly simulate seasonal and interannual variability of the clear-sky radiation budget (Slingo (1997)). However, the validation of simulated irradiance with observations is a precursor to their use in such studies. While simulated outgoing longwave irradiance at the top of the atmosphere was validated against satellite observations by Slingo *et al.* (1998), there has been no such evaluation of model irradiance at the surface. The present study, while not validating simulated irradiance at the surface in its entirety, constitutes an attempt at both critically assessing the spatial and temporal variability of simulated irradiance and also identifying possible biases in empirical and observational data sets as well as the simulation itself.

Simulated $\mathrm{SDL}_c$ was compared with semi-empirical formula estimates and in situ observations of $\mathrm{SDL}_c$. The empirical formula allows a global comparison of $\mathrm{SDL}_c$ although relies on ERA to provide parameter specifications so cannot be a completely independent test for the simulation. Observations, while providing such an independent test and allowing a detailed comparison over a high temporal resolution, also suffer from limitations such as high observational uncertainty, lack of information regarding cloud amount and the localised nature of the data. Nevertheless, two stations were selected to test the simulation for two vastly different climatic regimes: the tropical western Pacific and a land based sub-arctic region.

The main conclusions of these comparisons are as follows:

1) The strong dependence of $\mathrm{SDL}_c$ on near-surface temperature and total column moisture demands the accurate estimation of these terms if a robust simulation of $\mathrm{SDL}_c$ is to be attained.

2) The findings of Dutton (1993) are re-emphasised: simulated $\mathrm{SDL}_c$ tends to be greater than observed values for warmer, moister profiles while the reverse is true for drier, colder profiles. This change in $\mathrm{SDL}_c$ difference may be explained in terms of systematic changes in the observational error such as cloud contamination or solar heating of the radiometer. Alternatively, a systematic change in simulation error due, for example, to

the water vapour continuum parameterization, the lack of account for aerosol radiative properties or errors in the ERA temperature and moisture fields may explain this result. Further work is required to decide between these explanations.

3) Much of the tendency for simulated $SDL_c$ to be greater than observed values in the warm, moist tropical western Pacific may be explained by considering the disparity between temperature interpolation used in the simulation and the observed profile of temperature between the surface and the lowest model layer. While the atmosphere immediately above the surface is assumed to have a temperature directly dependent on the surface skin temperature, observations show that this is not the case (e.g. Weller and Anderson (1996)). The observed 2.3 $m$ temperatures are about 1.5 $K$ less than ERA skin temperatures for this site and this discrepancy may account for much of the overestimation of simulated $SDL_c$ compared to the observations.

4) Values of simulated $SDL_c$ that are greater than observed values at the sub-arctic station during the summer may be explained by the apparent overestimation of total column moisture by ERA during times of clear-skies. However, it is proposed that the ERA profiles are at too coarse a temporal resolution to capture brief cloud-free times that are relatively dry compared to average. Similar biases may arise when comparing, for example, time-mean clear-sky filtered irradiance from satellite with climate model estimates (e.g. Cess *et al.* (1992)).

5) The tendency for observed $SDL_c$ to be greater than simulated values during the winter at the sub-arctic station may be explained by underestimations in ERA near surface temperature, total column moisture or both, compared to observations. Alternatively the clear-sky observations are cloud contaminated thus producing unrealistically high $SDL_c$, or simulated $SDL_c$ is underestimated because no account is made for aerosol radiative effects.

6) The semi-empirical formula (Prata (1996)) performs well in reproducing the global distribution of monthly mean $SDL_c$ simulated by CLERA. However, departures from climatological lapse rates of temperature and moisture implicitly assumed in the Prata model produce large discrepancies between estimated and simulated $SDL_c$. Therefore its performance on finer spatial and temporal scales is anticipated to be inadequate. A more recent $SDL_c$ formula (Dilley and O'Brien (1998)) marginally outperforms the Prata formula but this is mainly because the new formula bypasses estimating $u$ from surface conditions.

7) The exploitation of observations of both clear-sky irradiance and meteorological parameters in determining the Prata model make it a valuable technique in assimilating all surface irradiance observations which may highlight biases in the spatial distribution of $SDL_c$. For example, the general overestimation of the Prata model compared to the simulation may be due either to (i) cloud contamination in irradiance observations used to derive the empirical constants, (ii) the lack of account for the longwave radiative effects of

aerosols in the simulation or (iii) incorrect specification of the radiative parameterizations such as the water vapour continuum (e.g. Kilsby *et al.* (1992)).

The general agreement of simulated $SDL_c$ variability with observations over a temporal scale and with a simple formula over spatial scales help to validate the simulation of the Earth's clear-sky longwave radiation budget. Therefore more weight may be ascribed to their testing of climate model variability of the clear-sky radiation budget which is possible on a 6-hourly time scale and 2.5 by 2.5° horizontal grid. However, two points must be made with reference to the comparison of simulated $SDL_c$ with observations. Firstly, at the observational stations considered, there is likely to be a larger input of meteorological data into the ERA assimilation system than in regions containing few observations. Therefore ERA profiles, and consequently also the simulation of $SDL_c$, are anticipated to be less accurate in regions of relatively few observations. A second point relates to the inadequate derivation of clear-sky irradiance observations. Both the shortwave and longwave clear-sky filtering techniques suffer from severe limitations (e.g. Dutton (1993)) and need, at the very least, to be validated against or used in conjunction with comprehensive observations of cloud amount and type at the surface. This clearly shows the need to measure independently the cloud cover and use this to accomplish the clear-sky sampling at the surface.

The observational comparisons of the present study imply that the SDL variability is significantly less than surface shortwave irradiance variability in the tropics. However, over the time scales relevant to climate change the $SDL_c$ is likely to become relatively much more important in influencing the surface energy budget (e.g. Schneider *et al.* (1997b)). Thus there is a need to accurately represent this parameter and its variability. To obtain a much more accurate representation of the surface radiation budget, comprehensive observations of cloud amount, near surface temperature and total column moisture are required at the surface in conjunction with accurate in situ irradiance observations.

# Chapter 5

# THE SIMULATED DEPENDENCE OF THE EARTH'S CLEAR-SKY RADIATION BUDGET ON TEMPERATURE AND HUMIDITY

## 5.1 Introduction

Outgoing longwave radiation to space (OLR) is the fundamental cooling mechanism of the Earth-atmosphere system. Knowledge of its dependence on surface and atmospheric parameters is therefore required for a quantitative understanding of the climate and climate change. The response of the climate system to a change in the Earth's radiation budget is made more complex by feedbacks, one of which involves a change in water vapour amount and distribution in response to a change in surface temperature, $T_s$. Water vapour is generally regarded to provide a positive feedback with climate models implying an amplification of surface warming of about 1.6 (e.g. IPCC (1990)).

Raval and Ramanathan (1989) used satellite Earth Radiation Budget Experiment (ERBE) observations of clear-sky OLR ($OLR_c$) to argue in favour of a positive water vapour feedback, by showing an increase in normalised atmospheric greenhouse trapping with spatially increasing $T_s$. However, spatial variations cannot be used reliably to infer water vapour

changes in a warming climate; Spencer and Braswell (1997) argued that a positive feedback will always apply spatially between the ascending and descending branches of the tropical circulation systems. Rind *et al.* (1991) showed satellite-derived water vapour amounts to increase with the greater convection associated with hemispheric warming over the seasonal cycle. They conclude that the quantitative agreement with climate model predictions strengthens the argument in favour of a positive water vapour feedback. Ramanathan and Collins (1991) infered a positive feedback spatially and over short time-scales such as the seasonal cycle and the El Niño/Southern Oscillation (ENSO). However, Lau *et al.* (1996) asserted that it is not prudent to assume that feedbacks operating over these time-scales are relevant for climate change on decadal time-scales unless entire circulation systems are accounted for. Soden (1997) examined the change in the atmospheric greenhouse effect over the ENSO cycle, and pointed out that infered sensitivities are highly dependent on which particular months are analysed. Thus it is more informative to relate $\mathrm{OLR}_c$ to surface and atmospheric parameters using an array of monthly means.

Bony *et al.* (1995) infered the sensitivity of ERBE $\mathrm{OLR}_c$ to $T_s$ using the monthly-means of 1987 and 1988 and related this to the column moisture variation associated with changes in temperature, temperature lapse rate and relative humidity, $RH$. Results were compared with climate model experiments over seasonal and interannual time-scales. The difference between the sensitivity of $\mathrm{OLR}_c$ to $T_s$ over different time-scales and between the ERBE and climate model warming experiments was attributed to changes in temperature lapse rate and $RH$. Raval *et al.* (1994) also noted the strong seasonal correlation between ERBE OLR and column mean $RH$ for both clear and cloudy skies over the tropical oceans. Slingo and Webb (1997) showed that $RH$ in the upper troposphere describes much of the variation in $\mathrm{OLR}_c$ in the water vapour absorption bands and related this to radiative transfer theory. The relationship between upper tropospheric $RH$ ($UTH$), deep convection frequency and the normalised clear-sky atmospheric greenhouse trapping was examined by Soden and Fu (1995). From the correlation, they inferred that variations in $UTH$ explain about half of the deviation of normalised greenhouse trapping from its climatological mean, with the remainder being tentatively explained by variations in the temperature lapse rate and moisture at lower levels. Sinha and Harries (1997) showed that while $\mathrm{OLR}_c$ is most sensitive to upper tropospheric $RH$, changes in $RH$ in the middle troposphere are largest. The prime motivation of the present study is to extend this earlier work by using a simulation of $\mathrm{OLR}_c$ based on 15 years of data. The longer period of analyses, than earlier studies, allows a more robust characterisation of the variability; and the use of a model to simulate $\mathrm{OLR}_c$ allows the causes of the variability to be more clearly identified than is possible using statistical analyses, where relationships between variables may not adequately imply a direct causal

link.

Another focus for this study is to examine the occurrence of the super-greenhouse effect (SGE; e.g. Hallberg and Inamdar (1993)). This describes an apparently unstable clear-sky longwave radiative feedback operating at high sea surface temperatures whereby $OLR_c$ is anti-correlated with $T_s$. The feedback is thought to apply at the surface (e.g. Inamdar and Ramanathan (1994)). An additional process must operate to stabilise tropical sea surface temperatures; suggested mechanisms are short-wave cloud radiative forcing (Ramanathan and Collins (1991)), evaporative feedbacks (Hartmann and Michelsen (1993)) and heat export to the extra-tropics (Pierrehumbert (1995)). Bony *et al.* (1997b) explain the occurrence of the SGE by considering the changes in convective regime associated with the large-scale circulation over the seasonal and interannual time-scale.

The present study uses the CLERA simulation of the Earth's clear-sky longwave radiation budget, described in Chapter 2, to assess the impact of changes in temperature and humidity throughout the atmosphere on $OLR_c$. Recall that the simulation uses the ECMWF Reanalysis (ERA) which benefits from the consistent analysis system used to assimilate both conventional and satellite-based observational data. Slingo *et al.* (1998) showed the quality of the simulation by comparing $OLR_c$ with that from ERBE. The present study benefits from a sufficiently long data set (1979-1993) to allow climate fluctuations on a longer time-scale than the ERBE period to be resolved, and includes several ENSO events. Land and oceans are sampled, thus ensuring global coverage of clear-sky irradiance and sampling of the entire atmospheric circulation system. Thus the sensitivity of $OLR_c$ to surface and atmospheric parameters may be calculated in a global-mean sense. The framework of interpretation of the present analysis was set out in Chapter 3. Results are described in Sec. 5.2 and 5.3. Discussion with reference to the SGE and the water vapour feedback are presented in the final section.

## 5.2 Regression Studies

Using the monthly-mean CLERA irradiance in conjunction with the ERA data, the sensitivity and degree of correlation of irradiance quantities with atmospheric and surface parameters were computed. The least squares fit (LSQF) technique (e.g. Freund (1976)) was employed using the 12 months of the seasonal cycle or the 15 year interannual time-scale for a particular month. A correlation coefficient ($r$) of greater than 0.75 or less than -0.75 is required for a significant correlation at the 99.5% confidence level for the smallest sample size used (12 months).

### 5.2.1 The super-greenhouse effect

The SGE was first defined by Vonder Haar (1986) as a potentially unstable longwave radiative feedback at the surface. Essentially increases in $T_s$ are accompanied by decreases in the longwave cooling (i.e. positive $dF_{net}/dT_s$ where $F_{net}$ is the clear-sky net downward longwave irradiance at the surface). A SGE was also identified at the top of the atmosphere (e.g. Ramanathan and Collins (1991)) in which $dOLR_c/dT_s$ is negative. In this situation the surface-atmospheric column is less able to cool to space via clear-sky longwave radiation and thus provides, when considered in isolation from additional feedbacks, an unstable heating of this column. The feedback was shown to apply at the ocean surface (e.g. Lubin (1994)); although the atmosphere is less able to cool to space over warmer tropical regions, it more readily cools to the surface, with $\mathrm{SDL}_c$ increasing substantially with $T_s$ (Inamdar and Ramanathan (1994)). However, additional feedbacks must be present to counteract this effect and avoid a runaway warming effect over the tropical oceans (e.g. Pierrehumbert (1995)).

Figure 5.1 shows the regression correlation for $\mathrm{OLR}_c$ and $T_s$ calculated over the seasonal cycle for 1985. There is a strong positive correlation between $\mathrm{OLR}_c$ and $T_s$ for latitudes pole-wards of about $\pm 30°$. In the tropics the correlation tends to be negative, showing that changes in atmospheric structure act to counteract the direct $\Delta T_s$ contribution to changing $\mathrm{OLR}_c$. In these regions, simulated $\mathrm{OLR}_c$ decreases with increasing $T_s$, constituting a SGE. Over high latitude oceans, changes in atmospheric temperature act to amplify the sensitivity of $\mathrm{OLR}_c$ to $T_s$ (e.g. Webb *et al.* (1993)); $\mathrm{OLR}_c$ changes are greater than changes in surface emission due to large increases in the atmospheric component of $\mathrm{OLR}_c$ ($\mathrm{OLR}_a$) with increased $T_s$. In this situation the parameter, $\alpha$ in Eq. 3.7, is large because atmospheric temperatures are changing at a greater rate than $T_s$. The relationship between $\mathrm{OLR}_c$ and $T_s$ over the seasonal cycle of other years is similar to that of 1985.

Over the interannual time-scale for July (Fig. 5.1(b)) a SGE at high $T_s$ is still present. These regions are confined to the tropical oceans and are less coherent than for the seasonal cycle. Strong positive correlation is confined mainly to land areas of latitude greater than about 45° where changes in $T_s$ are greatest and convection strongly couples atmospheric and surface temperatures thus increasing $\alpha$. The simulated sensitivities are between about 1 and 3 $Wm^{-2}K^{-1}$ away from the tropical oceans and are negative over the tropical oceans; this is consistent with Bony *et al.* (1995) who used ERBE data from 1987 to 1989 and a climate model applied to seasonal and interannual time-scales. Applying the LSQF analysis to interannual time-scales for months other than July results in similar sensitivities of $\mathrm{OLR}_c$ to $T_s$, although regions exhibiting a SGE vary slightly in latitude.

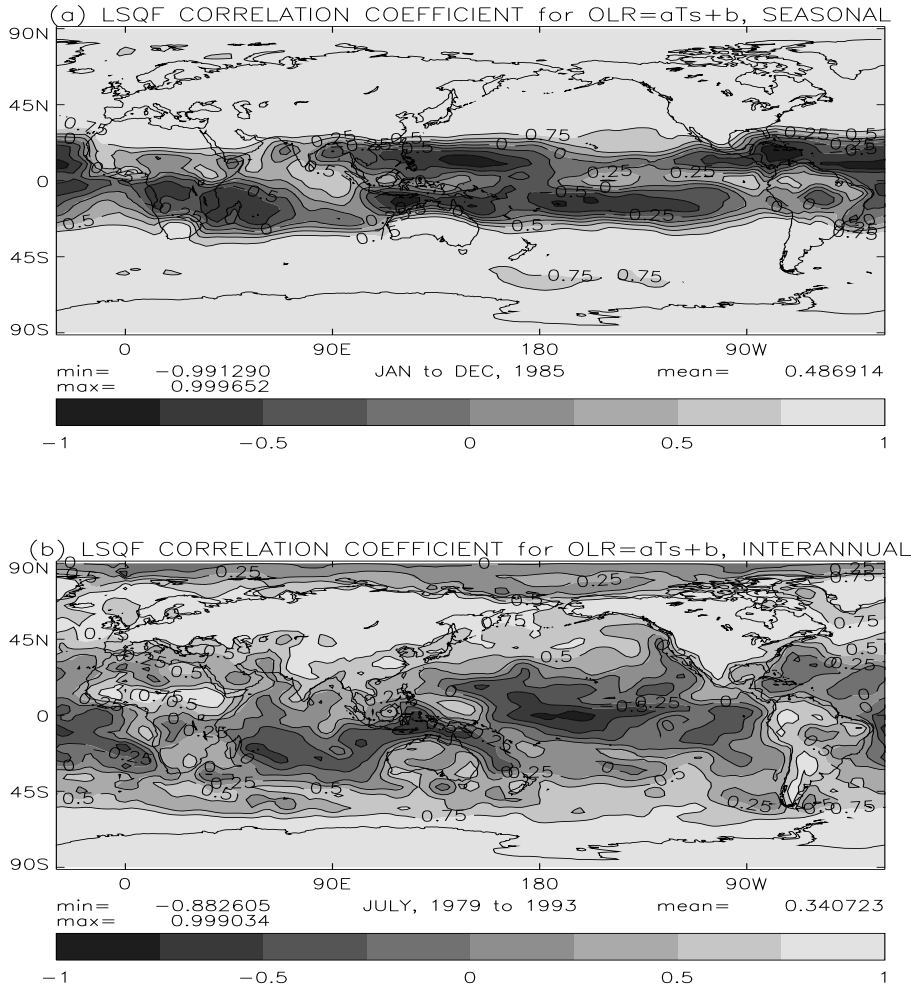


Figure 5.1: *LSQF correlation coefficient for* $OLR_c = aT_s + b$ *using the CLERA simulation over (a) the seasonal cycle for 1985 and (b) the interannual time-scale for July. The contour interval is 0.25.*

The regions exhibiting a SGE are consistent with the results of Bony *et al.* (1997b) who utilised ERBE $OLR_c$ from 1985 to 1989 and may be explained by considering the changes in the large-scale circulation. Over the seasonal cycle (Fig. 5.1(a)), regions exhibiting a SGE are generally situated within the 5 to 15° latitudinal zones either side of the equator. The change in convective regime related to the north-south shift of the Hadley Cell over the seasonal cycle is larger in these regions than at the equator and forces large changes in $RH$ which decouple the $OLR_c$ from surface emission. Over the interannual time-scale, the shift in the Hadley circulation is small, although a residual SGE signal is present over the Atlantic and Indian oceans. The strongest SGE signal is evident in the tropical central Pacific, due to shifts in the Walker circulation associated with ENSO events.

The sensitivity of $OLR_c$ to changes in $T_s$ are now explained in terms of atmospheric temperature and moisture variability. Fig. 5.2 displays the calculated sensitivity of ERA atmospheric parameters and CLERA irradiance quantities to changes in $T_s$ over ocean regions between 60° S and 60° N. The variability about the mean value of each $T_s$ bin is characterised by the standard deviation which is plotted either above or below each curve as a vertical error bar. The calculations are applied to the seasonal cycle of 1985 (solid line) and the interannual time-scale for July (dashed line). Column moisture generally increases with rising $T_s$ (Fig. 5.2(a)). The sensitivity is significantly larger over the seasonal cycle than over the interannual time-scale. This is partially explained by considering the changes in atmospheric temperature with $T_s$ over both time-scales (Fig. 5.2(b)): the 450 $hPa$ temperature increases at a greater rate than $T_s$ over the seasonal cycle but at a lesser rate than $T_s$ over the interannual time-scale. Because a warmer atmosphere potentially holds more water vapour, the large changes in atmospheric temperature over the seasonal cycle provide a thermodynamic explanation for the large changes in atmospheric moisture. At high $T_s$ the changes in column moisture are not explained entirely by thermodynamics because atmospheric temperature changes only fractionally with $T_s$ over both time-scales. The changes in column moisture in the deep tropics are rather explained by changes in $RH$ which increases with $T_s$ over the interannual time-scale and to an even greater extent over the seasonal cycle for high $T_s$ (Fig. 5.2(c)).

The increased atmospheric moisture and the small changes in atmospheric temperature with $T_s$ explain the negative $dOLR_c/dT_s$ at high $T_s$ in Fig. 5.2(d) and therefore explain the SGE. This conclusion was also arrived at by Bony *et al.* (1995). $dOLR_c/dT_s$ is more negative over the seasonal cycle than the interannual time-scale at $T_s > 295K$ because $RH$ changes are larger over the seasonal cycle than over the interannual time-scale. At higher latitudes, the $OLR_c$ sensitivity to $T_s$ is more positive over the seasonal cycle compared to the interannual values. This is explained by the large increases in $OLR_a$ due to substantial atmospheric temperature increases with surface warming over the seasonal cycle, which is less marked over the interannual time-scale. This has been previously noted, for example by Webb *et al.* (1993).

Over the seasonal cycle, a strong SGE at the surface applies to most ocean grid points as denoted by positive $dF_{net}/dT_s$ in Fig. 5.2(e). A surface SGE mainly affects the warmest regions ($T_s > 295K$) over the interannual time-scale where the $SDL_c$ is increasing at a greater rate than the surface emission. The large increases in $SDL_c$ are a product of the significant increases in column moisture with $T_s$ that in turn induce a quadratic increase in water vapour continuum emission as described in Chapter 3. While thermodynamics can

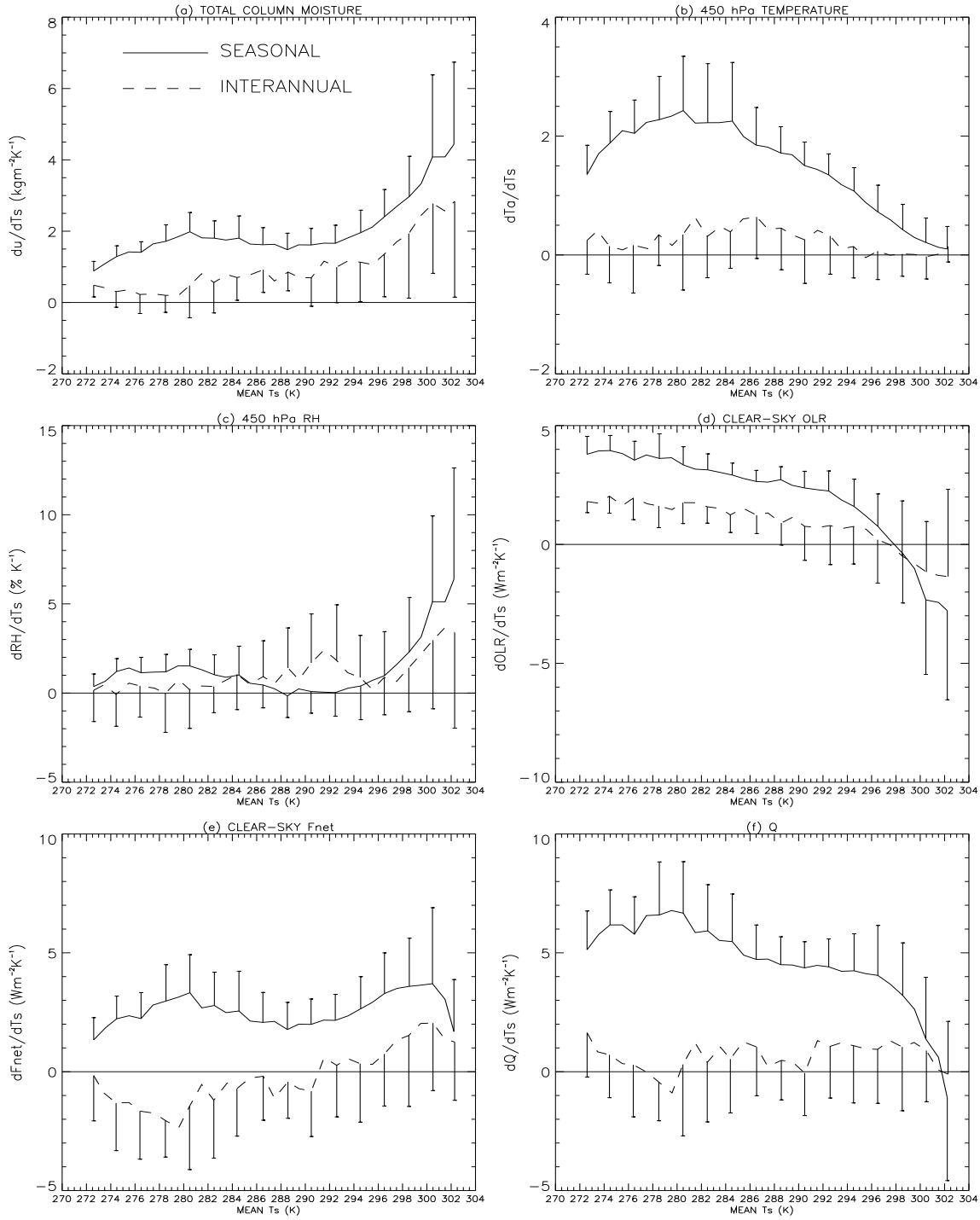


Figure 5.2: *LSQF calculated sensitivity of (a) ERA total column moisture, (b) ERA 500 hPa Temperature, (c) ERA 500 hPa RH, (d) CLERA $OLR_c$, (e) CLERA $F_{net}$ and (f) CLERA clear-sky column radiative divergence, Q, to changes in $T_s$. The seasonal cycle of 1985 (solid line) and the the interannual time-scale for July (dashed line) are presented. Ocean regions between 60 °S and 60 °N only are considered and the calculated sensitivity is averaged in 2 K sea surface temperature bins. Vertical bars denote one standard deviation from the mean value of the bin and are plotted above or below each lines to enhance clarity.*

explain the SGE at the surface over the seasonal cycle for most ocean regions, this appears not to be the case over the interannual time-scale. At high latitudes the small increases in atmospheric temperatures and therefore relatively small thermodynamic increases in column moisture with rising $T_s$ result in a negative $dF_{net}/dT_s$. At low latitudes, although a surface SGE is identified, the changes in column moisture are primarily explained by variation in $RH$ with $T_s$ and therefore are not thermodynamically induced.

The increase in cooling of the atmosphere to the surface with increased $T_s$ generally causes atmospheric column cooling (Q) to increase with increased $T_s$, despite the diminished cooling to space at higher $T_s$ (Fig. 5.2(f)). However, at the highest $T_s$ bin over the seasonal cycle, the rapid decrease in $\mathrm{OLR}_c$ with $T_s$ results in negative $dQ/dT_s$ despite the increased cooling to the surface. Thus the conclusions of Inamdar and Ramanathan (1994), that the SGE is manifest as an unstable feedback at the surface rather than in the atmosphere, does not hold for some tropical regions over the seasonal cycle. Changes in column heating with $T_s$ are small over the interannual time-scale. Investigating the profile dependence of clear-sky longwave cooling rates on $T_s$ will be subject to further investigation elsewhere.

### 5.2.2 The Dependence of clear-sky OLR on Tropospheric Relative Humidity

Increasing $RH$ acts to decrease the surface component of the $\mathrm{OLR}_c$ by decreasing $Tr$ in Eq. 3.7 and effectively shifts the height of atmospheric longwave emission to space up to a colder level thus decreasing $\mathrm{OLR}_a$. As absorption bands are radiatively less saturated with decreasing humidity, the sensitivity of $\mathrm{OLR}_c$ to $RH$ is most negative for drier profiles and also for changes in $RH$ in the relatively dry upper troposphere. This is complicated by the absorption properties of the water vapour continuum (e.g. Clough *et al.* (1992)) which, in the moister profiles, acts to decrease the surface component of the $\mathrm{OLR}_c$ with increased $RH$ in the lower troposphere.

To illustrate this point the narrow-band model was applied to the tropical standard profile which has $RH$ set to 40% between 100 and 1000 $hPa$. The changes in $\mathrm{OLR}_c$ are plotted as a function of wavenumber in Fig. 5.3 for specified uniform changes in $RH$ between 100 and 1000 $hPa$. In the major water vapour bands (approximately wavenumbers less than 600 $cm^{-1}$ and greater than 1200 $cm^{-1}$), absolute changes in $\mathrm{OLR}_c$ are greater for a given decrease in $RH$ than for the same magnitude *increase* in $RH$ confirming the non-linear increase in $\mathrm{OLR}_c$ with decreasing $RH$. In the window region of the spectrum (approximately 800 to 1200 $cm^{-1}$) there is an approximately linear negative dependence of $\mathrm{OLR}_c$ on $RH$. As was shown in Chapter 2, the water vapour bands vary in their degree of satura-

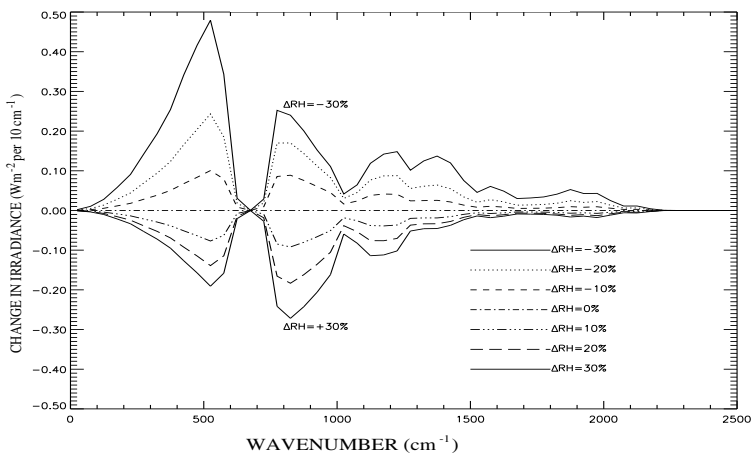


Figure 5.3: *Narrow band model calculated spectral changes in clear-sky OLR as a function of wavenumber ($cm^{-1}$) with uniform RH changes between 100 and 1000 hPa for a tropical standard profile with the RH set initially at 40%. Irradiance changes are averaged over 50 $cm^{-1}$ spectral intervals.*

tion, so the altitude of maximum contribution to $\mathrm{OLR}_c$ varies throughout the upper and middle troposphere (i.e. about 100 to 800 $hPa$) depending on wavenumber. Because continuum absorption in the window region mainly acts in the lower troposphere (i.e. pressures greater than about 600 $hPa$), $RH$ variations throughout the atmosphere are significant in determining $\mathrm{OLR}_c$. This is consistent with the findings of Shine and Sinha (1991). The strong contribution to the changes in $\mathrm{OLR}_c$ from wavenumbers less than about 600 $cm^{-1}$ is apparent when humidity is low; this is consistent with Sinha and Harries (1995).

Considering Eq. 3.7, a $TRH$ parameter that adequately describes variations in $\mathrm{OLR}_c$ must account for the changes in $RH$ in the regions of the atmosphere that are most important in determining $\mathrm{OLR}_c$ variability. The dependence of $\mathrm{OLR}_c$ on changes of $RH$ ($\Delta OLR_{\Delta RH}$) may be written as a function of its sensitivity to $RH$ at pressure, $p$, and the change in $RH(p)$:

$$\Delta OLR_{\Delta RH} = \frac{\partial OLR}{\partial RH(p)} \Delta RH(p). \tag{5.1}$$

Figure 5.4(a) characterises the ERA $RH$ variability by calculating its standard deviation at each sigma level for the monthly-means of July (1979 to 1993) between 40° N and 40° S (solid line). The $\partial OLR/\partial RH(p)$ term is provided by the narrow band scheme applied to a tropical standard atmosphere for 1% increases in $RH$ (Fig. 5.4(b)). While $\mathrm{OLR}_c$ is most sensitive to $RH$ in the upper troposphere (about 250 $hPa$), variations in ERA $RH$ are greatest in the middle and lower troposphere (about 600 to 800 $hPa$). Therefore the inferred $\mathrm{OLR}_c$ variation due to ERA $\Delta RH(p)$, from Eq. 5.1, is greatest between about 200 to 850 $hPa$ with contribution from the entire troposphere (Fig. 5.4(c), solid line). The calculated $\mathrm{OLR}_c$

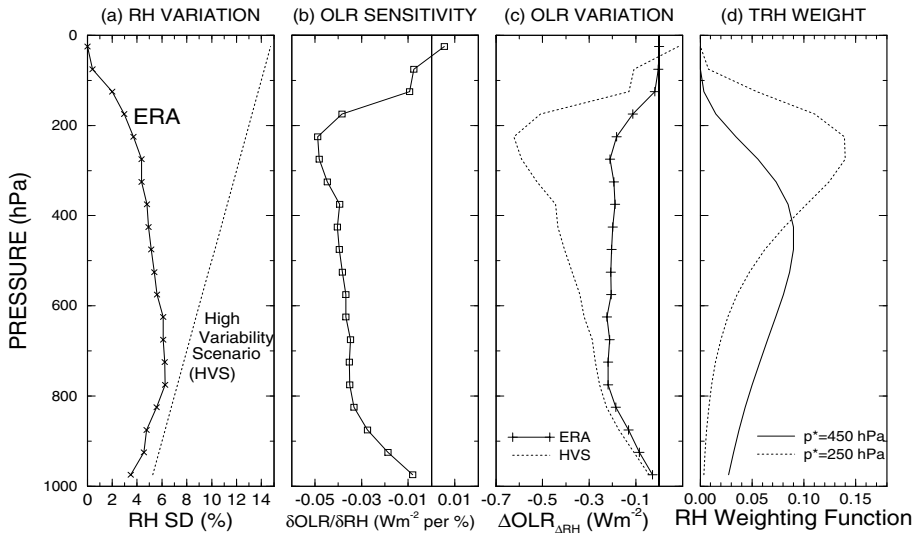


Figure 5.4: *The importance of height dependent RH variations on clear-sky OLR variability: (a) 40 °S to 40 °N mean ERA RH Standard Deviation with pressure for the 15 monthly-mean July's of the ERA period (solid line) and a 'high variability scenario' (HVS) RH standard deviation (dotted line), (b) narrow band calculated sensitivity of clear-sky OLR to height dependent 50 hPa slab changes in RH for the tropical standard atmosphere, (c) inferred variation of $OLR_c$ due to ERA RH variations (solid line) and for the HVS RH variations (dotted line) and (d) weighting functions applied to RH for evenly spaced 50hPa vertical slabs that are used to calculate TRH for p*=450 hPa and p*=250 hPa (Eq. 5.2).*

variation assumes that ERA provides a good representation of the true $RH$ variability. In reality, there is significant uncertainty attached to the humidity throughout the atmosphere, especially at higher altitudes (e.g. McNally and Vesperini (1996)). Therefore estimates of $RH$ interannual variability must be received with caution. A further calculation was performed whereby $RH$ standard deviation was assumed to increase linearly from 5% at 1000 $hPa$ to 15% at the top of the atmosphere (Fig. 5.4(a), dotted line). This 'high variability scenario' (HVS) assumes ERA humidity variability to be underestimated with the largest underestimation at high altitudes. By calculating the resulting $\mathrm{OLR}_c$ variability (dotted line, Fig. 5.4(c)), the potential impact of the uncertainty in $RH$ variability at higher altitudes is illustrated. The maximum $\mathrm{OLR}_c$ variability due to $RH$ variations is at about 250 $hPa$, but with significant contribution to the $\mathrm{OLR}_c$ variability from $RH$ variations at lower altitudes. It is seen that the upper troposphere has the *potential* to affect the $\mathrm{OLR}_c$ variability to a greater extent than lower levels if ERA humidity variation in the upper troposphere is underestimated. This caveat should be considered when using the ERA humidity in studies such as the present one and thus highlights the need for further work in addressing this uncertainty. Such data sets are becoming available (e.g. Chiou *et al.* (1997), Gierens *et al.* (1997), Jackson *et al.* (1998), Chaboureau *et al.* (1998)) but the validation of

ERA humidity is beyond the scope of the present study.

Soden and Fu (1995) used satellite retrievals of UTH (approximately 200 to 500 $hPa$ $RH$) to show that the clear-sky normalised atmospheric greenhouse effect is strongly correlated with upper tropospheric $RH$, although they note that the lapse rate and lower tropospheric moisture may explain about half of this dependence. CLERA monthly-mean $OLR_c$ also shows a strong negative correlation with upper tropospheric $RH$ in the tropics (not shown). Considering the importance of $RH$ variations over the entire troposphere shown in Fig. 5.4, some of the correlation between upper tropospheric $RH$ and $OLR_c$ may be due to a coupling between $RH$ in the upper troposphere and $RH$ at lower altitudes.

Taking the results of Fig. 5.4 into account, the parameter $TRH$ is defined to account for $RH$ throughout the troposphere, but to apply maximum weight to the mid-troposphere:

$$TRH = \frac{\sum_{i=1}^{31} exp(-2(ln(p_i) - ln(p^*))^2) RH(p_i) \Delta p_i}{\sum_{i=1}^{31} exp(-2(ln(p_i) - ln(p^*))^2) \Delta p_i}, \tag{5.2}$$

where $i$ denotes sigma level and $p^*$ is the pressure at which maximum weight is prescribed to $RH$. The weighting function is plotted in Fig. 5.4(d) for evenly spaced 50 $hPa$ thick slabs for $p^*$=450 $hPa$ and $p^*$=250 $hPa$. A Gaussian form is chosen so as not to exclude entirely the $RH$ variations in the regions of the atmosphere less important to the determination of $OLR_c$. This is also more consistent with the form of the satellite derived upper tropospheric $RH$ weighting function used by Soden and Fu (1995) than taking a column mean $RH$. It was decided to calculate $TRH$ using $p^*$=450 $hPa$ so as not to exclude the contribution of $RH$ variation in the lower troposphere to changes in $OLR_c$ variability. Although there is significant uncertainty with regard to $RH$ variability in the upper troposphere and stratosphere, the low weight prescribed to pressures less than 150 $hPa$ is still valid given that $OLR_c$ is relatively insensitive to changes in $RH$ at these levels (Fig. 5.4(b)). The calculated mean July $TRH$ from 1979 to 1993 is plotted in Fig. 5.5. The dry descending regions of the sub-tropics are highlighted by $TRH$ of below about 30%, while the ascending regions of the tropical warm pool and the Asian Monsoon as well as over central Africa are characterised by high $TRH$ of above 60%.

There is a strong negative correlation between $OLR_c$ and $TRH$ over the seasonal cycle of 1985 within about 30° of the equator (Fig. 5.6(a)). Away from the tropics, the correlation is smaller and tends to be positive which implies that changes in other parameters are influencing $OLR_c$ changes. The region of strong negative correlation over the interannual time-scale for July extends up to 45° away from the equator and the global average correlation coefficient is -0.7 (Fig. 5.6(b)). $TRH$ explains more of the variance in $OLR_c$ over

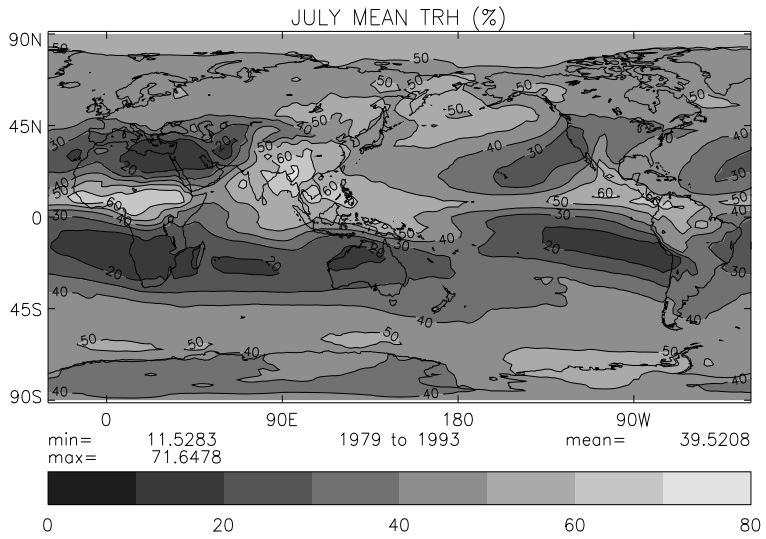


Figure 5.5: *Calculated July mean TRH (%) for the ERA period. The contour interval is 10%.*

the interannual time-scale than over the seasonal cycle because temperature fluctuations are smaller from year to year than over a season. The correlation distribution is similar when setting $p^*$ to 250 $hPa$ (not shown). Comparing Fig. 5.6 and Fig. 5.1 it is apparent that $TRH$ explains most of the $\mathrm{OLR}_c$ variations at low latitudes while $T_s$ is important in explaining $\mathrm{OLR}_c$ variations at high latitudes.

Figure 5.7 shows the July $\mathrm{OLR}_c$ sensitivity to $TRH$ ($dOLR_c/dTRH$) with mean $TRH$ for grid points where correlation is significant at the 99.5% significance level. The corresponding values calculated by the narrow-band scheme when $RH$ between 100 and 1000 $hPa$ is varied in the tropical standard profile are also plotted (solid line). The scatter of points about the narrow band calculated sensitivity are likely to be the result of $\mathrm{OLR}_c$ sensitivity to temperature variations. The $TRH$ parameter also cannot capture the changes in $RH$ throughout the atmosphere, introducing an additional source of error. Nevertheless, the simulation captures the tendency for $dOLR_c/dTRH$ to be most negative in the regions with the lowest mean $TRH$ because the water vapour absorption bands are saturating with increasing $RH$ (Fig. 5.3). The increased sensitivity of $\mathrm{OLR}_c$ to $TRH$ for the drier descending regions of low $TRH$ highlighted in Fig. 5.5 are important with regard to the water vapour feedback for two further reasons: (a) The dry descending regions contain a high proportion of clear-skies and cover large areas of the tropics and, (b) radiative processes in these regions significantly affect the total heating.

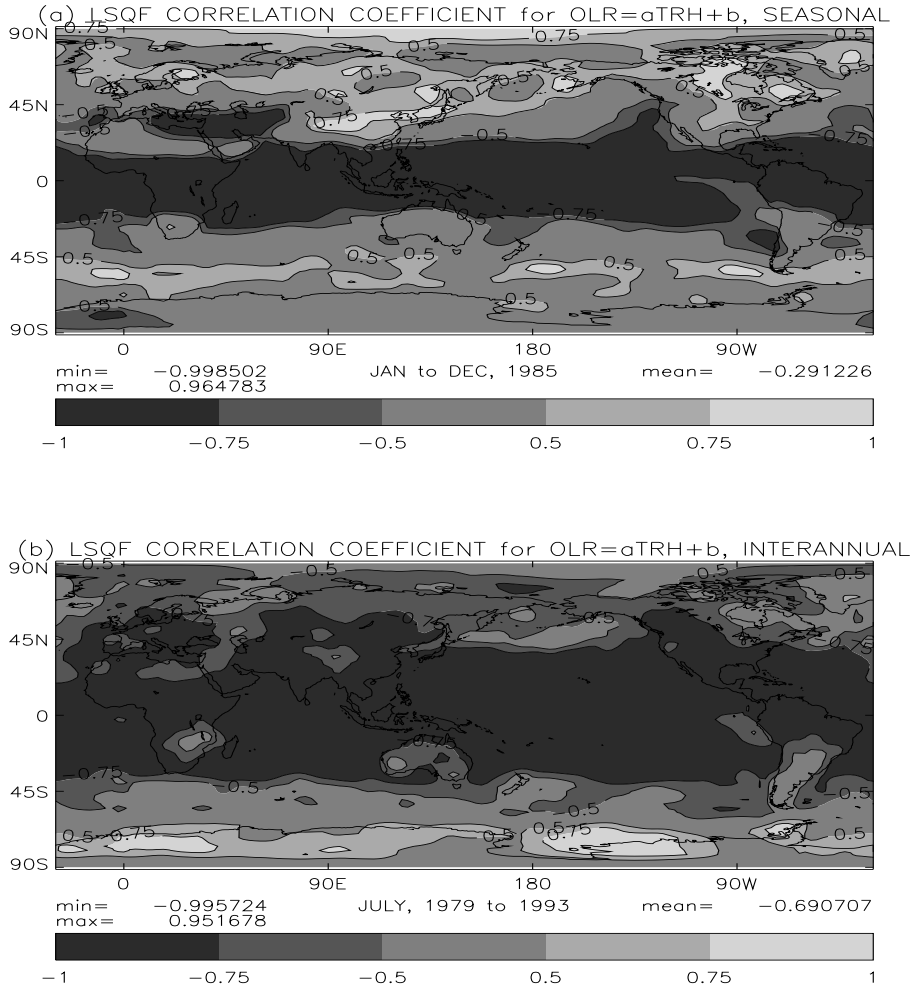


Figure 5.6: *LSQF correlation coefficient for* $OLR_c = aTRH + b$ *from CLERA over (a) the seasonal cycle of 1985 and (b) for July over the ERA period.*

## 5.3 Height Dependent Variation of Relative Humidity and clear-sky OLR

While Sec. 5.2.2 highlights the strong negative correlation between $TRH$ and $\mathrm{OLR}_c$, further experiments are necessary to quantify the effects of $RH$ variation throughout the atmosphere. For this purpose, 5 additional experiments were undertaken whereby monthly-mean $\mathrm{OLR}_c$ was calculated by the CLERA system using the 15 monthly-mean July fields from ERA. This differs from the reference version of CLERA used in the previous section which accumulated the monthly-mean $\mathrm{OLR}_c$ from values calculated every 6-hours. To assess the affect of $RH$ variations on the $\mathrm{OLR}_c$, a control experiment was run using the 15 monthly-mean ERA fields. Perturbation experiments were subsequently run in which specific humidity was varied with ERA temperature to conserve ERA 15 year July mean

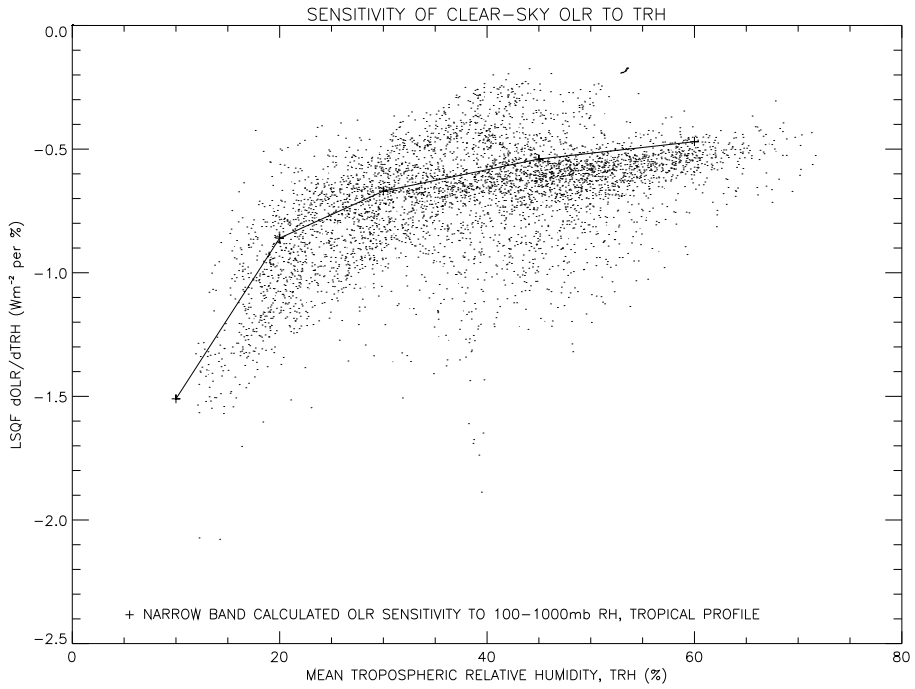


Figure 5.7: *LSQF sensitivity of clear-sky OLR calculated by CLERA to changes in TRH ($Wm^{-2}$ per %) with mean TRH for July, 1979 to 1993. Only grid points of significant correlation above the 99.5 % level are plotted. The solid line denotes the corresponding narrow band calculated sensitivities when RH is varied between 100 and 1000 hPa for the tropical profile.*

*RH* at each grid point at specified sigma ($\sigma$) levels as defined in Table 5.1. The experiments are described as follows:

CTRh - Reference version of the CLERA simulation which used 6-hourly fields to construct monthly-mean irradiance and allowed *RH* to vary throughout the atmosphere.

CTRm - Control experiment in which *RH* was allowed to vary throughout the atmosphere. The only difference from CTRh is that monthly-mean input was used.

CONRH - *RH* was prescribed throughout the atmosphere by the 15 year July mean value.

UTRH - *RH* was allowed to vary only in the upper troposphere (see Table 1).

MTRH - *RH* was allowed to vary only in the middle troposphere (see Table 1).

LTRH - *RH* was allowed to vary only in the lower troposphere (see Table 1).

Note that the labels are used for convenience and are most appropriate for the tropical troposphere; in the extra-tropics, much of what is labelled as "upper troposphere" lies in the lower stratosphere.

Table 5.1: *Description of the 5 experiments using the CLERA simulation that calculate July monthly-mean $OLR_c$ for the 15 years of the ERA period using monthly-mean ERA profiles of $T$ and $q$.*

| **Experiment** | **$\sigma$-levels** | **q($\sigma$)** | **Approximate pressure levels between which $RH$ varies** |
|---|---|---|---|
| CTRm | 1 to 31 | ERA | ALL |
| CONRH | 1 to 31 | $0.01\overline{RH(\sigma)}q_s(T(\sigma))$ | NONE |
| UTRH | 5 to 14 | ERA | 100 to 400 $hPa$ |
| | $5> \sigma >14$ | $0.01\overline{RH(\sigma)}q_s(T(\sigma))$ | (Upper Troposphere) |
| MTRH | 15 to 21 | ERA | 400 to 700 $hPa$ |
| | $15> \sigma >21$ | $0.01\overline{RH(\sigma)}q_s(T(\sigma))$ | (Middle Troposphere) |
| LTRH | 22 to 29 | ERA | 700 to 1000 $hPa$ |
| | $22> \sigma >29$ | $0.01\overline{RH(\sigma)}q_s(T(\sigma))$ | (Lower Troposphere) |

Where $RH$ is held constant, the specific humidity ($q$) is calculated as:

$$q(\sigma) = 0.01\overline{RH(\sigma)}q_s(T(\sigma)), \tag{5.3}$$

where $\sigma$ denotes sigma-level height coordinate, $\overline{RH(\sigma)}$ denotes the calculated 15 year July mean $RH$ at a given level and $q_s(T(\sigma))$ denotes the saturation specific humidity for the ERA temperature of each level using an empirical form of the Clausius Clapeyron equation. At levels where $RH$ is allowed to vary, ERA monthly-mean $q(\sigma)$ for the given year is used. Because of the non-linear dependence of $OLR_c$ on $q$ and $T$, the global-mean $OLR_c$ from monthly-mean profiles (CTRm) is 1.8 $Wm^{-2}$ less than the corresponding value for the reference version of CLERA which used 6 hourly calculations (CTRh) as shown in Table 2. Experiment CTRm was thus necessary to ensure consistency between perturbation and control experiments.

### 5.3.1 Global-mean clear-sky OLR variability

The variability of the simulated $OLR_c$ can be characterised by its standard deviation ($SD_{OLR}$) for the 15 years. Table 5.2 shows that the global-mean standard deviation from CTRm is almost identical to that from CTRh, indicating that using monthly-mean input does not affect the interannual variability. However, the global mean standard deviation for CONRH, where $RH$ is constant, is roughly half that of CTRm in which $RH$ varies. Where

$RH$ is allowed to vary only in the upper, middle or lower troposphere, the standard deviation of $\mathrm{OLR}_c$ is larger than for experiment CONRH showing that $RH$ variations throughout the troposphere affect the global-mean $\mathrm{OLR}_c$ variability. For these three experiments, the $\mathrm{OLR}_c$ standard deviation for MTRH is the greatest and LTRH gives the lowest value. Therefore the order of importance for global variation in $\mathrm{OLR}_c$ due to tropospheric $RH$ variations is the middle, upper and then lower troposphere.

The correlation between *global-mean* $\mathrm{OLR}_c$ and $T_s$ is not significant at the 99.5 % level for experiment CTRh and CTRm. However, when $RH$ is not allowed to vary (CONRH), a strong positive correlation of 0.85 is calculated with global-mean $\mathrm{OLR}_c$ increasing at the rate of 2.3 $Wm^{-2}K^{-1}$. Changes in $RH$ act to mask the dependence of $\mathrm{OLR}_c$ on $T_s$ in a global-mean sense. When all 180 global monthly mean $\mathrm{OLR}_c$ values are used from CTRh, and the seasonal cycle is filtered out, a statistically significant correlation at the 99.9 % level is attained (r=0.49) with a $dOLR_c/dT_s$ of 2.1 $Wm^{-2}K^{-1}$. Thus changes in $RH$ do not appear to greatly affect the dependence of $\mathrm{OLR}_c$ on $T_s$, but merely the degree of linear correlation. The sensitivity of global-mean $\mathrm{OLR}_c$ to $T_s$ is similar to that inferred from climate models as discussed by Cess *et al.* (1990).

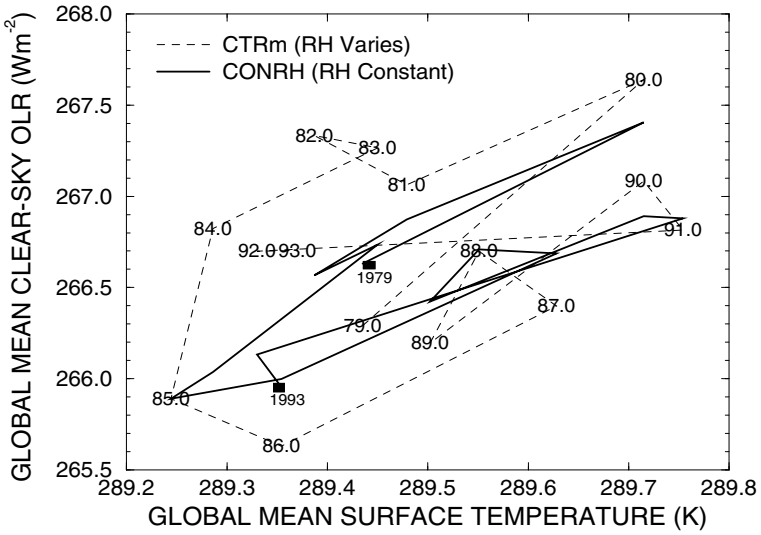


Figure 5.8: *Global-mean clear-sky OLR ($Wm^{-2}$) for experiments CTRm (dashed line) and CONRH (solid line) plotted with global-mean $T_s$ (K) for the 15 monthly-mean July's of the ERA period. Numbers within the frame denote year; individual years are annotated for CTRm and end points are noted for CONRH.*

Figure 5.8 shows the global-mean $\mathrm{OLR}_c$ plotted for each July with global-mean $T_s$ for experiments CONRH (solid line) and CTRm (dotted line) and highlights the increase in

correlation once the $RH$ signal is removed. When considering years before 1985 the $OLR_c$, for a given $T_s$, is greater than for years after 1985 for experiment CONRH. An additional run with the CLERA simulation was performed whereby the well mixed greenhouse gases were set at July 1979 levels while all other parameters are as defined in CTRm for July 1993. The global-mean $OLR_c$ difference due to changes in greenhouse gases over the 15 year period are calculated as 0.5 $Wm^{-2}$ for the July 1993 profiles. This is enough to explain the apparent decrease of $OLR_c$ at a given $T_s$ in Fig. 5.8. When $OLR_c$ is adjusted to account for the increasing concentrations of greenhouse gases, the correlation between global-mean $OLR_c$ and $T_s$ increases for all experiments.

When only upper tropospheric $RH$ is allowed to vary, in experiment UTRH, the sensitivity of global-mean $OLR_c$ to $T_s$ is greater than for experiment CONRH (Table 5.2). Conversely, when only lower or middle tropospheric $RH$ are allowed to vary $\frac{dOLR_c}{dT_s}$ is less than for experiment CONRH. This suggests that upper tropospheric $RH$ variations counteract the thermodynamic positive water vapour feedback while $RH$ variations in the lower and middle troposphere enhance the thermodynamic positive water vapour feedback. Using a t-test (Freund (1976)), the values of $dOLR_c/dT_s$ for experiments CONRH and UTRH are not significantly different at the 95% confidence level. Therefore a longer data set is required to identify a negative feedback due to upper tropospheric $RH$. Thus, there is weak evidence that the negative water vapour feedback mechanism proposed by Lindzen (1990) may operate, but only in a small portion of the atmosphere. The remainder of the atmosphere appears to counteract the upper troposphere effect, causing the overall water vapour feedback to be strongly positive and to be determined primarily by thermodynamics.

Table 5.2: *July global-mean clear-sky OLR and the global-mean standard deviation of $OLR_c$ ($\overline{SD_{OLR}}$) for CLERA experiments. LSQF sensitivity of global-mean OLR to global mean $T_s$ and its correlation coefficient is displayed in columns 4 and 5. ** denotes statistically significant correlation at greater than the 99.5 % confidence level. * denotes statistically significant correlation at greater than the 95 % confidence level.*

| EXPERIMENT | $OLR_c$ ($Wm^{-2}$) | $\overline{SD_{OLR}}$ ($Wm^{-2}$) | LSQF $\frac{dOLR}{dT_s}$ ($Wm^{-2}K^{-1}$) | LSQF r for $\overline{OLR} = a\overline{T_s} + b$ |
|---|---|---|---|---|
| CTRh | 268.5 | 3.0 | 1.38 | 0.41 |
| CTRm | 266.7 | 2.9 | 1.42 | 0.42 |
| CONRH | 266.5 | 1.5 | 2.28 | 0.85** |
| UTRH | 266.6 | 1.9 | 2.46 | 0.81** |
| MTRH | 266.6 | 2.1 | 1.66 | 0.60* |
| LTRH | 266.5 | 1.7 | 1.93 | 0.76** |

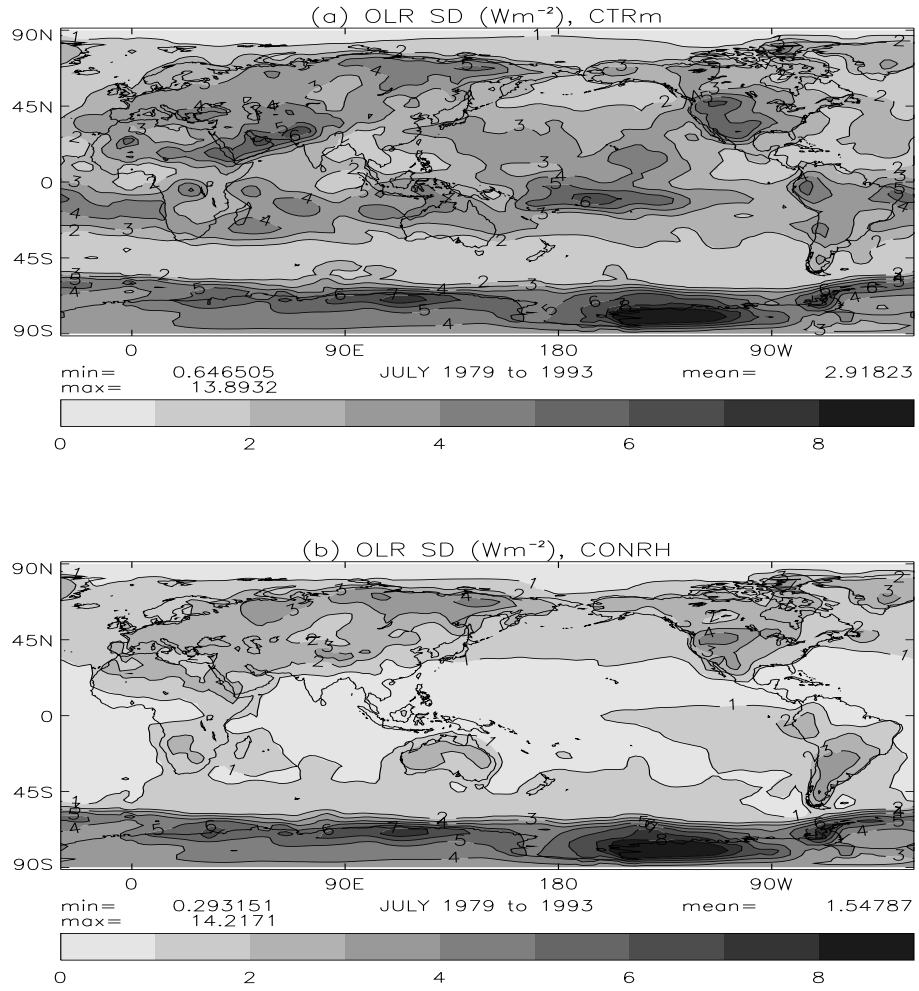


Figure 5.9: *Clear sky OLR Standard deviation ($Wm^{-2}$) for July 1979 to 1993, plotted globally where (a) RH is allowed to vary (experiment CTRm) and (b) RH is held constant throughout the atmosphere (experiment CONRH). The contour interval is 1 $Wm^{-2}$.*

Correlation between global-mean total column moisture ($u$) and $T_s$ is strongly positive for all experiments ($r$ >0.8). The calculated sensitivity, $du/dT_s$ for experiment CTRm of 3.3 $kgm^{-2}K^{-1}$ is significantly greater than the value of 2.1 $kgm^{-2}K^{-1}$ calculated from experiment CONRH where moisture is directly coupled to temperature. Therefore the effect of allowing $RH$ to vary increases the global-mean column water vapour sensitivity to global-mean $T_s$ beyond the thermodynamic constraints. Because $RH$ is strongly dependent on dynamics, this implies that the dynamic portion of the water vapour feedback enhances that of the thermodynamic water vapour feedback, at least in the lower troposphere where most of the column moisture resides.

The OLR standard deviation is plotted for experiments CTRm in Fig. 5.9(a) and CONRH in Fig. 5.9(b). The large $SD_{OLR}$ of greater than 3 $Wm^{-2}$ is present in both experiments for high latitude regions (most especially Antarctica) where the variation of $OLR_c$ is more dependent on changes in temperature than on changes in RH. The largest reduction in the $SD_{OLR}$ occur over ocean regions within about 30° of the equator, most especially in the tropical central Pacific and the region north of the Arabian Sea. As stated previously, changes in $RH$ control $OLR_c$ variation over middle and low latitudes while $T_s$ appears to dominate the OLR variability over high latitude land regions.

### 5.3.2 Height dependent RH variation and clear-sky OLR

Comparing standard deviations indicates the difference in variability over the 15 months between the experiments. However, a better measure of the fraction of $OLR_c$ variability due to changes in $RH$ is to consider $OLR_c$ anomaly differences between the control and perturbation experiments. Therefore the fraction of the $OLR_c$ anomaly ($\Delta OLR$) due to changes in $RH$ may be calculated as follows for each grid point:

$$f_j = \frac{1}{N}\sum_{i=1}^{N}\left[\frac{(\Delta OLR_{i,j} - \Delta OLR_{i,CONRH})}{\Delta OLR_{i,CTRm}}\right], \tag{5.4}$$

where $i$ denotes year, $N$ is the number of years and $j$ denotes experiments UTRH, MTRH, LTRH or CTRm. Only grid points where $\mid \Delta OLR_{i,CTRm} \mid > 2\ Wm^{-2}$ are considered, to increase signal to noise ratio.

Figure 5.10 shows $f$ averaged over 1 $K$ $T_s$ bins over ocean regions only for changes in $RH$ throughout the troposphere ($f_{RH}$), and for changes in upper, middle and lower tropospheric $RH$ calculated using Eq. 5.4. $f_{RH}$ is about equal to the sum of $f_{UTRH}$, $f_{MTRH}$ and $f_{LTRH}$. There is a rapid rise in $f_{RH}$ with $T_s$, with $RH$ explaining nearly all of the variation in $OLR_c$ at temperatures of about 300 $K$. For temperatures below about 290 $K$, much of this $OLR_c$ dependence on $RH$ is due to middle tropospheric $RH$ variations. At temperatures greater than about 290 $K$, changes in upper tropospheric $RH$ become increasingly important as they do for changes in lower tropospheric $RH$ at temperatures above 295 $K$. $f_{UTRH}$ decreases at temperatures above about 300 $K$ (mainly due to the tropical west Pacific regions). While the mid-tropospheric $RH$ appears to be the dominant control on $OLR_c$ away from high latitudes, the variations of $RH$ *throughout* the troposphere contribute significantly to $OLR_c$ variability. When $f$ is binned in land surface temperature intervals (not shown), values are generally lower than over the ocean. However, the importance of mid-tropospheric $RH$ and the rapid increase in $f$ with $T_s$ are both still evident.

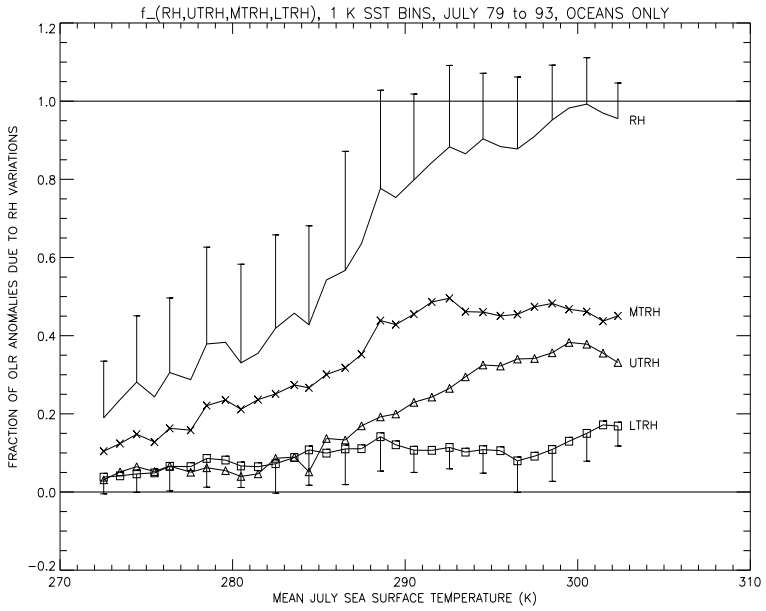


Figure 5.10: *Fraction of clear-sky OLR anomalies due to changes in RH for 1K sea surface temperature bins calculated from experiments CTRm, CONRH, UTRH, MTRH and LTRH. Only grid points of clear sky OLR anomalies greater in magnitude than 2 $Wm^{-2}$ are considered. Vertical bars denote one standard deviation about the mean value of f every alternate temperature bin for $f_{RH}$ and $f_{LTRH}$ to enhance the clarity.*

Figure 5.11(a) to (c) shows the global distribution of $f$ for UTRH, MTRH and LTRH respectively. Experiment MTRH explains a significant amount of $\mathrm{OLR}_c$ variability across much of the globe excluding Antarctica. This is especially so off the west coast of South America where middle tropospheric $RH$ variations appear to exclusively control $\mathrm{OLR}_c$ variations. Global-mean $f_{MTRH}$ is 0.33 which implies that mid-tropospheric RH variations account for, on average, about one third of the $\mathrm{OLR}_c$ variation. $f_{UTRH}$ is generally above 0.4 within about 40° of the equator and accounts for about 21% of the variation in clear-sky OLR variability. LTRH appears to contribute little to the $\mathrm{OLR}_c$ variation (Fig. 5.11(c)). However, when averaged over the globe, about 11% of the $\mathrm{OLR}_c$ variability is explained by changes in lower tropospheric $RH$.

### 5.3.3 Relative Humidity and the Super-greenhouse Effect

Section 5.2.1 shows a SGE to act over tropical ocean regions for the interannual time-scale. This is explained in terms of the change in the convective regime due to the ENSO cycle that are associated with changes in $T_s$. When $RH$ is held constant, as in experiment CONRH, there are no regions exhibiting a statistically significant SGE. This is consistent with Hallberg and Inamdar (1993) who show that thermodynamics alone is not enough to

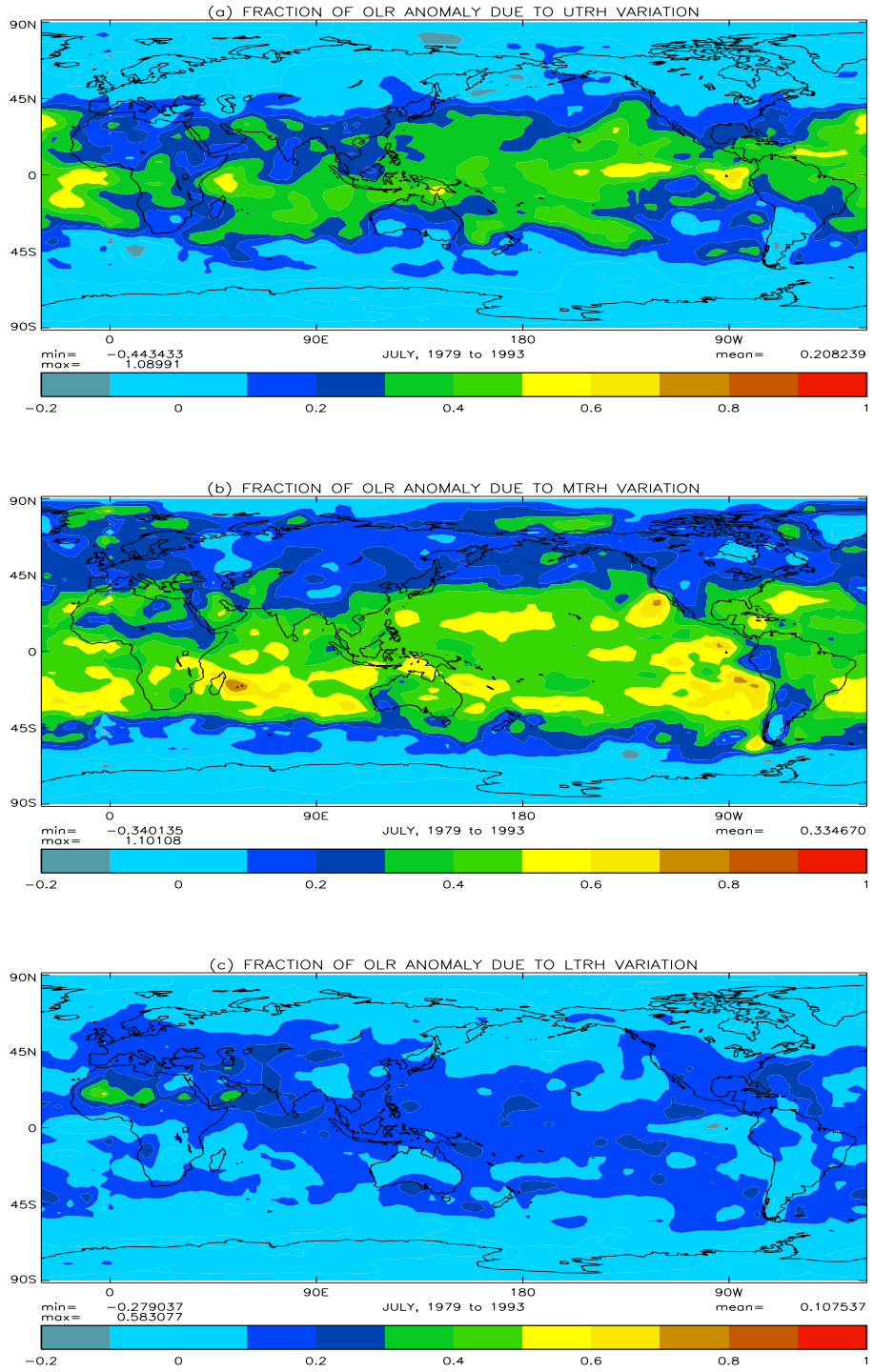


Figure 5.11: *Fraction of clear-sky OLR anomalies due to changes in (a) upper, (b) middle and (c) lower tropospheric RH over the interannual time-scale for July. Only grid points where clear-sky OLR anomalies are greater in magnitude than* $2\,Wm^{-2}$ *are considered. The contour interval is 0.1*

explain the SGE. Figure 5.12 shows $dOLR_c/dT_s$ for experiments CTRm, CONRH, UTRH, MTRH and LTRH binned into 1 $K$ intervals of $T_s$ over the oceans. All ocean grid points are considered. Thus values at the highest $T_s$ for CTRm differ to those calculated over the interannual time scale in Fig. 5.2(d) which removes regions of small variability in $T_s$ (mainly in the tropical warm pool region). The binned sensitivity for experiment CONRH ranges from between about 1.0 $Wm^{-2}K^{-1}$ in the tropics to about 1.9 $Wm^{-2}K^{-1}$ elsewhere. A SGE is not apparent in any of the $T_s$ bins for experiment CONRH while a SGE applies at sea surface temperatures above about 296 $K$ for experiment CTRm albeit with a large scatter about the mean value for the bin. Allowing changes in $RH$ for each layer results in a decreased $dOLR_c/dT_s$ compared to the CONRH experiment such that the following is true:

$$\left[\left(\frac{dOLR_c}{dT_s}\right)_{CTRm} - \left(\frac{dOLR_c}{dT_s}\right)_{CONRH}\right] = \sum_{j=1}^{3}\left[\left(\frac{dOLR_c}{dT_s}\right)_j - \left(\frac{dOLR_c}{dT_s}\right)_{CONRH}\right], \quad (5.5)$$

where $j$ denotes experiments UTRH, MTRH or LTRH. A decrease in $dOLR/dT_s$ at high $T_s$ for experiment CONRH shows that thermodynamics contributes to producing SGE situations because over the tropical oceans, $\mathrm{OLR}_c$ is essentially decoupled from $T_s$. This is due to the large column moisture and therefore a small $Tr$ term in Eq. 3.7. Allowing $RH$ to vary only in the lower troposphere in experiment LTRH results in a similar $dOLR/dT_s$ to experiment CONRH. However for experiments MTRH and UTRH, $dOLR/dT_s$ is significantly lower at high sea surface temperatures. Thus it is mainly the changes in upper and middle tropospheric $RH$ that cause SGE situations to occur. Similar conclusions have been drawn from other studies (e.g. Hallberg and Inamdar (1993)).

## 5.4 Discussion

A simulation of the Earth's clear-sky longwave radiation budget is used to examine the dependence of $\mathrm{OLR}_c$ on surface and atmospheric temperature and relative humidity throughout the troposphere. Changes in $T_s$ appear to dominate the $\mathrm{OLR}_c$ variation at high latitudes, especially over the land regions, while over low latitudes, changes in tropospheric $RH$ appear to control $\mathrm{OLR}_c$ variability. Globally, tropospheric $RH$ explains a larger proportion of $\mathrm{OLR}_c$ variation over an interannual time-scale than over the seasonal cycle. This is because for a given change in $RH$ variations in $T_s$ are less over the interannual time-scale in all but the tropics.

A SGE is identified over both the seasonal and interannual time scales at the top of the atmosphere. A strong surface SGE is also identified over the seasonal cycle and over the interannual time-scale over tropical ocean regions. A SGE also acts in the atmosphere

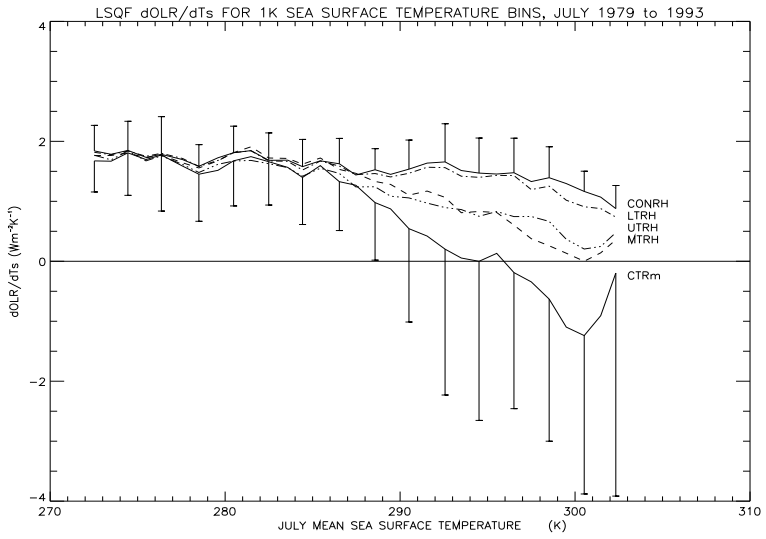


Figure 5.12: *LSQF clear-sky OLR sensitivity to changes in $T_s$ over the oceans ($Wm^{-2}K^{-1}$) for July 1979 to 1993 calculated in 1 K $T_s$ bins for experiment CTRm, CONRH, UTRH, MTRH and LTRH. Vertical bars denote one standard deviation about the mean value of $dOLR_c/dT_s$ and are plotted for experiments CONRH and CTRm only for reasons of clarity.*

over the seasonal cycle for the warmest ocean regions, contrary to previous suggestions (e.g. Lubin (1994), Inamdar and Ramanathan (1994)). When $RH$ is held constant or only allowed to vary in the lower troposphere, no statistically significant SGE results. However, when upper or mid-tropospheric $RH$ are allowed to vary, a SGE is identified over the interannual time-scale. The necessary change in $RH$ is provided only when a change in $T_s$ is associated with a transition between strong and weak convection. This may only occur where ascent is imposed by the large-scale circulation (Bony *et al.* (1997b)). Over the seasonal cycle, the shift in the Hadley circulation imposes such a transition in the tropics (although away from the equator) which corresponds with the regions exhibiting a SGE. On the interannual time-scale, the shift in the Walker circulation associated with ENSO is sufficient to alter the degree of convection in the tropical Pacific necessary to produce a SGE situation. Because the SGE mainly constitutes an unstable radiative feedback to the surface (Inamdar and Ramanathan (1994)), stabilising mechanisms such as shortwave cloud radiative feedbacks, evaporative feedbacks and heat export to the extra tropics are required to prevent a local runaway greenhouse effect from operating (Pierrehumbert (1995)). This is discussed further in Chapter 6.

The sensitivity of $\mathrm{OLR}_c$ to $TRH$ is most negative in regions of low $TRH$. This can be explained by the saturation of the water vapour absorption bands with increasing $RH$. In all but the most moist regions, $\mathrm{OLR}_c$ is most sensitive to a given $RH$ variation if that

change is in the upper troposphere; Spencer and Braswell (1997) use this result to argue that upper tropospheric $RH$ is highly important for climate change. However, because $RH$ variations in the upper troposphere are generally associated with larger changes in $RH$ at lower levels, the importance of upper tropospheric $RH$ with regard to the $\mathrm{OLR}_c$ may have been overstated. Because the ERA $RH$ variations are greatest between about 600 and 800 $hPa$, the *middle* tropospheric $RH$ contributes most to $\mathrm{OLR}_c$ variability over the interannual time-scale. This is supported by previous analyses (e.g. Clough *et al.* (1992), Sinha and Harries (1997)). By allowing $RH$ to vary only in either the upper, middle or lower troposphere, it is shown that the middle troposphere (about 400 to 700 $hPa$) contributes about one third of the $\mathrm{OLR}_c$ variability. The upper and lower troposphere contribute about 21% and 11% respectively. Therefore $RH$ *throughout* the troposphere contributes significantly to $\mathrm{OLR}_c$ variation. Changes in surface and atmospheric temperature account for the remaining 35% of the variability. There is weak evidence in support of a negative water vapour feedback, as suggested for example by Lindzen (1990)), although this is only the case for the upper tropospheric $RH$ variations; changes in $RH$ at lower levels of the troposphere counteracts this effect, resulting in an overall positive contribution from $RH$ variations to the water vapour feedback. The results presented are relevant for interannual variation between Julys. Therefore conclusions are relevant for the interannual variability due to changes in the large scale circulation for this month. For example, changes in the Asian monsoonal circulation may be significant in dictating the variability of $RH$ between Julys. The profound link between clouds and water vapour also render the present study incomplete with regard to the overall response of the climate system to a radiative forcing. For the experiments undertaken, changes in $RH$ do not appear to significantly alter the relationship between global-mean $\mathrm{OLR}_c$ and $T_s$, but merely decrease their linear correlation.

While information concerning the sensitivity of the Earth's radiation budget to observed changes in surface and atmospheric parameters yields valuable information as to the mechanisms acting in the climate system, climate model experiments are required to perform relevant climate sensitivity calculations. Unfortunately these studies themselves are limited by the potential inability of the model to parameterize accurately the moist convection so important in determining the water vapour and cloud feedbacks. Therefore it should be a pre-requisite that climate models can reproduce the sensitivities and variability that are provided by observations and simulations such as the present study.

A major limitation of the CLERA simulation is the reliance on the numerical model calculations used in the ERA project. This is especially true of the upper troposphere and the dry descending oceanic 'deserts' where observational data is limited. Hence a

large uncertainty is attached to ERA humidity and its variability in these regions. The inference of the present study, that $\mathrm{OLR}_c$ variability is dependent mainly on $RH$ variations in the middle troposphere as opposed to the upper troposphere, is therefore dependent on the validation of ERA humidity variability, most especially in these dry regions of the atmosphere. The dry descending regions of low $TRH$ are likely to be important with regard to the water vapour feedback. Not only is $\mathrm{OLR}_c$ most sensitive to $TRH$ variations in these regions but, unlike the moist tropics the cloud amount is small thus increasing the importance of clear-sky feedbacks. Also, the radiative cooling is a dominant diabatic term in the descending portions of the Hadley circulation. Thus in understanding the climate system and the water vapour feedback, attaining robust observations of humidity in these regions must be paramount. By testing the ability of climate models to capture the variability of moisture and the associated variability in the clear-sky greenhouse effect over sufficiently long time-scales confidence can be increased in prediction of future climate change.

# Chapter 6

# TOP OF ATMOSPHERE ALL-SKY IRRADIANCE VARIABILITY

## 6.1 Introduction

One of the largest uncertainties in current predictions of future climate is the treatment of the cloud feedback (IPCC (1996)). This uncertainty lies not only in the parameterizations of cloud radiative processes (e.g. Stephens (1984)), but also in our limited understanding of the processes that control cloud distribution and micro-physical properties (e.g. J. M. Slingo (1980)). To accurately model the effect of clouds on future climate, an adequate representation of the relevant feedback process must be implemented. A sufficient level of complexity in cloud distribution and properties are required if questions relating to the sign and magnitude of the cloud feedback in the climate system are to be answered. Many studies have shown the general circulation and the climate response to greenhouse gas forcing to be sensitive to the parameterizations of cloud distribution and properties implemented (e.g. Slingo and Slingo (1988), Mitchell *et al.* (1989)). However, information provided by climate models is of use only if these parameterizations provide realistic approximations to the observed variability of cloud radiative and dynamical processes. A primary aim of this chapter is to provide estimates of the variability of cloud radiative effects and their dependence on atmospheric and surface parameters that may be subsequently used to test the proficiency of climate models.

There have been many attempts to investigate the influence of cloud amount and properties on the Earth's climate, an early assessment being by Schneider (1972). There are

generally two main approaches used. Firstly, model parameterizations of cloud properties are used to assess the potential influence or to simulate feedbacks introduced by clouds in response to a climate perturbation such as greenhouse gas induced warming (e.g. Slingo (1990)). Such studies depend on the accurate parameterization of cloud properties and distribution (e.g. J. M. Slingo (1987)). Inter-model evaluation and comparison of cloud radiative forcing with satellite radiation budget results are subsequently required to validate the climate models (e.g. Cess *et al.* (1997)). A second type of experiment uses observations of both cloud amount and irradiance at the top of the atmosphere to quantify the effect of changes in cloud amount or properties with space and time on the Earth's radiation budget (e.g. Ringer and Shine (1997)). While this provides direct correlations between cloud variables and the radiation budget, the dependence of cloud amount and properties on atmospheric and surface properties must also be assessed for a quantitative understanding of the cloud feedback to climate. An alternative method is to use observed satellite radiation data to investigate the influence of atmospheric variables on cloud properties and the cloud radiative forcing (e.g. Weare (1995), Raval *et al.* (1994)). The present work uses this approach to quantify the Earth's radiation budget variability due to changes in cloud amount/properties. ECMWF re-analysis (ERA) parameters are used in conjunction with Earth Radiation Budget Experiment (ERBE; Barkstrom (1984)) satellite observations for this purpose. The simulation of the clear-sky longwave radiation budget described in Chapter 2 (Slingo *et al.* (1998)) provides estimates of clear-sky outgoing longwave radiation ($OLR_c$) required to calculate the longwave cloud radiative forcing that are derived from and therefore consistent with the ERA data.

As discussed in Chapter 3 there are two effects of clouds on the clear-sky feedbacks calculated from climate model experiments (e.g. Cess *et al.* (1990)) or inferred observationally (e.g. Raval and Ramanathan (1989)). Firstly, the mere presence of cloud modifies the clear-sky radiative feedbacks even without changes in cloud properties or distribution. However, potentially the larger influence on climate feedbacks is the response of cloud amount and properties to the variations in surface and atmospheric parameters associated with the changing climate. The present study aims to explain the cloud influence on the radiation budget in terms of these two mechanisms. A key question to be addressed is, how do clouds influence the variability of the Earth's radiation budget and to what extent is the cloud radiative impact associated with fluctuations in temperature and humidity? This extends the analyses of Raval *et al.* (1994) and Bony *et al.* (1997b) who use the ERBE satellite radiation budget data in these calculations over ocean grid-points only. Of interest are the regions that experience a clear-sky super-greenhouse effect (SGE) as discussed in Chapter 5 (see also Hallberg and Inamdar (1993)).

A novel approach of the present study is the use of simulated $OLR_c$ to calculate the cloud longwave radiative forcing as opposed to the ERBE estimates. The motivation behind this is twofold. Firstly the clear-sky fluxes estimated by satellite are limited in their spatial and temporal coverage and are prone to cloud contamination of clear-sky scenes (e.g. Slingo and Webb (1992)). Secondly the satellite method of deriving clear-sky fluxes is inconsistent with that calculated diagnosticly by climate models, as discussed in Chapter 1 (see also Cess *et al.* (1992)). Also the satellite clear-sky sampling differs in spatial and temporal extent to operational analyses, which are relevant for all-sky conditions, that are often used in conjunction with the satellite clear-sky fluxes (e.g. Raval *et al.* (1994), Bony *et al.* (1997a)). A limitation to the present study is that errors in temperature and humidity given by ERA will affect the simulated $OLR_c$ and therefore the calculated cloud longwave radiative forcing. Thus an additional aim of this chapter is to highlight errors within and inconsistencies between the simulated $OLR_c$, the ERA data and the ERBE data.

The data sets employed in the present study are described in the following section. Section 6.3 attempts to quantify the irradiance variability on seasonal and interannual time-scales both globally and locally. The use of simulated $OLR_c$ is critically assessed by comparison with corresponding ERBE values in Sec. 6.4. Sections 6.5 and 6.6 present analyses of the radiation budget variability and its dependence on temperature and humidity fluctuations. Conclusions are drawn in the final section.

## 6.2 Method and Data

The Earth Radiation Budget Experiment consisted of instruments on two sun-synchronous polar orbiting satellites (NOAA-9 and NOAA-10) and a 57° medium inclination orbiting satellite (ERBS) which combined to provide estimates of the monthly mean top of atmosphere irradiance (S-4 archive as described by Barkstrom *et al.* (1990)). All satellites carried identical instrument packages (see Ringer (1994)) and the data were provided on a 2.5° latitude-longitude grid from February 1985 to January 1990. The most comprehensive ERBE data sets were provided by the scanner measurements on each satellite. The ERBS and NOAA-9 satellites worked in unison between February 1985 and January 1987, after which the NOAA-9 scanners failed. The NOAA-10 scanners operated between September 1986 and May 1989 after which only the ERBS data was collected. Thus, all three satellite-scanners were operational for the limited period between September 1986 and January 1987. While both NOAA-9 and NOAA-10 were in sun-synchronous orbits, their nominal equator crossing times differed slightly and so this must be considered when interpreting the ERBE data. Wide Field of View (WFOV) estimates of the radiation budget were also installed

on the ERBS satellite, and these provide a longer time series of irradiance although this is of value only at low latitudes (e.g. Minnis *et al.* (1993)). Thus the present study uses the ERBE monthly mean data from the scanner instruments.

The simulation of Clear-sky Longwave radiation from the ECMWF Re-Analysis (CLERA) is described in Chapter 2 (see also Slingo *et al.* (1998)). Monthly mean simulated $\mathrm{OLR}_c$ for the period 1985 to 1990 is used in the present study in conjunction with ERBE observations of the all-sky monthly-mean irradiance at the top of the atmosphere. To maximise the spatial coverage of cloud radiative forcing, the longwave and shortwave components are estimated in the following manner. The longwave cloud radiative forcing ($LWCF$) is calculated by subtracting ERBE all-sky OLR from the $\mathrm{OLR}_c$ simulated by CLERA. This method allows a greater spatial coverage compared to ERBE-derived longwave cloud radiative forcing and is consistent with the 'Method II' technique used in climate model studies (Cess and Potter (1987); discussion in Chapter 1). However, shortcomings in the ERA fields and the radiative transfer calculations are likely to introduce new errors. Rather than use the ERBE shortwave cloud radiative forcing ($SWCF$) products which suffer from limited spatial coverage, ASR is used to assess information on the shortwave effects of clouds. Changes in ASR are also influenced by changes in surface albedo, which will be large in regions of temporary snow or ice cover, and also by changes in aerosol optical depth. Therefore in such regions changes in ASR will not be a good approximation for $SWCF$. The large seasonal changes in insolation, most especially at high latitudes, also render estimates of $SWCF$ variability prone to mis-interpretation. However, ERBE shortwave cloud forcing products contain missing data for part or all of the time period assessed for latitudes greater than about 45° and the identification of clear-sky scenes over regions of snow or ice is also prone to error (Nemesure *et al.* (1994)) and are unlikely to increase the information concerning changes in $SWCF$ significantly.

To obtain information concerning cloud feedbacks and to assess the effect of clouds on the sensitivity of the Earth's radiation budget to surface and atmospheric parameters, the method of least squares fit linear regression (LSQF) (e.g. Freund (1976)) was utilised as in Chapter 5. Grid points containing missing satellite data for any monthly mean used in the calculation were excluded from the analysis so that the same temporal coverage is applied. Because the satellite data provided only 4 years of global coverage (1985 to 1989), calculating LSQF regression over an interannual time-scale for a particular month contains a rather small sample size to obtain meaningful statistics. Thus interannual calculations used all January, April, July and October monthly means and filter out the seasonal cycle by calculating anomalies from the 4 year mean of that particular month, rather than from

the mean of all months. An interannual anomaly ($X'$) where $X$ is a generic variable such as OLR, was calculated thus:

$$X'_{ij} = X_{ij} - \frac{1}{N}\sum_{j=1}^{N}(X_{ij}), \tag{6.1}$$

for month $i$ and year $j$ and where $N$ denotes the number of years. For the interannual time-scale, the sample size is 16 for which a statistically significant correlation at the 95 % confidence level requires a correlation coefficient, $r$, of greater magnitude than 0.5. This compares with the 12 month annual cycle where a statistically significant correlation requires a magnitude of $r$ greater than 0.58.

## 6.3 Seasonal and Interannual Irradiance Variability

To characterise the variability of the CLERA and ERBE top of atmosphere irradiance, the standard deviation ($SD$) is calculated over the seasonal cycle for each grid point:

$$SD_X = \sqrt{\frac{1}{12}\sum_{i=1}^{12}(X_i - \overline{X})^2}, \tag{6.2}$$

where X denotes the irradiance quantity (e.g. OLR) and $i$ denotes the month of the year. An over-bar denotes the time-mean of the given variable. Standard deviation over the interannual time-scale is calculated as:

$$SD_X = \sqrt{\frac{1}{N}\sum_{i=1}^{N/4}\sum_{j=1}^{4}(X_{ij} - \overline{X_j})^2}, \tag{6.3}$$

where N denotes the number of monthly means used, $i$ denotes the year since 1984 and $j$ denotes the month. Also calculated is the SD of the global mean irradiance ($SD_{\overline{X}}$) for the two time scales considered. Table 6.1 presents the calculated standard deviation and mean irradiance for the seasonal cycle of 1988 and for the interannual time scale for the ERBE period.

### (a) Global Means

For all monthly means considered, the $LWCF$ is calculated to range between about 25 and 32 $Wm^{-2}$ which includes values lower than the range 30.1 to 32.2 $Wm^{-2}$ for January, April, July and October 1985 calculated by ERBE (Harrison *et al.* (1990)). The variability of global mean clear-sky and all-sky OLR, $LWCF$ and ASR between February 1985 and May 1989 are presented in Fig. 6.1. The strong annual cycle in $OLR_c$ is evident, with a maximum during the northern hemisphere summer. This is caused mainly by the contribution of the

Table 6.1: *Mean Irradiance and Standard Deviation calculated using ERBE and CLERA data over the seasonal cycle of 1988 and the interannual time-scale for the ERBE period.* $\overline{SD_X}$ *denotes the mean standard deviation of the irradiance variable, X, averaged over all grid points, while* $SD_{\overline{X}}$ *denotes the standard deviation of the global mean X.*

| Time scale | X | Mean ($Wm^{-2}$) | $\overline{SD_X}$ ($Wm^{-2}$) | $SD_{\overline{X}}$ ($Wm^{-2}$) |
|---|---|---|---|---|
| Seasonal | | | | |
| 1988 | $OLR_c$ | 263.9 | 10.1 | 3.3 |
| | OLR | 236.6 | 16.3 | 2.7 |
| | $LWCF$ | 27.3 | 9.4 | 0.8 |
| | ASR | 240.8 | 67.1 | 4.3 |
| Interannual | | | | |
| (1985- | $OLR_c$ | 263.4 | 2.9 | 0.5 |
| 1989) | OLR | 235.4 | 7.1 | 1.4 |
| | $LWCF$ | 27.9 | 5.8 | 1.1 |
| | ASR | 240.5 | 9.1 | 1.1 |
| | NET | 5.1 | 6.5 | 0.9 |

northern hemisphere land masses which undergo a large change in $T_s$. This annual cycle is also seen in the global-mean ERBE all-sky OLR, although there is more scatter for each month than for the $OLR_c$. This scatter represents a residual variability which, providing errors in OLR and $OLR_c$ are small, represents the effects of cloud variability on OLR. The calculated scatter of $LWCF$ for each month is of the order 4 $Wm^{-2}$, although there also appears to be a systematic change in $LWCF$ over the seasonal cycle with a maximum apparent in May.

The standard deviation of global mean values (Table 6.1) show clear-sky and all-sky OLR seasonal variability to be of similar magnitude while the OLR variability due to clouds is less. This is because the changes in $T_s$ over the course of a year are large and cause the clear-sky component of OLR to be the dominant mode of longwave irradiance variability. This is not the case for the interannual time-scale where changes in global mean $T_s$ are much smaller than over the seasonal cycle. The interannual variability of OLR is greater than for $OLR_c$ as inferred from the interannual standard deviations displayed in Table. 6.1. This is highlighted by plotting the time evolution of the interannual anomalies for ERBE OLR (solid line) and for CLERA $OLR_c$ (dotted line) in Fig. 6.2. The anomalies are filtered by averaging over four months, thus removing intraseasonal variability. However, much of the interannual variability of ERBE OLR is determined by a rapid change of greater than 2 $Wm^{-2}$ between

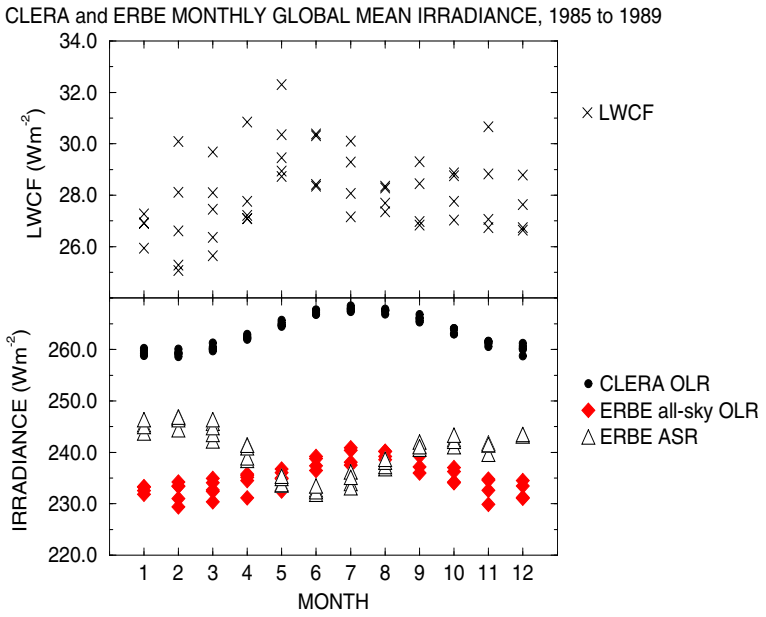


Figure 6.1: *Global monthly-mean CLERA clear-sky OLR, ERBE all-sky OLR, CLERA-ERBE inferred longwave cloud radiative forcing (LWCF) and ERBE absorbed solar radiation at the top of the atmosphere (ASR) between February 1985 and May 1989, plotted for each month of the seasonal cycle (January to December). Units are* $Wm^{-2}$.

negative anomalies before January 1987 to positive anomalies afterwards. A shift of smaller magnitude and opposite sign is also observed in the ASR interannual monthly anomalies (not shown). It is postulated that some of this variation may be artificially introduced by the changes in satellite combinations from the NOAA-9 to the NOAA-10 combination with ERBS that occurs at this time. To remove this potential error, the ERBS OLR was considered separately (dot-dashed line) which covers the 60° S to 60° N region. A shift from negative to positive ERBS OLR anomalies occurs at approximately the same time as the shift in anomalies shown by the ERBE data, although the magnitude change is less than half that of ERBE OLR and is of similar magnitude to the interannual fluctuations of the simulated $OLR_c$. Wide Field of View data sampled within 40° of the equator also shows a similar magnitude shift in OLR anomalies as the ERBS data at this time, although it is small compared to the perturbations associated with the eruption of Mt. Pinatubo (IPCC (1995) [p.187, after Minnis *et al.* (1993)]). Nevertheless, this suggests that the perturbation to the radiation budget is physically based, for example associated with the 1987 ENSO event. However, the magnitude of the change in OLR anomalies appears to be overestimated by the ERBE data due to the change in satellite combinations. Thus the interannual variability in global-mean $OLR_c$ is likely to be of greater importance in determining the all-sky OLR variability than is indicated by considering the interannual standard deviations in Table 6.1.

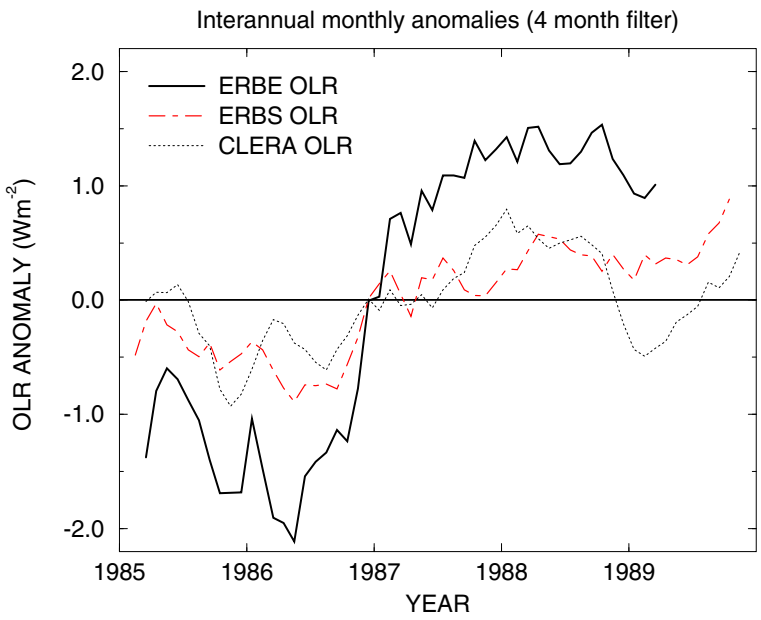


Figure 6.2: *Global-mean interannual monthly anomalies of CLERA clear-sky OLR (dotted line), ERBE all-sky OLR (solid line) and ERBS all-sky OLR (dot-dashed line) from 1985 to 1989. Year labels coincide with January. Units are* $Wm^{-2}$.

### (b) Global distribution of variability

The mean variability of all grid points, as denoted by $\overline{SD_X}$ in Tab. 6.1, is significantly greater for all-sky OLR than for clear-sky OLR over the seasonal cycle. This is not the case when considering the variability of global mean values ($SD_{\overline{X}}$). While the effects of clouds act to increase the OLR variability locally, as a global-mean the distribution of changes in cloud amount and properties influence the global mean OLR variability only slightly (i.e. $SD_{\overline{LWCF}}$ is small). This is because increases in $LWCF$ are cancelled to a certain extent by decreases in $LWCF$ in other regions due to shifts in the large scale circulation. Also the presence of a cloud layer (especially at higher altitudes) will diminish the OLR variation that is due to changes in surface and near-surface temperature. This is highlighted by considering Fig. 6.3: the OLR variability over high latitude land regions, which experience large perturbations to surface and near-surface temperature over the period of a year, are generally higher for clear-sky conditions than for all-sky conditions. The reverse is true at low latitudes. Figure 6.3(c) shows double peaks in $LWCF$ variability separated by the equator where $SD_{LWCF}$ is small. This may be explained by considering that the largest changes in convective regime over the seasonal cycle occur on the pole-ward extremities of the ITCZ as it migrates latitudinally throughout the year. The monsoon regions of India

and Australia, where seasonal changes in humidity and cloud amount are consequently large, also exhibit large variability in OLR.

Figure 6.4 shows that the standard deviation of $OLR_c$ is a small fraction of the all-sky values over much of the globe for the interannual time scale. $LWCF$ appears to account for much of the interannual variability in all-sky OLR in all but high latitude regions and over the dry descending regions of the Hadley circulation. The double peaks in OLR variability due to clouds present in the seasonal time scale (Fig 6.3) are not present for the interannual time scale because the position of the ITCZ shows little variability between years. The largest OLR variability is centred on the equator at 180°. This results from the large changes in convective regime associated with the 1987 to 1988 ENSO cycle.

The largest $LWCF$ variability over the interannual time-scale is over the tropical central pacific (Fig. 6.4(c)), while the corresponding variability maximum over the seasonal cycle appears to be within 30° of the tropics although excluding the dry descending regions of the Sahara and the ocean westwards of southern Africa and South America (Fig. 6.3(c)). The areas of high $SD_{LWCF}$ correspond to SGE regions characterised over both time scales in Chapter 5. The regions displaying the largest variation in $LWCF$ are caused by the substantial changes in convective regime, and hence degree of cloudiness, that are associated with the latitudinal shift in the Hadley circulation over the seasonal cycle and with the shift in the Walker circulation over the interannual time scale. The zonal mean standard deviation for clear-sky OLR, all-sky OLR, ASR and NET for the interannual time scale is shown in Fig. 6.5. The largest zonal mean standard deviation is that of ASR with a maximum of 13 $Wm^{-2}$ at 2.5° N. All-sky OLR standard deviation at low latitudes is also large with a maximum of nearly 12 $Wm^{-2}$ at the same latitude. However, because of the compensating longwave and shortwave radiative effects of clouds (e.g. Ramanathan and Collins (1991), Kiehl (1994)), the standard deviation of net radiation at the top of the atmosphere at low latitudes is much smaller (about 6 to 7 $Wm^{-2}$). Over mid-latitudes, the variability of all-sky OLR is much smaller than ASR. The standard deviation of net radiation is close to that of ASR implying that much of the variability of the radiation budget at higher latitudes is explained by changes in ASR, which is in turn explained by changes in shortwave cloud radiative forcing and changes in surface albedo. The zonal mean standard deviation of $OLR_c$ is generally between about 3 to 4 $Wm^{-2}$ which is about half of the net radiation standard deviation. The $OLR_c$ appears to contribute about 30% to the variance in net radiation.

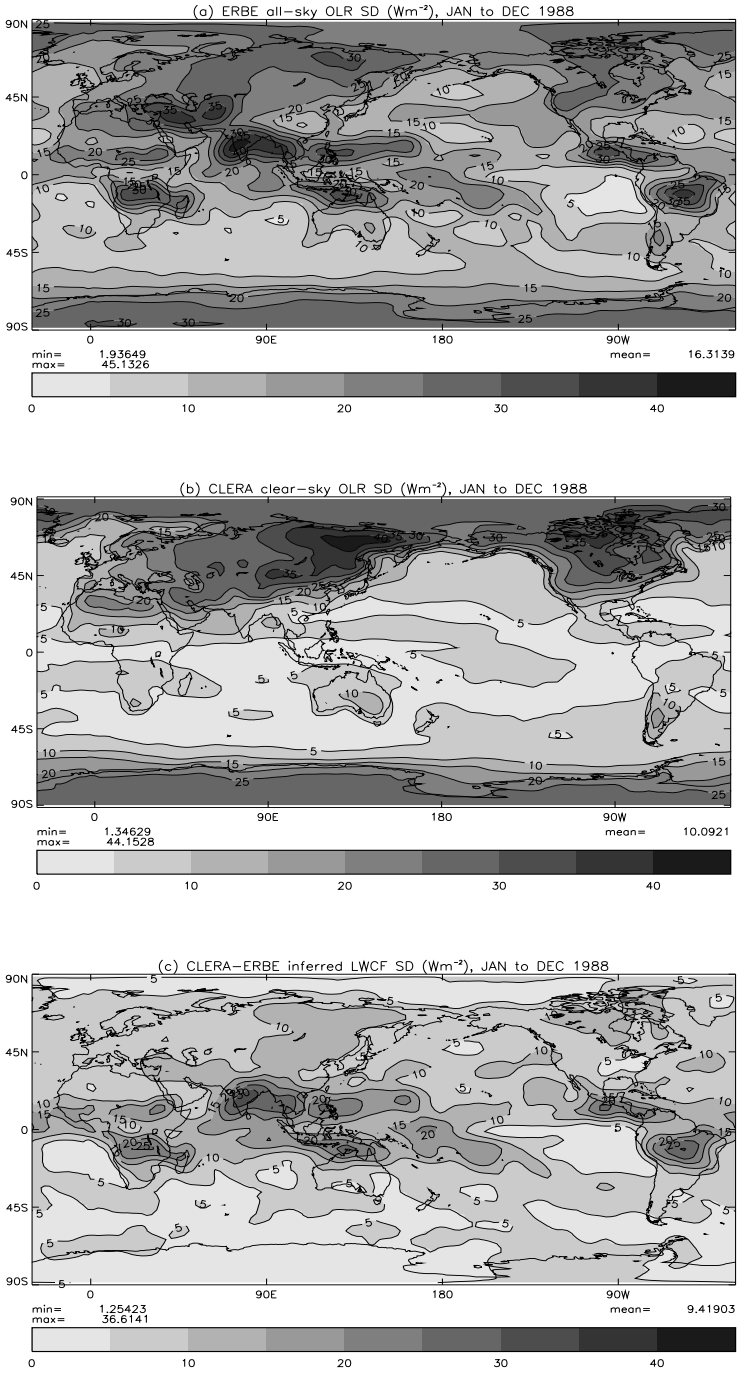


Figure 6.3: *Standard deviation (in $Wm^{-2}$) for (a) ERBE all-sky OLR, (b) CLERA clear-sky OLR and (c) CLERA-ERBE inferred longwave cloud radiative forcing over the seasonal cycle of 1988.*

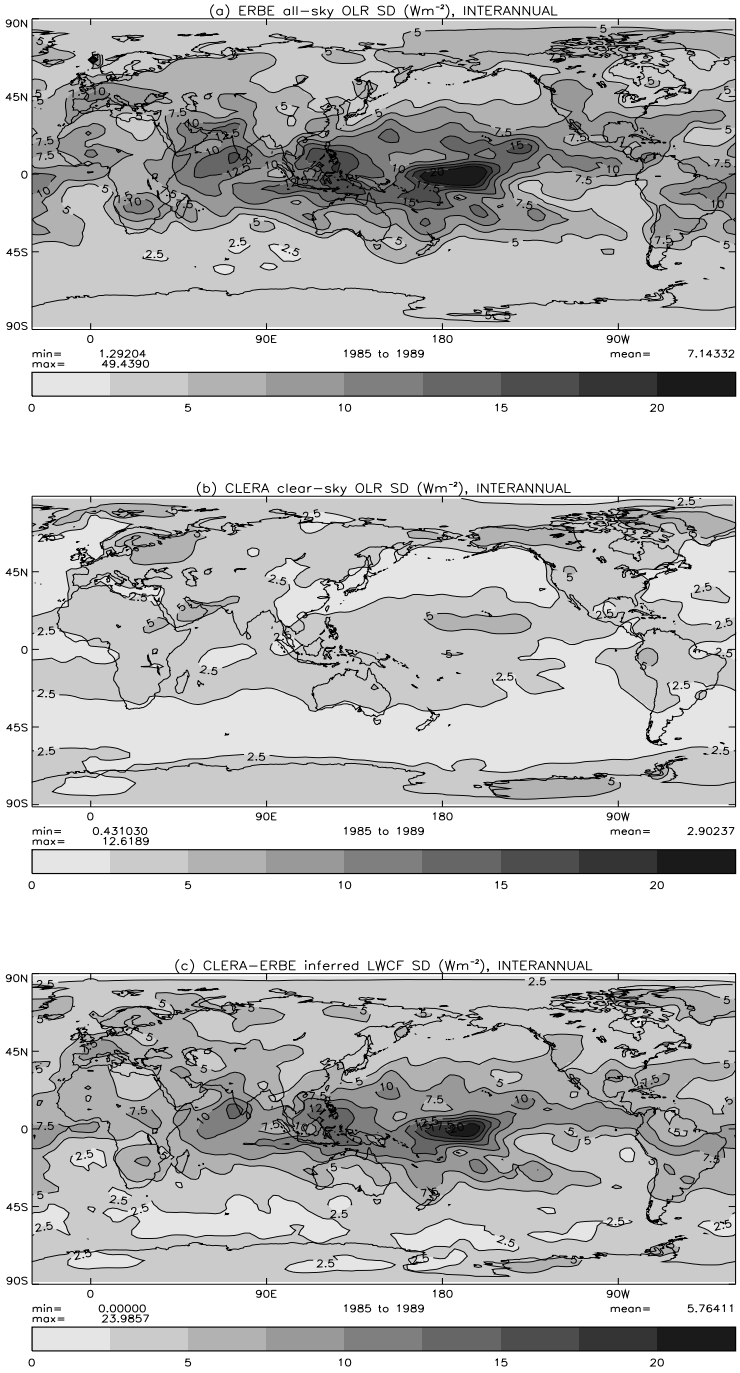


Figure 6.4: *Standard deviation (in $Wm^{-2}$) for (a) ERBE all-sky OLR, (b) CLERA clear-sky OLR and (c) CLERA-ERBE inferred longwave cloud radiative forcing over the interannual time-scale between 1985 to 1989.*

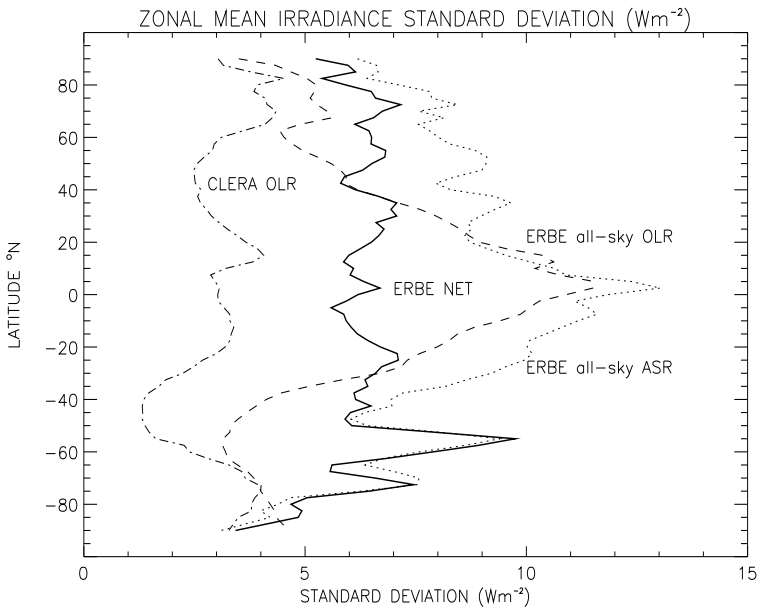


Figure 6.5: *Zonal mean of the standard deviation of CLERA clear-sky OLR and ERBE all-sky OLR, absorbed solar radiation and net radiation at the top of the atmosphere over the interannual time-scale between 1985 to 1989. Units are* $Wm^{-2}$*)*

## 6.4 Clear-sky OLR differences between ERBE and CLERA

To quantify the radiative effects of clouds and their variability, it is necessary to derive a clear-sky component of the observed or modelled irradiance. In Chapter 1, two main methods of deriving clear-sky irradiance were described, the first being to sample only for regions deemed to be clear (e.g. Cess and Potter (1987)). This is essentially the technique used by ERBE, although the spatial and temporal averaging techniques required complicate the procedure (Brooks *et al.* (1986)). The second method, conventionally used in climate model studies, is to calculate the clear-sky irradiance globally as a diagnostic parameter by setting cloud amount to zero. This is consistent with $\mathrm{OLR}_c$ simulated by CLERA. The ERBE technique is potentially prone to contamination of clear-sky observations with cloud (e.g. Weare (1995)). Also the changes in clear-sky irradiance using the ERBE data are inconsistent with atmospheric parameters derived by re-analyses such as the ERA data, because these do not separate clear and overcast conditions. Thus inferring changes in ERBE clear-sky irradiance associated with changes in all-sky parameters (e.g. Raval *et al.* (1994)) potentially incurs errors due to the cloud contamination problem and also the inconsistent use of clear-sky and all-sky parameters. Therefore it is of value to compare estimates of the sensitivity of $\mathrm{OLR}_c$ to changes in $T_s$ and $RH$ using both ERBE and CLERA.

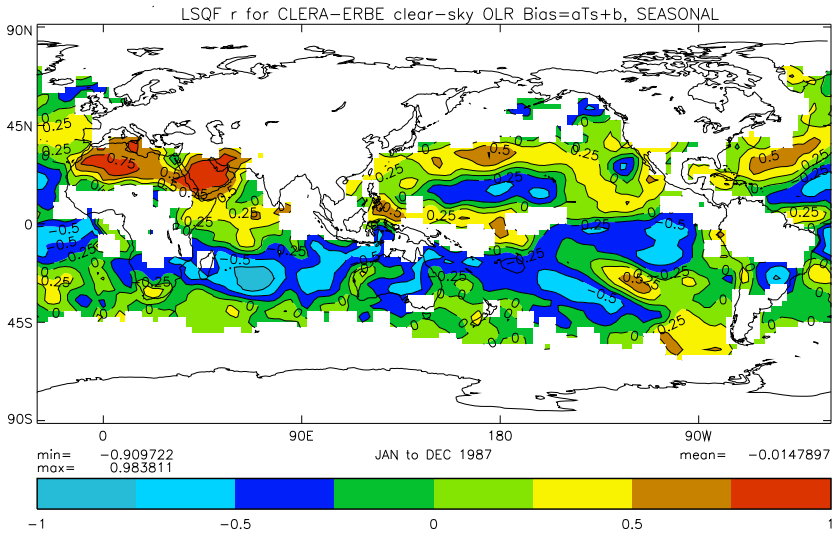


Figure 6.6: *LSQF correlation between CLERA-ERBE $OLR_c$ differences and $T_s$ over the seasonal cycle of 1987. Grid points that contain missing monthly mean ERBE clear-sky OLR data for any of 1987 are discarded. Significant correlation at the 95% confidence level is attained where $\mid r \mid > 0.58$.*

### 6.4.1 Surface temperature

The general pattern of correlation for CLERA $\mathrm{OLR}_c$ shown in Chapter 5 is reproduced by ERBE (not shown). The difference between ERBE and CLERA is highlighted in Fig. 6.6 by plotting the correlation between CLERA minus ERBE $\mathrm{OLR}_c$ differences ($\delta OLR_c$) and $T_s$. Regions displaying a negative correlation between $\delta OLR_c$ and $T_s$ also correspond loosely to the SGE regions identified in Chapter 5. This may be explained by considering that SGE regions are explained by the significant change in convective regime associated with changes in $T_s$ (Bony *et al.* (1997b)). Because CLERA $\mathrm{OLR}_c$ tends to be less than ERBE values over convective regimes, and the opposite is generally true over subsiding regimes (e.g. Slingo *et al.* (1998)), a strengthening of convective regime associated with increased $T_s$ will lead to a decrease in $\delta OLR_c$. Thus the ERBE observed clear-sky SGE appears too weak compared to that simulated by CLERA; this is supported by observational evidence in the tropical Pacific (Valero *et al.* (1997)).

A positive correlation between $\delta OLR_c$ and $T_s$ is present over Saudi Arabia and the Sahara. This is consistent with the surface emissivity ($\epsilon_s$) being significantly less in these regions than the value of 1.0 prescribed by ERA, which will therefore cause an overestimate in CLERA $\mathrm{dOLR}_c/\mathrm{d}T_s$. An apparent overestimate of CLERA $\mathrm{OLR}_c$ of order 10 $Wm^{-2}$ is present throughout the year for this region. Slingo *et al.* (1998) performed sensitivity calculations using the CLERA simulation system and found this disparity to be consistent with the simulated minus observed difference in $\epsilon_s$. Errors in ERA $T_s$, while being significant with

regard to the $OLR_c$ in this region, were found by Slingo *et al.* to be of the wrong sign to explain the $OLR_c$ differences in winter months. Although prescription of unit $\epsilon_s$ may explain the simulated $OLR_c$ overestimation in the Sahara, errors in the ERBE detection of cloud cannot be discounted as an alternative explanation and requires further investigation. This is beyond the scope of the present study however.

### 6.4.2 Relative Humidity

The positive correlation between $\delta OLR_c$ and $T_s$ over regions experiencing large changes in convective regime suggest that the large changes in $RH$ also experienced may be important in determining the nature of the $OLR_c$ disparity. The regression between $OLR_c$ and 200 to 800 $hPa$ column mean $RH$ was carried out for CLERA, ERBE and the CLERA-ERBE difference ($\delta OLR_c$) for the seasonal and interannual time scales. For each regression, only grid points containing data for the entire period were considered. A strong negative correlation within 30° of the tropics for CLERA $OLR_c$ is similar to the pattern calculated for 1985 in Chapter 5. The area covered by significant negative correlation between $OLR_c$ and $RH$ is smaller for ERBE than CLERA (not shown). The reduced correlation may be due to a poor representation of humidity variations by ERA. To explore the nature of the disparity it is instructive to calculate the regression between the differences in $OLR_c$ between ERBE and CLERA and the $RH$ (Fig. 6.7) With decreasing column-mean $RH$, $\delta OLR_c$ becomes more positive. Again, this is consistent with the known negative ERBE $OLR_c$ bias over subsiding regions and the positive bias over convective regions (Slingo *et al.* (1998), Collins and Inamdar (1995)). Similar results are drawn by plotting the interannual correlation (not shown) although the $OLR_c$ difference shows even stronger correlation with $RH$, most especially over the tropical warm pool.

Figure 6.8 shows the calculated $dOLR_c/dRH$ for CLERA and ERBE, and also the sensitivity of the ERBE-CLERA $OLR_c$ difference to changes in $RH$ ($\frac{d(-\delta OLR_c)}{dRH}$), for 5% bins of mean $RH$ over the seasonal cycle of 1988. One standard deviation about the mean for each bin is plotted as an error bar. CLERA $dOLR_c/dRH$ is significantly more negative, typically by about 0.2 $Wm^{-2}$ per %, than that of ERBE for all values of $RH$. This difference is even larger, about 0.3 to 0.4 $Wm^{-2}$ per %, over the interannual time scale (not shown). To explain this result, the seasonal changes in $\delta OLR_c$ are considered for the region 65 to 75° E and 10 to 30° S. Fig. 6.9 shows the change in $\delta OLR_c$ to be negatively correlated with 450 $hPa$ $RH$. Between June and August CLERA $OLR_c$ is of order 2 $Wm^{-2}$ greater than that of ERBE. The reverse is true at other times of the year with CLERA $OLR_c$ being 5 $Wm^{-2}$ less than ERBE values in March. While the $OLR_c$ difference is generally within the estimated ERBE error of $\pm 5$ $Wm^{-2}$ the trend highlights two mechanisms acting

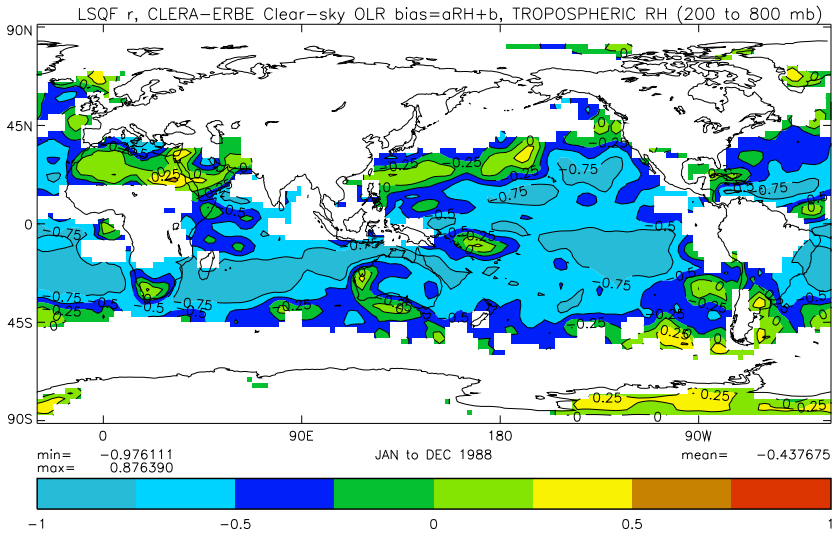


Figure 6.7: *LSQF correlation between CLERA-ERBE $OLR_c$ bias ($\delta OLR_c$) and 200 to 800 hPa column mean RH over the seasonal cycle of 1988. Grid points that contain missing monthly mean ERBE clear-sky OLR data for any of 1988 are discarded. Significant correlation at the 95% confidence level is attained where* $\mid r \mid > 0.58$.

that effectively reduce the $\mathrm{OLR}_c$ response to changes in $RH$ given by ERBE compared to climate models. Firstly, the positive $\delta OLR_c$ when $RH$ is low may be explained by cloud contamination of ERBE clear-sky fluxes which are believed to cause an underestimation in ERBE $\mathrm{OLR}_c$ (e.g. Slingo and Webb (1992)). Secondly, the negative $\delta OLR_c$ when $RH$ is high can be ascribed to the different temporal and spatial sampling of clear-sky fluxes between ERBE and CLERA. Because ERBE preferentially samples lower $RH$ than that given by ERA which samples $RH$ for clear *and* cloudy conditions, ERBE appears not to reproduce as low values of $\mathrm{OLR}_c$ compared to the simulated values. The over active ITCZ in ERA (Kallberg (1997)) may alternatively explain the change in $\delta OLR_c$ over the seasonal cycle. However, the positive ERBE $\mathrm{OLR}_c$ bias for regions of high $RH$ and negative $\mathrm{OLR}_c$ bias for when $RH$ is low is also reproduced in the tropics using different sets of analyses (Ho *et al.* (1998)). The previous explanations therefore appear to explain why the $\mathrm{OLR}_c$ variability as given by ERBE is less than that given by CLERA for the given variation of ERA $RH$.

An increase in the likelihood of scene mis-identification with decreasing humidity for the regions of low $RH$ is likely to explain the increased $d(-\delta OLR_c)/dRH$ shown in Fig. 6.8. Consider a convectively suppressed region of low free-tropospheric $RH$. If low-altitude cloud is present, the high transmission of longwave radiation through the dry atmosphere above the cloud top may cause mis-identification of clear-skies by the ERBE cloud detection

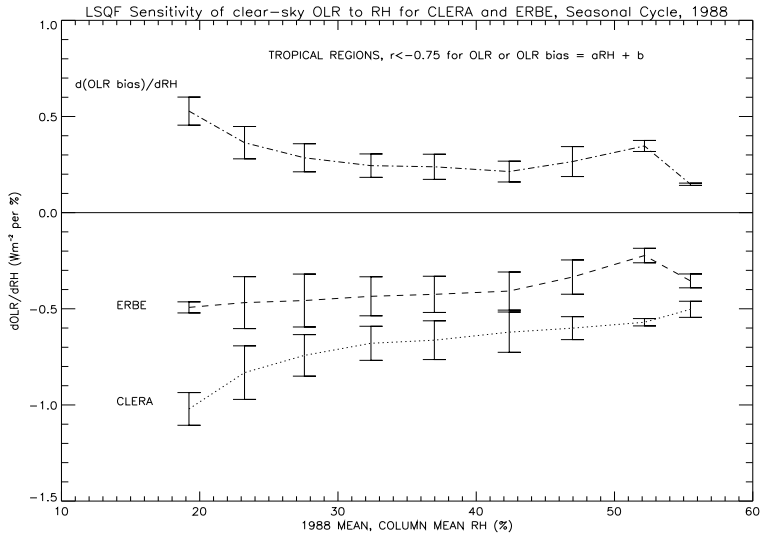


Figure 6.8: *LSQF $dOLR_c/dRH$ for CLERA, ERBE and the ERBE-CLERA $OLR_c$ bias ($-\delta OLR_c$) for 5% bins of RH for the seasonal cycle of 1988. One standard deviation about the mean is plotted for each bin as an error bar and are displayed to highlight the statistical scatter associated with the calculated sensitivity rather than the physical uncertainty associated with the models and data. Only regions for which r < -0.75 for all three regressions are considered.*

algorithm. For regions of high humidity, the different methods of defining $OLR_c$ between ERBE and CLERA explain the disparity. Because ERA parameters, including $RH$, are assimilated for all-sky conditions, the inconsistency with ERBE clear-sky products suggest that it is of more relevance to utilise the CLERA irradiance products in the present study. In validating the simulated $OLR_c$ and its variability using the ERBE clear-sky products, the irradiance for the $RH$ as sensed by ERBE clear-sky scenes must be considered and attempt must be made to remove cloud contamination biases.

## 6.5 All-sky Irradiance Sensitivity to Surface Temperature

The presence and variability of cloud amount and properties contribute to the variability of the Earth's radiation budget significantly, as discussed in Chapters 1 and 3. Section 6.3 characterised the top of atmosphere radiation budget variability by calculating the seasonal and interannual irradiance standard deviations. The purpose of this section is to build on this analysis by ascertaining how the presence and variability of cloud affects the clear-sky irradiance sensitivity to changes in ERA $T_s$. The clear-sky longwave analysis presented in Chapter 5 is extended by using the ERBE all-sky irradiance in conjunction with the $OLR_c$ simulated by CLERA, in particular assessing how the longwave and shortwave cloud effects influence the SGE situation.

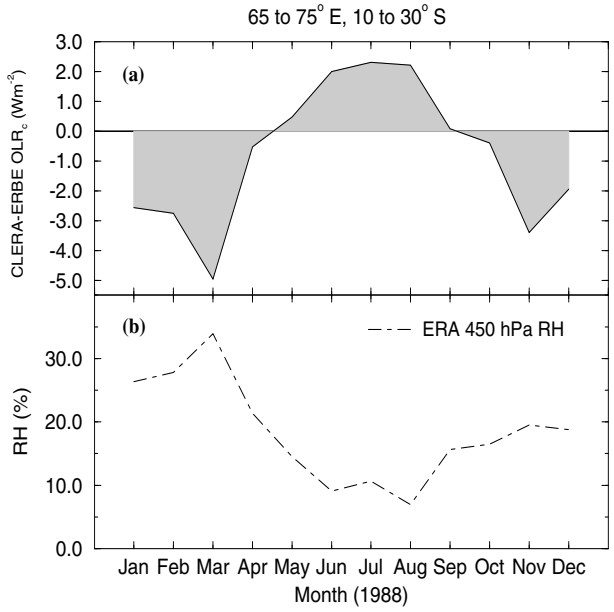


Figure 6.9: *Changes in (a) CLERA minus ERBE $OLR_c$ and (b) ERA 450 hPa RH over the seasonal cycle of 1988.*

### 6.5.1 Seasonal Cycle

Figure 6.10 shows the correlation coefficient for ERBE all-sky OLR (top) and CLERA-ERBE inferred $LWCF$ (bottom) with $T_s$ for the seasonal cycle of 1988. There is a strong positive correlation between OLR and $T_s$ at latitudes greater than about 30°. At lower latitudes the correlation tends to be negative, highlighting the regions experiencing a SGE. The correlation distribution for OLR is similar to that displayed in Chapter 5 for $OLR_c$ over the seasonal cycle of 1985 (Fig. 5.1(a)) and is consistent with work by Raval *et al.* (1994) and Bony *et al.* (1997b). The SGE regions are similar for clear-sky and all-sky conditions indicating that changes in $LWCF$ do not offset the clear-sky SGE. This is to be expected, because the increase in atmospheric moisture with $T_s$, crucial in explaining the clear-sky SGE, is likely to be associated with an increase in (deep convective) cloud amount. Therefore the decreases in OLR due to increased moisture will be compounded by a further reduction in OLR due to a larger greenhouse effect of clouds. By plotting the correlation coefficient between the $LWCF$ and $T_s$ (Fig. 6.10 (bottom)) it is evident that the magnification of the SGE by clouds is strongest in the tropical central Pacific where the correlation is strongly positive. Here an increase in temperature is associated with diminished OLR due to changes in cloud amount as inferred from changes in the difference between clear-sky and all-sky OLR with changes in $T_s$. Over mid-latitude ocean regions, the correlation tends to be negative. Here an increase in $T_s$ is accompanied by a decrease in $LWCF$. Positive correlation over Canada and Eastern Eurasia indicate an increase in

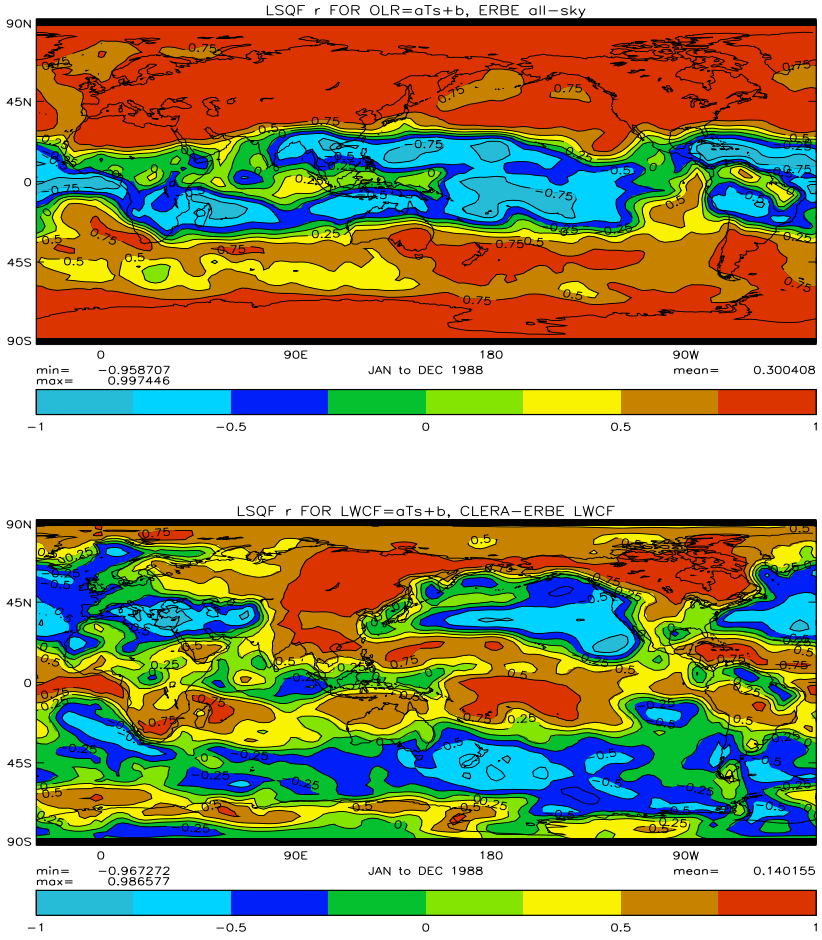


Figure 6.10: *LSQF correlation coefficient for ERBE all-sky OLR=$aT_s+b$ and (top) and CLERA-ERBE inferred LWCF=$aT_s+b$ (bottom) for the seasonal cycle of 1988. Significant correlation at the 95% confidence level is attained where* $\mid r \mid > 0.58$.

$LWCF$ with increasing $T_s$.

The calculated sensitivity of OLR and $\mathrm{OLR}_c$ to changes in $T_s$ are plotted as a function of the mean surface temperature for 1988 in Fig. 6.11. Below temperatures of about 273 $K$, the effect of clouds is to reduce the sensitivity of $\mathrm{OLR}_c$ to changes in $T_s$ while the reverse is true for temperatures between about 273 and 298 $K$, in particular over the high latitude ocean regions. Above about 298 $K$, $\mathrm{dOLR}_c/\mathrm{d}T_s$ is negative, denoting the clear-sky SGE. However, ERBE $dOLR/dT_s$ is about four times more negative than the clear-sky sensitivity for temperatures above about 300 $K$. Therefore the longwave radiative effect of clouds magnify the clear-sky SGE substantially, as denoted by a strong increase in $LWCF$ with increasing $T_s$.

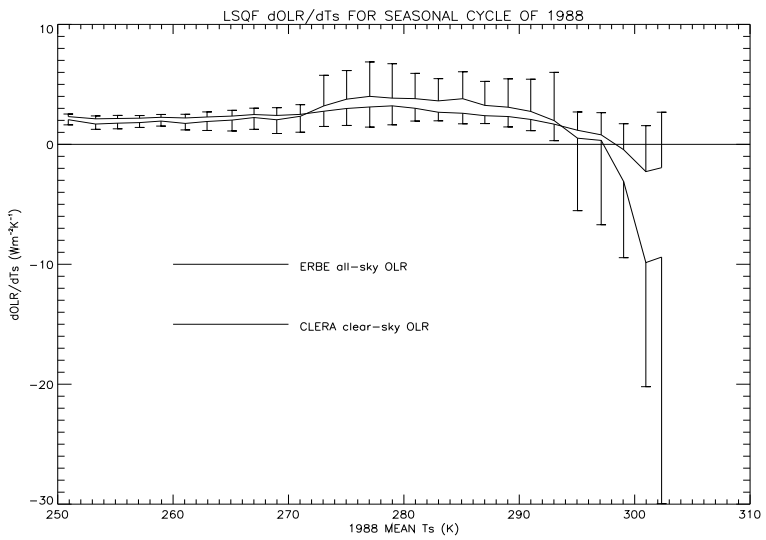


Figure 6.11: *Least squares fit $dOLR/dT_s$ for CLERA clear-sky and ERBE all-sky OLR with mean $T_s$ for the seasonal cycle of 1988. Error bars denote one standard deviation of values for each $T_s$ bin and are plotted either above or below the mean value only for reasons of clarity. The bars are displayed to highlight the statistical scatter associated with the calculated sensitivity rather than the physical uncertainty associated with the models and data.*

### 6.5.2 Interannual time-scale

Figure 6.12 shows the correlation coefficient for OLR=a$T_s$+b for (a) CLERA $OLR_c$ and (b) ERBE all-sky OLR over the interannual time-scale. The general pattern of correlation for $OLR_c$ is similar to that presented in Chapter 5, which shows the consistency between the two methods for inferring interannual sensitivities. The strong positive correlation at high latitudes for $OLR_c$ is not present in the ERBE all-sky OLR calculations, indicating that the presence of clouds reduces the OLR variability due to changes in $T_s$. This conclusion only holds where $LWCF$ is significant; errors in ERA $T_s$ may also reduce the correlation between ERBE OLR and $T_s$. Negative correlation in the tropical central Pacific shown in Fig. 6.12(a) highlight regions experiencing a clear-sky SGE. This signal is much stronger for ERBE all-sky OLR (Fig. 6.12(b)), indicating that clouds act to enhance the clear-sky SGE. This is further highlighted by plotting the CLERA-ERBE inferred $LWCF$ correlation with $T_s$ (Fig. 6.13(a)). The strong positive correlation between longwave cloud radiative forcing and $T_s$ present over the tropical central Pacific show that an increase in $T_s$ is associated with an increase in $LWCF$ in these regions. Plotting the correlation between ERBE ASR and $T_s$ (Fig. 6.13(b)) it is shown that strong *negative* correlation is present over the tropical central Pacific, indicating that the shortwave effects of clouds counteract the longwave effects over the interannual time-scale in this region. There are few regions of strong correlation between ERBE net radiation and $T_s$ indicating that the shortwave irradiance variability cancels out

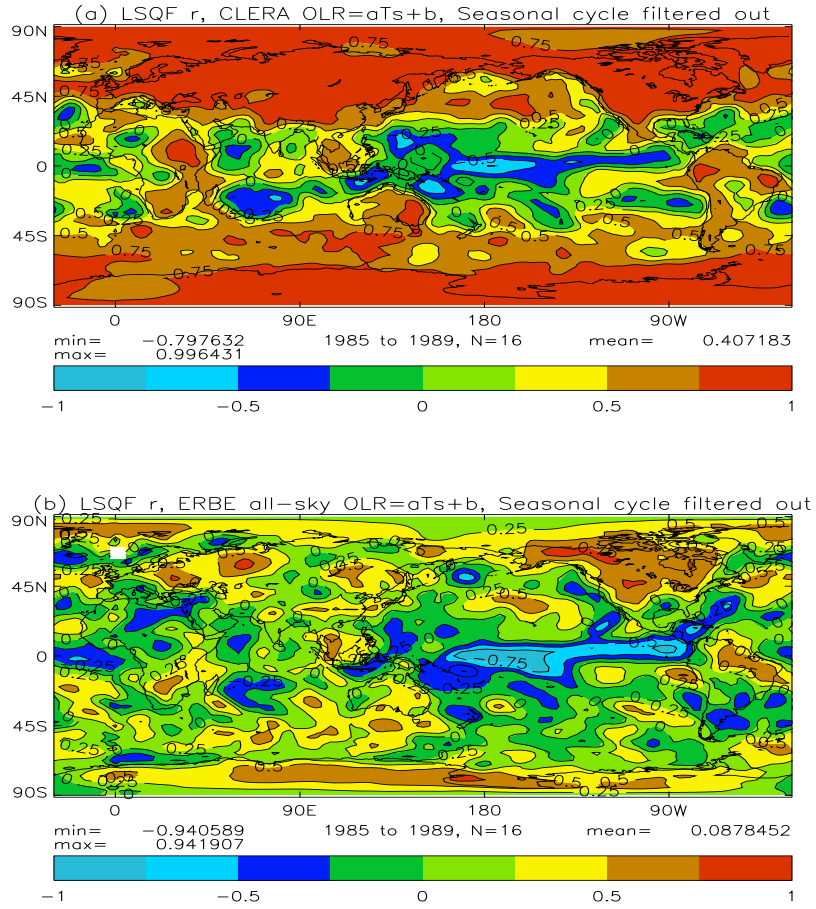


Figure 6.12: *Least squares fit correlation coefficient for OLR=$aT_s$ +b for (a) CLERA clear-sky OLR and (b) ERBE all-sky OLR for the interannual time scale. Significant correlation at the 95% level is attained at* $| r | > 0.5$.

the longwave radiation variability. However, in the tropical central and eastern Pacific there is significant positive correlation (Fig. 6.13(c)). The situation in the tropical central Pacific appears to be mirrored in mid-latitude regions of the northern central Pacific. Here the correlation between $ASR$ and $T_s$ is positive, while the $LWCF$ is negatively correlated, albeit weakly, with $T_s$. In the tropical eastern Pacific, positive correlation between $LWCF$ and $T_s$ are combined with only weak negative correlation between $ASR$ and $T_s$.

The sensitivity of irradiance to changes in $T_s$ are plotted with 1 $K$ bins of mean $T_s$ between 290 and 302 $K$ in Fig. 6.14. The tropical Pacific (100° E to 100° W; 30° S to 30° N) is considered to increase the signal to noise ratio, and to allow comparison with Bony *et al.* (1997a). Error bars denote one standard deviation about the mean for each

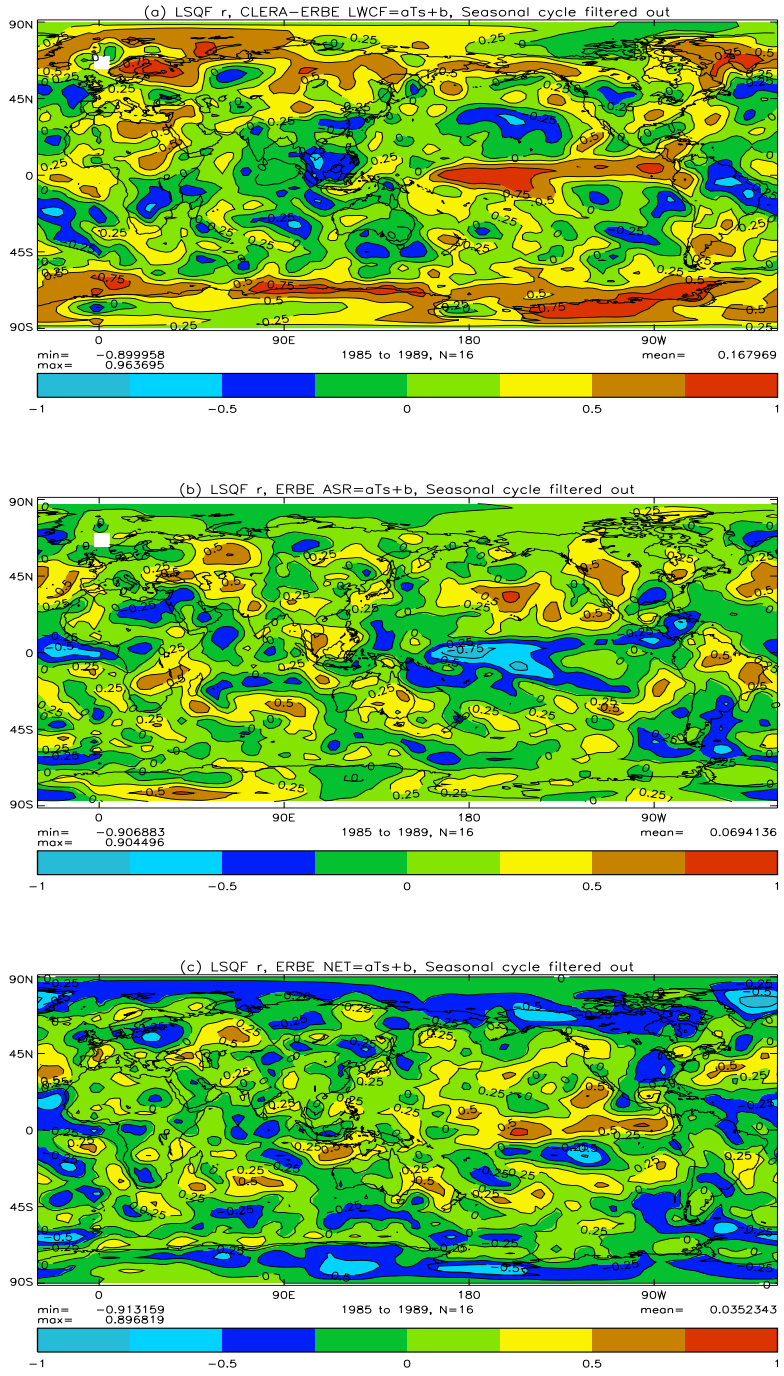


Figure 6.13: *LSQF correlation coefficient for (a) CLERA-ERBE inferred LWCF=$aT_s+b$ and (b) ERBE ASR=$aT_s+b$ and (c) ERBE NET=$aT_s+b$ for the interannual time scale. Significant correlation at the 95% level is attained at $|r| > 0.5$.*

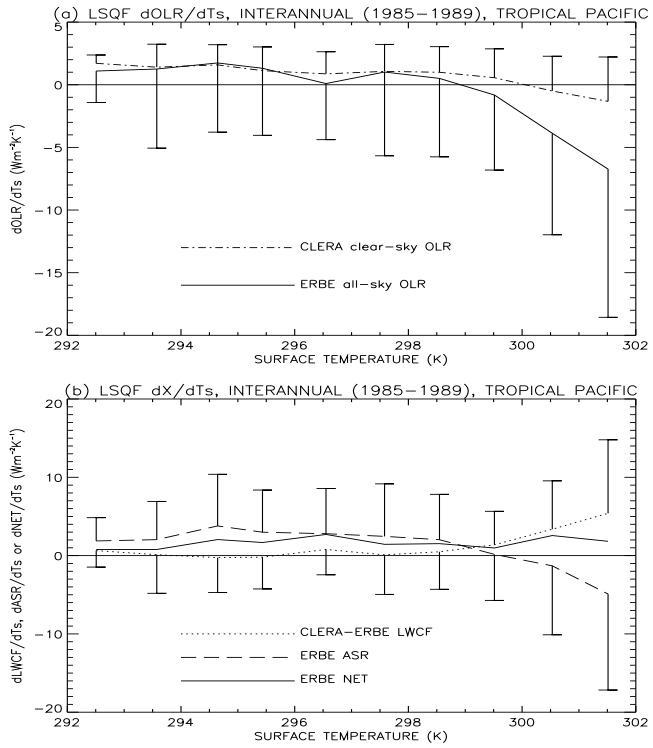


Figure 6.14: *Least squares fit sensitivity of (a) ERBE all-sky OLR and CLERA clear-sky OLR and (b) CLERA-ERBE longwave cloud radiative forcing, ERBE absorbed solar radiation and ERBE net downwelling top of atmosphere radiation to changes in $T_s$ for 1 K $T_s$ bins for the interannual time scale over the tropical Pacific. Error bars represent one standard deviation about the mean value for the temperature bin and are plotted either above or below the line only. The bars are displayed to highlight the statistical scatter associated with the calculated sensitivity rather than the physical uncertainty associated with the models and data.*

$T_s$ bin, and are plotted either above or below the lines only for clarity. At high $T_s$ all-sky $dOLR/dT_s$ is strongly negative, but with a large scatter about the mean value. Again, the clear-sky SGE is magnified by the effects of clouds. The $\mathrm{OLR}_c$ sensitivity to changes in $T_s$ are similar to those calculated by Bony *et al.* (1997a) who consider monthly differences between 1988 and 1987 for individual temperature bins and plot sensitivity with July 1988 mean sea surface temperature.

Fig. 6.14(b) shows CLERA-ERBE inferred $dLWCF/dT_s$ and ERBE $dASR/dT_s$ and $dNET/dT_s$ with mean $T_s$ for the same interannual time-scale. Below 298 $K$, the sensitivity of $ASR$ to changes in $T_s$ tend to dominate over the $LWCF$, which shows a small sensitivity to $T_s$. Thus $dNET/dT_s$ is also positive, although over most regions this positive relationship is not statistically significant. This implies that low level stratus cloud may be important in these regions; changes in low cloud amount, for example, produce only a

small change in $LWCF$ due to relatively high cloud top temperatures, while they effectively increase the albedo of the surface (e.g. Sinha and Shine (1995)). Because $dASR/dT_s$ is generally positive in these $T_s$ bins, it is postulated that changes in cloud amount and/or properties associated with an increase in $T_s$ act to decrease the reflectivity of the Earth-atmosphere system. One mechanism for this would be a decrease in low cloud amount with increasing $T_s$ over the interannual time-scale. Decreases in cloud optical depth with surface temperature over ocean regions, which may also explain this result, have been observed by Tselioudis *et al.* (1992).

At high $T_s$ there is an increased scatter of sensitivities for each temperature bin. However, there is a tendency for $dLWCF/dT_s$ to be positive (denoting an amplification of the clear-sky SGE) and for $dASR/dT_s$ to be negative. The shortwave and longwave cloud effect tend cancel each other in terms of the radiation budget response to changes in $T_s$ at the top of the atmosphere over the interannual time scale. This cancellation was noted by Ramanathan and Collins (1991) who ascribed it to an increase in deep convective cloud associated with $T_s$ for the highest tropical surface temperatures. Kiehl (1994) argued that this cancellation is a fortuitous facet of the tropical tropopause height. This result is also highlighted by Bony *et al.* (1997a) although the different analysis method used gives cloud forcing values approximately double those of the present study for the ERBE data. A positive $dNET/dT_s$ for high $T_s$ is evident in Fig. 6.14(b) despite the cancelling between longwave and shortwave cloud radiative forcing. This may be explained in part by the clear-sky SGE (negative $\mathrm{dOLR}_c/\mathrm{d}T_s$) contribution to the changes in the all-sky radiation budget. Considering Fig. 6.13(c), it is apparent that significant positive correlation between NET and $T_s$ is mainly distributed across the central and eastern equatorial zone. These areas are subject to generally large atmospheric and oceanic divergence which are therefore likely to re-distribute heat from the positive radiative feedback over the interannual time-scale. Despite the small sensitivity of longwave cloud radiative forcing to changes in $T_s$ at temperatures below 299 $K$, the sensitivity of net radiation at the top of the atmosphere is significantly less than $dASR/dT_s$; again, the contribution of the clear-sky longwave effects (positive $dOLR_c/dT_s$) explains this.

### 6.5.3 Regional Studies

The correlation studies of the previous section show regions of strong coupling between components of the radiation budget at the top of the atmosphere and $T_s$. The nature of this strong coupling is now assessed. Three regions are chosen for this purpose and are defined in Table 6.2. These regions all show significant correlation between cloud radiative forcing and $T_s$ over the interannual time-scale (Fig. 6.13).

Table 6.2: *Definition and mean irradiance for three regions. Values in parentheses denote the standard deviation for monthly mean anomalies (i.e. over the interannual time scale). NCP = north central Pacific, TCP = tropical central Pacific and TEP = tropical east Pacific.*

| Region | Boundary | $T_s$ $(K)$ | $LWCF$ $(Wm^{-2})$ | $ASR$ $(Wm^{-2})$ | $NET$ $(Wm^{-2})$ |
|---|---|---|---|---|---|
| NCP | 30 to 45°N, 170 to 210°E | 290.5 (0.5) | 37.7 (3.2) | 277.3 (4.8) | -0.8 (4.3) |
| TCP | -10 to 10°N, 170 to 200°E | 301.7 (0.7) | 39.9 (12.6) | 323.7 (13.5) | 16.1 (3.5) |
| TEP | 0 to 10°N, 220 to 280°E | 299.5 (0.8) | 30.3 (6.0) | 312.1 (6.4) | 58.6 (5.0) |

The tropical eastern Pacific (TEP) receives the most net radiation at the top of the atmosphere, but the highest mean $T_s$ are encountered in the tropical central Pacific (TCP). The northern central Pacific (NCP) receives a net deficit in radiation at the top of the atmosphere. Here the interannual variability (denoted by the interannual standard deviation displayed in parentheses) of ASR is greater than that of $LWCF$ and tends to contribute the most to the variability in the net radiation. Over the TCP, the variability of $LWCF$ and ASR are similar in magnitude and the anomalies opposite in sign. This is evident when plotting monthly mean ASR, $LWCF$, and $T_s$ anomalies from 1985 to 1990 (Fig. 6.15). The strong coupling between ASR, $LWCF$ and $T_s$ as highlighted in Fig. 6.12 is also evident in the time series. Changes in $T_s$ are associated with variations of $LWCF$ of like sign and changes in ASR of opposite sign. This is a likely result of the coupling between deep convective cloud amount and $T_s$ variation over the 1987-1988 ENSO event. The compensation between ASR and $LWCF$ is particularly revealing; a correlation coefficient of -0.96 is calculated between ASR and $LWCF$ anomalies. The gradient $dASR/dLWCF$ of -1.0 implies a near perfect cancellation of shortwave and longwave effects of clouds at the top of the atmosphere over this region. This had been previously explored by Kiehl (1994). Pierrehumbert (1995) argued that this result minimises the importance of cloud on the top of atmosphere radiation budget in these regions. However, the shortwave cloud radiative effects are manifest at the surface while the longwave cloud radiative effects generally affect the atmospheric radiative cooling (e.g. Harshvardhan *et al.* (1989)). Thus it is naive to argue that the radiative impact of changes in deep convective cloud on climate may be discounted.

There is less compensation between $ASR$ and $LWCF$ in the tropical eastern Pacific (Fig. 6.15(b)) than for the central Pacific (Fig. 6.15(a)). The stronger coupling between $LWCF$ and $T_s$ than for $ASR$ and $T_s$ is apparent in the TEP; Ringer and Shine (1997) explained similar findings for the 1983 ENSO in terms of decoupling between low-altitude cloud

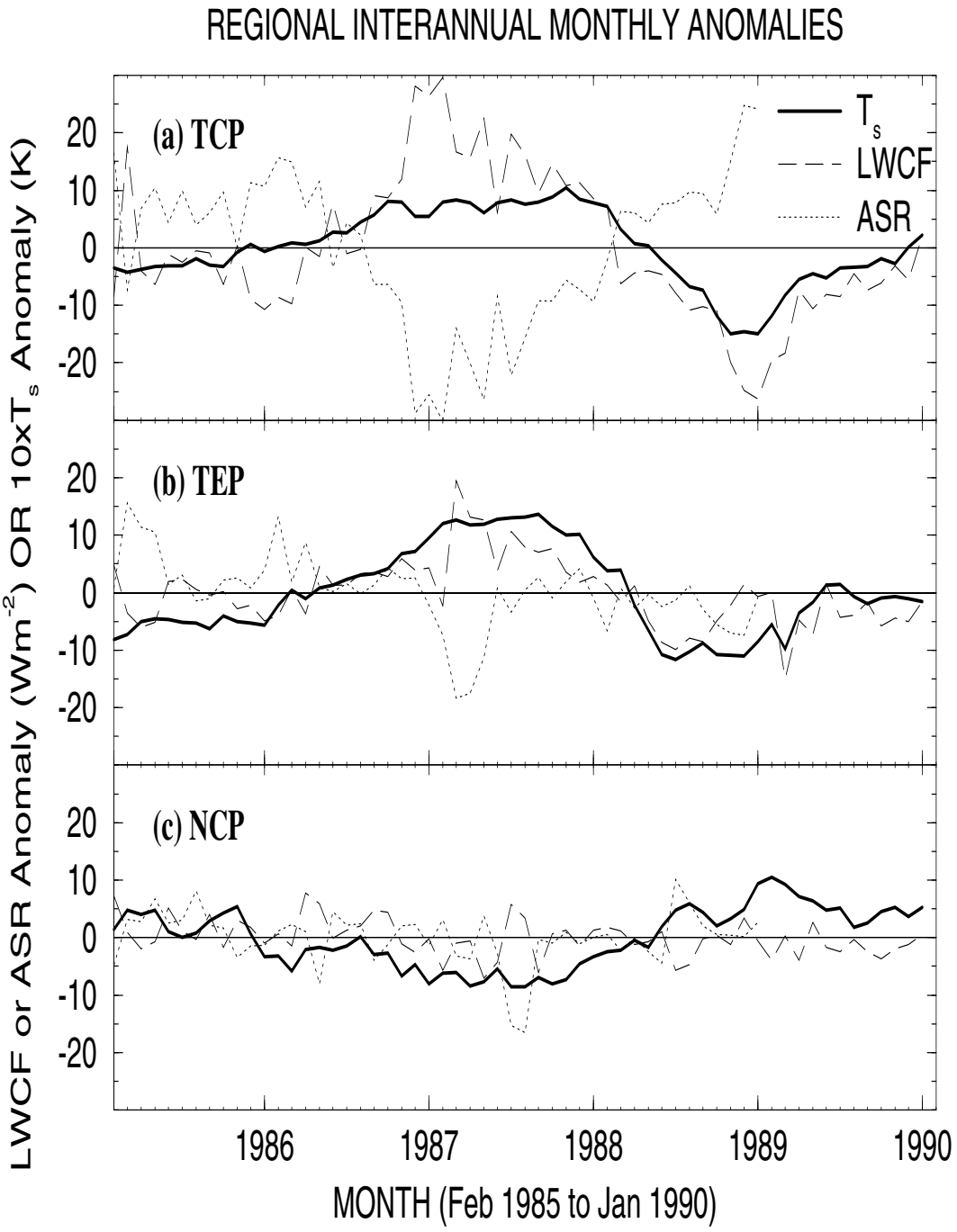


Figure 6.15: *Interannual monthly anomalies of ASR ($Wm^{-2}$), LWCF ($Wm^{-2}$) and $T_s$ ($10 \times K$) for (a) the tropical central Pacific (TCP), (b) the tropical eastern Pacific (TEP) and (c) the northern central Pacific (NCP).*

amount and higher altitude cloud amount. The apparent negative relationship between $T_s$ and $ASR$ in the NCP illustrated in Fig. 6.13(b) is determined primarily by the strong negative $ASR$ anomaly during June and July of 1987 and the positive anomaly the following, warmer July (Fig. 6.15(c)).

Surface warming in the TCP and TEP is generally associated with increases in the net radiation received at the top of the atmosphere with $dNET/dT_s$ of 3.4 $Wm^{-2}K^{-1}$ for the TCP and 4.2 $Wm^{-2}K^{-1}$ for the TEP with significant correlation at the 99.9% significance level. This is due to the SGE dominating over the cloud albedo effect over the TCP: where the shortwave and longwave cloud radiative effects cancel at the top of the atmosphere, the strong clear-sky greenhouse effect dominates the net radiation budget. Over the TEP, a positive feedback due to the longwave radiative effects of cloud tends to dominate the net radiation budget at the top of the atmosphere.

## 6.6 All-sky Irradiance Sensitivity to Relative Humidity

Chapter 5 highlighted the strong dependence of $\mathrm{OLR}_c$ on changes in $RH$, especially in tropical regions. Because cloud amount and liquid water path are determined to a large extent by $RH$, the OLR response to changes in this parameter is dependent on the direct clear-sky effects and also the indirect effects of changes in cloud amount and properties. Shortwave cloud radiative forcing will also be affected indirectly by $RH$ if indeed cloud amount is strongly dependent on $RH$.

### 6.6.1 Seasonal Cycle

Figure 6.16 shows the correlation coefficient for (a) CLERA $\mathrm{OLR}_c$ and (b) ERBE all-sky OLR with $RH$ and also for (c) CLERA-ERBE inferred $LWCF$ with $RH$ for the seasonal cycle of 1988. The clear-sky correlation distribution is similar to that presented in Chapter 5 (Fig. 5.6(a)) despite the different year and alternative definition of tropospheric $RH$ used. All-sky OLR shows a similar correlation distribution, to the clear-sky case, with strong negative correlation of less than -0.75 over much of the tropics. Regions of strong positive correlation south of New Zealand and across north eastern China, which highlight areas where temperature effects are both dominating and counteracting the effects of $RH$ changes on the OLR, are also common to both clear and all-sky OLR. Figure 6.16(c) shows that $LWCF$ is positively correlated with $RH$ over large portions of the globe. Studies such as J.M. Slingo (1980) have shown cloud amount to be related to $RH$. It is therefore likely that increases in $RH$ lead to an increase in cloud amount which in turn acts to decrease OLR. Changes in cloud properties and cloud altitude, however, may also be correlated with

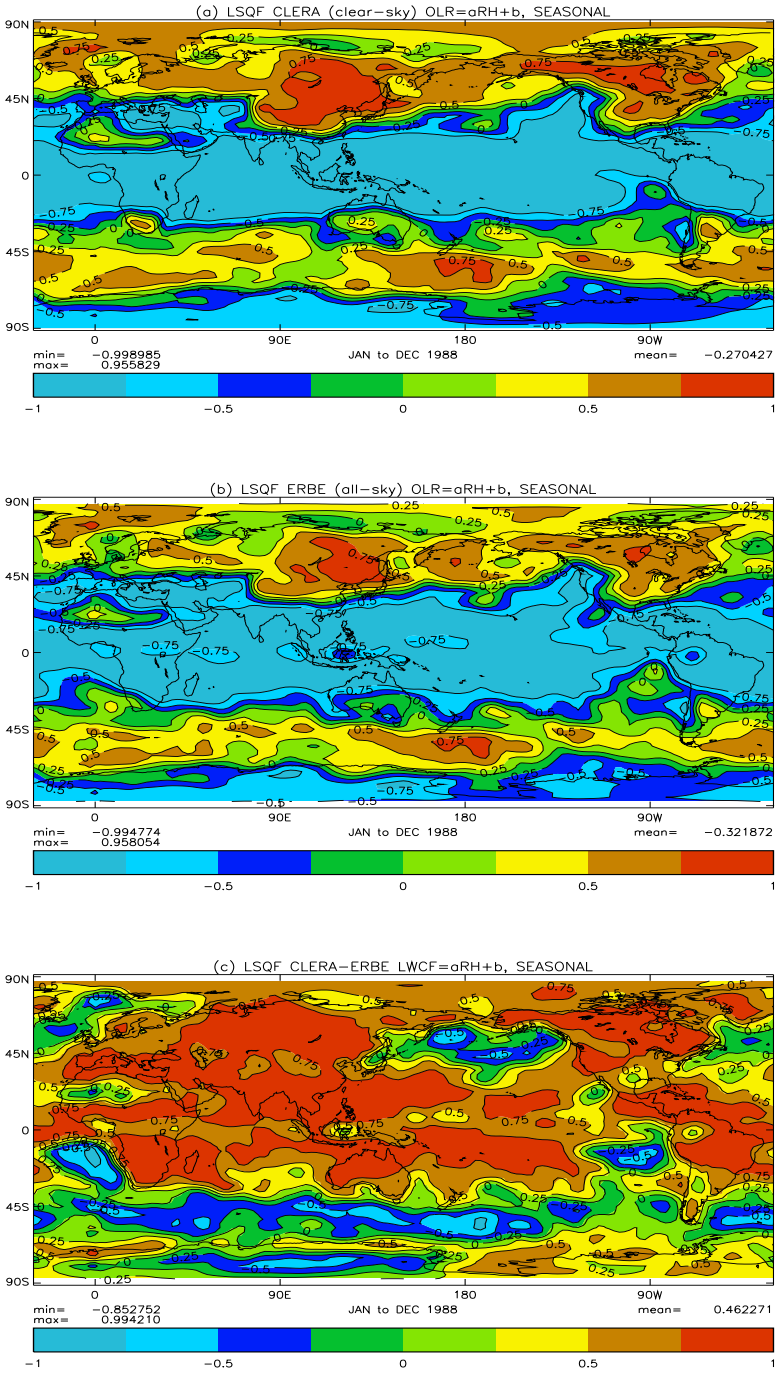


Figure 6.16: *LSQF correlation coefficient for (a) CLERA clear-sky OLR=aRH+b, (b) ERBE all-sky OLR=aRH+b and (c) ERBE-CLERA inferred LWCF=aRH+b for the seasonal cycle of 1988. RH is defined as the column mean relative humidity weighted by pressure thickness of slab between 200 and 800 hPa. Significant correlation at the 95% confidence level is attained for* $\mid r \mid > 0.58$.

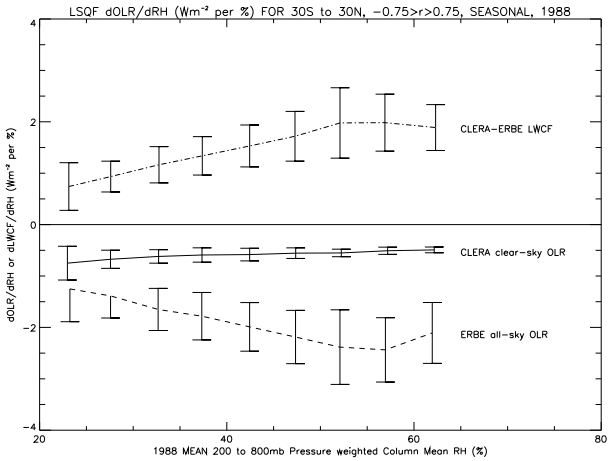


Figure 6.17: *LSQF dOLR/dRH for CLERA clear-sky and ERBE all-sky OLR with mean RH for the seasonal cycle of 1988. Also plotted is the CLERA-ERBE inferred dLWCF/dRH. Grid points within 30 ° of the equator for which* $-0.75 > r > 0.75$ *are used. One standard deviation about the mean is plotted as an error bar for each bin and are displayed to highlight the statistical scatter associated with each calculated sensitivity rather than the physical uncertainty associated with the models and data.*

$RH$ thus rendering this argument over-simplistic.

The irradiance sensitivity to changes in $RH$ is plotted for 5% bins of mean $RH$ over the seasonal cycle of 1988 (Fig. 6.17). Grid points of significant correlation at the 99.5 % confidence level are used, with error bars denoting one standard deviation about the mean sensitivity for the bin. The tendency for the $\mathrm{OLR}_c$ sensitivity to changes in $RH$ to become more negative for lower $RH$, described in the previous chapter, is reproduced using the different definitions of column mean $RH$. However, for $RH$ of less than 50%, the opposite is true when considering all-sky OLR. The sensitivity of $LWCF$ to changes in $RH$ tends to increase with increasing humidity for $RH < 50\%$. This may be explained as follows: when $RH$ is low for a given grid point, the fraction of the grid point that may potentially become overcast following an increase in $RH$ is also low. At progressively higher grid mean $RH$, the fractional area that may become overcast for a given increase in $RH$ is likely to increase. Thus the sensitivity of $LWCF$ to changes in $RH$ increases with the mean $RH$ for each grid point. In the most moist regions (i.e. $RH > 50\%$) the fractional area that is already overcast is likely to be large; thus further increases in grid mean $RH$ will produce marginally smaller increases in cloud amount and consequently smaller increases in $LWCF$. An extreme case would be where the entire grid point is overcast - here increases in $RH$ will fail to increase cloud amount further. Changes in cloud properties associated with changes in $RH$ complicate this simple explanation.

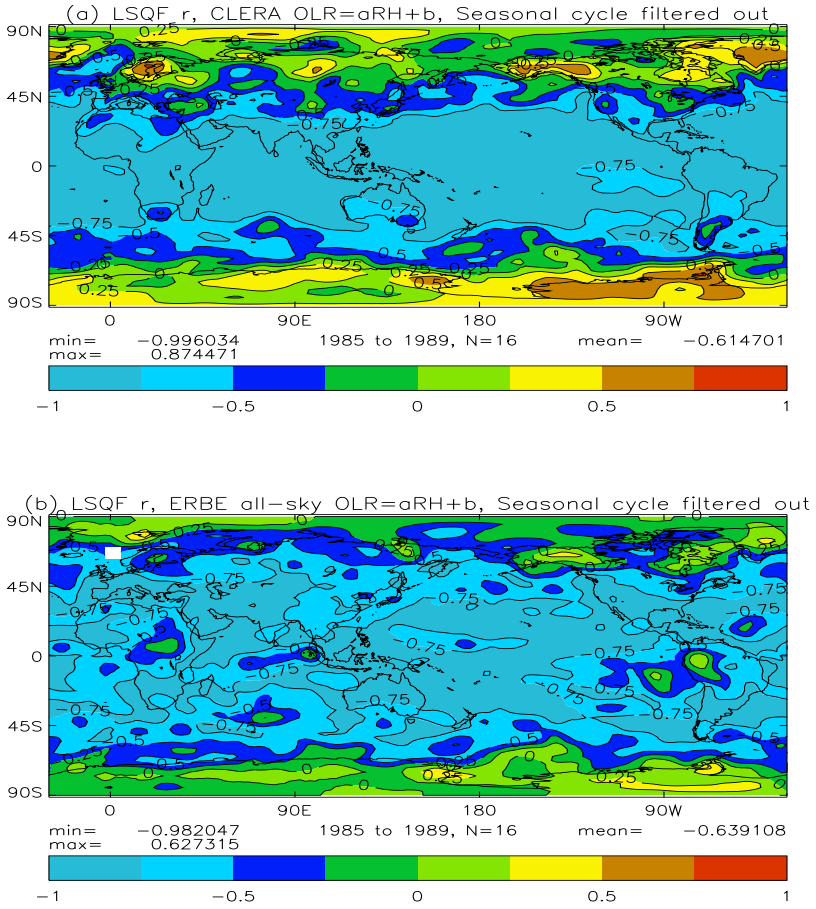


Figure 6.18: *LSQF correlation coefficient for OLR=aRH+b for (a) CLERA clear-sky OLR and (b) ERBE all-sky OLR for the interannual time scale. Significant correlation at the 95% confidence level is attained where* $| r | > 0.5$.

### 6.6.2 Interannual Time-Scale

The strong negative correlation between $\mathrm{OLR}_c$ and $RH$ over the interannual time scale in Chapter 5 is reproduced for the different method of inferring interannual statistics, and for the alternative definition of $RH$ (Fig. 6.18(a)). For ERBE all-sky OLR, the regions of strongest correlation are less coherent although there is a negative correlation for most grid points (Fig. 6.18(b)). Globally, changes in $RH$ appear to be more important with regard to both clear-sky and all-sky OLR over the interannual time-scale than over the seasonal time scale.

Generally, $LWCF$ shows positive correlation with $RH$ (Fig. 6.19(a)) while ASR shows a negative correlation (Fig. 6.19(b)), although there are notable exceptions such as the

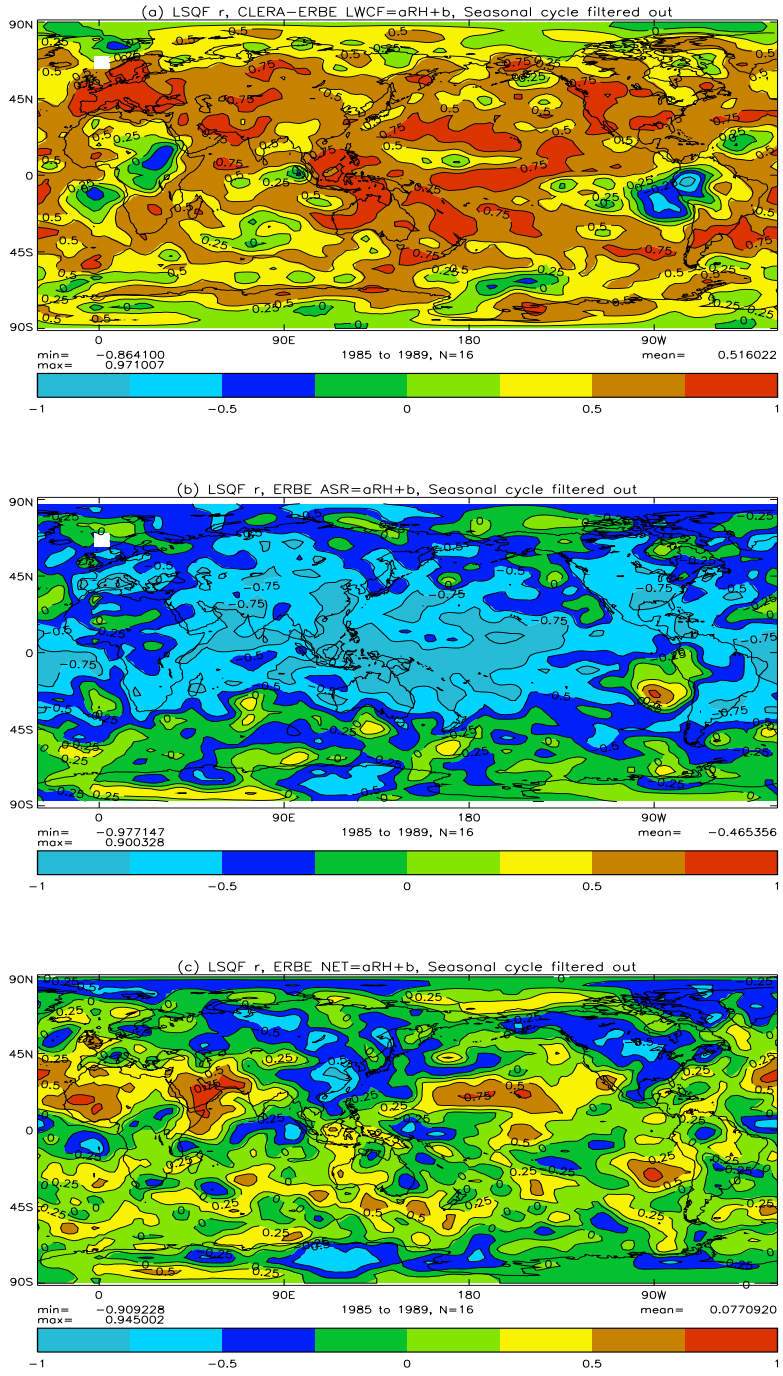


Figure 6.19: *LSQF correlation coefficient for (a) CLERA-ERBE inferred LWCF=aRH+b, (b) ERBE ASR=aRH+b and (c) ERBE NET=aRH+b for the interannual time scale. Significant correlation at the 95% confidence level is attained where* $|r| > 0.5$.

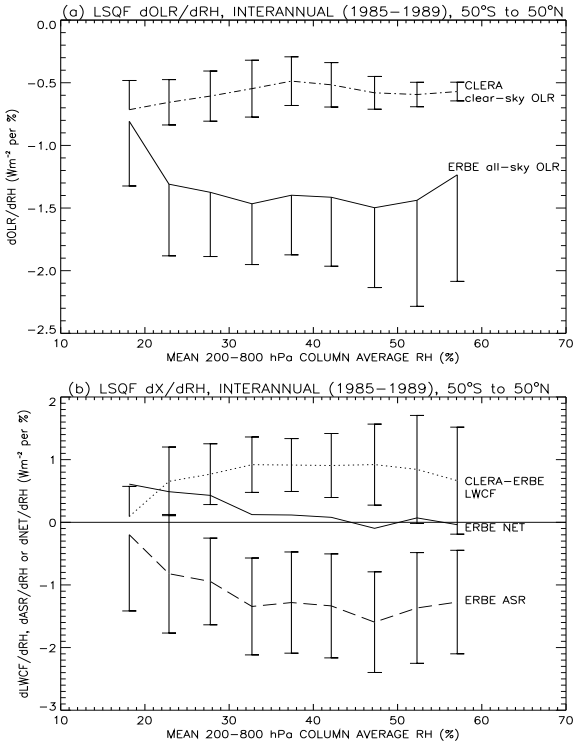


Figure 6.20: *LSQF all-sky and clear-sky dOLR/dRH (a), and dLWCF/dRH, dASR/dRH and dNET/dRH (b) for the interannual time-scale for 5% bins of mean RH. Units are* $Wm^{-2}$ *per %. Vertical error bars denote one standard deviation about the mean sensitivity calculated for each RH bin and are displayed to highlight the statistical scatter associated with each calculated sensitivity rather than the physical uncertainty associated with the models and data.*

coastal regions of South America, central Africa and the Amazon basin. The reasons for these disparate correlations are discussed in Sec. 6.6.3. The compensating effects between the longwave and shortwave effects of clouds causes correlation between NET and $RH$ to be insignificant over much of the globe. However moderate positive correlation is recorded over the coastal regions of north west Africa and central Chile as well as Saudi Arabia and the northern sub-tropical Pacific.

The calculated sensitivity of clear-sky and all-sky OLR to changes in $RH$ is shown in Fig. 6.20(a) while the $LWCF$, $ASR$ and NET sensitivities are displayed in 6.20(b). The sensitivities are plotted for 5% bins of mean $RH$ within 50° of the equator. The compensation between $LWCF$ and $ASR$ is apparent, although the shortwave effects generally tend to dominate over the longwave cloud effects for most grid points. Thus the changes in cloud amount and properties associated with changes in $RH$ generally conspire to locally cool regions for an increase in $RH$ as $dLWCF/dRH + dSWCF/dRH$ tends to be negative. This is offset by the clear-sky longwave effects with the net downward radiation at the top

of the atmosphere showing little sensitivity to changes in $RH$ in all but the driest regions. In these dry regions, increases in $RH$ are generally associated with increased net radiation trapped by the Earth-atmosphere system. Because the cloud effects are small over these dry regions, the strong $\mathrm{OLR}_c$ sensitivity to changes in $RH$ described in Chapter 5 may explain this result. This is investigated further in the following section. As was the case for the seasonal time scale, there appears to be a general increase in $dLWCF/dRH$ with $RH$ for the drier regions, while the reverse is true for the regions of high $RH$. A corresponding maximum magnitude of $dASR/dRH$ is apparent over the regions where mean $RH$ is between about 40 to 50%. However, it must be noted that the scatter of points about the mean values for each bin is large.

### 6.6.3 Regional Studies

Finally, the irradiance correlation with $RH$ discussed in the previous section are examined locally in greater detail. The purpose of this section is to answer two questions, the first being: are the positive relationships between NET and $RH$ explained by the strong $\mathrm{OLR}_c$ dependence on $RH$ in the sub tropics? The second question is, what causes the anomalous negative correlation between $LWCF$ and $RH$ over tropical Africa, the Amazon and the Peruvian coastal regions?

Dealing with the Amazon region first, the area 280 to 290° E and 8° S to 2° N was considered. Fig. 6.21 shows the interannual monthly anomalies of ERBE all-sky OLR and CLERA $\mathrm{OLR}_c$ (a) and CLERA minus ERBE inferred $LWCF$ and 450 $hPa$ $RH$ from ERA (b) for each month from February 1985 to January 1989. The tendency for $RH$ anomalies to be associated with $LWCF$ anomalies of opposite sign is apparent in Fig. 6.21(b). However, on closer inspection it is found that positive $LWCF$ anomalies and negative $RH$ anomalies are generally found in the first half of the time-series while the reverse is true for the second half. The changes in $LWCF$, rather than being explained by changes in all-sky OLR, appear to be a result of generally positive $\mathrm{OLR}_c$ anomalies before January 1987 and negative anomalies after this date (Fig. 6.21(a)). Chapter 5 showed $\mathrm{OLR}_c$ to be determined to a great extent by $RH$ in tropical regions. Indeed fluctuations in $\mathrm{OLR}_c$ are negatively correlated with $RH$, which appears to become more positive with time after 1986. The change in $RH$ anomalies are consistent with the error in ERA, as discussed in Chapter 2, whereby artificially produced desert conditions in the Amazon region before 1987 were rectified by discarding the assimilation of erroneous surface pressure observations. To reiterate, a trend for ERA $RH$ to increase over Amazon regions after 1986 is an artifact of ERA which introduces a corresponding spurious decrease in interannual $\mathrm{OLR}_c$ anomalies from 1987 onwards in CLERA. Over tropical Africa a trend for $RH$ to *decrease* over the interannual

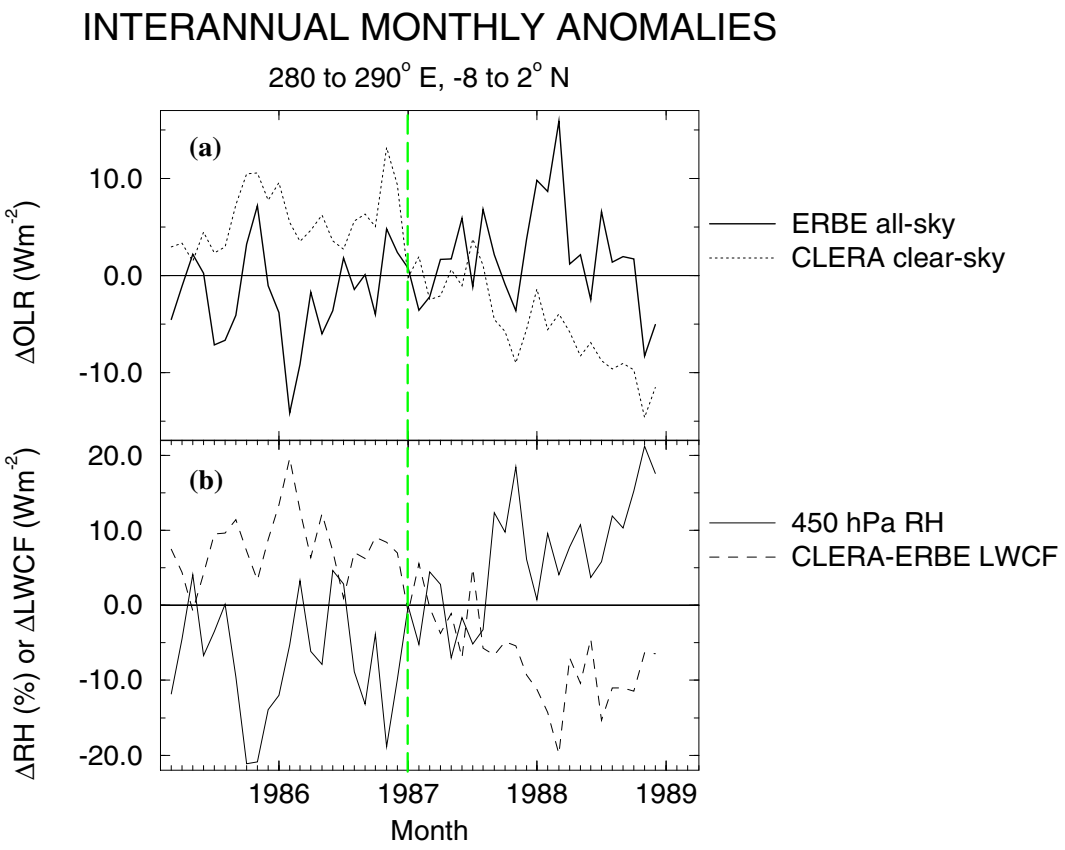


Figure 6.21: *Interannual monthly anomalies of (a) ERBE all-sky OLR and CLERA clear-sky $OLR_c$ and (b) ERA 450 hPa RH and CLERA minus ERBE inferred LWCF over the period, February 1985 to January 1989. The vertical dashed line marks the apparent change in the ERA RH trend.*

time-scale appears to explain the anomalous correlation between $LWCF$ and $RH$ over this region (not shown). This is associated with the southward shift in the African ITCZ in ERA (Kallberg (1997)) which occured at a similar time to the Amazon climate shift as discussed in Chapter 2. Thus the method of calculating $LWCF$ in the present study is prone to error over these regions and causes an erroneous negative correlation between $LWCF$ and $RH$ that is not generally seen over other parts of the globe.

The cause of the local positive relationship between net absorbed irradiance at the top of the atmosphere and $RH$ is now addressed. To increase the signal to noise ratio a region that displays a positive correlation between NET and $RH$ was chosen where interannual changes in $T_s$ are small. The sub-tropical north Pacific region, 170 to 210° E and 10 to 25° N was chosen. Figure 6.22(a) shows the positive relationship between $LWCF$ and ERA 450 $hPa$ $RH$ and the negative correlation between ASR and $RH$. Interannual cloud radiative forcing variability is greater than 20 $Wm^{-2}$ while $RH$ anomalies fluctuates by about 20% over the period February 1985 to January 1989. Increases in $RH$ appear to explain the

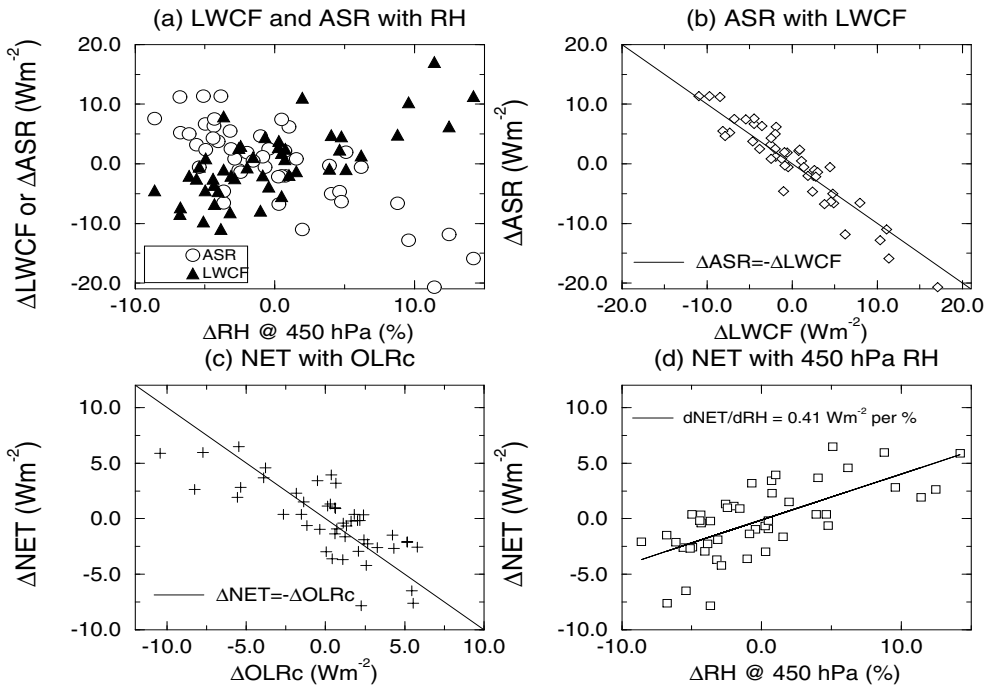


Figure 6.22: *Relationships between interannual monthly anomalies of the top of atmosphere irradiance and RH for the northern sub-tropical Pacific (170 to 210° E and 10 to 25° N) over the period February 1985 to January 1989. (a) LWCF (triangles) and ASR (Circles) with ERA 450 hPa RH. (b) ERBE ASR with CLERA-ERBE inferred LWCF. (c) ERBE net downward irradiance with CLERA clear-sky OLR. (d) ERBE net downward irradiance with ERA 450 hPa RH.*

change in cloud radiative forcing, the mechanism proposed being that increases in $RH$ are associated with increased cloud amount. The changes in longwave and shortwave cloud radiative forcing are of opposite sign; this is clearly seen in Fig. 6.22(b) which displays interannual monthly anomalies of ASR with $LWCF$. The negative relationship is close to the solid line which denotes $\Delta ASR = -\Delta LWCF$. Thus it may be argued that changes in cloud radiative forcing exert only a small influence on the net radiation at the top of the atmosphere for the tropics (e.g. Kiehl (1994)). If this is the case, it is intuitive that the significant correlation between NET and $RH$ is ascribed to variations in the clear-sky irradiance. Interannual changes in clear-sky ASR are small compared to $\mathrm{OLR}_c$ fluctuations. Therefore the changes in $\mathrm{OLR}_c$ should explain the interannual dependence of NET on $RH$. Figure 6.22(c) indeed shows changes in $\mathrm{OLR}_c$ to be strongly correlated with NET (the solid line shows $\Delta NET = -\Delta OLR_c$). Chapter 5 showed the strong negative dependence of $\mathrm{OLR}_c$ on $RH$ - increases in $RH$ act to decrease $\mathrm{OLR}_c$ which thus increase NET. This is consistent with the positive relationship between NET and $RH$ ($\mathrm{dNET/d}RH = 0.4\,Wm^{-2}$ per %) highlighted in Fig. 6.22(d).

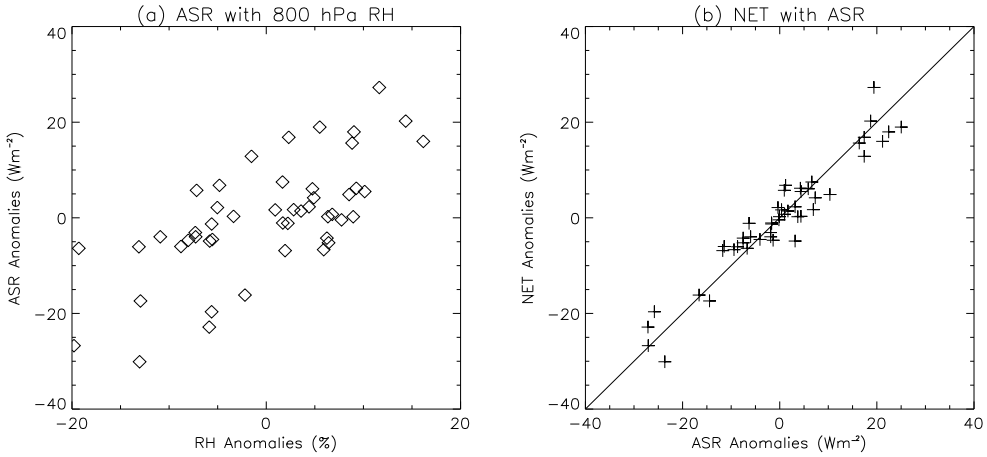


Figure 6.23: *Interannual monthly anomalies of ASR with 800 hPa RH (a) and interannual monthly anomalies of NET and ASR (b) for the region 265 to 275° E and 18 to 28° S over the period February 1985 to January 1989.*

Changes in $\mathrm{OLR}_c$ associated with $RH$ fluctuations appear to be important with regard to the all-sky net irradiance at the top of the atmosphere, albeit for the sub-tropical region considered. This explanation does not hold for the positive $\mathrm{d}NET/\mathrm{d}RH$ off the coast of Chile. Here variability in NET is determined primarily by the ASR. The positive $\mathrm{d}NET/\mathrm{d}RH$ are explained by positive correlation between ASR and column mean $RH$ rather than the negative $\mathrm{d}LWCF/\mathrm{d}RH$ which is small. The reason for this correlation is not obvious and is at odds with the generally negative relationship between interannual ASR anomalies and $RH$ which is intuitively explained by the positive coupling between cloud amount and $RH$. It is postulated that changes in low-altitude cloud, which affect the ASR but only influence the OLR slightly, and which is decoupled from the column mean $RH$, explain this result. Indeed, the main stratocumulus regions tend to show weak correlation between ASR and column mean $RH$ (Fig. 6.19(b)). This is supported by the analysis of Klein (1997), who used surface observations and thermodynamic soundings to show that stratocumulus cloud amount is negatively correlated with $RH$ immediately above the boundary layer while showing a positive relationship with $RH$ within the important cloud layer at about 900 $hPa$. Indeed, ASR is strongly and positively correlated with ERA $RH$ above the boundary layer at 800 $hPa$ (Fig. 6.23(a)) although there is only weak negative correlation with $RH$ at pressures greater than 850 $hPa$ (not shown). The strong dependence of interannual NET anomalies on ASR variability is highlighted in Fig. 6.23(b) with values generally within 10 $Wm^{-2}$ of the solid line which represents $\Delta NET = \Delta ASR$.

## 6.7 Summary and Discussion

Satellite observations of the Earth's radiation budget at the top of the atmosphere are used in conjunction with simulated $OLR_c$ to assess the variability of radiation budget components and their dependence on changes in temperature and humidity. The longwave cloud radiative forcing is calculated as the difference between simulated $OLR_c$ and observed satellite all-sky OLR. This ensures global coverage and is consistent with the calculation of cloud forcing used in climate model studies (e.g. Cess *et al.* (1992)) and avoids cloud contamination of clear-sky scenes (e.g. Slingo and Webb (1992)). However errors in the ERA climate introduce additional irradiance errors. Analysis suggests that surface emissivity errors over desert areas (Slingo *et al.* (1998)) and erroneous humidity trends over the Amazon and tropical Africa (Kallberg (1997)) limit the use of simulated $OLR_c$ in these regions. The ERBE absorbed solar radiation is used to infer information concerning shortwave cloud radiative forcing. Again, this ensures global coverage. However, where fluctuations in surface albedo or aerosol optical depth are significant, the ASR may not be primarily determined by changes in cloud amount and properties. Also, inferring interannual statistics for high latitude regions is problematic because of the large seasonal variation in insolation. A more consistent method of calculating shortwave cloud radiative forcing would be to extend the simulation of clear-sky longwave radiation to include clear-sky shortwave irradiance estimates using realistic surface albedo and atmospheric profiles of absorbing and scattering gases such as water vapour, ozone and aerosols. Using this in conjunction with satellite all-sky shortwave irradiance would provide estimates of shortwave cloud radiative forcing that is consistent with climate model calculations. This is beyond the scope of the present study, however.

The range of $OLR_c$ observed by ERBE for variations in $RH$ is generally found to be less than simulated by CLERA. This is consistent with previous studies (e.g. Collins and Inamdar (1995), Slingo *et al.* (1998), Ho *et al.* (1998)). The reason for the apparent underestimation of ERBE $OLR_c$ variation with changes in $RH$ is twofold. Firstly, cloud contamination over dry regions causes the high $OLR_c$ in these regions to be underestimated by ERBE (e.g. Weare (1995)) and secondly the ERBE $OLR_c$ is not as low as CLERA $OLR_c$ in regions of high $RH$ due to the different definitions of clear-sky fluxes used by ERBE and CLERA (e.g. Cess *et al.* (1992)). It is of greater consistency when calculating irradiance sensitivity to ERA parameters, which are assimilated for clear and cloudy conditions, to use the CLERA definition of $OLR_c$. This is because clear-sky fluxes sampled by ERBE are generally for less humid conditions than sampled by ERA monthly means. This is consistent with the spatial gradient of $OLR_c$ with column average $RH$ being more negative for

the CLERA simulation than for ERBE (see Slingo *et al.* (1998), their Fig. 12) and could result in studies such as Raval *et al.* (1994) underestimating the $\mathrm{OLR}_c$ sensitivity to column mean relative humidity. Comparing CLERA and ERBE $\mathrm{OLR}_c$ more realistically would require that CLERA irradiance be filtered in the same manner as that of ERBE clear-sky products. This comprehensive undertaking is not considered in the present study but may be addressed in the future.

Estimates of irradiance variability over the seasonal and interannual time-scales show $LWCF$ to enhance the OLR variability at low latitudes. It is anticipated that variation in cloud amount may explain this result. At high latitudes the presence of clouds causes OLR fluctuations associated with variability of $T_s$ to be reduced. This is because changes in surface emission are essentially absorbed by the cloud deck and translated to a diminished OLR variation by the smaller variation in cloud-top emission. This only applies where $LWCF$ is significant - in predominantly clear-sky regions OLR variability is mainly determined by the clear-sky component. While clouds act to increase OLR variability locally, the cancelling effect between regions due to subtle shifts in the large-scale circulation cause their effect on global mean OLR variability to be much smaller. A similar conclusion was drawn by Rossow and Zhang (1995). The effect of clouds on global OLR variability is reduced further when considering that some of the interannual variability is an artificial result of the satellite combinations used in the ERBE data. Using ERBS OLR and considering the Wide Field of View ERBS data (Minnis *et al.* (1993)), it is shown that the large change in ERBE OLR anomalies between November 1986 and February 1987 are likely to be in part due to the change from NOAA-9 to NOAA-10 sun-synchronous orbiting satellites that were used in conjunction with ERBS. This constitutes a serious uncertainty in the ERBE interannual variability statistics. With this caveat in mind, considering the variance in components of the radiation budget globally, the variability of $\mathrm{OLR}_c$ appears to contribute about 30 % to the variability of the net irradiance with the remainder being ascribed to the residual between the longwave and shortwave cloud radiative forcing.

At low latitudes, clouds act to amplify the clear-sky super-greenhouse effect (SGE) because increases in temperature are generally associated with increased $RH$ and deep convective cloud, both of which act to reduce the OLR. In the tropical Pacific, the longwave and shortwave cloud radiative forcing appear to cancel with an observed positive $\mathrm{dNET}/\mathrm{d}T_s$ being explained by the clear-sky SGE. This is consistent with previous analyses (e.g. Ramanathan and Collins (1991), Kiehl (1994)). Over the eastern Pacific, the greenhouse effect of clouds appears to dominate over the cloud albedo effect and this helps to explain the positive $\mathrm{dNET}/\mathrm{d}T_s$ observed in these regions. This is a region of significant

atmospheric and oceanic divergence and therefore this apparent positive radiative feedback is likely to be counteracted by heat export to the extra tropics (e.g. Sun and Trenberth (1998)). In regions of small divergence such as the tropical warm pool an alternative mechanism is required to provide a restraint on a runaway greenhouse effect (Pierrehumbert (1995)).

The changes in OLR and ASR are strongly correlated with $RH$, most especially over the interannual time-scale. This is partially explained by the dependence of cloud amount on $RH$ (e.g. J. M. Slingo (1980)). The strongest sensitivity of longwave and shortwave cloud radiative forcing to changes in $RH$ is generally encountered over regions of intermediate $RH$ of about 50%, where the largest fraction of the grid-box is likely to saturate with respect to water vapour for a given change in $RH$ compared to regions of low $RH$ which are predominantly clear or regions of high $RH$ which are predominantly cloudy. However, the cancellation between the shortwave and longwave cloud radiative forcing with changes in $RH$ result in small changes in NET in all but the dry descending regions. Here, there is a residual positive dNET/d$RH$ and it is postulated that the strong sensitivity of $\mathrm{OLR_c}$ to $RH$ in these regions may provide an explanation, emphasising the importance of clear-sky feedbacks in these dry descending regions on the Earth's radiation budget (e.g. Spencer and Braswell (1997)). This argument appears to apply to the northern sub-tropical Pacific with the interannual net radiation anomalies at the top of the atmosphere being in close agreement with the $\mathrm{OLR_c}$ anomalies simulated by CLERA. This is not the case in the the south-eastern Pacific positive dNET/d$RH$ zone. Here, changes in cloud amount are not coupled with column mean $RH$ and the net radiation fluctuations are primarily dependent on the ASR. This suggests that changes in low-altitude cloud that are not dependent on the column mean $RH$ and do not influence the $LWCF$ significantly, are important with regard to the net radiation budget in these regions. Indeed observations show stratocumulus cloud amount to be dependent on boundary layer $RH$ while being negatively correlated with $RH$ above the boundary layer (e.g. Klein (1997)). This is supported by the strong positive correlation between ASR and ERA $RH$ at 800 $hPa$. It is postulated that this situation arises because increased suppression of convection and the associated low free-tropospheric $RH$ are associated with an increased likelihood of high humidity and cloud amount in the inversion-capped boundary layer. When the boundary layer is less well defined and upward transport of moisture is permitted, increased free tropospheric $RH$ results. This is associated with the diminished likelihood of stratocumulus formation and a resulting increase in ASR.

The presence of clouds exert a large influence on the Earth's radiation budget locally although globally there exists a degree of cancelling between regions with regard to cloud radiative forcing. The strong local dependence of longwave and shortwave components of the radiation budget on $RH$ is less marked when considering entire circulation systems. Also the counteracting effects of the longwave and shortwave cloud radiative forcing cause only small perturbations to the net radiation balance. Systematic changes in temperature due to internal climate forcing result in small changes in the radiation budget components locally, but are important on a global scale. Therefore the huge potential impact of clouds on the Earth's radiation balance and climate, while still being highly significant, is much reduced when considering (a) entire circulation systems and (b) the net radiation. However, this conclusion applies at the top of the atmosphere. Shortwave cloud radiative forcing is manifest primarily at the surface while the longwave trapping of cloud acts mainly in the atmosphere (e.g. Harshvardhan *et al.* (1989)). Thus the effect of clouds on the radiation budget and the influence on the atmospheric circulation are more complex (Rossow and Zhang (1995)). The nature of the present study does not allow the quantification of cloud radiative feedbacks, but highlights regions of apparent strong coupling between cloud radiative forcing and temperature/humidity and provides a test for climate models to reproduce the simulated coupling regionally and over the entire globe. It also highlights inconsistencies within and between data sets. These comprise of cloud contamination and inter-satellite calibration problems in ERBE, surface emissivity errors and spurious local trends in humidity in the ERA data set and the inconsistency between ERA humidity and the clear-sky sampling of ERBE. The resulting errors are significant compared to the interannual irradiance variability and therefore suggest interannual statistics must be viewed with an air of caution. A longer data set with fewer inconsistencies and a more accurate determination of cloud amount and type are required for a better understanding of the climate system and its interannual variability.

# Chapter 7

# CONCLUSIONS

The use of models to understand the present climate and to predict reliably the future climate is limited by insufficient knowledge of the climate feedback processes operating. Climate model output must therefore be validated by comparisons with observations or observationally-derived quantities before their use as scientific tools are fully justified. The motivation behind this thesis is the need to improve our understanding of the radiative feedbacks operating, such as that involving water vapour. The primary tool used to address this requirement was a simulation of the clear-sky longwave radiation budget (CLERA, described in Chapter 2). The simulation used the ECMWF Re-Analysis (ERA) from which clear-sky longwave irradiance was calculated. While being strongly determined by the radiative transfer model used and the ECMWF model representation of the climate over the period 1979 to 1993, the simulated irradiance implicitly included a strong observational element given the extensive use of conventional and satellite-derived observations of meteorological parameters to constrain the general circulation model. It is important to establish firstly that the simulation realistically captures the mean fields and the variability in the Earth's radiation budget. If ERA is incapable of simulating observed quantities well, the proficiency of non-observationally constrained climate models must be seriously questioned. Thus the aims of this thesis were twofold. Firstly, extending work by Slingo *et al.* (1998), the simulated irradiance was evaluated at the surface utilising ground-based radiometric observations (Chapter 4). Secondly, the simulation was used with the ERA data to provide information on the clear-sky feedbacks operating in the present day climate (Chapter 5). Subsequently the influence of cloud and its variability on these feedbacks were investigated by combining satellite observations of the top of atmosphere radiation budget with the CLERA and ERA data (Chapter 6). An accurate narrow-band radiative transfer model and an array of standard atmospheric profiles and radiosonde soundings were also used extensively to aid interpretation (Chapters 2 and 3). The main findings are presented in

the following section.

## 7.1 Main Findings

**What parameters are most important in influencing clear-sky longwave irradiance variability and determining its uncertainty?**

The clear-sky downwelling longwave irradiance at the surface ($SDL_c$) is determined primarily by two parameters. The total column moisture ($u$) is important, especially in the warmer, moister profiles, because it directly influences the water vapour continuum emission from the lower troposphere in the window region of the longwave spectrum. In the strongly absorbing regions of the spectrum, the atmosphere approximates to a black-body emitter and therefore results in the strong sensitivity of the $SDL_c$ to the atmospheric temperature directly above the surface. Thus, fluctuations and uncertainty in $u$ and $T_0$ strongly affect the variability and uncertainty in $SDL_c$ and therefore also the net downward clear-sky longwave irradiance at the surface ($F_{net}$). The surface emissivity error is also important with regard to $F_{net}$ for land regions, especially over deserts. Unrealistic interpolation of moisture and most especially temperature between near-surface model levels introduces additional errors. The clear-sky outgoing longwave irradiance to space ($OLR_c$) is strongly dependent on atmospheric moisture and temperature. The strong dependence of $OLR_c$ on surface and atmospheric temperature is evident over latitudes greater than about 40°. At lower latitudes, it is primarily changes in relative humidity ($RH$) that determine the $OLR_c$ variability. The saturation of the water vapour rotation bands with increasing $RH$ explains why $OLR_c$ is most sensitive to $RH$ in dry regions of the atmosphere such as the sub-tropical upper troposphere.

**Can a simulation of the Earth's clear-sky longwave radiation budget which uses the ECMWF re-analysis accurately represent irradiance variability?**

Slingo *et al.* (1998) demonstrated the quality of the simulated $OLR_c$ by comparison with satellite irradiance observations by ERBE. The present study extended this investigation by comparing simulated $SDL_c$ with radiometric observations at the surface. A significant component of the analysis relied on the estimation of clear-sky observations using the available radiation budget data. This constituted a severe limitation of the present study and highlights the need for direct observations of cloud amount and type to accompany radiation budget measurements at the surface. Nevertheless, the comparison yielded reasonable results with the simulated irradiance generally being within the observational uncertainty of 10 $Wm^{-2}$. Periods of rapid changes in $SDL_c$ present in the observations also feature

in the simulation - further evidence of skill in simulated irradiance at the surface. For the sub-arctic region, the root mean squared difference between the observed and simulated $SDL_c$ ranges from 8.4 $Wm^{-2}$ using the longwave irradiance clear-sky filtering technique to 12.6 $Wm^{-2}$ using the shortwave irradiance clear-sky filtering technique. This compares with a root mean squared difference between simulated and observed $SDL_c$ of 9.2 $Wm^{-2}$ for the tropical warm pool. Much of these differences can be attributed to systematic differences between observed and simulated irradiance.

The tendency for $SDL_c$ to be greater than the observed values for warm, moist profiles and less than observed clear-sky irradiance for drier, colder profiles is in agreement with a similar study by Dutton (1993). The differences are greater than 10 $Wm^{-2}$ in many cases. Using the narrow-band model in conjunction with collocated radiosonde soundings and ERA profiles at the sub-arctic site, the differences were explained partly by the tendency for ERA profiles to be too moist and/or warm in the sub-arctic summer while being too dry and/or cold for the sub-arctic winter. It is postulated that preferential clear-sky sampling of drier instantaneous observed profiles, compared to the ERA 6-hourly averaged profiles, explains the moist ERA bias in summer. The known cold bias of ERA surface temperatures over land regions (Kallberg (1997)) is consistent with the ERA cold bias compared to observations during winter and spring months. Cloud contamination of clear-sky inferred observations is also consistent with the observed $SDL_c$ being greater than simulated values during the winter and spring. Differences of about 1.5 $K$ between observed surface and 2.6 $m$ altitude temperatures in the tropical western Pacific are not well represented by ERA and are consistent with the tendency for simulated $SDL_c$ to be of order 10 $Wm^{-2}$ greater than extrapolated observed values. Further comparisons between irradiance measured and simulated at the surface are required to confirm these conclusions.

A recently developed formula based on observations for estimating the surface longwave irradiance (Prata (1996)) compared favourably with monthly-mean irradiance simulated by CLERA. The root mean squared $SDL_c$ difference of about 8 $Wm^{-2}$ reduces to about 6 $Wm^{-2}$ when $u$ is prescribed by ERA rather than estimated from surface conditions. Much of the remaining differences are explained by the tendency for the formula to calculate $SDL_c$ that is of order 10 $Wm^{-2}$ greater than simulated values over mid-latitude regions. This difference is likely to be explained primarily by (i) the limited spatial coverage of irradiance and meteorological variables used to derive the empirical constants in the formula, (ii) cloud contamination of observed irradiance used to derive the empirical constants, and/or (iii) errors in the CLERA simulation. Further work is required to apportion the error among these reasons. While the formula is limited in its ability to predict $SDL_c$ accurately

on smaller time and space scales, its main advantage over alternative formulas, such as Dilley and O'Brien (1998), is its reliance on radiometric and meteorological observations to determine model constants empirically. The generally sparse ground-based radiometric measurements and the problems of increasing both the spatial extent and the accuracy of the surface observational network in the future therefore necessitates the use of alternative radiation budget data, such as that simulated by CLERA, to evaluate the surface fluxes produced by climate models.

**What are the primary limitations of the CLERA simulation, the ECMWF re-analysis data and the ERBE satellite data?**

The first and foremost limitation of the CLERA simulation is that the effect of clouds and shortwave irradiance on the Earth's radiation budget are not considered. A future undertaking would be to extend the simulation to include these effects. As it stands, the clear-sky simulation nevertheless remains a powerful tool for understanding the dependence of the clear-sky greenhouse effect on atmospheric parameters and for testing the ability of climate models to reproduce the clear-sky greenhouse effect and its variability. The present study identified the following more specific problems with the simulation:

1) Artificial drifts in the ERA climate over central Africa and the Amazonas region of South America (Kallberg (1997)) correspond with erroneous interannual trends in simulated $\mathrm{OLR}_c$ after 1986. The analysis of interannual variations in simulated $\mathrm{OLR}_c$ in conjunction with satellite observations of all-sky OLR are therefore of limited use in these regions.

2) The strong sensitivity of $\mathrm{OLR}_c$ to $RH$ in the upper troposphere combined with the paucity of free-tropospheric humidity measurements as input to ERA hinder the assessment of $RH$ fluctuations and its influence on the variability of $\mathrm{OLR}_c$.

3) The unit specification of $\epsilon_s$ over desert regions is at odds with observations (e.g. Sutherland (1986)) and explains the differences between simulated $\mathrm{OLR}_c$ and satellite observations over these regions, in agreement with Slingo *et al.* (1998). Analysis suggests that the resulting simulated irradiance error at the desert surface will be greater still.

4) The interpolation of temperature between the lowest atmospheric model layer and the surface is at odds with observations from the tropical western Pacific (e.g. Weller and Anderson (1996)) and is likely to explain the overestimation of $\mathrm{SDL}_c$ over tropical ocean regions. It is important to bear this in mind when comparing irradiance at the surface between models and observations.

5) While ERA employed a consistent assimilation system throughout the analysis period, the spatial and temporal availability of observations was subject to significant variability. The artificial trends resulting from this inconsistency therefore constitute a further

limitation on the identification of climate variability.

Limitations of the satellite data were also identified:

1) Cloud contamination of clear-sky observations can explain the tendency for ERBE $OLR_c$ to be less than CLERA values for regions of low $RH$.

2) Clear-sky sampling by satellite is inconsistent with analysed products which vary markedly between clear-sky and overcast regions. Thus, ERBE $OLR_c$ is sampled for lower $RH$ than is given by ERA monthly-means because periods of clear-skies sustain lower $RH$ compared to the entire monthly sample which contains both clear and cloudy scenes. This explains the tendency for simulated $OLR_c$, which is derived directly from ERA $RH$, to be less than ERBE $OLR_c$ over moist tropical regions. This inconsistency and point (1) explain why the sensitivity of ERBE $OLR_c$ to changes in ERA $RH$ is apparently smaller in magnitude than the sensitivity simulated by CLERA.

3) Inter-satellite calibration problems at the end of 1986 are likely to explain the large shift in ERBE global-mean interannual OLR anomalies from negative before January 1987 to positive after this date. The global-mean interannual variability of OLR is therefore likely to be overestimated by ERBE.

A peculiarity of the ERBE observation period is that three independent and significant events take effect almost simultaneously at approximately January 1987, these being (1) the ERBE satellite inter-calibration problem, (2) the artificial changes in ERA climate over the Amazon and central Africa and (3) the onset of the 1987 El Niño. This therefore precludes clear identification of the causes of interannual variability of the radiation budget. To improve our understanding of the Earth's radiation budget and its dependence on atmospheric and cloud parameters it is paramount that these limitations be addressed. A prime goal is to produce an observational data set that is sampled in a consistent manner to surface, atmospheric and cloud properties.

**The Super-greenhouse Effect**

The super-greenhouse effect (SGE) describes an unstable clear-sky longwave radiative feedback whereby longwave cooling decreases with increased warming. It is defined at the surface by positive $dF_{net}/dT_s$ and at the top of the atmosphere as negative $dOLR_c/dT_s$. Previous studies, for example by Inamdar and Ramanathan (1994), have argued that thermodynamics cannot explain the observed negative $dOLR_c/dT_s$ and that the SGE observed at the top of the atmosphere is manifest as an unstable feedback to the surface rather than the atmosphere. While this is generally true, the present study has shown small regions of the tropical upper troposphere (i.e. about 175 $hPa$) capable of producing a SGE when relative humidity remains constant. Also the SGE occurs not only at the surface but

also in the atmosphere over the seasonal cycle in the tropics. The SGE at the top of the atmosphere corresponds with large changes in convective regime associated with shifts in the Hadley circulation over the seasonal cycle and the meridional variation of the Walker circulation over the interannual time-scale and is consistent with a similar study by Bony *et al.* (1997b). The increases in $RH$, most especially at pressures between 100 and 700 $hPa$, that accompany the warming and associated change in convective regime are the primary explanation for the SGE.

Although increases in the magnitude of shortwave cloud radiative forcing with increasing $RH$ provides a mechanism that counteracts the SGE, the observed cancellation of shortwave and longwave cloud radiative forcing in the tropics (e.g. Kiehl (1994)) appears to necessitate an alternative explanation for the stability of tropical sea surface temperatures (e.g. Pierrehumbert (1995)). Pierrehumbert (1995) also argued that evaporative heat exchanges cannot constitute a stabilising mechanism when considering the top of atmosphere SGE, because cooling at the surface is counteracted by the latent heating of the atmosphere when considering the column mean heat budget. However, Gershunov *et al.* (1998) showed the distribution of SGE regions to be decoupled from evaporative cooling of the surface, implying that moisture transport results in evaporative cooling of the surface over less convective regions of the tropics and exerts a latent heating of the atmosphere within the mean ascending regions of the tropics. Also, recall that the SGE is manifest primarily as an unstable longwave radiative feedback to the surface (Lubin (1994), Inamdar and Ramanathan (1994)) and that the shortwave cloud radiative forcing is manifest at the surface while longwave cloud radiative forcing mainly affects the atmosphere (e.g. Harshvardhan *et al.* (1989)). Therefore the SGE at the ocean surface may be counteracted by the shortwave shading effect of clouds. Sun and Trenberth (1998) showed that both the shortwave cloud radiative forcing at the surface and the oceanic heat-export to the extra-tropics stabilises the clear-sky unstable longwave radiative heating of the surface. Atmospheric export of energy to the extra-tropics is also important in balancing the residual between the latent heating and the radiative cooling of the atmosphere. These mechanisms are thought to play a crucial role in the export of heat from the tropics over the 1986-87 ENSO and further begin to explain the equability of tropical sea surface temperature. Thus in understanding the SGE and the radiative and dynamic feedbacks operating over tropical regions an integrated approach in analysing both the dynamic and radiative components of the heat budget is required over entire circulation systems (e.g. Lau *et al.* (1996)).

**How do changes in Relative Humidity influence the water vapour feedback?**

There is a wealth of evidence to suggest a positive water vapour feedback to increasing $T_s$ (e.g. Manabe and Wetherald (1967), Cess *et al.* (1990), Rind *et al.* (1991)). However, variations in free-tropospheric moisture, which are relatively uncertain and less coupled with $T_s$ compared to the boundary layer, require further study. Using the CLERA simulation system and the ERA data, the effect of changes in $RH$ were shown to exert significant influence locally on the $\mathrm{OLR}_c$. Although $\mathrm{OLR}_c$ is most sensitive to a given change in $RH$ if that change is in the upper troposphere, the variability of ERA $RH$ in tropical regions is greatest in the mid-troposphere. Changes in $RH$ throughout the troposphere, but most particularly in the mid-troposphere (i.e. 400 to 700 $hPa$), are found to exert significant influence on $\mathrm{OLR}_c$. This is supported by the analysis of Sinha and Harries (1997). However, the effect of subtle shifts in the large-scale circulation, that locally cause large changes in $RH$ and therefore significant $\mathrm{OLR}_c$ variability, are much reduced when considering the global-mean radiation budget. Globally, changes in $RH$ have only a small influence on the strongly positive water vapour feedback encountered when relative humidity remains constant. There is weak evidence to suggest that changes in upper tropospheric $RH$ counteract this positive feedback. This is consistent with the proposed mechanism of Lindzen (1990) whereby an increasingly vigorous circulation in a warmer climate would detrain water vapour at a higher, colder altitude in the tropics, thereby supplying less water vapour to the sub-tropics and causing an increase in $\mathrm{OLR}_c$ over these sub-tropical regions. However, changes in $RH$ at lower altitudes appear to overwhelm the upper tropospheric $RH$ effect with the overall water vapour feedback being even more positive than the constant $RH$ water vapour feedback in the ERA climate. These conclusions are dependent on ERA providing a reasonable representation of free-tropospheric water vapour amount and its variability. Humidity at higher altitudes of the troposphere in ERA is subject to significant uncertainty. This limitation needs to be addressed before confidence can be ascribed to the ERA depiction of the water vapour feedback.

**What effect do clouds have on the variability of the Earth's Radiation Budget?**

The presence of cloud reduces the OLR variability at high latitudes due to the diminished effectiveness of surface emission fluctuations in influencing OLR. At low latitudes the variability of cloud amount and properties increase the OLR variability relative to clear-sky conditions. The effect of cloud on the radiation budget at the top of the atmosphere is reduced when considering (a) the cancellation between their longwave and shortwave radiative effects and (b) the regional cancellation between cloud radiative forcing when considering the global-mean irradiance. Point (a) is particularly evident in tropical regions (e.g. Kiehl

(1994)) and results in the interannual variability of net absorbed irradiance at the top of the atmosphere being almost exclusively determined by $OLR_c$ over some regions, for example the northern sub-tropical Pacific. In such regions, changes in $RH$ are likely to have a significant impact on the net radiation budget.

The cloud radiative forcing is strongly dependent on $RH$. Increases in $RH$ are generally associated with increased longwave and shortwave cloud radiative forcing over much of the globe. This is consistent with previous observational studies such as J. M. Slingo (1980) which show cloud amount to be dependent on $RH$. The stratocumulus regions tend to display weak correlation between cloud radiative forcing and column mean $RH$ including a strong anomalous positive relationship between absorbed solar radiation at the top of the atmosphere (ASR) and 800 $hPa$ $RH$ over ocean regions to the west of central Chile. This anomalous correlation is explained by considering the observational results of Klein (1997), who showed stratocumulus cloud amount to be positively correlated with $RH$ in the boundary layer but negatively correlated with $RH$ above the boundary layer. When large-scale atmospheric descent is weak in these regions, vertical moisture transport from the boundary layer reduces $RH$ near to the surface thus decreasing the likelihood of low-altitude cloud formation. The resulting higher $RH$ above the boundary layer is therefore associated with reduced stratocumulus albedo effects thereby increasing ASR. This explains the tendency for ASR to increase with free-tropospheric $RH$ in these regions.

## 7.2 Future Work

### Surface Radiation Budget

The validation of surface fluxes simulated by climate models is dependent on robust surface observations on a global scale. The Global Energy Budget Archive (GEBA) has been one source of data of use in validating surface fluxes in climate models (e.g. Wild *et al.* (1995)). The need for a comprehensive surface irradiance data set is currently being addressed by the Baseline Surface Radiation Network (BSRN; Philipona *et al.* (1998))[1], the Integrated Surface Irradiance Study (ISIS; Hicks *et al.* (1996))[2] and Darnell *et al.* (1996)[3]. The present study has highlighted the need for simultaneous observations of cloud amount, surface properties and atmospheric profiles of temperature and water vapour concentration combined with any broadband radiation budget data set at the surface. A more rigorous

[1]WWW address(1998): http://ezksun2.unizh.ch/

[2]WWW address(1998): http://www.srrb.noaa.gov/

[3]Darnell, W. L., *et al.*, Surface Radiation Budget: A long-term Global Dataset of Shortwave and Longwave Fluxes, ©1996 American Geophysical Union, WWW address(1998): http://www.agu.org/eos_elec/95206e.html

test of radiation schemes demands their evaluation against spectrally resolved observations. It is only after such direct comparisons are undertaken, combined with sufficiently accurate information on the surface and atmospheric properties, that confidence may be ascribed to the modelled radiative properties of water vapour and clouds. Han *et al.* (1997) demonstrated the value of comparing observed and modelled irradiance across the longwave spectrum in view of improving, albeit empirically, the performance of the Clough *et al.* (1989) (CKD) water vapour continuum parameterization. The Atmospheric Radiation Measurement (ARM)[4] programme is currently comparing observed spectral irradiance at the surface with line-by-line modelled irradiance. Preliminary results by Revercomb(1998)[5] suggested the CKD_2.2 foreign broadened continuum, which is used in this thesis, was too large by a factor of 3 at $400cm^{-1}$ although the sensitivity of the results to errors in water vapour and temperature profiles and the selection of clear-sky scenes were emphasised. As was illustrated in Chapter 2, the tropical atmosphere at the surface approximates a black-body emitter across much of the longwave spectrum. Thus it is important to observe spectral irradiance at higher altitudes (e.g. Kilsby *et al.* (1992), Rudman *et al.* (1994)) and higher latitudes (e.g. Walden *et al.* (1998)) where water vapour amount is low and the longwave spectrum rich in structure. Our understanding of the radiative properties of water vapour may then be tested more severely. This applies especially to the water vapour continuum, which has thus far been determined empirically using laboratory measurements and spectrally resolved irradiance observations.

**Top of Atmosphere Radiation Budget**

Satellite observations of the radiation budget at the top of the atmosphere and derived atmospheric and surface parameters allow, in combination with surface irradiance data and conventional observations of surface and atmospheric parameters, the simultaneous validation of climate models at the surface, the top of the atmosphere and throughout the atmosphere. They also provide valuable information on climate variability and the important feedback processes operating within the the climate system. The following projects will build on the recent success of the ERBE project:

1) CERES - The Clouds and Earth's Radiant Energy System[6] forms a major part of the Earth Observing Systems (EOS) program[7]. It is anticipated to be one of the primary tools for the global validation of climate model representations of clear-sky and cloud ra-

[4]WWW address(1998): http://www.arm.gov

[5]H. E. Revercomb(1998), AERI-ER at the SHEBA Ice Station: Far Infrared $H_2O$ Continuum, WWW address(1998): http://www.arm.gov/docs/research/science/R00029.html

[6]WWW address(1998): http://asd-www.larc.nasa.gov/ASDhomepage.html

[7]WWW address(1998): http://eospso.gsfc.nasa.gov/

diative forcing and feedbacks (e.g. Wielicki *et al.* (1998)). The first CERES system was installed on the Tropical Rainfall Measurement Mission satellite in 1997 and is included on the EOS-AM and -PM satellites due for launch in 1998 and 2000 respectively. CERES is essentially the follow-on project to ERBE and will sample the shortwave, thermal window region and total radiation broad band radiance at a 20 $km$ resolution. Inamdar and Ramanathan (1997) outlined the benefits of the window channel for understanding the greenhouse effect. Advantages over ERBE include increased irradiance accuracy, provision of radiative fluxes within the Earth's atmosphere, estimates of cloud amount and property sampled in a consistent manner to the irradiance and an improved cross-track scanner that is likely to improve on the ERBE angular models of Brooks *et al.* (1986) (Wielicki *et al.* (1998)). The addition of spectral radiance data from MODIS (described in the following sub-section) is expected to increase the validation potential of the CERES system with regard to modelled irradiance. For example, the observed spectral signature of climate change may eventually be used to validate climate model signatures, such as those described by Slingo and Webb (1997).

2) ScaRaB - The Scanner for Radiation Budget Experiment[8] (Kandel *et al.* (1998)) also complements the earlier ERBE top of atmosphere radiation budget. One significant improvement over ERBE is the provision of two narrow band channels (0.55 to 0.65 $\mu m$ visible channel and 10.5 to 12.5 $\mu m$ longwave window channel) as well as the shortwave and total broadband channels. Top of atmosphere radiance of accuracy better than 1% in the longwave and 2% in the shortwave domain was provided between January 1994 and March 1995 (Kandel *et al.* (1998)). A second ScaRaB system has recently been launched.

3) GERB - Geostationary Earth Radiation Budget[9]: A major disadvantage of ERBE, ScaRaB and CERES radiances are their poor temporal sampling (i.e. about two measurements per day at a given location) and the need for spatial and temporal radiance modelling (e.g. Brooks *et al.* (1986)). The GERB project (Mueller (1997)) is expected to provide 15 minute sampling resolution for radiance and will therefore be able to resolve the diurnal cycle and measure the time-evolution of radiances. Total broadband radiance (0.35-30 $\mu m$) and the shortwave component (0.32-4 $\mu m$) are to be provided. Accuracy is anticipated to be 1% in the shortwave and 0.5% in the longwave domains. The geostationary satellite (METEOSAT Second Generation) carrying the GERB scanners will fly over zero latitude and longitude; ascertaining the domain over which sufficiently accurate radiance is measured must therefore be addressed. Provision of ground-based radiation data collocated with GERB will allow simultaneous validation of irradiance simulated at the surface and the top of the atmosphere by climate models.

[8] WWW address(1998): http://w3.gkss.de/ muelj/ScaRaB.html

[9] WWW address(1998): http://www.ssd.rl.ac.uk/gerb/WEB_PAGE.HTM

### Upper Tropospheric Water Vapour

A limitation of the ERA climate is the uncertainty regarding water vapour amount and its variability in the free-troposphere. Inaccuracy in radiosonde humidity measurements at high altitude and the poor vertical resolution and uncertainties involved in the satellite derivation of this quantity hinder our understanding of the water vapour feedback to surface warming. Recent and future advances in the measurement of water vapour amount and its variability provide a means of addressing this problem. Elliot (1995) argues that increasing accuracy of radiosonde humidity measurements at higher altitudes together with increasing consistency between the radiosondes used by different countries auger well for the future of conventionally based measurements of upper tropospheric moisture. However, the remote sensing of water vapour profiles by satellite is likely to improve significantly in the future with the improvement of existing data sets and the launch of new, more versatile instruments:

1) TOVS - The TIROS N Operational Vertical Sounder has provided information on atmospheric water vapour since 1979. Using the high-resolution infrared radiation sounder (HIRS) brightness temperatures, estimates of upper tropospheric humidity have recently provided a means of assessing the uncertainty attatched to this parameter in climate models (e.g. Chen *et al.* (1996), Bates and Jackson (1997)). Significant discrepancies in the means and the variability were identified and further studies are required to resolve the causes of these differences. A new analysis of the HIRS data combined with the TOVS microwave sounding unit (MSU) data was recently described by Chaboureau *et al.* (1998). The new generation of HIRS/MSU instruments combine the Atmospheric Infrared Sounder (AIRS), the Advanced Microwave Sounding Unit (AMSU) and the Humidity Sounder Brazil (HSB)[10]. Temperature and moisture profiles will be constructed from the microwave channels by cloud-clearing using the infrared channels (wavelength ($\lambda$) from 3.74 to 15.4 $\mu m$ with resolution $\lambda/\Delta\lambda$=1200) of AIRS.

2) SAGE II - Stratospheric Aerosol and Gas Experiment[11]: A seven channel photometer aboard the ERBS satellite (launched in 1984) provided estimates of water vapour mixing ratio in the stratosphere and upper troposphere for over 5 years using the solar occultation technique (McCormick (1987)). This data set provided one of the first clues in support of the positive water vapour feedback produced in climate models (Rind *et al.* (1991)). Chiou *et al.* (1997) presented estimates of the water vapour mixing ratio vertical distributions and seasonal variability within 55° of the equator and between 6 $km$ and 40 $km$ altitude. These were consistent with METEOSAT estimates of upper tropospheric

[10]WWW address(1998) http://www-airs.jpl.nasa.gov/about_airs.html
[11]WWW address(1998): http://arbs8.larc.nasa.gov/sage2/sageii.html

humidity variability (e.g. see Soden and Bretherton (1993)). The follow-on experiment (SAGE III[12]) is expected to improve on the accuracy of humidity measurements, extending the water vapour coverage to altitudes between 50 $km$ and the planetary boundary layer.

3) HALOE - Halogen Occultation Experiment[13]: Water vapour profiles from 0.002 $hPa$ to just below the tropopause were presented by Jackson *et al.* (1998). A broad band filter at 6.6 $\mu m$ provided this information from solar occultation. The data are likely to be of limited use with regard to tropospheric humidity much below the top of the troposphere, although Jackson *et al.* (1998) believe it to be more accurate than SAGE II over convective regions.

4) MOZAIC - Measurement of Ozone Aboard In-service airCraft[14]: A humidity sensor installed on aircraft provided information regarding humidity fluctuations between approximately 290 $hPa$ and 166 $hPa$, mainly over the Atlantic region (Gierens *et al.* (1997)). This is a unique data set, independent of satellite and radiosonde estimates, and has been available since 1994. Were humidities to be routinely measured and available for operational purposes, they would provide valuable information on water vapour amounts and their variability that could be subsequently used to evaluate climate model estimates and the ERA representation of the upper tropospheric humidity.

5) MODIS - The Moderate Resolution Imaging Spectro-radiometer[15] is a 36 channel radiometer that measures between 0.4 and 14.4 $\mu m$ (e.g. Running *et al.* (1994)) and is capable of providing information on water vapour concentrations. Unique to MODIS are the five near-infrared channels around the 0.94 $\mu m$ water vapour band which will provide information on column moisture and eventually vertical profiles of water vapour.

### Cloud amount and properties

One of the largest uncertainties in predicting the future climate stems from our incomplete knowledge of the macro- and micro-physical properties of clouds and how they will respond to a warming climate (IPCC (1996)). Therefore the careful monitoring of clouds is paramount to our understanding of the climate system. Rossow and Cairns (1995) recommended that a minimum requirement for cloud monitoring included global coverage with at least 6 observations per day for each 50 $km$ sampling region. They further asserted that the continuous measurement for at least 10 years with high precision instrument calibration of about 1% accuracy is needed to resolve the decadal changes in climate.

1) ISCCP - The International Satellite Cloud Climatology Project (Rossow and Schif-

[12]WWW address(1998): http://www-arb.larc.nasa.gov/sage3/Index.html
[13]WWW address(1998): http://haloedata.larc.nasa.gov/home.html
[14]WWW address(1998): http://www.cnrm.meteo.fr:8000/mozaic/
[15]WWW address(1998): http://ltpwww.gsfc.nasa.gov/MODIS/MODIS.html

fer (1991)) has provided global coverage of cloud amount and type since 1983. Combining ISCCP and ERBE data has provided valuable information regarding the dependence of cloud radiative forcing on changes in cloud parameters (e.g. Ringer (1994), Weare (1995)) and was used by Rossow and Zhang (1995) to derive the radiation budget at the surface.

2) CERES - Estimates of cloud radiative forcing, in a similar manner but more accurate and of higher spatial resolution than ERBE products, will combine with consistent estimates of cloud physical properties and atmospheric and surface properties over a 15 year period. Results from the CERES system on-board the TRMM satellite (launched in 1997) are currently becoming available.

3) MISR - The Multi-angle Imaging Spectro-radiometer[16]: Cloud albedo and cloud-top altitude will be derived by measuring shortwave radiance in 4 bands (446 $nm$, 558 $nm$, 672 $nm$ and 866 $nm$) and at nine separate angles. The MISR is anticipated to measure albedo ten times more accurate than using just one, downward pointing sensor. The MISR system is launched on the EOS-AM satellite in 1998 which also contains the CERES system. The albedo is calculated using additional measurements from the single sensor on the CERES system that samples the entire solar spectrum.

4) MODIS - The multi-spectral radiances from MODIS will provide information on global cloud cover, cloud optical thickness and particle radius. A multi spectral approach is expected to improve on the accuracy of cloud cover estimations which have previously only utilised the 10-12 $\mu m$ window region of the longwave spectrum. Multi-spectral radiance observations are expected to detect cloud cover globally including semi-transparent cirrus clouds. Three distinct bands (8.6 $\mu m$, 11 $\mu m$ and 12 $\mu m$) will also differentiate between the different phases of cloud (ice, liquid and vapour). Daytime visible and near infrared cloud-phase techniques will complement the longwave radiance method. Cloud optical thickness and effective radius will be derived during the day using seven bands from 0.66 to 11 $\mu m$. MODIS will also improve on existing cloud detection techniques in accuracy and spatial resolution (250 to 1000 $m$).

### Direct Extension of this Thesis

The results presented in this thesis are relevant for the data sets utilised and for the periods of time considered in the analyses. For example, the comparison of simulated surface irradiance with observations may usefully be extended by employing all available surface radiation budget data such as provided by the BSRN. The analysis of $OLR_c$ dependence on temperature and relative humidity may be extended to months other than July and using the re-analysis of the National Centre for Environmental Prediction (NCEP) rather

[16] WWW address(1998): http://www-misr.jpl.nasa.gov/

than ERA. Analysing the simulated changes in atmospheric heating rates associated with temperature and humidity changes is also likely to complement the investigation in Chapter 5. The effect of clouds on the Earth's radiation budget, as presented in Chapter 6, would further benefit from the use of cloud climatologies such as ISCCP. Nevertheless, the present study has helped to show the quality of the CLERA simulation and its successful implementation as a tool for assessing the variability of the Earth's radiation budget. The simulation therefore provides a powerful method for validating the clear-sky irradiance and heating rates simulated by climate models (e.g. Slingo (1997)). The subject of future research is to compare climate model irradiance variability and sensitivity to temperature and humidity fluctuations with CLERA. Initially, this may be completed for clear-sky longwave irradiance, thus evaluating the climate model depiction of clear-sky radiative feedbacks compared to ERA. Extending the study to include satellite irradiance and utilising cloud climatologies (e.g. Rossow and Schiffer (1991)), the ability of climate models to reproduce the variability of cloud amount and cloud radiative forcing may also be assessed. The advantage of using the CLERA simulation in conjunction with satellite data to estimate cloud longwave radiative forcing is the removal of biases in the satellite-derived $OLR_c$. However, limitations in the ERA climate must be considered in this evaluation. Rectifying these problems would require a re-run of the ECMWF re-analysis which would also benefit from new data sets such as SAGE II and HALOE and the revisiting of existing data sets such as TOVS and the radiosonde data base to provide a more complete and more consistent analysis of the atmosphere. A future project, ERA-40, will extend the 15 year ERA project to 40 years. Therefore decadal climate variability may be assessed which cannot be resolved by ERA-15. At the beginning of the ERA-40 period (1958), the small amount of assimilated observational data is likely to mean that the ERA-40 climate will approximate to a free-running climate model. However, valuable information will be provided by assessing the impact of the generally increasing amount and accuracy of conventional or remotely sensed observational data on the ERA-40 climate.

## 7.3 Final Comments

The increasingly extensive temporal and spatial coverage of Earth radiation budget measurements combined with consistent sampling of surface, atmospheric and cloud parameters will both increase our understanding of the the climate system as well as help the evaluation of climate models in predicting the future climate. The results presented in this thesis help to validate, assess the limitations and exploit a new method of assessing the clear-sky and cloud radiative feedbacks operating in the present climate which is model-based but observationally constrained. A future aim is to utilise new radiation and water vapour data sets

to build on the present study. This information may be used to test and improve the climate models vital in predicting the future climatic change and from which impacts on the Earth's biota, and thence human-kind, may be quantified. One of the greatest challenges in this respect is to be able to accurately predict potential regional changes in climate. Because of our reliance on the present climatic regime, a change in the climate distribution as well as the change in global mean climate are likely to exert a severe impact on human-kinds' future well-being.

# Bibliography

Alados-Arboledas, L., Vida, J., and Jimenez, J. I. (1988). Effects of solar radiation on the performance of pygreometers with silicon domes. *J. Atmos. Oceanic Techno.*, **5**, 666–670.

Angell, J. K. (1988). Variations and trends in tropospheric and stratospheric global temperatures, 1958-1987. *J. Climate Appl. Meteor*, **1**, 1296–1313.

Arrhenius, S. (1896). On the influence of carbonic acid in the air upon the temperature of the ground. *Phil. Mag. Series 5*, **41**, 237–276.

Barkstrom, B. R. (1984). The Earth radiation budget experiment (ERBE). *Bull. Amer. Met. Soc.*, **65**, 1170–1185.

Barkstrom, B. R., Harrison, E. F., Lee, R. B., and the ERBE Science Team (1990). Earth Radiation Budget Experiment (ERBE) archival and April 1985 results. *Bull. Amer. Met. Soc.*, **70**, 1254–1262.

Bates, J. J. and Jackson, D. L. (1997). A comparison of water vapor observations with AMIP I simulations. *J. Geophys. Res.*, **102**(D18), 21837–21852.

Bolin, B., Doos, B., Jager, J., and Warrick, R. (1986). *The Greenhouse Effect, Climate Change and Ecosystems*. John Wiley and Sons, London. SCOPE 29.

Bony, S., Duvel, J.-P., and Le Treut, H. (1995). Observed dependence of the water vapor and clear-sky greenhouse effect on sea surface temperature: Comparison with climate warming experiments. *Climate Dynamics*, **11**, 307–320.

Bony, S., Sud, Y., Lau, K. M., Susskind, J., and Saha, S. (1997a). Comparison and satellite assessment of NASA/DAO and NCEP-NCAR reannalyses over the tropical ocean: Atmospheric hydrology and radiation. *J. Climate*, **10**, 1441–1462.

Bony, S., Lau, K., and Sud, Y. C. (1997b). Sea surface temperature and large-scale circulation influences on tropical greenhouse effect and cloud radiative forcing. *J. Climate*, **10**, 2055–2077.

Brooks, D. R., Harrison, E. F., Minnis, P., Suttles, J. T., and Kandel, R. S. (1986). Development of algorithms for understanding the temporal and spatial variability of the Earth's radiation balance. *Rev. Geophys.*, **24**, 422–438.

Budyko, M. I. (1974). *Climate and Life*. Academic Press.

Cess, R. D. (1989). Gauging the water vapour feedback. *Nature*, **342**, 736–737.

Cess, R. D. and Potter, G. L. (1987). Exploratory studies of cloud radiative forcing with a general circulation model. *Tellus*, **39**(Ser. A), 460–473.

Cess, R. D., Potter, G. L., Blanchet, J. P., Boer, G. J., Ghan, S. J., Le Treut, J. T. K. H., Li, Z. X., Liang, X. Z., Mitchell, J. F. B., Morcrette, J. J., Randall, D. A., Riches, M. R., Roeckner, E., Schlese, U., Slingo, A., Taylor, K. E., Washington, W. M., Wetherald, R. T., and Yagai, I. (1989). Interpretation of cloud climate feedback as produced by 14

atmospheric general circulation models. *Science*, **245**, 513–516.

Cess, R. D., Potter, G. L., Blanchet, J. P., Boer, G. J., Del Genio, A. D., Deque, M., Dymnikov, V., Galin, V., Gates, W. L., Ghan, S. J., Kiehl, J. T., Lacis, A. A., Le Treut, H., Li, Z. X., Liang, X. Z., McAvaney, B. J., Meleshko, V. P., Mitchell, J. F. B., Morcrette, J. J., Randall, D. A., Rikus, L., Roeckner, E., Royer, J. F., Schlese, U., Sheinin, D. A., Slingo, A., Sokolov, A. P., Taylor, K. E., Washington, W. M., Wetherald, R. T., Yagai, I., and Zhang, M. H. (1990). Intercomparison and interpretation of climate feedback processes in 19 atmospheric general circulation models. *J. Geophys. Res.*, **95**, 16601–16615.

Cess, R. D., Potter, G. L., Gates, W. L., Morcrette, J. J., and Corsetti, L. (1992). Comparison of general circulation models to earth radiation budget experiment data: Computation of clear-sky fluxes. *J. Geophys. Res.*, **97**(D18), 20421–20426.

Cess, R. D., Zhang, M. H., Potter, G. L., Alekseev, V., Barker, H. W., Bony, S., Colman, R. A., Dazlich, D. A., Del Genio, A. D., Déqué, M., Dix, M. R., Dymnikov, V., Esch, M., Fowler, L. D., Fraser, J. R., Galin, V., Gates, W. L., Hack, J. J., Ingram, W. I., Kiehl, J. T., Kim, Y., Le Treut, H., Liang, X. Z., McAvaney, B. J., Meleshko, V. P., Morcrette, J. J., Randall, D. A., Roeckner, E., Schlesinger, M. E., Sporyshev, P. V., Taylor, K. E., Timbal, B., Volodin, E. M., Wang, W., Wang, W. C., and Wetherald, R. T. (1997). Comparison of the seasonal change in cloud-radiative forcing from atmospheric general ciculation models and satellite observations. *J. Geophys. Res.*, **102**(D14), 16593–16603.

Chaboureau, J. P., Chedin, A., and Scott, N. A. (1998). Remote sensing of the vertical distribution of atmospheric water vapor from the TOVS observations: Method and validation. *J. Geophys. Res.*, **103**(D8), 8743–8752.

Chen, C., Roeckner, E., and Soden, B. J. (1996). A comparison of satellite observations and model simulations of column-integrated moisture and upper-tropospheric humidity. *J. Climate*, **9**, 1561–1585.

Chiou, E. W., McCormick, M. P., and Chu, W. P. (1997). Global water vapour distributions in the stratosphere and upper troposphere derived from 5.5 years of SAGE II observations (1986-1991). *J. Geophys. Res.*, **102**(D15), 19105–19118.

Clough, S. A., Kneizys, F. X., and Davies, R. W. (1989). Line shape and the water vapor continuum. *J. Atmos. Sci.*, **23**, 229–241.

Clough, S. A., Iacono, M. J., and Moncet, J. L. (1992). Line-by-line calculation of atmospheric fluxes and cooling rates: Application to water vapor. *J. Geophys. Res.*, **95**, 15761–15785.

Collins, W. D. and Inamdar, A. K. (1995). Validation of clear-sky fluxes for tropical oceans from the Earth Radiation Budget Experiment. *J. Climate*, **8**, 569–578.

Collins, W. D., Valero, F. P. J., Flatau, P. J., Lubin, D., Grassl, H., and Pilewskie, P. (1996). Radiation effects of convection in the tropical pacific. *J. Geophys. Res.*, **101, D10**, 14999–15012.

Cullen, M. J. (1993). The unified forecast/climate model. *Metorol. Mag.*, **122**, 81–94.

Del Genio, A. D., Lacis, A. A., and Ruedy, R. A. (1991). Simulations of the effect of a warmer climate on atmospheric humidity. *Nature*, **351**, 382–385.

Dilley, A. C. and O'Brien, D. M. (1998). Estimating downward clear sky long-wave irradiance at the surface from screen temperature and precipitable water. *Quart. J. Roy. Meteorol. Soc.*, **124**, 1391–1401.

Dutton, E. G. (1993). An extended comparison between LOWTRAN7 computed and observed broadband thermal irradiance: Global extreme and intermediate surface conditions. *J. Atmos. Oceanic Techno.*, **10(3)**, 326–336.

Edwards, J. M. and Slingo, A. (1996). Studies with a flexible new radiation code: I: Choosing a configuration for a large scale model. *Quart. J. Roy. Meteorol. Soc.*, **122**, 689–719.

Ellingson, R. G., Ellis, J., and Fels, S. (1991). The intercomparison of radiation codes used in climate models: Long wave results. *J. Geophys. Res.*, **96**, 8929–8953.

Elliot, W. P. (1995). On detecting long-term changes in atmospheric moisture. *Climate Change*, **31**, 349–367.

Forster, P. M. d. F. and Shine, K. P. (1997). Radiative forcing and temperature trends from stratospheric ozone depletion. *J. Geophys. Res.*, **102**, 10841–10855.

Freckleton, R. S., Highwood, E. J., Shine, K. P., Wild, O., Law, K. S., and Sanderson, M. G. (1998). Greenhouse gas radiative forcing: Effects of averaging and inhomogeneities in trace gas distribution. *Quart. J. Roy. Meteorol. Soc.*, **124**, 2099–2127.

Freund, J. E. (1976). *Statistics, A first course.* Prentice-Hall.

Frey, R. A., Ackerman, S. A., and Soden, B. J. (1996). Climate parameters from satellite spectral measurements. Part i: Collocated AVHRR and HIRS/2 observations of spectral greenhouse parameter. *J. Climate*, **9**, 327–344.

Garratt, J. R. and Prata, A. J. (1996). Downwelling long-wave fluxes at continental surfaces - a comparison of observations with GCM simulations and implications for the global land-surface radiation budget. *J. Climate*, **9**, 646–655.

Gershunov, A., Michaelsen, J., and Gautier, C. (1998). Large-scale coupling between the tropical greenhouse effect and latent heat flux via atmospheric dynamics. *J. Geophys. Res.*, **103**(D6), 6017–6031.

Gibson, J. K., Kallberg, P., Uppala, S., Nomura, A., Hernandez, A., and Serrano, E. (1997). ERA description: ECMWF re-analysis project report series. Technical Report 1, ECMWF.

Gierens, K. M., Schumann, U., Smit, H. G. J., Helten, M., and Zangl, G. (1997). Determination of humidity and temperature fluctuations based on MOZAIC data and parameterisation of persistent contrail coverage for general circulation models. *Ann. Geophys. -Atmos. Hydro. Space. Sci.*, **15**(8), 1057–1066.

Grant, A. L. M. and Hignett, P. (1998). Aircraft observations of the surface energy balance in TOGA-COARE. *Quart. J. Roy. Meteorol. Soc.*, **124**, 101–122.

Gupta, S. K. (1989). A parameterization for longwave surface radiation from sun-synchronous satellite data. *J. Climate*, **2**, 305–320.

Gutzler, D. S., Kiladis, G. N., Meehl, G. A., Weickmann, K. M., and Wheeler, M. (1994). The global climate of December 1992-February 1993. Part II: Large-scale variability across the tropical western pacific during TOGA COARE. *J. Climate*, **7**, 1606–1622.

Hallberg, R. and Inamdar, A. K. (1993). Observations of seasonal variations in atmospheric greenhouse trapping and its enhancement at high sea surface temperature. *J. Climate*, **6**, 920–931.

Han, Y., Shaw, J. A., Churnside, J. H., Brown, P. D., and Clough, S. A. (1997). Infrared spectral radiance measurements in the tropical Pacific atmosphere. *J. Geophys. Res.*, **102**(D4), 4353–4356.

Harries, J. E. (1996). The greenhouse Earth: A view from space. *Quart. J. Roy. Meteorol. Soc.*, **122**(532B), 799–818.

Harries, J. E. (1997). Atmospheric radiation and atmospheric humidity. *Quart. J. Roy. Meteorol. Soc.*, **123**(544B), 2173–2186.

Harrison, E. F., Minnis, P., R.Barkstrom, B., Ramanathan, V., Cess, R., and Gibson, G. G. (1990). Seasonal variation of cloud radiative forcing derived from the earth radiation budget experiment. *J. Geophys. Res.*, **95**, 18687–18703.

Harshvardhan, Randall, D. A., Corsetti, T. G., and Dazlich, D. A. (1989). Earth radiation budget and cloudiness simulations with a general circulation model. *J. Atmos. Sci.*, **46**, 1922–1942.

Hartmann, D. L. and Michelsen, M. L. (1993). Large-scale effects on the regulation of tropical sea surface temperatures. *J. Climate*, **6**, 2049–2062.

Hess, S. L. (1959). *Introduction to Theoretical Meteorology*. Henry Holt and Co., New York.

Heymsfield, A. J. and Miloshevich, L. M. (1995). Relative humidity and temperature influences on cirrus formation and evolution - observations from wave clouds and FIRE-II. *J. Atmos. Sci.*, **52, No. 23**, 4302–4326.

Hicks, B. B., DeLuisi, J. J., and Matt, D. R. (1996). The NOAA Integrated Surface Irradiance Study (ISIS) - a new surface radiation monitoring program. *Bull. Amer. Met. Soc.*, **77**(12), 2857–2864.

Ho, C. H., Chou, M. D., Suarez, M., Lau, K. M., and Yan, M. M. H. (1998). Comparison of model-calculated and ERBE-retrieved clear-sky outgoing longwave radiation. *J. Geophys. Res.*, **103**(D10), 11529–11536.

Inamdar, A. K. and Ramanathan, V. (1994). Physics of greenhouse effect and convection in warm oceans. *J. Climate*, **7**, 715–731.

Inamdar, A. K. and Ramanathan, V. (1997). On monitoring the atmospheric greenhouse effect from space. *Tellus*, **49B**(2), 216–230.

IPCC (1990). *Climate Change, the IPCC Scientific Assessment.* Cambridge University Press.

IPCC (1995). *Climate Change 1994. Radiative Forcing of Climate Change and an Evaluation of the IPCC IS92 Emissions Scenarios.* Cambridge University Press.

IPCC (1996). *Climate Change 1995, the second IPCC Assessment of Climate Change.* Cambridge University Press.

Jackson, D. R., Driscoll, S. J., Highwood, E. J., Harries, J. E., and Russel III, J. M. (1998). Troposphere to stratosphere transport at low latitudes as studied using HALOE observations of water vapour 1992-1997. *Quart. J. Roy. Meteorol. Soc.*, **124**, 169–192.

Johns, T. C., Carnell, R. E., Crossley, J. F., Gregory, J. M., Mitchell, J. F. B., Senior, C. A., Tett, S. F. B., and Wood, R. A. (1997). The second Hadley Centre coupled ocean-atmosphere GCM: Model description, spinup and validation. *Climate Dynamics*, **10**(2), 103–134.

Kallberg, P. (1997). Aspects of the re-analysed climate: ECMWF re-analysis project report series. Technical Report 2, ECMWF.

Kandel, R., Viollier, M., Raberanto, P., Duvel, J. P., Pakhomov, L. A., Golovko, V. A., Trishchenko, A. P., Mueller, J., Raschke, E., Stuhlmann, R., and the International ScaRaB Scientific Working Group (ISSWG) (1998). The ScaRaB radiation budget dataset. *Bull. Amer. Met. Soc.*, **79**(5), 765–783.

Kiehl, J. T. (1994). On the observed near cancellation between longwave and shortwave cloud forcing in tropical regions. *J. Climate*, **7**(4), 559–565.

Kiehl, J. T. and Trenberth, K. E. (1997). Earth's annual global mean energy budget. *Bull. Amer. Met. Soc.*, **78**(2), 197–207.

Kilsby, C. G., Edwards, D. P., Saunders, R. W., and Foot, J. S. (1992). Water-vapour continuum absorption in the tropics: Aircraft measurements and model comparisons. *Quart. J. Roy. Meteorol. Soc.*, **118**, 715–748.

Klein, S. A. (1997). Synoptic variability of low-cloud properties and meteorological parameters in the subtropical trade wind boundary layer. *J. Climate*, **10**, 2018–2039.

Lal, M. and Ramanathan, V. (1984). The effects of moist convection and water-vapor radiative processes on climate sensitivity. *J. Atmos. Sci.*, **41**(14), 543–552.

Lamb, H. H. (1982). *Climate, History and the Modern World.* Methuen.

Lau, K. M., Ho, C. H., and Chou, M. D. (1996). Water vapor and cloud feedback over the tropical oceans: Can we use ENSO as a surrogate for climate change? *Geophys. Res. Lett.*, **23**(21), 2971–2974.

Le Treut, H. and Li, Z. X. (1991). Sensitivity of an atmospheric general circulation model to prescribed SST changes: Feedback effects associated with the simulation of cloud optical properties. *Climate Dynamics*, **5**, 175–187.

Li, Z., Leighton, H. G., Masuda, K., and Takashima, T. (1993). Estimation of SW flux absorbed at the surface from TOA reflected flux. *J. Climate*, **6**, 317–330.

Lindzen, R. S. (1990). Some coolness concerning global warming. *Bull. Amer. Met. Soc.*, **71**, 288–299.

Liou, K.-N. (1980). *An Introduction to Atmospheric Radiation.* Academic Press.

Long, C. N. (1996). *Surface Radiative Energy Budget and Cloud Forcing: Results from TOGA COARE and Techniques for Identifying and Calculating Clear Sky Irradiance.* Ph.D. thesis, The Pennsylvanian State University.

Lubin, D. (1994). The role of the tropical super greenhouse effect in heating the ocean surface. *Science*, **265**, 224–227.

Manabe, S. and Wetherald, R. T. (1967). Thermal equilibrium of the atmosphere with a given distribution of relative humidity. *J. Atmos. Sci.*, **24**, 241–259.

McClatchey, R. A., Fenn, R. A., Selby, R. A., Voltz, P. E., and Garing, J. S. (1972). Environmental research paper. Technical Report 411, Air Force Cambridge Research Labs., MA.

McCormick, M. P. (1987). SAGE II: An overview. *Adv. Space Res.*, **7(3)**, 219–226.

McNally, A. P. and Vesperini, M. (1996). Variational analysis of humidity information from TOVS radiances. *Quart. J. Roy. Meteorol. Soc.*, **122**, 1521–1544.

Meyers, G., Donguy, J. R., and Reed, R. K. (1986). Evaporative cooling of the western equatorial pacific ocean by anomalous winds. *Nature*, **323**, 523–526.

Minnis, P., Harrison, E. F., Gibson, G. G., Denn, F. M., Doelling, D. R., and Smith Jr., W. L. (1993). Radiative forcing by the erruption of mt. pinnatubo. *Science*, **259**, 1411–1415.

Mitchell, J. F., Senior, C. A., and Ingram, W. J. (1989). $CO_2$ and climate: a missing feedback? *Nature*, **341**(6238), 132–134.

Mueller, J. (1997). Geostationary earth radiation budget (GERB) instrument calibration plans. *Adv. Space Res.*, **19**(9), 1307–1316.

Nemesure, S., Cess, R. D., Dutton, E. G., DeLuisi, J. J., Li, Z., and Leighton, H. G. (1994). Impact of cloud on the shortwave radiation budget of the surface-atmosphere system for snow covered surfaces. *J. Climate*, **4**, 579–585.

Philander, G. S. (1990). *El Niño, La Niña and the Southern Oscillation.* Academic Press,London.

Philipona, R., Frohlich, C., Dehne, K., DeLuisi, J., Augustine, J., Dutton, E., Nelson, D., Forgan, B., Novotny, P., Hickey, J., Love, S. P., Bender, S., McArthur, B., Ohmura, A., Seymour, J. H., Foot, J. S., Shiobara, M., Valero, F. P. J., and Strawa, A. W. (1998). The Baseline Surface Radiation Network pyrgeometer round-robin calibration experiment. *J. Atmos. Oceanic Techno.*, **15**(3), 687–696.

Pierrehumbert, R. T. (1995). Thermostats, radiator fins and the local runaway greenhouse effect. *J. Atmos. Sci.*, **52**, 1784–1806.

Pinnock, S. and Shine, K. P. (1998). The effects of changes in HITRAN and uncertainties in the spectroscopy on infrared irradiance calculations. *J. Atmos. Sci.*, **55**, 1950–1964.

Pinto, J. O., Curry, J. A., and Fairall, C. W. (1997). Radiative characteristics of the Arctic atmosphere during spring as inferred from ground-based measurements. *J. Geophys. Res.*, **102**(D6), 6941–6952.

Prata, A. J. (1996). A new longwave formula for estimating downwelling clear sky radiation at the surface. *Quart. J. Roy. Meteorol. Soc.*, **122**, 1127–1151.

Räisänen, P. (1996). The effect of vertical resolution on clear-sky radiation calculation: Tests with two schemes. *Tellus*, **48A**, 403–423.

Ramanathan, V. (1981). The role of ocean-atmosphere interactions in the $CO_2$ climate problem. *J. Atmos. Sci.*, **38**, 918–930.

Ramanathan, V. and Collins, W. (1991). Thermodynamic regulation of ocean warming by cirrus clouds deduced from observations of the 1987 El Niño. *Nature*, **351**, 27–32.

Raval, A. and Ramanathan, V. (1989). Observational determination of the greenhouse effect. *Nature*, **342**, 758–761.

Raval, A., Oort, A. H., and Ramaswamy, V. (1994). Observed dependence of outgoing longwave radiation on sea surface temperature and moisture. *J. Climate*, **7**, 807–821.

Rind, D., Chiou, E. W., W.Chu, Lasen, J., Oltmans, S., Lerner, J., McCormick, M. P., and McMaster, L. (1991). Positive water vapour feedback in climate models confirmed by satellite data. *Nature*, **349**, 500–503.

Ringer, M. A. (1994). *Interannual Variability of the Earth's Radiation Budget and Cloudiness: A Satellite View.* Ph.D. thesis, Reading University.

Ringer, M. A. and Shine, K. P. (1997). Sensitivity of the Earth's radiation budget to interannual variations in cloud amount. *Climate Dynamics*, **13**, 213–222.

Rodgers, C. D. and Walshaw, C. D. (1966). The computation of infra-red cooling rate in planetary atmospheres. *Quart. J. Roy. Meteorol. Soc.*, **92**, 67–92.

Rossow, W. B. and Cairns, B. (1995). Monitoring changes of clouds. *Climate Change*, **31**, 305–347.

Rossow, W. B. and Schiffer, R. (1991). ISCCP cloud data products. *Bull. Amer. Met. Soc.*, **72**(1), 2–20.

Rossow, W. B. and Zhang, Y. C. (1995). Calculations of surface and top of atmosphere radiative fluxes from physical quantities based on ISCCP data sets. 2. validation and first results. *J. Geophys. Res.*, **100**, 1167–1197.

Rothman, L. S., Gamache, R. R., Tipping, R. H., Rinsland, C. P., Smith, M. A. H., Benner, D. C., Devi, V. M., Flaud, J. M., Camypeyret, C., Perrin, A., Goldman, A., Massie, S. T., Brown, L. R., and Toth, R. A. (1992). The HITRAN molecular database - editions of 1991 and 1992. *J. Quant. Spec. Rad. Trans.*, **48**(5-6), 469–507.

Rudman, S. D., Saunders, R. W., Kilsby, C. G., and Minnett, P. J. (1994). Water vapour continuum absorption in mid-latitudes: Aircraft measurements and model comparisons. *Quart. J. Roy. Meteorol. Soc.*, **120**, 795–807.

Running, S. W., Justice, C. O., Salomonson, V., Hall, D., Barker, J., Kaufmann, Y. J., Strahler, A. H., Huete, A. R., Muller, J. P., Vanderbilt, V., Wan, Z. M., Teillet, P., and Carneggie, D. (1994). Terrestrial remote-sensing science and algorithms planned for EOS MODIS. *Int. J. Remote Sens.*, **15**(17), 3587–3620.

Schneider, E. K., Lindzen, R. S., and Kirtman, B. P. (1997a). A tropical influence on global climate. *J. Atmos. Sci.*, **54**(10), 1349–1358.

Schneider, E. K., Kirtman, B. P., and Lindzen, R. S. (1997b). Upper tropospheric water vapour and climate sensitivity. Technical Report 45, COLA.

Schneider, S. H. (1972). Cloudiness as a global climate feedback mechanism: the effects on the radiation balance and surface temperature on variations in cloudiness. *J. Atmos. Sci.*, **29**, 1413–1422.

Seager, R., Kushnir, Y., and Cane, M. A. (1995). On heat flux boundary conditions for ocean models. *J. Phys. Ocean.*, **25**, 3219–3230.

Shaw, G. E., Stamnes, K., and Hu, Y. X. (1993). Arctic haze - Perturbation to the radiation-field. *Meteorology and Atmospheric Physics*, **51**(3-4), 227–235.

Shine, K. P. and Sinha, A. (1991). Sensitivity of the Earth's climate to height-dependent changes in water vapour mass mixing ratio. *Nature*, **354**, 382–384.

Simpson, G. (1927). Some studies in terrestrial radiation. *Mem. R. Meteor. Soc.*, **2**, 69–95.

Simpson, G. (1928). Further studies in terrestrial radiation. *Mem. R. Meteor. Soc.*, **3**, 1–26.

Sinha, A. and Harries, J. E. (1995). Water vapour and greenhouse trapping: The role of far infra-red absorption. *Geophys. Res. Lett.*, **22**(16), 2147–2150.

Sinha, A. and Harries, J. E. (1997). The Earth's clear-sky radiation budget and water vapour absorption in the far infrared. *J. Climate*, **10**, 1601–1614.

Sinha, A. and Shine, K. P. (1995). Simulated sensitivity of the earth's radiation budget to changes in cloud properties. *Quart. J. Roy. Meteorol. Soc.*, **121**, 797–819.

Slingo, A. (1990). Sensitivity of the Earth's radiation budget to changes in low clouds. *Nature*, **343**, 49–51.

Slingo, A. (1997). Assessing the treatment of radiation in climate models. *Ambio*, **26**(1), 52–57.

Slingo, A. and Slingo, J. M. (1988). The response of a general-circulation model to cloud longwave radiative forcing .1. Introduction and initial experiments. *Quart. J. Roy. Meteorol. Soc.*, **114**(482), 1027–1062.

Slingo, A. and Webb, M. J. (1992). Simulation of clear-sky outgoing longwave radiation over the oceans using operational analyses. *Quart. J. Roy. Meteorol. Soc.*, **118**, 1117–1144.

Slingo, A. and Webb, M. J. (1997). The spectral signature of global warming. *Quart. J. Roy. Meteorol. Soc.*, **123**, 293–307.

Slingo, A., Pamment, J. A., and Webb, M. J. (1998). A 15-year simulation of the clear-sky greenhouse effect using the ECMWF re-analyses: Fluxes and comparisons with ERBE. *J. Climate*, **11**, 690–708.

Slingo, J. M. (1980). A cloud parameterization scheme derived from GATE data for use with a numerical model. *Quart. J. Roy. Meteorol. Soc.*, **106**, 747–770.

Slingo, J. M. (1987). The development and verification of a cloud prediction scheme for the ECMWF model. *Quart. J. Roy. Meteorol. Soc.*, **113**, 899–927.

Soden, B. and Fu, R. (1995). A satellite analysis of deep convection, upper tropospheric humidity and the greenhouse effect. *J. Climate*, **8**, 2333–2351.

Soden, B. J. (1997). Variations in the tropical greenhouse effect during El Niño. *J. Climate*, **10**, 1050–1055.

Soden, B. J. and Bretherton, F. P. (1993). Upper tropospheric relative humidity from the GOES 6.7 $\mu m$ channel: Method and climatology for july 1987. *J. Geophys. Res.*, **98**(D9), 16669–16688.

Spencer, R. W. and Braswell, W. D. (1997). How dry is the tropical free troposphere? Implications for global warming theory. *Bull. Amer. Met. Soc.*, **78**, 1097–1106.

Stephens, G. L. (1984). The parameterizations of radiation for numerical weather prediction and climate models. *Mon. Wea. Rev.*, **112**, 826–867.

Stephens, G. L. and Webster, P. J. (1981). Clouds and climate: Sensitivity of simple systems. *J. Atmos. Sci.*, **38**, 235–247.

Stephens, G. L., Campbell, G. G., and Vonder Haar, T. H. (1981). Earth radiation budgets. *J. Geophys. Res.*, **86**(C10), 9739–9760.

Stone, R. S. (1997). Variations in western Arctic temperatures in response to cloud radiative and synoptic scale influences. *J. Geophys. Res.*, **102**(D18), 21769–21776.

Sun, D. Z. and Trenberth, K. E. (1998). Coordinated heat removal from the equatorial Pacific during the 1986-1987 El Niño. *Geophys. Res. Lett.*, **25**(14), 2659–2662.

Sutherland, R. A. (1986). Broadband and spectral emissivities (2-18 $\mu m$) of some natural soils and vegetation. *J. Atmos. Oceanic Techno.*, **3**, 199–202.

Thompson, S. L. and Warren, S. G. (1982). Parameterization of outgoing infrared radiation derived from detailed radiative calculations. *J. Atmos. Sci.*, **39**, 2667–2680.

Tiedtke, M. (1989). A comprehensive massflux scheme for cumulus parameterization in large-scale models. *Mon. Wea. Rev.*, **117**, 1779–1800.

Tselioudis, G., Rossow, W. B., and Rind, D. (1992). Global patterns of cloud optical thickness variation with temperature. *J. Climate*, **5**, 1484–1495.

Udelhofen, P. M. and Hartmann, D. L. (1995). Influence of tropical cloud systems on the relative humidity in the upper troposphere. *J. Geophys. Res.*, **100**(D4), 7423–7440.

Uppala, S. (1997). Observing system performance in ERA. ECMWF re-analysis project report series. Technical Report 3, ECMWF, Reading, England.

Valero, F. P. J., Collins, W. D., Pilewskie, P., Bucholtz, A., and Flatau, P. J. (1997). Direct radiometric observations of the water vapor greenhouse effect over the equatorial pacific ocean. *Science*, **275**, 1773–1776.

Vonder Haar, T. (1986). Surface radiation budget observations and analysis. Position paper in a report of the workshop on surface radiation budget for climate applications. *World Climate Research Program. WCP-115, WMO/TD*, **109**, 144p.

Walden, V. P., Warren, S. G., and Murcray, F. J. (1998). Measurements of the downward longwave radiation spectrum over the antarctic plateau and comparisons with a line-by-line radiative transfer model for clear skies. *J. Geophys. Res.*, **103**(D4), 3825–3846.

Watterson, I. G. and Dix, M. R. (1986). Influences on surface-energy fluxes in simulated present and doubled $CO_2$ climates. *Climate Dynamics*, **12**(5), 359–370.

Weare, B. C. (1995). Factors controling ERBE longwave clear sky and cloud forcing fluxes. *J. Climate*, **8**, 1889–1899.

Weaver, C. P., Collins, W. D., and Grassl, H. (1994). Relationship between clear-sky atmospheric greenhouse effect and deep convection during the Central Equatorial Pacific Experiment: Model calculations and satellite observations. *J. Geophys. Res.*, **99**(D12), 25891–25901.

Webb, M. J., Slingo, A., and Stephens, G. L. (1993). Seasonal variations of the clear sky greenhouse effect: the role of changes in atmospheric temperature and humidities. *Climate Dynamics*, **9**, 117–129.

Webster, P. J. and Lukas, R. (1992). TOGA COARE: The coupled ocean-atmosphere response experiment. *Bull. Amer. Met. Soc.*, **73**, 1377–1416.

Weller, R. A. and Anderson, S. P. (1996). Surface meteorology and air-sea fluxes in the western equatorial pacific warm pool during the TOGA coupled ocean-atmosphere response experiment. *J. Climate*, **9**, 1959–1990.

Wielicki, B. A., Barkstrom, B. R., Baum, B. A., Charlock, T. P., Green, R. N., Kratz, D. P., Lee, R. B., Minnis, P., Smith, G. L., Wong, T. M., Young, D. F., Cess, R. D., Coakley, J. A., Crommelynck, D. A. H., Donner, L., Kandel, R., King, M. D., Miller, A. J., Ramanathan, V., Randall, D. A., Stowe, L. L., and Welch, R. M. (1998). Clouds and the Earth's radiant energy system (CERES): Algorithm overview. *IEEE Trans. Geosci. Remote Sens.*, **36**(4), 1127–1141.

Wild, M., Ohmura, A., Gilgen, H., and Roeckner, E. (1995). Validation of general circulation model radiative fluxes using surface observations. *J. Climate*, **8**, 1309–1324.

Wild, M., Ohmura, A., and Cubasch, U. (1997). GCM-simulated surface energy fluxes in climate change experiments. *J. Climate*, **10**, 3093–3110.

Wu, M. L. C. and Chang, L. A. (1991). Differences in global sets of atmospheric and surface parameters and their impact on outgoing longwave radiation and surface downwelling flux calculations. *J. Geophys. Res.*, **96**(D5), 9227–9262.

Zhao, W., Khun, W. R., and Drayson, S. R. (1994). The significance of detailed structure in the boundary layer to thermal radiation at the surface in climate models. *Geophys. Res. Lett.*, **21**, 1631–1635.